2015

Damage analysis of wheel/rail contact associated to high adhesion condition

Khoa Duy Vo
University of Wollongong

UNIVERSITY OF WOLLONGONG

Damage analysis of wheel/rail contact associated to high adhesion condition

This thesis is presented as part of the requirements for the award of the Degree

DOCTOR OF PHILOSOPHY

of the

University of Wollongong

by

KHOA DUY VO

B.Eng.

Faculty of Engineering and Information Sciences

School of Mechanical, Materials and Mechatronic

March 2015

CERTIFICATION

I, Khoa D. Vo, declare that this thesis, submitted in fulfilment of the requirements for the award of Doctor of Philosophy, in the school of Mechanical, Materials and Mechatronic Engineering, University of Wollongong, Australia, is wholly my own work unless otherwise referenced and acknowledged. The document has not been submitted for qualifications at any other university or academic institution.

Khoa Duy Vo

March 2015

ACKNOWLEDGEMENTS

It would have been impossible to fulfil this doctoral dissertation without the help and support of the kind people around me, to only some of whom it is possible to give grateful mention here.

First and foremost, I wish to thank my supervisors, Professor Kiet Anh Tieu and Dr. Hongtao Zhu for offering me the outstanding opportunity to participate in such an excellent research group at University of Wollongong. Prof. Kiet has always been very supportive and constantly provided insightful discussions about the research. For his support and encouragement through the rough road to finish this thesis – personally and academically – I would like to express to him my sincere gratitude. I am also very grateful to Dr. Hongtao for his scientific advices and many discerning suggestions on my research. I also have to thank Dr. Buyung Kosasih, a lecturer at University of Wollongong, who has given valuable comments and constructive feedback on my publications as well as the research progress during the weekly group meeting.

I would like to express my appreciations to Professor Colin Cole, Dr. Maksym Spiryagin and other committee members of the project R3.119 “Locomotive Adhesion” funded by CRC for Rail Innovation, Australia. All your precious advices on my work during the monthly project meeting were very much appreciated. I will be forever thankful to CRC for Rail Innovation for awarding me scholarship to fulfil my PhD course, and giving me chances to meet and to work with many industrial experts. I would also acknowledge Susan Dole, Research and Education Manager at CRC for Rail Innovation for her caring and guidance since the days I began participating CRC for Rail Innovation as a research student.

Mao Liu, Bradley Davis, Peichun Xiao, Syamsul Hadi, Bingjing Ling, Yong Sun, Wenzhen Xia, and Lisa Bruffer, these are amazing people that I am very fortunate to meet, to work and to share the same office since 2011. Thanks so much for

everything! A special acknowledgement goes to my office mate, and also my house mate Youyou Wu, a brilliant and strong girl in too many ways! I would never forget all the days of working overtime during 2012 and 2013 when we were working hard together. She is the best friend I have ever had in Australia.

A talking about Vietnam: I would like to express my grateful appreciations to my supervisors in Ho Chi Minh City University of Technology, Dr. Hoang T. Nguyen, Dr. Anh T. Tran, Dr. Thao S.T. Nguyen, who have always been very supportive and encouraged me to pursue a higher degree.

Going back to my pre-UOW days, I have lovely Vietnamese friends to thank. Thank you to: Linh Nguyen, Van Nguyen, Duc Le, Dung Pham... and, I have to especially thank Trang Pham, whom I consider as my best friend ever since we met in elementary school. They have always been incredibly kind to me, and immensely help me through the difficulties when I first came to Australia until the end of PhD road.

Finally, a special thank to my family for providing me with their unequivocal support without which I could not have completed my dissertation. My parents always encourage me and gave me freedom to pursue my goals. Words cannot express how grateful I am to my parents and brother for all of the sacrifices that you have made on my behalf. Your prayer for me was what sustained me thus far. I dedicate this dissertation to my family.

PUBLICATIONS

K. D. Vo, A. K. Tieu, H. T. Zhu, and P. B. Kosasih, "A 3D dynamic model to investigate wheel-rail contact under high and low adhesion", International Journal of Mechanical Sciences, vol. 85, pp. 63-75, 2014. ***(IF 2.168)***

K. D. Vo, H. T. Zhu, A. K. Tieu, and P. B. Kosasih, "FE method to predict damage formation on curved track for various worn status of wheel/rail profiles", Wear, vol. 322-323, pp. 61-75, 2015. (***IF 1.862)***

K. D. Vo, H. T. Zhu, A. K. Tieu, and P. B. Kosasih, "A comparison of stress and heat generated by AC versus DC locomotives under diverse operational conditions", Wear, vol. 328-329, pp. 186-196, 2015**.** (***IF 1.862)***

K. D. Vo, A. K. Tieu, H. T. Zhu, and P. B. Kosasih, "The influence of high temperature due to high adhesion condition on rail damage", Wear, vol. 330-331, pp. 571- 580, 2015. (***IF 1.862)***

K. D. Vo, H. T. Zhu, A. K. Tieu, and P. B. Kosasih, "Rolling contact stress states of two contact points on curved track", the 10th World Congress on Railway Research, Sydney, Australia, 2013.

K. D. Vo, A. K. Tieu, H. T. Zhu, and P. B. Kosasih, "A tool to estimate the wheel/rail contact and temperature rising under dry, wet, oil conditions", Computers in Railways XIV: Railway Engineering Design and Optimization, vol. 135, p. 191, 2014.

K. D. Vo, A. K. Tieu, and H. T. Zhu, Wheel-rail contact by FEM modelling, in Final Report Project R3. 119: Locomotive Adhesion, CRC for Rail Innovation, Australia, 2013.

ABSTRACT

In wheel-rail contact, the locomotive adhesion characterises the capability of the locomotive to convert available friction into traction at the interface. Recently developed AC (Alternating Current) drive induces a higher adhesion level compared to DC (Direct Current) drive. This significantly affects the wheel-rail contact conditions such as damage initiation, high contact temperature due to frictional rolling, and wear of the rails.

Three-dimensional (3D) elasto-plastic finite element model (FEM) was used in this thesis to examine the wheel-rail contact on a straight track. Some sub-components of the track such as railpads, sleepers and ballast were also included in the model. Rolling contact stress states and material response of wheel/ rail under three contact situations (high adhesion, low adhesion and full slip) were investigated. Canted and non-canted rails were considered to determine the effect of the cant angle on the contact stress levels. Furthermore, the effects of contact curvature on the contact zone and contact pressure were also observed, and the response of material was predicted by a shakedown diagram.

The more complicated rolling phenomenon of the wheel on a curved track was also investigated numerically in this thesis. Due to the influences of super-elevation (also called track cant), angle of attack (AOA) and rail cant, stress states on the high rail are significantly different from that on the low rail. The new and worn profiles were considered in the simulation to examine different contact situations: new wheel/new rail, new wheel/worn rail, and worn wheel/worn rail contacts. Material responses, the formation of rail corrugation and fatigue defects on both low and high rails were anticipated based on the results from simulations.

In order to compare stress states AC and DC locomotives, two locomotive models of AC (C44ACi) and DC (Cv40-9i) currently run in Australia were evaluated under diverse operational situations (wheel loads, angle of attack and adhesion level). The

software LS-DYNA was employed to build up a comprehensive wheel/rail contact model. The numerical model was constructed based on Australian wheel/rail profiles. Moreover the analytical method was also applied to evaluate the temperature rise on the rail, respectively. Calculation of wear volume on rail was eventually performed using the Archard's wear model.

Finally a 3D coupled thermal-mechanical FE model was developed to examine the temperature rise due to high adhesion contact and the thermal influence on residual stress-strain, wear and rail life. The numerical model employed the moving heat source code developed by Goldak. The mechanical and thermal properties of the rail material were governed by temperature. The influence of repeated multi-passes from multiple wheels on one point of the rail was also taken into account. Moreover the formation of white etching layer (WEL) on the rail surface combined with rolling cycles can potentially lead to rail damage. A sub-2D FE model of WEL was also carried out to examine the stress state on the WEL if formed on the rail surface.

The current thesis focuses on modelling wheel-rail contact under high adhesion condition, and explanation of the subsequent damage formation on the rail. The model provides a better understanding of the influences of high adhesion condition on contact stress states, damage initiation and also temperature rise on the rail. To the best of the author's knowledge, the simulation of wheel-rail contact under high adhesion condition has not been studied elsewhere, and is presented in this study for the first time.

TABLE OF CONTENTS

LIST OF TABLES

LIST OF FIGURES

NOMENCLATURES

F_{DYN} = dynamic load

K_{DYN} = magnification factor

F_{STAT} = static load

a = semi-axis on the longitudinal direction

b = semi-axis on the lateral direction

F_x = longitudinal wheel load

F_y = lateral wheel load

F_z = normal wheel load

f_T = total tangential contact force (creep force)

f_x = longitudinal contact force on the rail head (longitudinal creep force)

f_y = lateral contact force on the rail head (lateral creep force)

f_z = vertical contact force on the rail head

$f_x^{'}$ = longitudinal contact force on the rail gauge

$f_y^{'}$ = lateral contact force on the rail gauge

$f_z^{'}$ = vertical contact force on the rail gauge

Σf_x = total longitudinal contact force

Σf_y = total lateral contact force

Σf_z = total vertical contact force

R^w, R^r = the radii of the wheel and rail at the contact zone

K_1, K_2, K_3, K_3, K_4 = constants which depend on material properties and wheel-rail geometries

m, n = Hertz coefficients, functioned by the angular parameter

ν = Poisson's ratio

ν^w, ν^r = Poisson's ratio of the wheel and rail material

G = material shear modulus

G^w, G^r = shear modulus of the wheel and rail material

E = Young's modulus

E^w, E^r = Young's modulus of the wheel and rail material

ω = angular velocity

ξ = creepage

ξ_x = longitudinal creepage

ξ_y = lateral creepage

φ = spin creepage

μ = coefficient of friction

μ_s = static coefficient of friction

μ_d = dynamic coefficient of friction

V = wheel forward velocity

V_T = translational velocity (Carter theory)

V_C = circumferential velocity (Carter theory)

k = Carter's creepage coefficient

Cij = Kalker's coefficients

L_x, L_y = elastic coefficients (or flexibilities) of the contact (Kalker's simplified theory),

u^{wr} = tangential surface displacement

γ = slip velocity

T = temperature

T_o = ambient temperature

P_o = maximum contact pressure

P_n = contact pressure at node number n

τ = frictional shear stress

τ_x = frictional shear stress on the longitudinal direction

τ_y = frictional shear stress on the lateral direction

τ_{lim} = limit frictional shear stress

Θ = rail cant angle

d = distance between two centres of the contact zones on the same rail

l = thickness of hardened layer on the rail

CHAPTER 1

INTRODUCTION

1.1. General background

Since the primary introduction in 16th century, railway vehicles have been operated for a few centuries. Although their performances have been through momentous improvements, railway accidents however keep happening unexpectedly. For instance, a railway accident occurred on 19 April 2008 when a train (5PS6) moving from Perth to Sydney derailed near Bates, SA Australia. The investigators found that the rail failed due to a bolt-hole crack initiated and propagated by the passing of the previous train (5MP5). When the train 5PS6 travelled over the rail, the crack developed fully in size until the rail was totally broken. The train loads caused the failure of sleepers, a secondary rail fracture and a small section of the rail was dislocated. The high impact forces caused the failure of the track system until the freight wagons inevitably derailed. Thirteen wagons were derailed and about 800 m of track was sabotaged. Luckily there were no injuries [1].

In Australia, the responsibility for rail safety is shared by government and industry. To assist in maintaining and continuously improving rail safety, governments from each states and the Northern Territory have implemented rail safety legislation and established a rail safety regulator. The regulators are responsible for establishing standards in order to meet community expectations and maintain public confidence. Plotted in Figure 1.1 are the rates of running line derailments per million km

travelled in each states of Australia [2]. It can be observed from the graph that derailment still happened regardless the effort of railway operators to improve the vehicle.

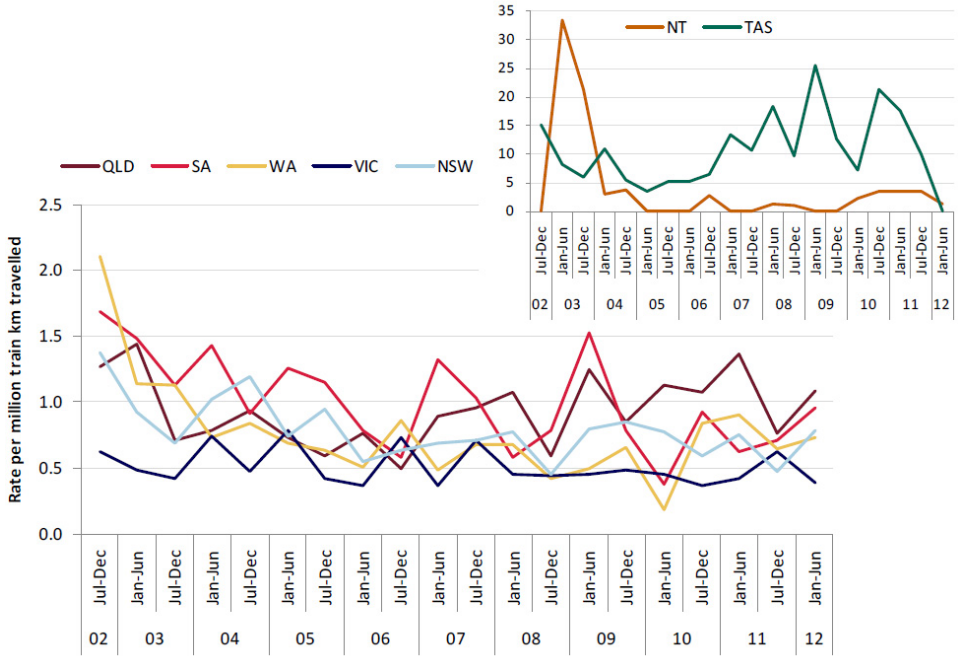

Figure 1.1 Normalised biannual rate of Australian running line derailments per million km travelled by jurisdiction and year, 1 July 2002 to 30 June 2012 [2]

One of the recent developments of Australian Railway is the introduction of the new AC (Alternative Current) locomotive, which has allowed the train to operate in a more advanced adhesion condition. In a report to the Australian railway network, Noel et al. [3] summarised the benefits of the AC-traction-motor unitization. The greatest gain was the much higher adhesion level that can be achieved from using AC traction. For example, if using the super-series creep control of EMD (Electro Motive Diesel), the adhesion level obtained from DC (Direct Current) drive was between 29 to 30%. However with AC traction locomotive, the adhesion level as high as 37 to 38% were potentially achievable [4].

Although the new AC drive has been operated for many years, the questions regarding the potential effects of the higher adhesion level on the rail vehicle dynamic behaviours, the wheel-rail contact characteristics and the track components reactions are still uncertain. Therefore further investigations of wheel-rail interaction under high adhesion condition need to be carried out.

1.2. Importance of this research project and research question

The more AC locomotives are utilized, the more frequent high longitudinal force is exerted on the track structure, which may cause more frequent damage to the track systems such as wheel-rail plastic flow, cracks on rail and substructure, and wheel-rail rolling contact fatigue defects. Therefore the wheel/rail contact problems associated to high adhesion conditions need to be studied in details.

The research explores the impacts of using high adhesion locomotives on different scenarios of wheel-rail contact on a straight/curved track, or by the combination of diverse locomotive types (AC and DC locomotives). Based on the investigated data, a better planning of maintenance schedule of the railway system will be forthcoming to maximize the service life of the train and tracks and minimize the railway accidents.

The overarching research question that this thesis sought to answer was:

How does the high adhesion condition affect the wheel/rail contact, the rail damages and the rail life?

1.3. Thesis overview

The lines of investigation in this study were directed by a number of research sub-questions. These questions set the theme for each chapter and research outcomes. These sub-questions and chapters are:

- Chapter 2: How have the others approached and what have been found in wheel-rail contact analysis so far?
- Chapter 3: Which methods and tools have been applied to answer the questions raised in this research project?
- Chapter 4: On a straight track, what are the impacts of high adhesion conditions on the wheel-rail contact characteristics and material behaviours?
- Chapter 5: On a curved track, how does the high adhesion level affect the stress states and the formation of rail damages?
- Chapter 6: Under diverse operational conditions (such as angle of attack, contact loads, or friction), how are the stress states and heat generated by AC versus DC locomotives?
- Chapter 7: How are the three-dimensional (3D) temperature distributions on the rail and the influences of high temperature due to high adhesion condition on rail damage?
- Chapter 8: What are the main conclusions obtained from this research and the recommendation for future works?

Chapter two provides an exploration of the literature relating to wheel-rail contact analysis up to date. This chapter establishes a foundation body of information from which the research direction of the thesis is determined. The review summarises the analytical, experimental and numerical approaches of wheel-rail contact so far.

Chapter three presents the methods and the devices applied in this study. Finite element method (FEM) was mainly applied with the supports of the commercial software ANSYS/LS-DYNA and high performance computer. Other than that, some other software products were also utilized such as CONTACT, LS-PREPOST, PRO/ENGINEER WILDFIRE, etc.

Chapter four focuses on the wheel-rail contact on a straight track under three contact situations, including high and low adhesion, and full slip. The stress states exerted on the rail were completely analysed. Furthermore the material behaviour of rail was also predicted by using the shakedown map.

Chapter five gives an estimation of rail damage formation on a curved track for different worn status of wheel-rail profiles. The detailed comparisons of stress states on the new/worn low/high rails were presented. Some predictions related to damage mechanisms and the responses of the rail material to the contact stresses on the rails had also been provided.

Chapter six compares the wheel-rail contact stresses generated by AC and DC Drives on both the worn low/high rails. The investigation was carried out on the leading and trailing axles of the 3rd locomotive, where the axle load is more severe than that on the 1st and 2nd locomotives. Two types of locomotives (AC and DC) currently run in Australia were evaluated under diverse operational situations (wheel loads, angle of attack and adhesion level). Moreover the temperature rise on the rail was evaluated analytically.

Chapter seven aims to determine the temperatures rise due to high adhesion contact and the thermal influence on the rail wear life. The three-dimensional (3D) elasto-plastic finite element model was applied to evaluate the growth of temperature, residual stress and strain. The numerical model was constructed in the commercial software ANSYS/LS-DYNA with the implementation of moving heat source code developed by Goldak. To predict the formation of White Etching Layer (WEL) and the rail life, the influence of multi-passes from multiple wheels of the locomotives on one point of the rail was also considered. Moreover, a sub-2D-FE model of WEL was also used to examine the stress states and contact forces on the WEL.

Chapter eight summarises the primary conclusions of the research project related to wheel-rail contact problems under high adhesion conditions. Some recommendations for future study were also included.

CHAPTER 2

LITERATURE REVIEW OF WHEEL-RAIL CONTACT

In this chapter, a summary of up-to-date wheel-rail contact investigations was presented. The descriptions of the railway system and the operation of the AC and DC locomotive were first introduced. Theoretical and numerical models to predict the contact patch behaviour in terms of the normal and tangential stresses were discussed in the next sub-sections. The influence of heat generation on the contact zone and surface damage mechanisms were eventually considered in the final stage of this literature review.

2.1. Overview of railway system

In this part of the literature, the differences between AC and DC locomotive drives, the constituent elements of the track, and loading on the railway system are described.

2.1.1. AC versus DC drives

The AC Drive has been launched for over two decades and is now being applied in railway locomotive. In comparison to DC type, AC drive has shown major improvements such as slip control, a higher adhesion values, better maintainability and braking efficiency. Moreover the number of locomotives would also be reduced, and a larger load can be hauled. These benefits have been published as in [5]. So the question here is what makes a locomotive with an AC drive more superior than the DC one?

Basically the main AC drive's excellence if compared to DC drive is its circuitry. The name DC standing for Direct Current is originated from the current's ability to travel in only one direction along a conductor. In contrast, the so-called AC in short for Alternating Current (also known as Variable Frequency Drive) operates in a very different fashion. The AC current can rapidly change the direction in a very short period of time [6]. Illustrated in Figure 2.1 are the currents of the two types of drives.

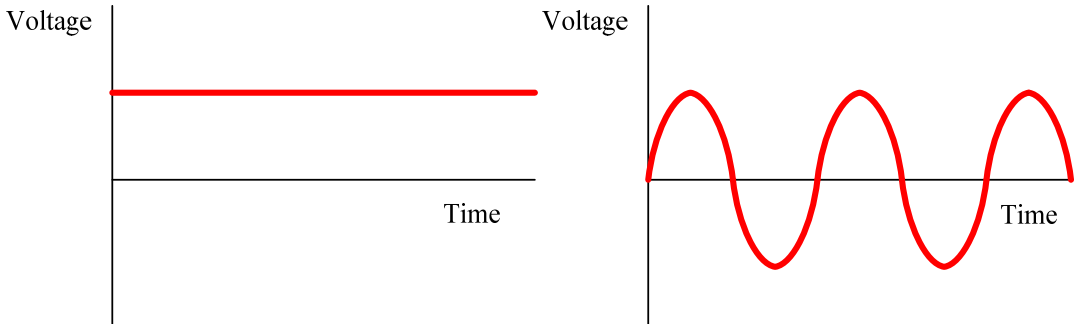

(a) DC Current (b) AC Current

Figure 2.1 Diagrammatic representations of two current types

In an ideal condition (clean and dry contact surfaces), the coefficient of friction (COF) between the wheel-rail contact can be very high. The COF measured on track and in the laboratory was compared by Olofsson and Telliskivi [7]. For non-lubricated tests (dry contact), the values were roughly the same and varied between 0.5 and 0.6. For a full-scale lubricated rail (wet and/or oil/grease lubricated), the coefficient of friction was lower and changed in the range of 0.2 to 0.4. Harrison et al. [8] applied the TriboRailer to measure to the friction coefficient. Under dry

condition, the coefficient of friction was approximately 0.5, and it varied between 0.05 and 0.3 under lubricated condition. The assorted locomotive adhesion corresponds to the ability of converting the available friction into usable friction at the contact interface. The value of adhesion is normally around 28% for DC, while it can be varied substantially to 38% for AC [4].

The three foremost reasons which help AC Drive to produce a higher adhesion level are that [9]:

- First of all, for DC, once wheel slip occurs, the traction motor tends to speed up, and runs away if the load is not decreased quickly. The increasing of slippage leads to a reduction of the friction coefficient and the traction load. The maximum adhesion, thus, is achieved by running at a secure limit below the maximum theoretical level. In contrast, the AC can create a rotating magnetic field which spins about 1% faster than the motor. Since the rotor cannot exceed the field speed, if a small slip which is less than 1% occurs, it can rapidly find out, and the axle load will be outright reduced by the drive.
- Secondly, different control settings produce various power levels which cannot generate a constant motor torque and speed in DC Drive. The tractive effort, hence, is influenced hugely by each operating level, and the maximum adhesion is hardly reached. For AC, however, the torque level can be controlled to permit a constant tractive effort for a high range of available adhesion.
- Finally the tractive effort is known to be in proportion to the weight on the drives. As a load is being dragged by the locomotive, the weight has a tendency to be transferred from the front axle to the rear axle of each track, and may be diminished at maximum tractive effort. In DC systems, the motors are fed from a common source, and the tractive effort will be calculated by the lightest axle. Thus, in effect, the equivalent locomotive weight is also reduced. On the contrary, the ability of weight transfer compensation has supported AC traction in improving adhesion level. When the lead axle experiences a light load, the AC drive system will reduce power

to that axle and apply more power to the rear axle without incurring wheel spin.

For a standard friction braking, the braking potentiality is in proportion to the weight of locomotive. However, with AC traction, since the way to eliminate the wheel slip in braking and in traction are the same; the braking produced by AC Drive, hence, is much higher than DC locomotives. Additionally, the higher adhesion levels in AC cause the locomotive can again lighter for the same amount of braking.

All in all, the AC Drive systems produce a larger adhesion range because of its ability to eliminate wheel slip and compensate for weight transfer. That would support the AC locomotive to provide more tractive effort for the same weight with DC locomotive.

2.1.2. Description of the railway system

In railway system, the main functions of the track are guiding the train, carrying the loads and distribute the loads to a larger area. For instant, a normal load of 10 tonnes, would create a few square centimetres contact zone, and is distributed to more than one square meter [10]. The structure of a track is shown in Figure 2.2, which includes some components such as rails, fastening, sleepers, ballast and sub-grade. The details of each component are as follows:

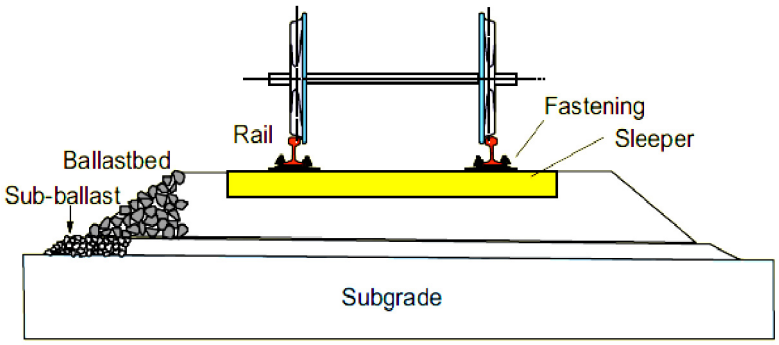

Figure 2.2 Cross section of the track system [11]

- Rail-pad and fastening [12-13]: The railpad's shape is usually a thin rectangular plate placed between the rail and the steel sleeper (timber sleeper may not need railpad). The railpad's applications are to protect sleepers from wear and damage due to the high impact loading, and also to reduce the high frequency vibration. The railpad stiffness is normally higher than the stiffness of the fastening. Thus the existence of fastening is usually neglected in track dynamics investigation. The role of fastening is to fix the rail in position and to prevent the rail from rolling over when it is affected by lateral forces.
- Sleeper [14-15]: The sleeper also plays an important role in track dynamic as well as railpad. In addition to electrical insulation benefit, this component allows the loads acting on the rail to transfer down to the ballast. The concrete sleeper has been widely used recently to replace the timber sleeper.
- Ballast and sub-ballast [16-17]: The standard ballast has the depth of 0.3 m. However, it is compacted to 0.5 m around the sleeper ends to maintain the lateral stability [10-11]. Years ago, the importance of ballast was not properly estimated, and the material placed beneath sleepers was not suitable for application. The old ballast were made from ashes, chalk and clay [18]. Nowadays the materials to form high-quality ballast consist of angular, crushed, uniformly-graded hard stone and rocks such as granite or limestone. Ballast supports the track against the loads from the train and keeps the sleepers aligned. The sub-ballast is usually made from sand and prevents the penetration of ballast and sub-grade.

From the dynamic point of view, each of the components above has significant influences on the operation of the railway system. Therefore study of the track system should account for the effects of these track components.

2.1.3. Loads on the track system

The wheel loads acting on the rail can be divided into three components, which are vertical, lateral and longitudinal forces. The vertical force results from the weight of the wheel and the car bodies. The lateral force is generated due to the movement of the wheelset on the rail, and is especially high on the curved track. The longitudinal force is the traction force which is produced by the locomotives. In general, the magnitude of the forces acting between the wheel and the rail must be set to a limit by railway organizations. For instance, to avoid any initiation of surface damages on the rail surface such as crack or plastic deformation, the international union of railways (UIC) sets the vertical wheel load to below 112.5 kN per wheel for static load, and from 160 kN to 200 kN per wheel for dynamic load depending on maximum speed of the train. When a train running on a small-radius-curved track (less than 600 m), the force is set to a limit of 145 kN for the quasi-static vertical force and 60 kN for the quasi-static lateral force [19].

Likewise the forces at the contact patch also include normal and two tangential components (longitudinal component acting along the running direction, and lateral component acting in the plane normal to the running direction). Illustrated in Figure 2.3 are the three elements of the contact forces.

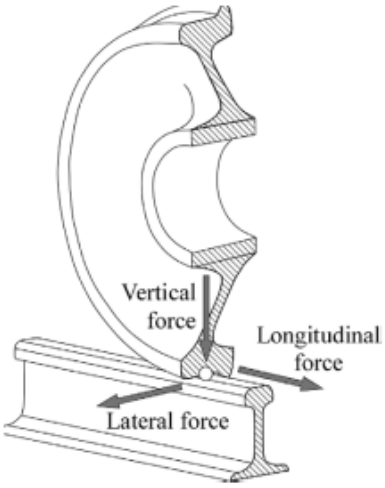

Figure 2.3 Contact forces at wheel-rail contact zone [20]

The loads producing at the contact area can be more severe due to the dynamic effects of the railway system [17, 21-24]. The dynamic effect of the whole system is formed by the car and bogies motion, the response of the track's sub-components such as ballast and sub-grade [23, 25]. For a static axle load, the dynamic load F_{DYN} can be estimated by multiplying the static load F_{STAT} with a magnification factor K_{DYN} which depends on the properties of the train and the train speed:

$$F_{DYN} = K_{DYN}F_{STAT} \tag{2-1}$$

Bahn [20] suggested the magnification factor could be calculated from the equation:

$$K_{DYN} = 1 + 3n\varphi \tag{2-2}$$

The value of n which depends on types of tracks varies from 0.15 to 0.25 and the magnitude of φ is:

$$\varphi = \begin{cases} 1 & \text{for } V \leq 60 \text{ km/h} \\ 1+\dfrac{0.5(V-60)}{190} & \text{for } 60 \leq V \leq 300 \text{ km/h (passenger trains)} \\ 1+\dfrac{0.5(V-60)}{80} & \text{for } 60 \leq V \leq 140 \text{ km/h (freight trains)} \end{cases} \tag{2-3}$$

2.1.4. Characteristics of the wheel-rail contact

The railway vehicle is designed to have some unique properties such as hunting motion, self-steering ability, and lateral dynamics which are generated from the wheel-rail guidance system and wheel-rail geometries. The wheel-rail profiles are always designed to follow the standards which depend on the operational conditions in each country. The main sections of a wheel profile include flange, tread and chamfer as plotted in Figure 2.4. The wheel profiles are normally inclined at a small angle. Drawn in Figure 2.5 are the main parts of rail head consisting of the head and gauge corners.

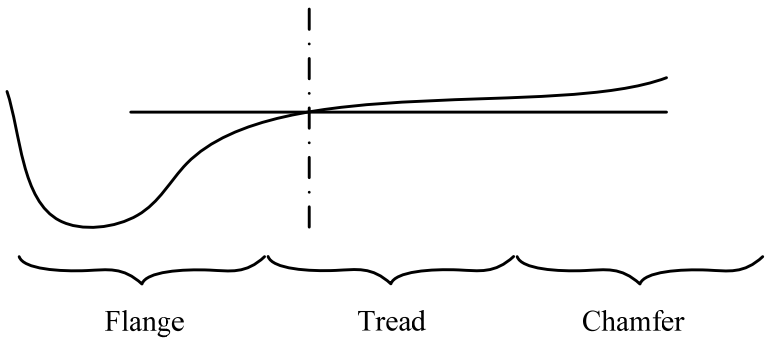

Figure 2.4 Sections of a wheel profile [10]

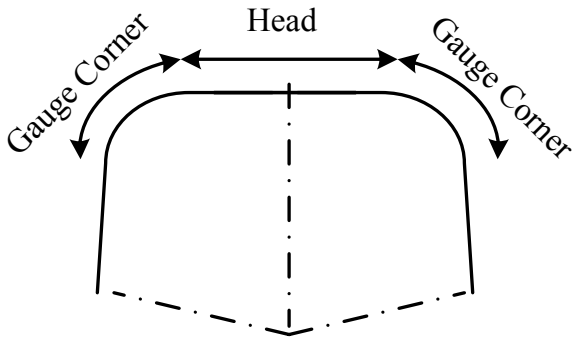

Figure 2.5 Sections of a rail profile

In the contact zone between two surfaces, the contact forces must be high enough to allow braking and providing traction; and also should be low enough to permit the wheel rolling with little resistance. The magnitudes of the contact forces depends on

the adhesion coefficient; i.e. the ratio of the tangential force and normal force. The adhesion condition is affected by many factors such as lubrication conditions, wheel-rail materials, and the profiles of contact bodies, contact temperature and the speed of the train. Numerous experiments [26-30] have been conducted to analyze its influence on the contact surfaces with the twin-disc tests or the wheelset equipments.

Doi et al. [29] designed a new experimental equipment called Creep Tester which could be utilized with the rail in the field, and a Windows PC program to control the machines. This machine could appraise the influence of the realistic contamination on the contact surface. The values of yaw angles, normal force were easily set up by using this device and the creep force – creepage curves could also be acquired.

Jin et al. [28] proposed a full-scale model with actual wheel and rail profile to simulate the wheel-rail adhesion. Different contact situations were examined to consider the influence of environmental conditions on adhesion under a variety of loads and speeds. Various contaminations such as dry, water and oil contact surfaces were also applied. The experimental results showed that an increase of the rolling speed would reduce the adhesion coefficient in the case of water lubrication. On the contrary, the adhesion coefficient was with an oil contamination. Moreover the larger was the axle load, the lower the adhesion coefficient regardless of the changes of speed and contamination.

Gallardo-Hernandez et al. [31] carried out the twin-disc test models to calculate the adhesion coefficient under diverse contact conditions (dry, wet and oil). His works also proved that the adhesion was reduced with an increase of train speed and contact forces. Other experimental studies of wheel-rail adhesion conditions were demonstrated in [8, 26, 32], and the comparison between experimental methods are shown in Table 2.1.

Table 2.1 Comparison of adhesion coefficient by a variety of test methods [31]

Authors	Test apparatus	Load/Contact pressure	Velocity (km/h)	Test Condition	Adhesion coefficient
Zhang et al. [26]	Full-scale roller-rig (using an actual bogie)	44 kN	10-70	Dry	0.57-0.5
		67 kN	10-70	Dry	0.55-0.44
		44 kN	120-240	Wet	0.13-0.07
		67 kN	80-240	Wet	0.11-0.05
		67 kN	140-300	Oil	0.055-0.045
		135 kN	140-300	Oil	0.05-0.04
Harrision et al. [8]	Triborailer (used on actual track) Push tribometer			Dry	0.52
				Dry	0.7
Nagese [32]	Instrumented bogie on test vehicle (run on test track and actual routes)	Variable	Variable	Dry	0.2-0.4
				Wet	0.05-0.2
				Oil	0.05-0.07
				Leaves	0.025-0.1
Gallardo-Hernandez et al. [31]	Twin-disc	1500 MPa 7.7 kN	3.54	Dry	0.6
			3.54	Wet	0.2
			3.54	Oil	0.07

In recent studies of wheel-rail contact [27, 33-34], a natural third body has been discovered on the surfaces of both locomotive wheels and rails. This solid interfacial

layer is comprised of non-oxidized particles and contamination from the wheel and the rail. The observations of the layer were examined by different analysis techniques such as optical microscopy and scanning electronic microscopy (SEM) and X-ray energy dispersive analysis (EDX), or metallographic cross-sections [27]. Niccolini et al. [33] had carried out the experiments to highlight the presence of the third body and to find out the influence of the third body on adhesion. The thickness of this layer ranged from a few micrometers to several dozen micrometers. The results obtained from experiments showed that without the third body, the adhesion would be limited. The on-site experiments also proved that the existence of the natural third body could help to reduce the wear and fatigue on the contact surfaces.

As the wheel travels on the rail, the appearances of the contact zone depend on the property of the track (straight track or curved track) and the status of the wheel-rail profiles (new or worn profiles). The contact situation can be any types performed in Figure 2.6:

- *The one-point contact case* [35] or the non-conformal contact is the contact between the two convex bodies. The contact patch is usually located on the top surface of the wheel tread and the rail head.
- *The two-point contact case* [36-38] includes one conformal contact and one non-conformal contact. The conformal contact is the contact between a convex body and a concave body, and the two contact surfaces are fitted each other. In wheel-rail contact, this kind of contact normally appears at the wheel flange/rail gauge when the wheel runs on a curved track.

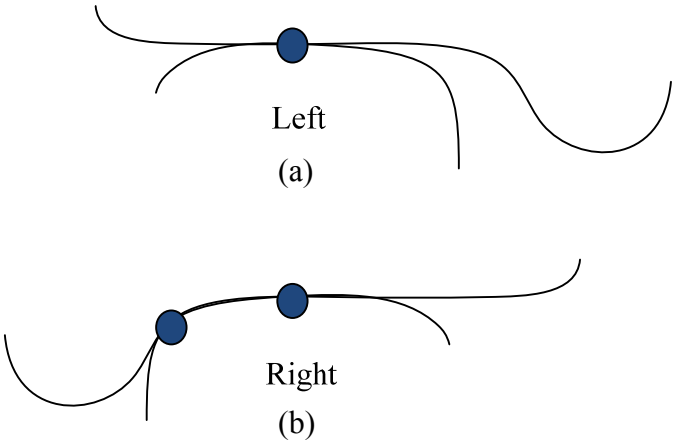

Figure 2.6 Possible contact situations between the wheel and the rail [39] (a) one-point contact (b) two-point contact

The contact areas either on the rail head or rail gauge are just a small patch compared to the rest of the bodies; and the high contact pressure is produced as a result of transferring the large force to a tiny patch. The stresses producing in the contact patch so-called contact stresses include normal stresses and two components of tangential stresses. In order to investigate the responses of contact patch, the normal and the tangential contact problems will be presented in the next sections.

2.2. The normal problem of wheel-rail contact

There are two kinds of computational approaches to estimate the wheel-rail contact problems, namely numerical and theoretical methods. To save time and cost, the investigations for the simple wheel-rail contact related problems are usually based on some classical theories. One of the popular theories to examine the normal contact problem is the one written by Heinrich Hertz (Feb 22. 1857 – Jan 1, 1894) [40-41].

2.2.1. Hertz's theory (1882)

Since the first introduction in 1882 [40-41], Hertz's theory has been commonly utilized due to its reasonable accuracy in most of wheel-rail contact situations. The geometry of the contact zone and the distribution of contact pressure can be determined from this theory.

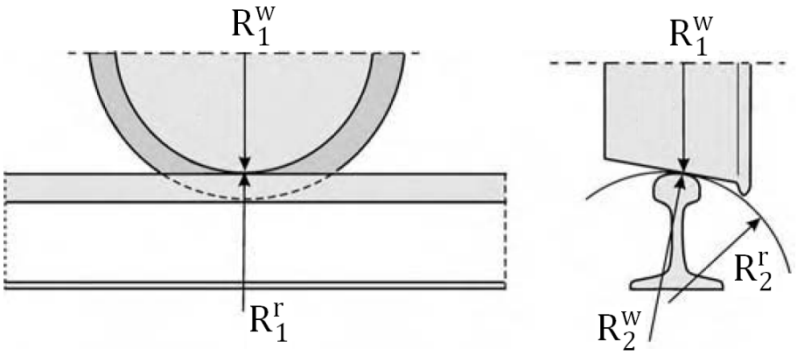

(a)

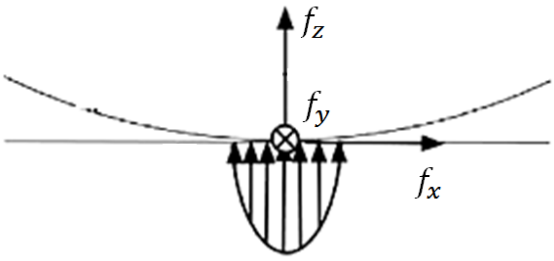

(b)

Figure 2.7 Wheel-rail contact (a) Wheel-rail curvature radii [42] (b) Wheel-rail contact forces [43]

The most important assumptions in Hertz's theory are [10]:

- The two contact bodies are linear elastic materials.
- The elastic displacement and the stresses become unnoticeable far from the contact area.
- The radii of the bodies at the contact must be larger than the contact size (semi-infinite bodies are assumed).
- The surfaces are smooth.
- The contact surface is elliptical and the contact pressure distribution is semi-ellipsoid.

Since the contact area is elliptical, the contact pressure is performed as the following equation:

$$P_z(x,y) = P_o\sqrt{1-\frac{x^2}{a^2}-\frac{y^2}{b^2}} \quad with \begin{cases} -a \le x \le a \\ -b \le y \le b \end{cases} \qquad (2-4)$$

in which a and b are the semi-axes on the longitudinal and lateral directions, the relationship between the maximum pressure P_o and the semi-axes is given by

$$P_o = \frac{3f_z}{2\pi ab} \qquad (2-5)$$

The semi-axes of the contact zone are defined as follows:

$$a = m\left[\frac{3\pi f_z(K_1+K_2)}{4K_3}\right]^{\frac{1}{3}} \qquad (2-6a)$$

$$b = n\left[\frac{3\pi f_z(K_1+K_2)}{4K_3}\right]^{\frac{1}{3}} \qquad (2-6b)$$

In equations 2-6a and 2-6b, K_1, K_2, K_3 are constants which depend on material properties, geometries of the wheel and rail, and are performed as follows

$$K_1 = \frac{1-(\nu^w)^2}{\pi E^w} \qquad (2-7a)$$

$$K_2 = \frac{1-(\nu^r)^2}{\pi E^r} \qquad (2-7b)$$

$$K_3 = \frac{1}{2}\left(\frac{1}{R_1^w}+\frac{1}{R_2^w}+\frac{1}{R_1^r}+\frac{1}{R_2^r}\right) \qquad (2-7c)$$

The Hertz coefficients m and n are functions of the angular parameter θ which is given by

$$\theta = \frac{1}{cos\left(\frac{K_4}{K_3}\right)} \qquad (2-8)$$

where

$$K_4 = \frac{1}{2} + \sqrt{\left(\frac{1}{R_1^w} - \frac{1}{R_2^w}\right)^2 + \left(\frac{1}{R_1^r} - \frac{1}{R_2^r}\right)^2 + 2\left(\frac{1}{R_1^w} - \frac{1}{R_2^w}\right)\left(\frac{1}{R_1^r} - \frac{1}{R_2^r}\right)\cos 2\psi} \qquad (2-9)$$

the axes of the wheel and the rail are not always parallel, and can differ by an angel ψ. The values of *m* and *n* are shown in Table 2.2

Table 2.2 Hertz Coefficients m and n

θ(deg)	**m**	**n**	**θ(deg)**	**m**	**n**	**θ(deg)**	**m**	**n**
0.5	61.4	0.1018	10	6.604	0.3112	60	1.4186	0.717
1	36.89	0.1314	20	3.813	0.4125	65	1.378	0.759
1.5	27.48	0.1522	30	2.731	0.493	70	1.284	0.802
2	22.26	0.1691	35	2.397	0.530	75	1.202	0.846
3	16.5	0.1964	40	2.136	0.567	80	1.128	0.893
4	13.31	0.2188	45	1.926	0.604	85	1.061	0.944
6	9.79	0.2552	50	1.754	0.641	90	1.0	1.0
8	7.86	0.285	55	1.611	0.678			

Note that once the radii of two bodies' curvature are determined, the direction of the contact ellipse can be predicted as follows

$$\frac{1}{R_1^w} + \frac{1}{R_1^r} \geq \frac{1}{R_2^w} + \frac{1}{R_2^r} \gg a \geq b \qquad (2-10a)$$

$$\frac{1}{R_1^w} + \frac{1}{R_1^r} < \frac{1}{R_2^w} + \frac{1}{R_2^r} \gg a < b \qquad (2-10b)$$

In general Hertz theory is useful to calculate the normal contact problems at the wheel tread-rail head contact. Nevertheless in two-point contact case (wheel tread-rail head and wheel flange-rail gauge contacts), the utilization of Hertz theory has

raised a question mark since the geometry condition at the wheel flange is not satisfied [41]. The dimensions of the contact area are approximately equal to the radii of the contact bodies at the wheel flange/rail gauge, which violates one of the initial suppositions of this theory, i.e. the radii of the bodies at the contact zone must be much larger than the contact size. Moreover, the maximum contact pressure produced at the contact zone can be very high and usually exceeds the endurance limit of most steels in railway application [10], whereas this theory is limited only in the linear assumption. The difference between the elastic-plastic model and the elastic model can be up to 300% [44]. Therefore a new model is required to overcome these drawbacks of the classical theory. Numerous models using Finite Element Method (FEM) and/or Boundary Element Method (BEM) have been widely applied [45-49] and will be introduced in section 2.4 of the literature review.

2.3. The tangential problems of wheel-rail contact

Fundamental in the analysis of frictional rolling contact is to comprehend how the tangential stresses at the surface of each body behave. The strains and deformations of the contact bodies are changing with position as well. The levels and location of the stress/strain can potentially affect the rail life. To examine this problem, some traditional theories have been considered here.

2.3.1. General remark

Within the contact area, the dynamics of the contacting bodies can be altered at different locations due to the elasticity of the bodies and the externally applied normal load. In part of the contact patch, particles of the opposing bodies may adhere (stick) to each other, while in other part relative movement occurs. This local relative sliding is named micro-slip [41]. For wheel-rail contact, the wheel moves forward in the positive longitudinal direction (x-direction) with velocity V^1, at the same time it rotates about its axis with the circumferential velocity $V^2 = \omega R$ as illustrated in

Figure 2.8. Under rolling conditions, we have $V^1 \approx V^2$, the difference V^1 - V^2 would form the stick-slip zones.

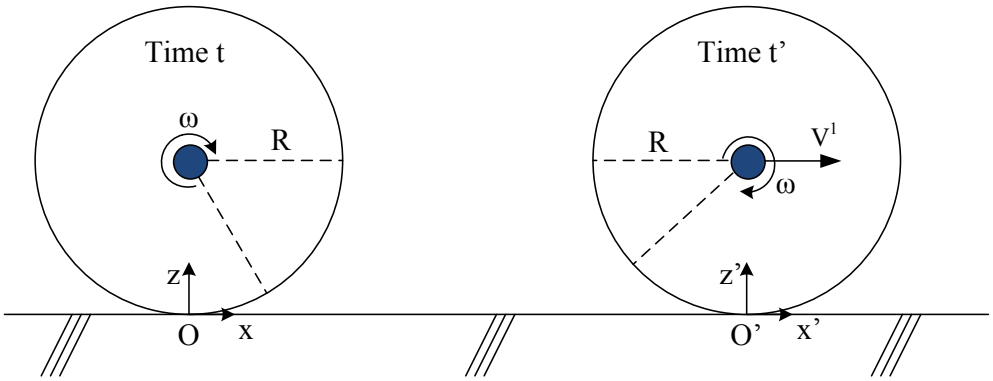

Figure 2.8 Schematic of wheel rolling

The dissimilarity of the two velocities is called the creep, and the tangential contact forces are also named creep forces. The general expression of creepage (micro-slip) for two rolling bodies is obtained from the absolute velocity at the contact interface as the following equation:

$$\text{creepage } (\xi) = \frac{\left|\overrightarrow{V^1}\right| - \left|\overrightarrow{V^2}\right|}{\frac{1}{2}\left(\left|\overrightarrow{V^1}\right| + \left|\overrightarrow{V^2}\right|\right)} \qquad (2-11)$$

where V^1 and V^2 are the absolute velocity at the contact patch, and $1/2(\overrightarrow{V^1} + \overrightarrow{V^2})$ is the mean velocity.

In wheel-rail contact, the stick zone is located adjacent to the leading edge of the contact area, and the slip region is confined to a single zone at the trailing edge [35]. It should be noted that the appearance of wear on the contact surface is due to frictional dissipation, which requires local relative slip and stresses between the contact surfaces [50-51]. The three important different aspects considered in a contact problem are:

i. The deformation of the separate bodies in reaction to the load applied on their surfaces. It largely depends on the geometry of the bodies and on their material behaviours [7, 22, 24].

ii. Overall motion of the bodies relative to each other such as: rest, impact [52], rolling [35] and/or sliding [53-54].
iii. The "contact conditions" at the contact interface: the compression and adhesion in the direction perpendicular to the interface, friction and micro-slip in the tangential directions [35, 55].

The last aspect is the primary concern of contact mechanics. The appearance of micro-slip (creepage) would generate the tangential forces and spin moment, which significantly affect the steering and stability of the railroad vehicle systems. The following sub-sections present some well-known theories to investigate tangential forces (also called creep-force theories).

2.3.2. The creep force theories

Several creep-force theories have been applied to solve the wheel-rail contact problems. It should be noted that some of the theories introduced in this section can only be applied for linear or special models. These theories are no longer valid for non-linear three-dimensional (3D) multibody system formulations in wheel-rail contact.

2.3.2.1. Carter's theory (1926)

The first two-dimensional (2D) model to calculate the creep forces was established by Carter [56] in 1926. The connection between the tangential force and the longitudinal creepage in the rolling direction was introduced based on the following assumptions:

- The wheel and the rail were considered by a cylinder and a thick plate, respectively.

- The wheel's radius was large compared with the circumferential length of the contact area.
- The dimension of the contact area is smaller than the radii of the contact bodies.

Carter explained that the difference between the translational speed and the circumferential speed of a driven wheel had a non-zero value when braking or acceleration is applied to the wheel. Shown in Figure 2.9 is the contact area according to Carter's theory. Point A is the first contact point. The curve ABA' represents the critical value of tangential traction, and the curve ADCA' stands for the real tangential traction value which starts from A and would never exceed the limitation of Coulomb's friction law [57].

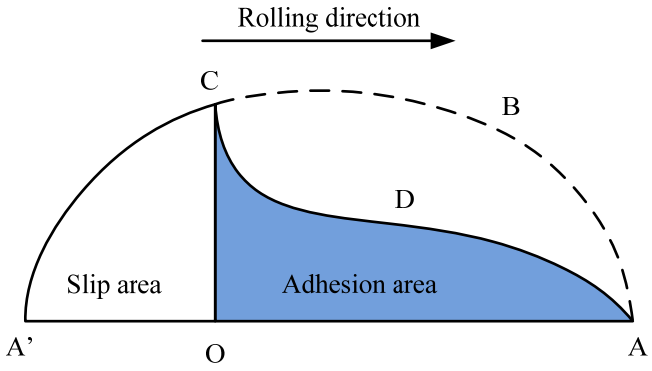

Figure 2.9 Contact area according to Carter [42]

Carter suggested the creepage – creep force (f_T) relationship regarding the driving-braking couple and the velocity difference:

$$\frac{f_T}{\mu f_Z} = \begin{cases} -k\xi + 0.25k^2\xi|\xi| & k|\xi| \le 2 \\ -sign(\xi) & k|\xi| \ge 2 \end{cases} \qquad (2-12)$$

where μ is the friction coefficient; the creepage ξ is described by tangential and circumferential velocity (equation 2-13a); k is the creepage coefficient which is a function of μ the wheel radius R^W, and the semi-axis of the contact patch in the longitudinal direction (equation 2-13b). V_T and V_C are the translational and circumferential velocities, respectively.

$$\xi = \frac{2\left(\left|\overrightarrow{V_T}\right| - \left|\overrightarrow{V_C}\right|\right)}{\left|\overrightarrow{V_T}\right| + \left|\overrightarrow{V_C}\right|} \qquad (2-13a)$$

$$k = \frac{4R^w}{\mu a} \qquad (2-13b)$$

In general Carter's formula is capable of predicting the frictional losses in a locomotive driving wheel. Nevertheless it is restricted to the elastic problem and displacements in the rolling direction only. Hence it cannot be used when there is lateral or spin movement of the driving wheel [58], and has been removed from the wheel-rail contact codes since 1960s.

2.3.2.2. Johnson and Vermeulen's theory (1958)

The first to solve the 3D rolling contact problem was Johnson. Based on Carter's model, Johnson developed Carter's model from 2D to 3D elastic model of two spheres for the longitudinal and lateral creepage in 1958 [41-42]. Then together with Vermeulen, in 1964, Johnson extended the model to smooth-half spaces without spin.

Johnson assumed that the adhesion area is elliptical and the contact surface is separated in two regions which are the slip region and the stick region as shown in Figure 2.10. The total tangential force $f_T = \begin{bmatrix} f_x & f_y \end{bmatrix}^T$ is calculated from the following equation [42]:

$$\frac{f_T}{\mu f_z} = \begin{cases} (1/\xi)\left[\left(1 - \frac{1}{3}\xi\right)^3 - 1\right]\left(\xi_x i + \xi_y j\right) & \text{for } |\xi| \le 3 \\ -(1/\xi)\left(\xi_x i + \xi_y j\right) & \text{for } |\xi| > 3 \end{cases} \qquad (2-14)$$

where f_z is normal force; μ is coefficient of friction; ξ_x and ξ_y are the longitudinal and lateral creepage which depend on the dimensions of the contact zone and material properties. $\xi = \sqrt{{\xi_x}^2 + {\xi_y}^2}$; $i = [1 \;\; 0]^T$; $j = [0 \;\; 1]^T$.

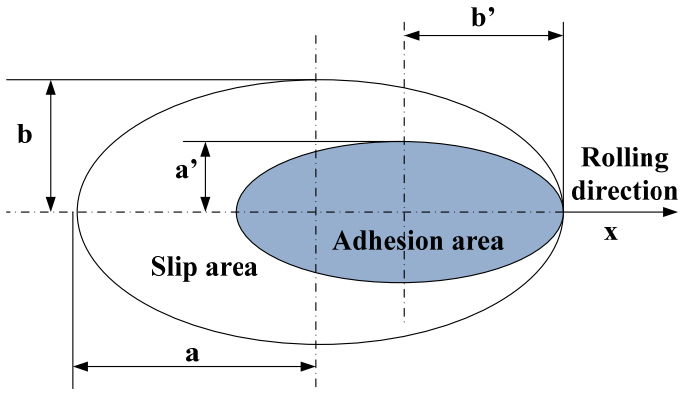

Figure 2.10 Contact area according to Johnson and Vermeulen [42]

From equation 2-14, it is noted that the effect of spin is neglected in Johnson and Vermeulen's theory. However the spin phenomenon has been recognised to have a crucial influence on railway problems, especially in a curved track where high spin normally appears. This theory, hence, can only be applied in no-spin case and is seldom used in the computer formulation of the creep-force nowadays.

2.3.2.3. Kalker's theories

During the past decades, J.J. Kalker (1933-2006) had been introducing a number of valuable wheel-rail contact theories [58-66]. These theories include: *Linear Theory* [42], *Strip Theory* [58], *Empirical Theory* [66], *Simplified Theory* [62-63], and *Exact Three Dimensional Rolling Contact Theory* [66], which are useful to determine the tangential force and spin moment between the wheel and the rail. Moreover Kalker also developed two popular software products named CONTACT [59-60, 65] and FASTSIM [63] to support the railway researchers in estimating wheel-rail contact problem.

a. General remark

As mentioned, the discrepancy between the overall forward velocity and circumferential velocity is called creep phenomenon. This relative movement is resisted by frictional shear stresses in the contact interface. If the circumferential speed is larger than the forward velocity, the net tangential force on the wheel is pointing forward *($f_T > 0$)* and accelerates the train. On the other hand, if the train is braking *($f_T < 0$)* then the circumferential velocity is lower than the forward velocity [65]. According to Kalker's theories, the longitudinal, lateral and spin creepages, respectively are defined as follows [66]:

$$\begin{cases} \xi_x = \dfrac{\left(\left|\overrightarrow{V^1}\right| - \left|\overrightarrow{V^2}\right|\right)}{\left|\vec{V}\right|} \\ \xi_y = \alpha \\ \varphi = -\dfrac{\dot{\alpha}}{V} cos\gamma + \dfrac{sin\gamma}{R} \end{cases} \qquad (2-15)$$

where V^1 and V^2 respectively are the forward velocity and rotational velocity of the wheel; α (also called the angle of attack) is the angle between the wheel plane and the plane $y = 0$; R is the wheel radius; and γ is the wheel conicity (Figure 2.11).

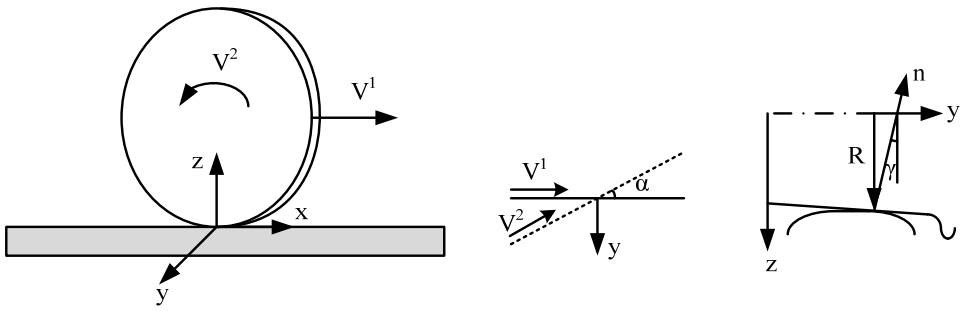

Figure 2.11 Creepage determination

Although numerous theories had been developed by Kalker, not all of them are applicable to the wheel-rail contact situations. For instant, the Strip Theory [67] was based on the assumption that the contact bodies can be considered to be made up of a series of strips parallel to the x axis and perpendicular to the surface. If the interaction between these strips can be ignored, each strip can be studied with the aid of Carter's two-dimensional theory. Hence this theory cannot be extensively applied in wheel-rail contact due to its limitation to a slender contact area. In this section, the

Linear Theory and the Simplified Theory which are still being used in rolling contact calculation are introduced.

b. Linear theory (1960)

In the 1960s, the experimental data had grown along with the quick development of technology. Based on these data, Kalker proposed the Linear Theory to examine creep force – creepage relationship and the spin effect was also considered in this model. The Linear Theory was included in his Doctoral thesis in 1967 [68].

For very small creepages, Kalker suggested that the slip area is very small and its effect can be ignored. Thus the adhesion area can be expected to be equal to the contact area. Using the traction-displacement relationship based on the general elastic theory and integrating the traction over the contact area, the tangential force and the torsion couple were determined as the linear functions of the creepages and spin as:

$$\begin{bmatrix} f_x \\ f_y \\ M \end{bmatrix} = -Gab \begin{bmatrix} C_{11} & 0 & 0 \\ 0 & C_{22} & \sqrt{ab}C_{23} \\ 0 & -\sqrt{ab}C_{23} & abC_{33} \end{bmatrix} \begin{bmatrix} \xi_x \\ \xi_y \\ \varphi \end{bmatrix} \qquad (2-16)$$

where a and b are the semi-axes length of the contact patch in the rolling direction and lateral direction; C_{ij} are the Kalker's coefficients which can be found in [10, 69]; G is the material shear modulus given by:

$$G = \frac{1}{2}\left(\frac{1}{G^w} + \frac{1}{G^r}\right) \qquad (2-17a)$$

$$\frac{\nu}{G} = \frac{1}{2}\left(\frac{\nu^w}{G^w} + \frac{\nu^r}{G^r}\right) \qquad (2-17b)$$

Figure 2.12 performs the traction distribution in the contact patch according to the Linear Theory. Since the particles enter the contact area from the leading edge, the traction here should be vanished and gradually builds up towards the trailing edge.

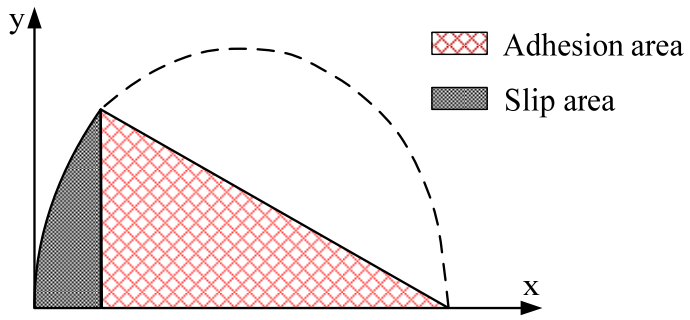

Figure 2.12 Traction distributions within the contact area (Kalker's Linear Theory)

In 1984, the model was utilized to calculate the values of creepages when the relative slip was small with the aid of the program CONTACT [59, 65]. The obtained error of less than 5% proved that the Kalker's coefficients are accurate enough for the examination of the wheel-rail contact problems.

c. Simplified theory (1973)

The *Simplified Theory* was formed in 1973 and being improved until 1982 [62-63]. It is generally applied in wheel-rail contact calculation where the contact area is elliptic, and an error of 15% can be produced [66]. By using the so-called compliant parameters in the longitudinal and lateral directions (L_x and L_y), the complex expression resulted from the general elastic theory can be simplified. The compliant parameters depend on the creepage and spin coefficients of linear theory. The relationship of tangential surface traction $f_T = \begin{bmatrix} f_x & f_y \end{bmatrix}^T$ and tangential surface displacement u^{wr} can be calculated as the following equation:

$$u^{wr} = u^w - u^r = [L_x f_{tx} \quad L_y f_{ty}]^T \qquad (2-18)$$

The tangential forces determined by integrating over the contact area:

$$f_x = \int_{-b}^{b} \int_{-a}^{a} f_{tx} dxdy = -\frac{8a^2 b \xi_x}{3L_x} \qquad (2-19a)$$

$$f_y = \int_{-b}^{b}\int_{-a}^{a} f_{ty}\,dxdy = -\frac{8a^2b\xi_y}{3L_y} - \frac{\pi a^3 b\varphi}{4L_y} \qquad (2-19b)$$

The compliant parameters are obtained by equating equations 2-19 and 2-16 (from the Linear Theory) as follows:

$$f_x = -\frac{8a^2b\xi_x}{3L_x} = -GabC_{11}\xi_x \qquad (2-20a)$$

$$f_y = -\frac{8a^2b\xi_y}{3L_y} - \frac{\pi a^3 b\varphi}{4L_y} = -Gab(C_{22}\xi_y + \sqrt{ab}C_{23}\,\varphi) \qquad (2-20b)$$

Therefore the compliant parameters are:

$$\begin{cases} L_x = \dfrac{8a}{3GC_{11}} \\ L_{y1} = \dfrac{8a}{3GC_{22}} \\ L_{y2} = \dfrac{\pi a^2}{4G\sqrt{ab}C_{23}} \end{cases} \qquad (2-21)$$

From equations 2-21, the compliant parameters depend closely on the material properties, geometries of the contact region, and creepages. Kalker carried out the calculation for a typical case, in which a/b = 1.0 and Poisson's ratio is 0.25, and found out that values of L_{y1} and L_{y2} differ significantly [60]. A single compliant parameter was proposed from the combination of three parameters as follows:

$$L = \frac{L_x|\xi_x| + L_{y1}|\xi_y| + L_{y2}\sqrt{ab}|\varphi|}{\sqrt{(\xi_x)^2 + \left(\xi_y\right)^2 + ab\varphi^2}} \qquad (2-22)$$

From the above equation, it can be seen that:

- L = L_x when $\xi_y = \varphi = 0$ (pure longitudinal creepage)
- L = L_{y1} when $\xi_x = \varphi = 0$ (pure lateral creepage)
- L = L_{y2} when $\xi_x = \xi_y = 0$ (pure spin)

Another program called FASTSIM had been developed by Kalker in 1982. The program is based on the simplified theory and is extensively applied in railroad computer programs. This theory can help to reduce the calculation time significantly with the application of the single compliant parameter L. If using FATSIM, the calculation time can be saved more than 400 times compared to CONTACT [63]. However this theory is limited to elliptical contact area which mean that assumption are common to Hertz's theory.

2.3.2.4. Polach's theory (1999)

Although CONTACT and FASTSIM have showed good accuracy in wheel-rail contact calculation, the computational time is often too long. FASTSIM is much faster than CONTACT, but the calculation is still time-consuming if applied to complicated multibody systems. In 1999, Polach introduced a model for calculating the wheel/rail creep forces [70-71]. Compared to some other approximation methods which usually differ significantly to the Kalker's theory, the result from Polach's model has shown a smaller deviation.

Polach's fundamental idea is that the creep force is acquired by integrating the shear stress distribution over the contact zone:

$$f = \iint \tau \, dx \, dy \qquad (2-23)$$

The contact area is assumed to be elliptical with the semi axes a, b and the coefficient of friction μ is considered as a constant in the contact area. The maximum tangential stress at any arbitrary point is

$$\tau_{max} = \mu\sigma \qquad (2-24)$$

where σ is normal stress.

As shown in Figure 2.13, the relative displacement between the wheel and the rail increases linearly from the contact point A on the right side of the contact area to the contact point C on the left side, and the tangential stress also build up linearly with the distance from the leading edge. As soon as the tangential stress achieves its maximum value, sliding phenomenon will happen. The tangential force distribution is obtained from the following equation:

$$f = -\frac{2\mu F_Z}{\pi}\left(\frac{\varepsilon}{1+\varepsilon^2} + arctan\varepsilon\right) \qquad (2-25)$$

where ε is the gradient of the tangential stress in the adhesion area, and is as follows:

$$\varepsilon = \frac{1}{4}\frac{G\pi abC_h}{\mu F_Z}\xi \qquad (2-26)$$

where G is the material shear modulus, C_h is a constant which depends on Kalker's coefficients, and ξ is the non-dimension creepage.

$$C_h = \sqrt{\left(C_{11}\frac{\xi_x}{\xi}\right)^2 + \left(C_{22}\frac{\xi_y}{\xi}\right)^2} \qquad (2-27)$$

$$\xi = \sqrt{{\xi_x}^2 + {\xi_y}^2} \qquad (2-28)$$

and the vector f_x and f_y are calculated from equation 2-20 using the following formulate:

$$f_i = f\frac{\xi_i}{\xi} \quad ; i = x, y \qquad (2-29)$$

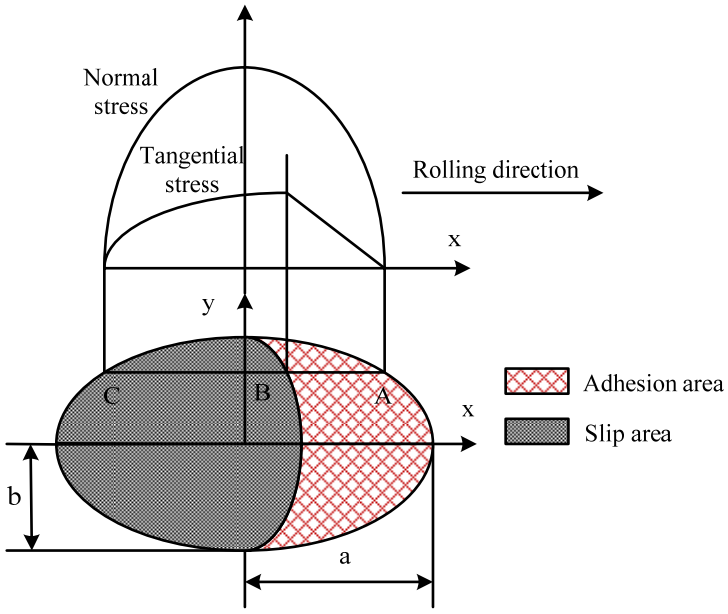

Figure 2.13 Normal and tangential stress distribution according to Polach theory [70]

If the effect of spin is accounted in the calculation, the modified lateral creepage is as follows:

$$\xi_{yc} = \begin{cases} \xi_y & ; \text{ if } |\xi_y + \varphi a| \le |\xi_y| \\ \xi_y + \varphi a & ; \text{ if } |\xi_y + \varphi a| \ge |\xi_y| \end{cases} \qquad (2-30)$$

hence

$$\xi = \sqrt{{\xi_x}^2 + {\xi_{yc}}^2} \qquad (2-31)$$

and the later creep force is given as:

$$f_{yc} = f_y + f_{ys} \qquad (2-32)$$

where f_{ys} is the increment of the tangential force resulted from the spin effect, and is given by:

$$f_{ys} = -\frac{9}{16} a\mu F_Z K \left[1 + 6.3\left(1 - e^{-\frac{a}{b}}\right)\right]\frac{\varphi}{\xi} \qquad (2-33)$$

K and δ are obtained from the following equations:

$$K = |\varepsilon_y|\left(\frac{\delta^3}{3} - \frac{\delta^2}{2} + \frac{1}{6}\right) - \frac{1}{3}\sqrt{(1-\delta^2)^3} \qquad (2-34)$$

$$\delta = \frac{\left(\varepsilon_y\right)^2 - 1}{\left(\varepsilon_y\right)^2 + 1} \tag{2-35}$$

where ε_y is the gradient of the tangential stress, and is calculated from:

$$\varepsilon_y = \frac{8}{3}\frac{Gb\sqrt{ab}}{\mu F_Z}\left[\frac{C_{23}\xi_{yc}}{1 + 6.3\left(1 - e^{-\frac{a}{b}}\right)}\right] \tag{2-36}$$

where C_{23} is the Kalker's coefficient. The creep forces are finally given as follows:

$$\begin{cases} f_x = f_{px}\dfrac{\xi_x}{\xi} \\ f_y = f_{py}\dfrac{\xi_y}{\xi} + f_{ys} \end{cases} \tag{2-37}$$

From Polach's model, the magnitudes of the tangential contact force accounted for the spin effect can be obtained. This theory has been added in some computer codes developed recently (ADAMS/Rail) for the dynamic analysis of railway vehicle systems. In 1999, a computer code using FORTRAN based on Polach's equations was introduced. In comparison to FASTSIM, the calculation time by using Polach's model is faster, and the results are in good agreement [70].

In addition to the theoretical methods discussed above, the numerical methods have also been applied extensively to analyse the wheel-rail contact related problems. A review of some numerical models of wheel-rail contact will be presented in next stage of the literature review.

2.4. Numerical approaches of wheel-rail contact

The development of technical software has made more realistic the simulation of complex physical phenomenon. Inputs of the models to reflect the boundary conditions are close to the practical circumstances.

Among the numerical methods, Multibody System (MBS) [72] and Finite Element Methods (FEM) [73] are the valuable and usual tools to investigate the wheel-rail contact problems. Numerous MBS models [42, 74-81] were carried out to examine the dynamic behaviour of railway vehicle systems, contact forces and the responses of the track system to the train loads. Different from MBS simulation, FEM model provides a deep understanding of contact stresses and damage analysis on wheel/rail. Furthermore the limitation of the classical theories such as linear elastic assumption can be easily overcome with FE methods. The results acquired from the FEM model compares well with those obtained from traditional methods like Hertz or CONTACT as long as material plastic deformation does not occur [35, 48].

In FEM simulations, finite element mesh plays an important role in obtaining accurate results. Nevertheless most of the railway FEM models are either the 2D model [53, 82-88], or simple 3D [84, 89-90], or tetrahedral mesh [49]. From the FEM standpoint, Mehmet et al [91] recently developed a 3D model in order to handle the meshing, the applied boundary and loads problem. The finite element mesh is illustrated in Figure 2.14. Since fine mesh could only be found at a certain length of the rail and the wheel, this model was only capable for static modelling of wheel-rail contact, and not suitable for dynamic problem.

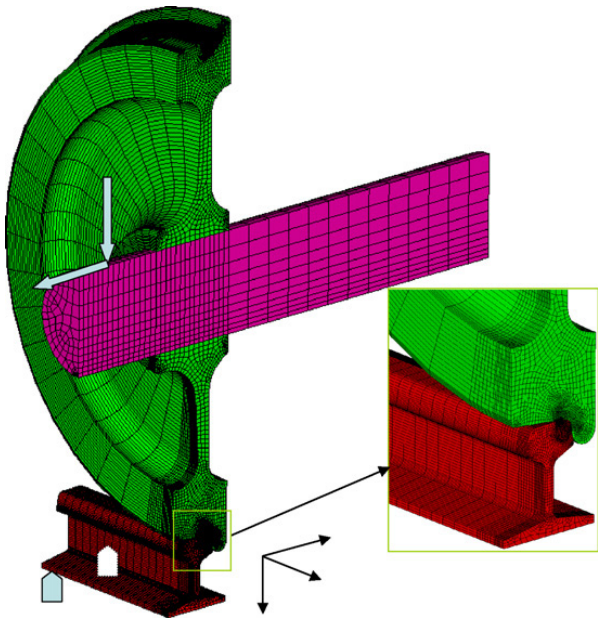

Figure 2.14 3D mesh and boundary condition of wheel-rail contact model [91]

Telliskivi et al.[44, 46] constructed an elastic-plastic FEM model of one wheel and a piece of rail to estimate the contact pressure and the maximum stresses at the wheel flange- rail head contact in sharp curved track (303 m radius). The wheel-rail profiles and the friction coefficient were measured by some special devices such as Tribometer and Miniprof. The contact point positions and contact forces were achieved from the results of MBS simulation (GENSYS/MEDYNA). The traditional methods (Hertz and Contact) were utilized to validate the FEM results at the wheel-rail gauge contact (case 1, Figure 2.15) and the wheel-rail head contact (case 2, Figure 2.15). It was found that the results from different methods were incomparable, especially on the rail gauge contact, due to the invalidity of the half-space assumption from classical theories. However, the dynamic effect was also neglected in this model, since only a short piece of rail was simulated.

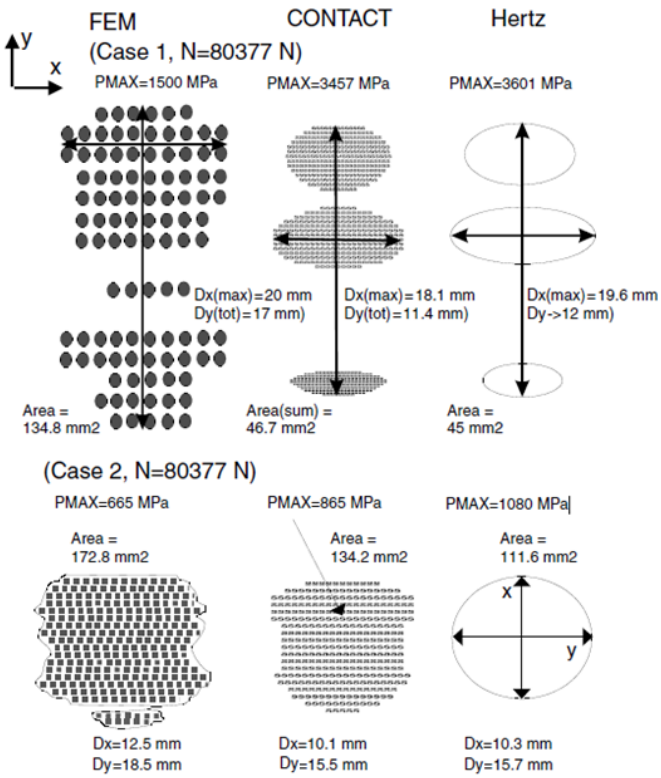

Figure 2.15 Comparison regarding to maximum pressure and the contact area between FEM model and classical methods [44, 46]

In another study, Telliskivi et al. [45] aimed to investigate the degradation of the wheel-rail profiles in curved track where severe wear and plastic deformation happened. The elastic-plastic FEM code was firstly applied to evaluate the contact area and contact pressure on the head and gauge of the rail. Data obtained from FEM models were used to predict wear (expressed by mass loss) on the rail surface. Figure 2.16 shows contact area and maximum contact pressure over the number of wheel passes. The rail in this model was still too short to simulate the dynamic effect, and rail cant angle was not considered.

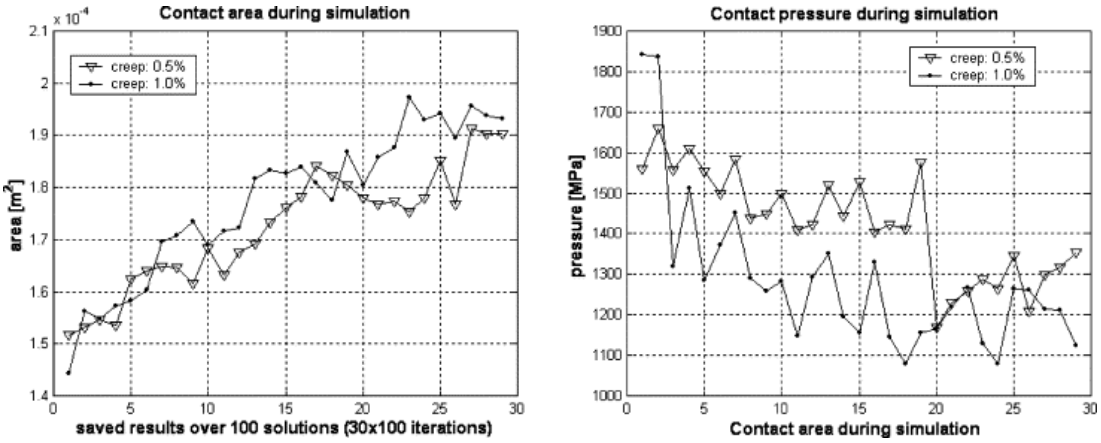

Figure 2.16 Contact area and maximum contact pressure vs. number of wheel passages [45]

Sladkowski et al. [49] carried out the research into the influence of the wheel-rail profiles on the stress distributions with FEM tool. Different angles of attack of the wheelsets were considered. The simulation outcomes confirmed that the stress distribution is close to Hertz's theory. The normal force distribution in the cases of one-point contact and two-point contact are shown in Figure 2.17. Nonetheless the model in hand did not account for the dynamic effects of the track system, and the mesh size at the contact zone was still very coarse.

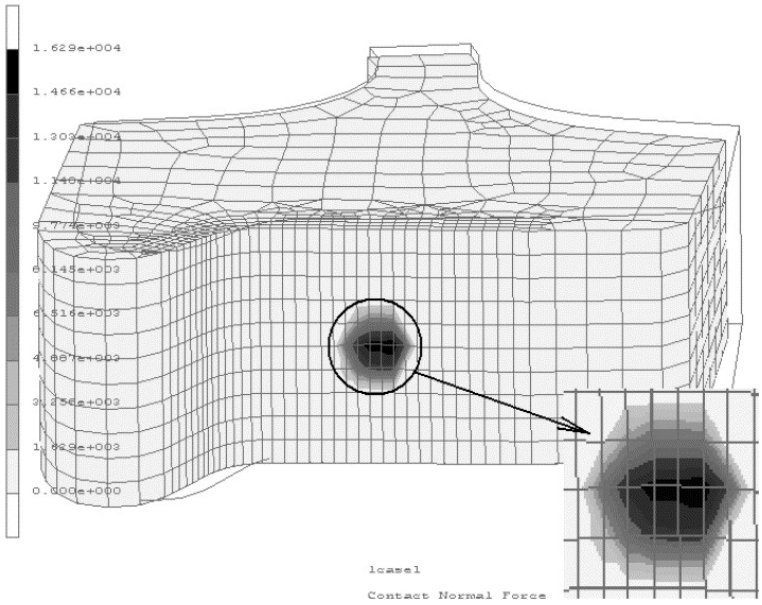

(a) One-point contact

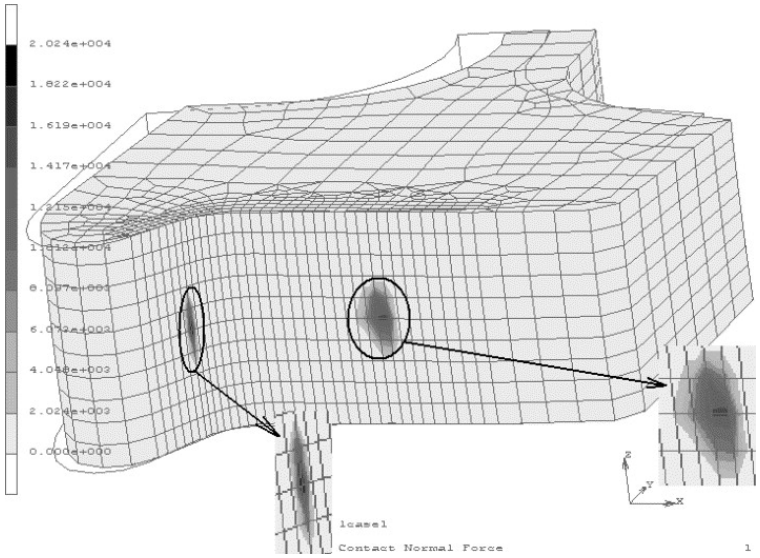

(b) Two-point contact

Figure 2.17 Distribution of contact nodal normal forces on the wheel [49]

Wiest et al. [47] applied diverse methods (Hertz [40-41], CONTACT [59, 65], elastic FEM and elastic-plastic FEM models by Abaqus [92]) to calculate the contact pressure in wheel-rail switch contact. The comparison of contact area between methods is shown in Figure 2.18. The Hertz and non-Hertzian method implemented in CONTACT are limited to linear-elastic material supposition, and the FEM model

can get over this limitation. The other sub-components of the track (such as sleepers, ballast, and railpad), however, were not included in this model.

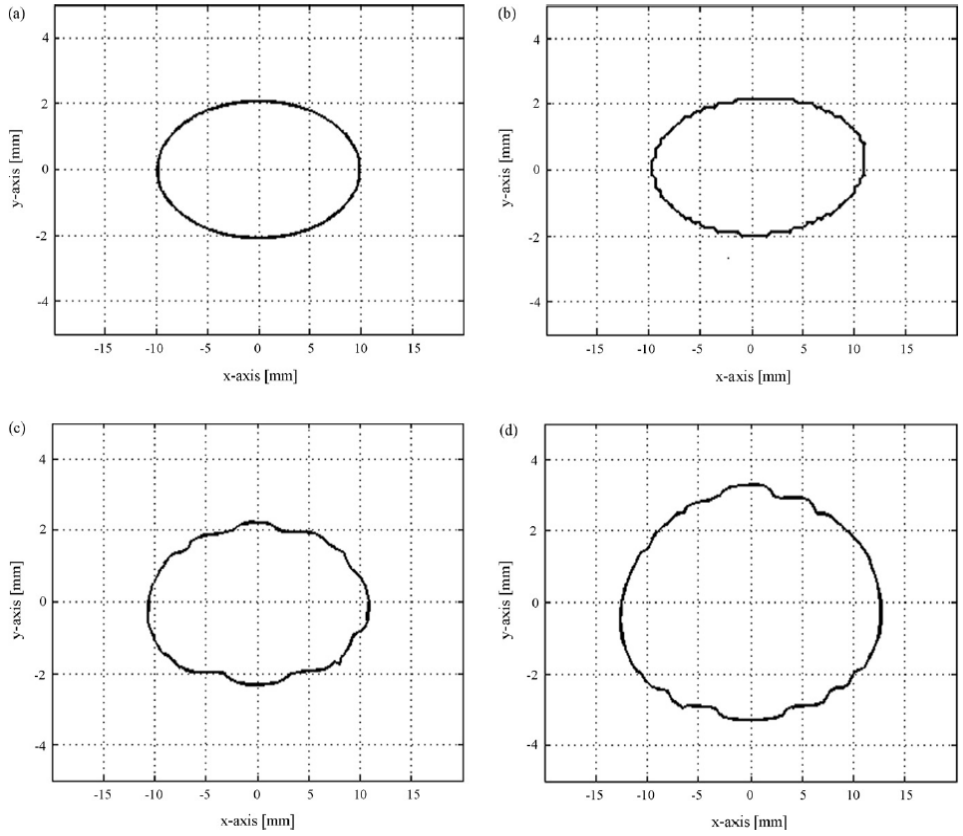

Figure 2.18 Contact area obtained from different methods: (a) Hertz, (b) CONTACT, (c) Elastic FEM model, (d) Elastic-plastic FEM model [47]

Wen et al. [52] introduced an FEM model coded in ANSYS/LS-DYNA to investigate the wheel-rail contact–impact behavior at the rail joint region. In this model, the implicit and explicit methods were combined to get the pre-load conditions on the rail. The achieved results showed that the axle load had a remarkable effect on stresses and strains on the rail head. The maximum impact load can be about 2.6 times of static contact force on the rail head. Moreover, the high axle load caused an increase of the dynamic load. On the contrary, the train speed has a negligible influence on the dynamic load. Another FEM model was developed by Wen et al. [93] with the implementation of an advanced cyclic plastic theory [94] to examine the wheel-rail contact stresses, and the effects of the partial slip on the residual strains/stresses. The normal contact pressure and the tangential contact

forces for three different levels of creepage are drawn in Figure 2.19. It was found that a higher creepage leads to the growth of the slip region.

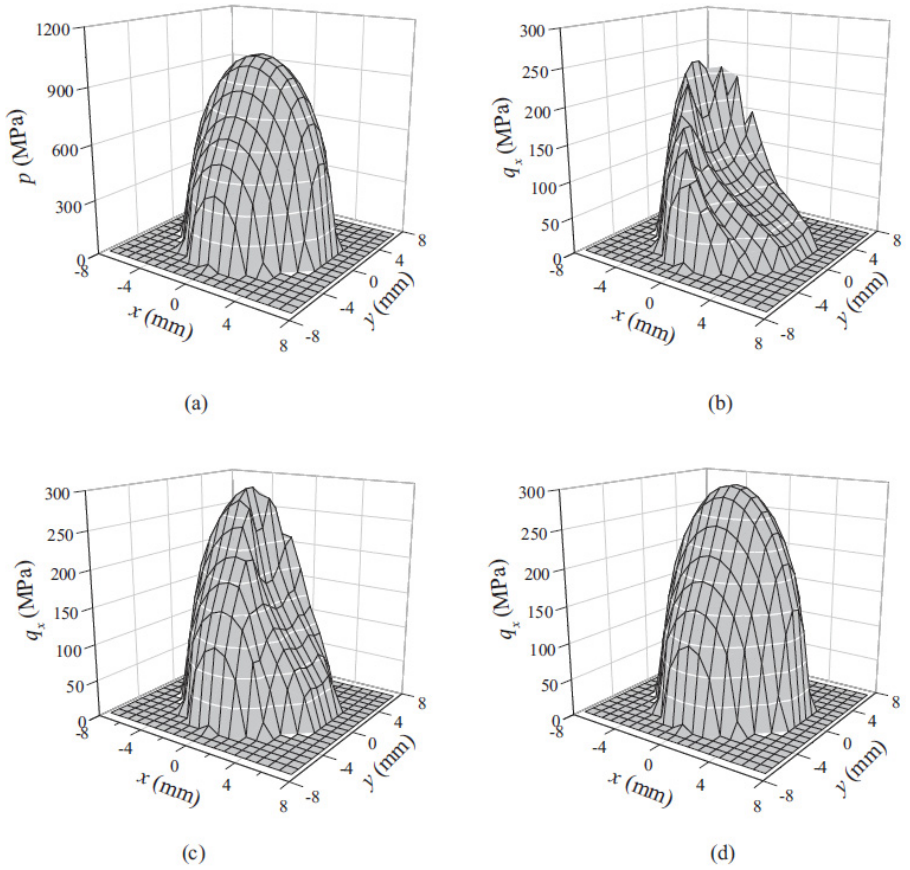

Figure 2.19 Contact stress distribution (a) Normal contact pressure and longitudinal tangential forces distribution for (b) ξ= -0.001 (c) ξ=-0.002 (d) ξ= -0.004

Zhao et al. [95] examined the dynamic stress states of the wheel-rail contact with the implementation of sub-components of the track in the FEM model. The stress states of two different cases of friction coefficient are shown in Figure 2.20 (μ = 0.3 and μ = 0.1). The results showed that an increase of the friction coefficient displaces the maximum von Mises stress from subsurface towards surface. In other words, the higher tangential force could cause damage initiated at the surface rather than beneath it. In addition, the normal stress was not influenced by the tangential force. In this model, only the new profiles were applied, which could not simulate the practical worn wheel-rail profiles.

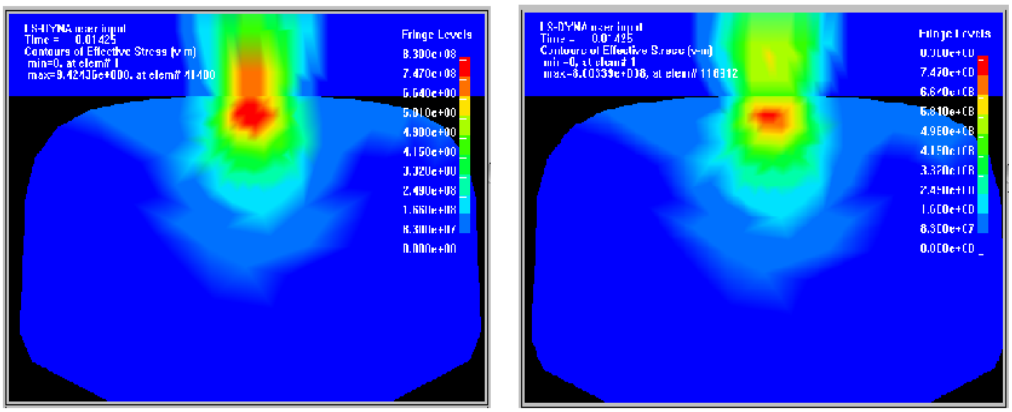

(a) μ = 0.3 (b) μ = 0.1

Figure 2.20 Von Mises stress contours on rail sections [95]

A 3D wheel-rail contact model also developed by Zhao et al. [48] to analyze both normal and tangential wheel-rail contact problems. Validation of FEM model was taken by comparing to Hertz's theory (for normal problems) and CONTACT program (for tangential problems). Table 2.3 presented a good agreement between the results from FEM and traditional methods. Regarding the tangential problems, stick-slip area distributions were analysed and illustrated in Figures 2.21 and 2.22. Nevertheless, the influence of vehicle vibration was not considered in this model, and only the smooth profiles were simulated.

Table 2.3 Comparisons between FEM model and classical methods [48]

Methods	Contact patch			Maximum pressure (MPa)
	Semi-axis a (mm)	Semi-axis b (mm)	Area (mm^2)	
Hertz	7.73	5.86	142.31	1340
CONTACT	7.80	5.69	139.68	1347
FEM	8.00	6.03	151.55	1344
Difference from Hertz	3.5%	2.9%	6.5%	0.3%
Difference from CONTACT	2.6%	6%	8.5%	-0.2%

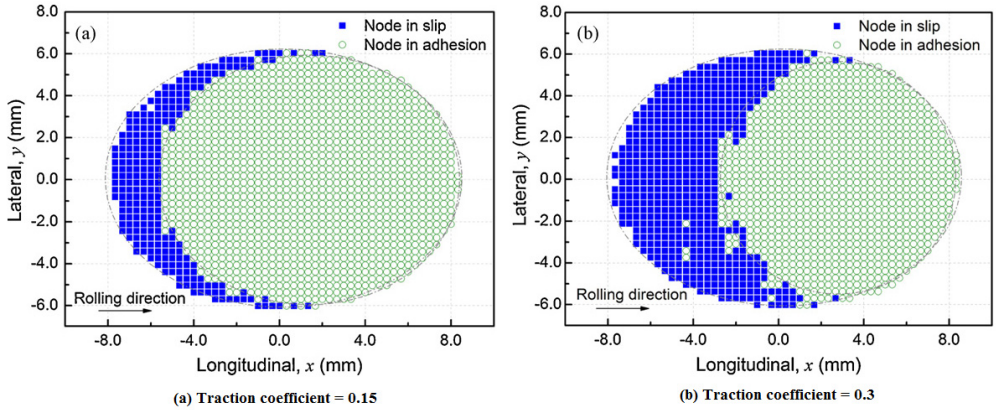

Figure 2.21 Distributions of adhesion-slip area obtained from FEM method (a) Traction coefficient = 0.15, (b) Traction coefficient = 0.3 [48]

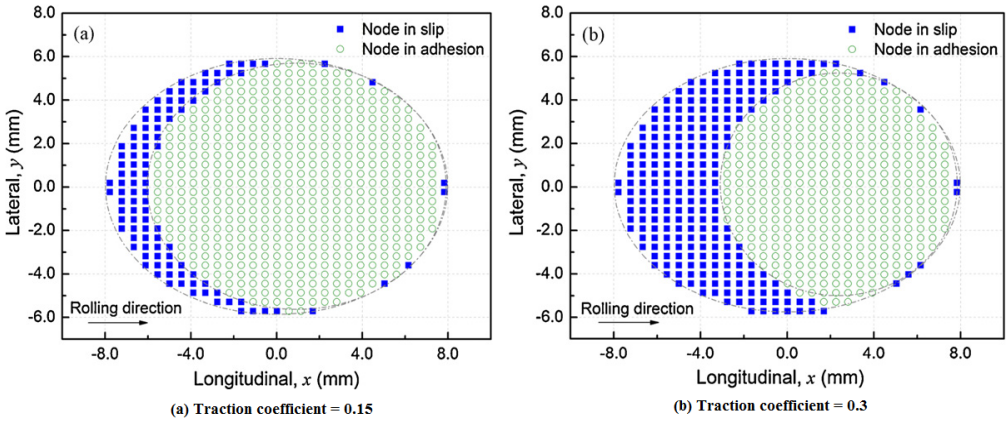

Figure 2.22 Distributions of adhesion-slip area obtained from CONTACT (a) Traction coefficient = 0.15, (b) Traction coefficient = 0.3 [48]

Since most of the experimental research on the wheel-rail rolling contact is expensive and also not easy to carry out, the numerical modelling is a good option to reduce the cost. In this section, some of the numerical models to investigate the wheel-rail contact had been summarized. In the next stage of the literature review, wheel-rail friction contact conditions which significantly affect the damage initiation will be discussed.

2.5. Friction conditions in wheel-rail contact

The wheel-rail failures are closely connected to the loading condition [96-97], train speed [98-99], and especially tribological status of the wheel-rail contact [100-101]. Therefore railway operators have been attempting to optimize the friction states in the wheel-rail contact to adapt to the operational condition of vehicle, and at the same time to minimize the damage of the rail. Figure 2.23 shows the ideal friction conditions for a pair of wheel-rail contact. For the rail head-wheel tread contact, the friction coefficient should be in range from 0.25 to 0.45, and less than 0.1 in the case of wheel flange- rail gauge contact [102].

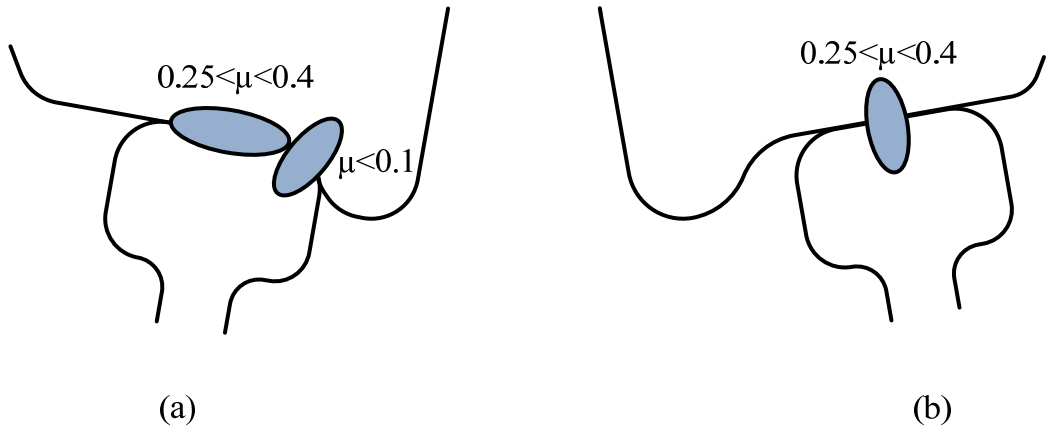

Figure 2.23 Ideal friction conditions in wheel-rail contact on (a) high rail (b) low rail [102

Numerous experiments have been conducted to study the friction of wheel-rail contact surface. It was found that the friction coefficient often surpasses the critical value to cause damage initiation. For example, Olofsson et al [7] compared the coefficient of friction measured on the track and in the laboratory. For non-lubricated tests (dry contact), the value was roughly the same and varied between 0.5 and 0.6. For a full-scale lubricated rail (wet and oil), the coefficient of friction was lower and changed in the range of 0.2 to 0.4. Harrison et al. [8] applied the TriboRailer to measure to the friction coefficient. Under dry condition, the coefficient of friction was approximately 0.5, and it varied between 0.05 and 0.3 under lubricated condition.

Experimental data has shown that the friction coefficient changes considerably with the variation of the contact conditions and the environmental status [103-105]. Thus it was recommended that friction should be considered as a consequence of contact condition and should not be utilized as an input parameter in wheel-rail contact calculation. Different friction laws were introduced in the literature to perform the dependence of friction coefficient on slip velocity [104, 106-107]. Vollebregt et al. [104] implemented the following velocity dependent friction laws in CONTACT software to investigate the time-dependent behaviour of contact model:

$$\mu = \mu_d + \frac{\mu_1}{1 + \left|\frac{\gamma}{\gamma_1}\right|} \qquad (2-38)$$

$$\mu = \mu_d + \frac{\mu_1}{1 + (\gamma/\gamma_1)^2} \qquad (2-39)$$

where μ_d is kinematic friction coefficient, γ is slip velocity, and μ_1 and γ_1 are initial friction coefficient and slip velocity.

Based on the simplified theory of Kalker (FASTSIM), the rolling contact modelling with variable friction is studied with some friction laws in [108]. The friction coefficient is assumed to be a function of slip velocity γ as:

- An exponential law which was also applied in [71]. The friction coefficient is performed as a function of static coefficient μ_0, a ratio of limiting friction coefficient α, and the parameter β which is related to the friction curvature:

$$\mu(\gamma) = \mu_0\left[\alpha + (1-\alpha)e^{-\beta\gamma}\right] \qquad (2-40)$$

- A linear approximation of the above function [106]. The friction depends μ_s and μ_d which are respectively, static and dynamics friction coefficient; and a threshold γ_c.

$$\mu(\gamma) = \begin{cases} \mu_s - \dfrac{\gamma(\mu_s - \mu_d)}{\gamma_c} & \text{if } 0 \le \gamma \le \gamma_c \\ \mu_d & \text{if } \gamma_c < \gamma \end{cases} \qquad (2-41)$$

- An exponential function which depends on the static and dynamics friction coefficients and decaying rate α and β.

$$\mu(\gamma) = \mu_s e^{-\alpha\gamma} + \mu_d\left(1 - e^{-\beta\gamma}\right) \qquad (2-42)$$

Rovisa et al. [108] conducted the twin disc experiment with the real wheel-rail contact conditions (dry, wet, oil) to obtain the friction values under different contact pressure. The values of friction coefficient are listed in Table 2.4.

Table 2.4 Constant μ for 1500 MPa and 900 MPa contact pressure

Pressure (MPa)	Dry	Wet	Oil
1500	0.49	0.17	0.06
900	0.61	0.20	0.06

2.6. Damage mechanisms on wheel-rail contact

The wheel-rail profile change and/or breakdown largely contribute to the maintenance or renewal cost for the track [109]. Depending on the wheel impact loads, wheel-rail materials may respond in different ways which result in various damage occurrences. The damage modes in wheel-rail contact can be classified into:

- Plastic deformation
- Wear
- Rolling contact fatigue

In this part of the literature, the fundamental mechanisms and the related studies so far of the damage processes are reviewed.

2.6.1. Heat induced by frictional rolling

Friction conditions can seriously affect the rail life, for instance heat generation at the contact zone. As discussed previously, the wheel-rail contact zone can be split

into stick and slip regions due to frictional rolling contact. If the traction or braking forces exceed the available adhesion, gross slipping happens which extensively generates heat at the contact spot [10]. Especially under high adhesion mode due to AC Drive, the temperature is expected to be noticeably high and as a result it may have significant influence on rail material properties and also the breakdown of wheel and rail.

Although contact temperatures under actual railway operating conditions can hardly be measured, there are still some special ways to obtain such values. Other than experimental approaches such as pin-on-disc test [110-111], twin-disc experiment [112], braked block on wheel tread [113-114], or electrically-heated railway wheel set [115]; the temperature rise in the contact area can also be calculated by either the analytical method [116-123] or the numerical method [53-54, 84, 87-89, 124-125].

Ertz et al. [120] analytically and numerically calculated the temperature rise on and below the contact surface based on Hertzian contact, in which the heat conduction from the wheel to the rail was taken into account. An approximate analytical solution for line contact model was further discussed in [122] by these authors. Fischer et al. [118] introduced a fully analytical approach based on a work done by Knothe [126] to determine the temperature field and thermal stress induced by the frictional contact. In combination of analytical model proposed in [120] and 'brick' model [127], Widiyatar presented a method to examine the thermal influence on wear and rolling contact fatigue. In all these studies, the authors mainly focused on the analytical answers to the thermal questions in wheel-rail contact.

Other than the analytical models mentioned above, there have been several numerical models of thermal calculation. Lunden [87] proposed a 2D thermo-elastic-plastic finite element model (FEM) performed with SOLVIA programme system to study the plastic stresses and strains in the contact area of the wheel. Spiryagin et al. [125] recommended a mathematical model to calculate the temperature in the wheel-rail flange contact to detect the lubricant type at this contact location. Numerical algorithm was applied by Chudzikiewicz et al. [88] to build up a thermoelastic model with elastic graded materials to investigate the frictional heat generation and heat

transfer across the contact surface. Another 2D FEM model built up by Wu et al. [53] was utilized to investigate the residual deformation, plastic strain and residual stress at the rail surface during wheel/rail sliding contact. Some other FEM models to calculate the wheel temperature could be found in [84-86] by using the moving heat source method. Very limited 3D models were proposed [84, 89] and these models were employed either to calculate temperature for wheel only or the finite element mesh was very coarse.

Studies of railroad wheel temperatures have shown that the operating temperatures for the wheel vary, but are normally found to be between 100^{o}C and 300^{o}C [115], or even reach 600^{o}C [126, 128]. The temperature on the rail depends on the sliding velocity and is also significantly high up to 630^{o}C [53], or more than 1000^{o}C [129] Furthermore, one point on the rail is normally subjected to a repeated loading from many wheels attached to the railway vehicle. The temperature field on the rail, therefore, increases with every cycle of rolling [124] which resulted in the formation of a 10-to100-μm-thick layer on the contact surface [130]. This layer which is also called White Etching Layer (WEL) [131-132] due to its white colour after etching in Nital has brittle property and is liable to crack initiation. This layer will be formed at a temperature of about 700^{o}C [130] but a high hydrostatic pressure also helps to create this layer at even lower temperature [133]. Twin-disc test carried out by R. I. Carroll [131-132] showed that the cracks initiated at the surface rapidly propagate within the WEL due to its brittle behaviour to the bulk material, and may cause the failure of the rail. Moreover wheel-rail materials can be softened due to high temperature [55].

2.6.2. Plastic deformation

Plastic deformation is the non-reversible material disfigurement, which is predominantly caused by high traction load [134]. During operational life, rails typically experience millions of load cycles from the passage of train wheels. The response of material subjected to repeated loading is governed by stress, strain, wear,

and temperature change [135], and can be one of the following types (a) – (d) shown in Figure 2.24. Type (a): material is perfectly elastic and reversible at low load level; type (b): a higher load will cause some plastic deformation, although it can be inhibited by an induced residual stress after a few cycles [136]. This effect may "shakedown" the response of the material to an elastic state in the sub-sequent cycles. This is named "elastic shakedown" [20, 122]; type (c): if the loading is even more severe, the cyclic stress-strain curve becomes a stabilised closed loop with a zero net plastic deformation that is called plastic shakedown; type (d): the response of material is known as rachetting [137] if plastic deformation is accumulated in every cycle. The accumulation of deformation continues until the ductility of the material is exceeded and it ruptures.

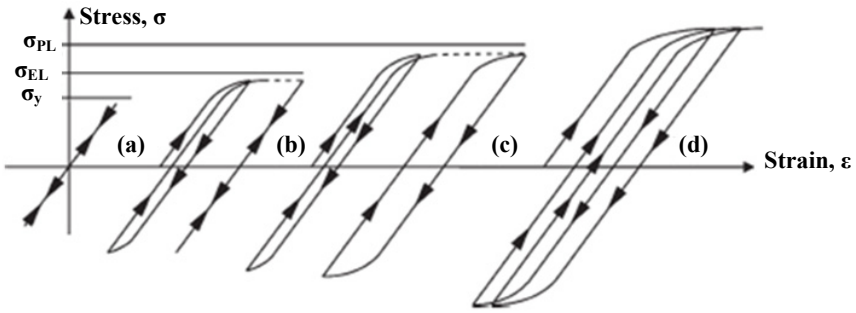

Figure 2.24 Material responses to cyclic loading [138-139]

To analyse the influence of the surface roughness on the evolution of the stress and plastic zone, Daves et al. [83] conducted the 2D FEM modelling of a micro part of a wheel pressed on a rail which exhibited a measured surface roughness. The investigation showed that the plastic deformation of asperities in case of nearly no friction contact was less than the result obtained from frictional contact. Moreover, after only three repeated normal loading, a plastification of 1 mm depth was produced from a 5 μm surface asperity; in other words, a high plastic zone was produced after a few cycles of rolling with a rough surface.

Wen et al. [93] and Jiang et al. [94] studied the development of residual stresses and the deformation of rail under repeated rolling processes by finite element simulation. It was found that under the condition of partial slip, the maximum residual stresses

are achieved at the subsurface. In addition, residual stresses are compressive for elements on or near the contact surface, and are tensile for those far away from contact surface. Xiao [140] discussed further the deformation in a railway crossing taking into account the non-linear material properties and the effect of the dynamic load. The investigation found that the maximum vertical displacement occurred at the crossing contact region, and varied linear approximately with the train speed and the axle load.

Research on plastic flow associated with the micro-structural observation by M. Busquet [141] confirmed that an increasing of the tangential force caused the yield at the surface rather than beneath it. In comparison to the longitudinal plastic flow, the magnitude of the lateral plastic flow was numerically much smaller.

On curved track, the plastic deformation usually appears since the contact load is higher than normal. A FEM model was set up by Wen et al. [24] to investigate the deformation at rail weld in the straight track, and was improved in [22] to include the partial slip effect and different material characteristic between the heat affected zone and base metal. It was found that contact forces and plastic deformation was significantly affected by the irregularity at the rail weld. Under the influence of the heat affected zone, the accumulated plastic deformation generated higher impact loads leading to the change of welded rail profile.

2.6.3. Wear

Wear is defined as the displacement or the loss of material on the contact surface. This phenomenon happens whenever the contact surfaces come into sliding on each other. According to Williams [50], wear was sorted out into “severe wear” and “mild wear”. In comparison to the original surface, a smoother surface will be generated if mild wear happens, but a rougher surface will be produced in case of severe wear.

Over the recent decades, many studies regarding the wear phenomenon both on field and in laboratory [50, 142-146] have been carried out to examine the wear behaviour of rail steel. As shown in Figure 2.25, Telliskivi et al. [45] calculated the mass loss of rail material based on the linear wear law by Archard [147] for different creepage. The higher was the creepage, the more material was worn away. The study also found that the wear could be up to 2.5 times higher when using an elastic–plastic material model compared with a linear-elastic material model.

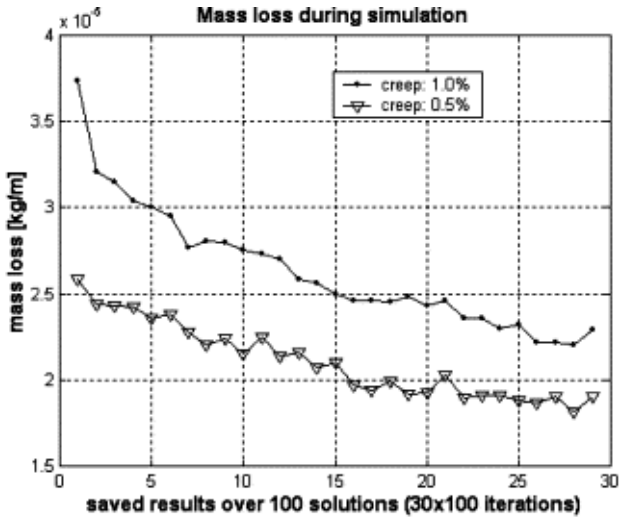

Figure 2.25 Mass loss vs. number of wheel passes [45]

Olofsson et al [7] measured a total of seventeen tracks over a period of two years to investigate the actual development of the damage mechanism on rail. Different wear mechanisms occurred at different parts of the rail. In particular, mild wear prevailed on the rail head, while severe wear predominated on the rail gauge. Experiments from laboratory also showed that at higher sliding speeds, a higher wear coefficient was produced, and the wear changed from mild wear to severe wear. From the collected data of field test and theoretical computation, the relationship between wear and oblique fatigue crack was studied by Wang et al. [148]. The research has concluded that the fatigue crack is slight even though serious wear occurs, and can be relieved with the increasing of wear rate.

Jin et al. [145] applied a large rolling-sliding contact test machine to determine the effects of different factors (normal load, relative sliding speed, geometry of the contact surface, and material properties) on wear. The higher angle of attack (AOA) resulted in the higher wear rate at the wheel flange and rail gauge corner. In addition to a higher lateral force, the wear increased by 1.4 and 2 times. By contrast, the wear rate was reduced significantly with the presence of the water lubrication. Lewis et al [149] examined the influence of surface temperature on the wear process. It was found that an increase of temperature caused the transition from mild wear to severe wear.

In addition to experimental method, some numerical models to predict wear process can be found in [143, 150]. Tomas [143] developed a tool for predicting a wheel profile due to wear. The prediction model was constructed by using Multi Body System (MBS) software named GENSYS. Chongyi et al. [150] introduced a methodology to predict the profile change for the wheel flange-rail gauge corner contact where Hertz theory is invalid. Both of static and dynamic FEM model using ABAQUS code was firstly built to get the rolling contact data. The results from the FEM model were then imported to Archard's wear model. Also a twin-disc test machine was utilized to validate the simulation results. The development of rail profiles is illustrated in Figure 2.26.

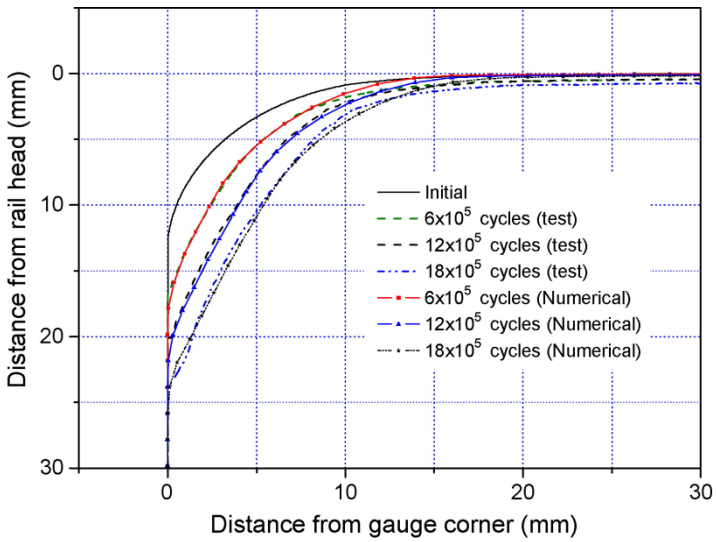

Figure 2.26 Comparison between simulated and measured wear process of rail [150]

A recent study by Franklin et al [146] on wear under the influence of the partial slip and direction of traction has emphasized the substantial role of traction coefficient on the wear rate. In contrast to traction coefficient, the effect of traction direction on wear rate can be neglected. Moreover, the wear rate has a linear relationship with the maximum contact pressure.

2.6.4. Rolling contact fatigue

In general, rail cracks are categorized into two groups which are subsurface-initiated and surface-initiated cracks. The cracks initially develop at the subsurface often result from the metallurgical defects. In addition, the travelling intensity (number of load cycles) and the axle load are two other main reasons causing surface-initiated crack.

Two typical types of cracks initiated at the rail surface are named “squats” and “head checks”. “Squats” usually occur at the running surface of the rail on straight track or on the large-radius curved tracks [20, 151] and can be easily recognized as a dark spot on the contact surface [10]. They originally develop from the White Etching Layer (WEL) [152]. The appearances of “head checks” [153-155] are different from squats. They usually show up on the curved track, in particular on the gauge corner of outer rail (high rail) [156]. Wheel passing causes the gross plastic deformation which leads to cracks. The cracks then develop at a flat angle to the travelling surface. The consequence of head check is material spalling between the cracks and fracture of the rail as shown in Figure 2.27.

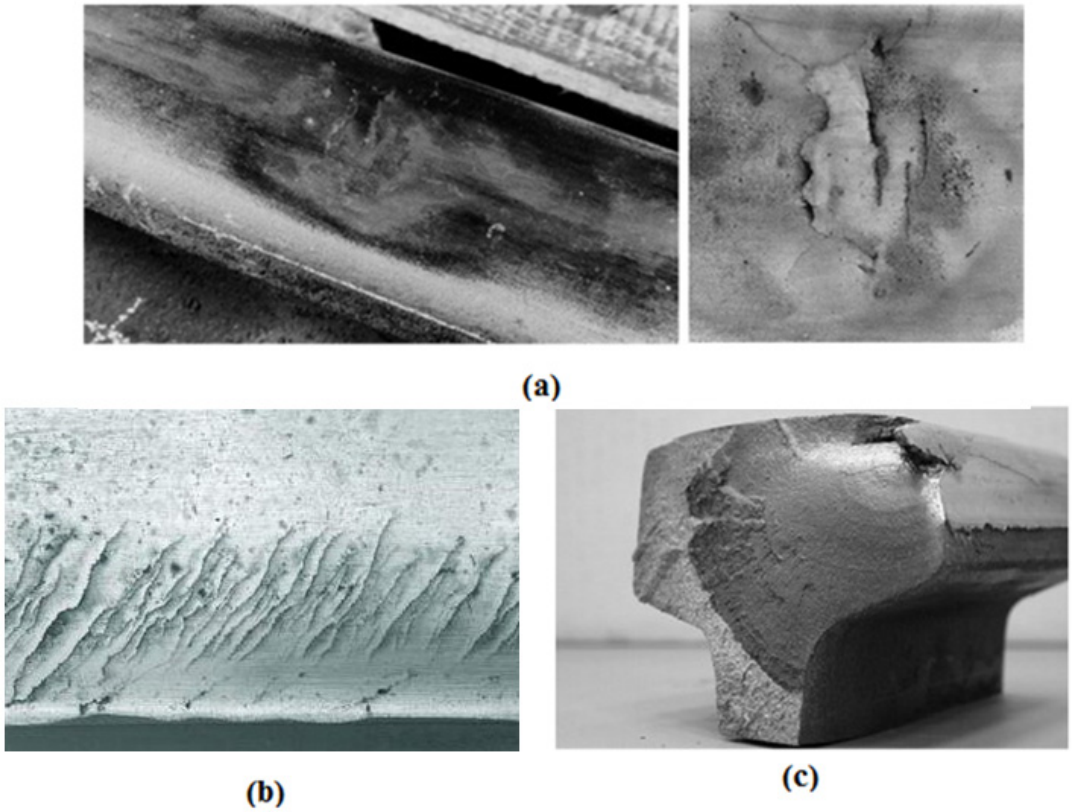

Figure 2.27 Crack on rail (a) Squats [8] (b) Head check propagation [157] (c) Fracture of the rail due to head check [8]

The performances of the railway vehicle nowadays are being improved significantly. In comparison to the old vehicle, not only the velocity is faster, but also the axle load becomes heavier. Numerous studies have been proposed to predict the initiation of rolling contact fatigue [138-139, 158-160] or to examine the fatigue crack behaviour under different conditions [151, 161-164] for both the wheel and the rail. Crack has a tendency of opening just before the contact load reaches the crack, and may be closed as the contact load passes over the crack a small distance. For a lubricated rail, the cracks can be filled with fluid (oil, grease, or water), and trap the fluid inside if the cracks are sealed. Numerical studies were carried to analyze the ability of liquid sucking into the crack phenomenon [161-162, 165-166]. Lubricant will delay the initiation of surface cracks [102], but can also acceleration of the crack propagation [167].

Olofsson et al. [168] compared the 900A rail material to UIC 1100 rail material to examine the growth of the crack during service time, and whether hard rail or soft rail should be utilized in curved tracks. The agreement was that both of these materials were sensitive to crack origination. However the hard rail (900A) seemed to be more sensitive to crack propagation and was easier to form head check cracks than the soft rail (UIC 1100).

Van et al. [169] presented a method to predict fatigue at different positions on the surface of the rail. By combination of an elasto-plastic FE model and a high-cycle fatigue method, the investigation led to conclusion that fatigue likely appeared on the top of the rail. Ringsberg, et al [139] applied the Dang Van's criterion to predict the fatigue crack initiation. A 2D FEM simulation of a twin disc test of wheel-rail contact was compared to rachetting model. The comparison came up with a good agreement in regards to shear strain distribution and the number of cycles to crack initiation. Another 2D linear-elastic an elastic-plastic FEM simulation using the ABAQUS code for the short crack by the same authors was also introduced in [161].

J. Seo [151] studied the behaviour of fatigue crack growth on the rail surface by 2D finite element model with consideration of the moving contact pressure and tangential force. The crack was simulated with an inclined angle from 30^{o} to 45^{o}; and was impacted by three separated load cases represented for pure rolling ($\mu = 0$), tractive force ($\mu = 0.4$), and braking force ($\mu = -0.4$). In [164], the authors conducted an analysis on the damage of White Etching Layer (WEL); and stresses and strains in WEL sub-surfaces by carrying out the twin-disc tests and 2D finite element simulation. The experimental results showed that crack potentially initiated at the interface of the WEL and base material or at the centre of WEL. The research also proved that the fatigue life at the end point of WEL length was longer than those at middle and starting points of WEL length. Another study of Seo et al. [170] on a configuration of damage named as "ballast imprint" had been carried out, in which the damage was found to be produced by the ballast particles snared between the wheel-rail contact surfaces.

2.7. Summary

In this chapter, an introduction to developments in railway research was given. The concentration of this chapter was to comprehensively review the wheel-rail contact problems by the analytical, numerical and experimental methods up to now. Firstly, the analytical methods to calculate the normal problems (Hertz theory) and tangential problems (creep-force theories) of wheel-rail contact were introduced, and the existing drawbacks of these traditional models were also discussed. Secondly the numerical and experimental approaches to analyse the wheel-rail contact forces, stress states and temperature due to frictional rolling were provided. Finally, some damage mechanisms including plastic deformation, wear and rolling contact fatigue were reviewed.

One of the recent applications of Australian Railway is the introduction of the new AC (Alternative Current) locomotive, which has allowed the train to operate in a more advanced adhesion condition. From the literature, it can be seen that the wheel-rail contact problems related to high adhesion level have not been investigated up to now. Furthermore the question of whether the levels of adhesion have any influence on the rail damage has not yet been fully answered. Therefore the core innovation embedded in this thesis is the investigation of the wheel-rail contact problems and the rail damage associated to high adhesion conditions and is divided into four key sections:

- ***Section 1*** describes the wheel-rail contact problems and material response on a straight track under low/high adhesion condition. This section will be presented in chapter 4.
- ***Section 2*** provides some predictions of damage formation due to wheel-rail contact on a curved track. The details of this section can be found in chapter 5.
- ***Section 3*** focuses on wheel-rail contact stress states generated by AC and DC Drives on both the worn low/high rails under diverse practical contact conditions. This section will be addressed in chapter 6.

- ***Section 4*** presents a comprehensive 3D coupled thermal mechanical model to estimate temperatures rise due to high adhesion contact, the formation of White Etching Layer (WEL), and the thermal influence on the rail life. Multi-wheel pass on the rail is considered and residual stress is also calculated. The content of this section will be discussed in chapter 7.

CHAPTER 3

RESEARCH METHODOLOGY

The developments of technical software have made the simulations of complex physical phenomenon become realistic. Therefore the numerical method has been selected in the current study. This chapter will briefly describe the software packages and the devices used to carry out the calculation.

3.1. Finite element method

Wheel-rail contact study can be carried out experimentally and/or numerically. However, the experimental procedures for railway research are known to be difficult to control and are expensive. On the contrary, numerical method has shown itself a valuable tool to analyse wheel-rail contact problem. Inputs of the models are easily manipulated to achieve the boundary conditions close to the practical circumstances. Outputs from the models are selected for a variety of wheel-rail contact problems. Hence the finite element method (FEM) was chosen in the current research as it has been known as the one of the most powerful tool to simulate the complex engineering problems.

3.2. Software products

The numerical method has been primarily applied throughout the thesis with the supports of several software products listed as follows:

- *PRO/ENGINEER WILDFIRE* version 5.0
- *ANSYS/LS-DYNA* version 13.0 – 14.5
- *LS-PREPOST* version 3.2 – 4.0
- *CONTACT* version 12.2

PRO/ENGINEER WILDFIRE developed by Parametric Technology Corporation (PTC) [171] offers a versatile CAD environment to design the most complicated product. This product was applied to create the geometries of wheel-rail bodies based on the Australian standard (ANZR1 wheel [172] and 60 kg/m rail [173]).

ANSYS/LS-DYNA has been introduced since 1996 as the result of a collaborative effort between Livermore Software Technology Corporation (LSTC) [174] and ANSYS, Inc [175]. This commercial engineering simulation software is specially designed for structural analysis, including linear, nonlinear and dynamic studies. A complete set of element behaviour, material models and time-tested explicit solver is provided for a wide range of mechanical design problems. In addition, ANSYS also offers thermal analysis and coupled physics capabilities including acoustic, piezoelectric, thermal-structural, and thermal-electric. Since wheel-rail contact is a highly dynamic and nonlinear problem, ANSYS/LS-DYNA is an ideal tool for solving the questions stated in the literature review.

LS-PREPOST also delivered by Livermore Software Technology Corporation (LSTC) [174] is an advanced pre and post-processing tool with a comprehensive LS-DYNA keyword support. The latest version of this software can be freely downloaded from official website of LSTC company. In this research, most of the basic steps to build up wheel-rail contact model were carried out in the ANSYS

Mechanical environment, whereas some further implementations and post-processing were required to be completed in LS-PREPOST.

CONTACT software supported by VORTECH BV and TUDelft [59, 65] can efficiently solve the general contact problems such as wheel-rail contact or roller bearing. Some of the rolling contact theories by E.A.H. Vollebregt [104] and J.J. Kalker [64] are implemented. The most advantage of CONTACT is the significant decrease of calculation time compared to the complete models based on finite element approaches. Hence this software was applied to validate some results from FEM models.

In addition, some other products were also utilized such as MATLAB and TRELIS [176]. The thesis also used some results obtained from Multibody Simulation (MBS) by GENSYS [177] and measured strain data on site [178] to validate the FEM models.

3.3. High Performance Computer (HPC) Cluster

The superior technical devices nowadays have extensively supported researchers to overcome the key barriers in gaining the excellent results. More powerful computers have been developed with advanced performances, and their capabilities have been upgraded yearly.

In this study, the finite element models were constructed by a Dell computer with Intel Core i7-2500 CPU at 3.3 GHz, 8 Gb installed memory (RAM) running on Window 7 professional. Very fine mesh can be produced in the contact surface region to achieve the best results.

A disadvantage of finite element method is that the finer the mesh is generated, the longer the calculation time is required due to the increasing of number of nodes and elements. Therefore high end computing resources are essential for carrying out the simulations. The University of Wollongong provides a number of High Performance Computers to researchers from any discipline. Parallel computing of the FEM model was carried out on a High Performance Computer Cluster (22 x 64 core Dell Power Edge C6145) to account for computational cost. As data sets increased significantly due to very fine mesh used, it took 5 days for each job running with 4 Cores at 2.3 GHz.

CHAPTER 4

WHEEL-RAIL CONTACT ON THE STRAIGHT TRACK UNDER HIGH AND LOW ADHESION CONDITIONS

In this chapter, the finite element elastic-plastic code ANSYS/LS-DYNA was utilised to investigate the stress states and material response of wheel/rail under three contact situations, including high and low adhesion, and full slip. Canted and non-canted rails were considered to measure how the cant angle affected the contact stress levels. Furthermore the effects of the worn wheel/rail profiles on the contact zone and contact pressure were also examined. The results showed that a higher level of adhesion would enlarge the slip region in the stick/slip contact patch and widen the surface damage to a larger area. Moreover, the worn wheel/rail profiles would result in a non-elliptical contact patch and an increase of the contact pressure. Based on the shakedown map, it was anticipated that the rail would be damaged from the ratchetting response of the material.

The content of this chapter has been published in [35]:

***K. D. Vo**, A. K. Tieu, H. T. Zhu, and P. B. Kosasih, "A 3D dynamic model to investigate wheel-rail contact under high and low adhesion," International Journal of Mechanical Sciences, vol. 85, pp. 63-75, 2014.*

4.1. Introduction

Rolling contact between wheel and rail can be greatly affected by many factors such as train speed, loading, wheel/rail profiles, and the reaction of the track components. The recent appearance of the new generation AC traction locomotive has brought many advantages to railway operators due to a much higher level of adhesion [9]. However, the more frequent AC locomotives are utilised, the greater the longitudinal force is exerted onto the track structure, which might cause a severe damage to the track. Moreover, the higher creepage generated from AC locomotives also causes a higher temperature and contact stresses. The stresses in the contact patch include normal stress and two components of tangential stress. In order to investigate the extent of any damage to the wheel and rail, these stress components need to be analysed in details. Research on railway dynamics has been conducted for a long time, and many solutions for rolling contact have already been proposed. Some traditional theories and numerical models were introduced in chapter 2.

In rolling contact, the relationship between the traction force (or adhesion coefficient) and creepage is illustrated in Figure 4.1. The traction force increases with creepage until it reaches a critical value [31]. However, it is also found that after the saturation point; the adhesion coefficient can drop off due to the softening of the rail material at high temperature or the utilization of friction modifiers such as greases [10]. The decrease of adhesion coefficient (or traction force) may lessen the magnitude of stresses exerted on the contact surfaces.

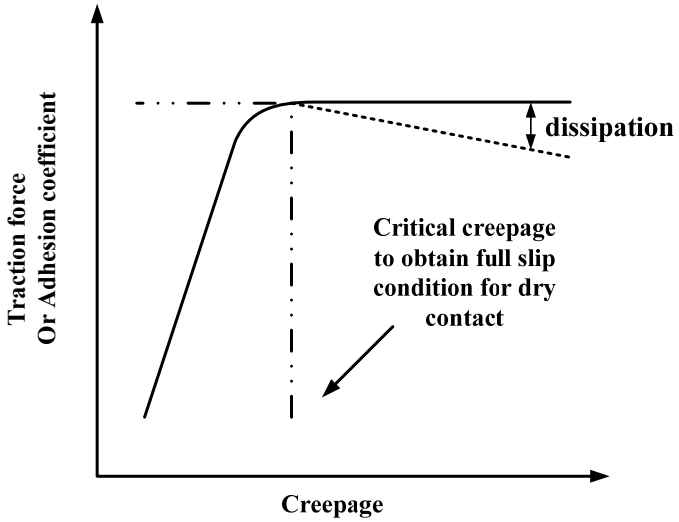

Figure 4.1 Traction force (or adhesion coefficient)-creepage relationship in wheel-rail contact

From the literature review, it is noted that the differences in stress states and the contact patch geometry under low/high adhesion levels or full slip conditions have not been distinctly clarified up to now. Furthermore, the question of whether the levels of adhesion have any influence on the fatigue damage has not yet been answered. In this chapter, 3D elastic-plastic FEM models by ANSYS/LS-DYNA codes for wheel/rail contact on a straight track were introduced. Both the new and worn profiles were utilized in these simulations. These models highlighted the stress states and the contact patch properties of frictional rolling contact under different adhesion levels, while the time history of stress states which included two regions of longitudinal stress (tensile and compressive) were presented. Some indications related to fatigue damage were discussed as well. The vibration of wheel, wheelset and vehicle and the track-vehicle interaction play important roles in wheel/rail contact stress analysis since it may increase the magnitude of stresses. However, the simulations in this study were carried out for a short straight track (600 mm), and the travelling time was fast; these effects, hence, would be neglected to simplify the input conditions. The effect of the frictional power dissipated at the contact and the consequent adhesion recovery due to the friction forces, which destroy the contaminants between wheel and rail [77, 179-180], was also not considered in this study.

4.2. Numerical modelling

4.2.1. FE model description

Since wheel-rail rolling contact is not symmetrical, 3D dynamic finite element models must be carried out to accurately determine the stress state of the wheel/rail. New profiles of the ANZR1 wheel [172] and 60 kg/m rail [173] were generated with the support of Pro ENGINEER Wildfire, and then imported into the finite element code ANSYS/LS-DYNA for further analysis. Since Australian rails are normally canted 1 in 20 [181], a cant angle θ equivalent to 1 in 20 was also applied onto the rail. A schematic of the FEM model is shown in Figure 4.2.

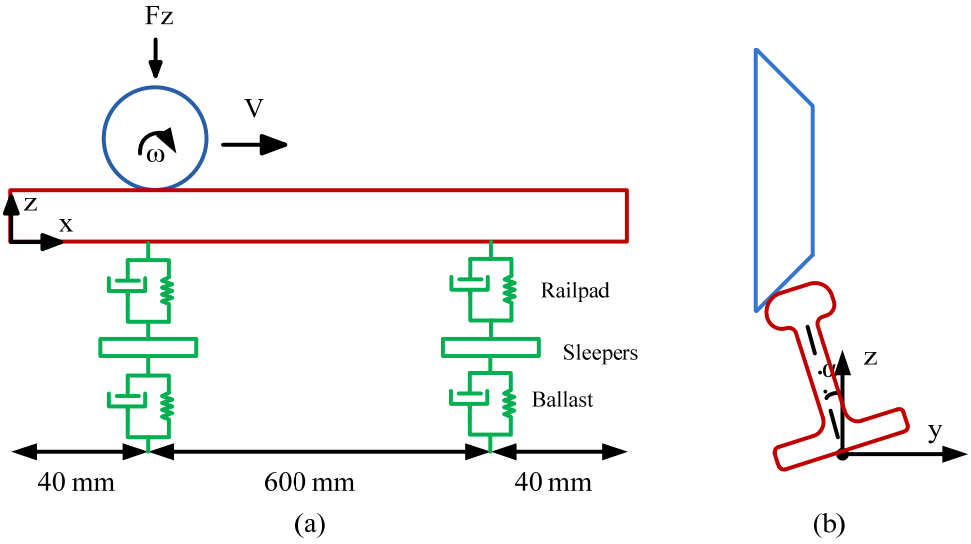

Figure 4.2 Schematic diagram of FEM model for straight track (a) illustration of FEM model (b) canted rail

A 680-mm track was modelled to cover the distance between two sleepers (600 mm) and a full wheel was simulated with the 8-node solid elements (SOLID164). The elements placed under the rail (rail-pads, sleepers, and ballast) were also included in the simulation, the sleepers were replaced by mass elements (MASS166), and the

equivalent spring and damping elements (COMBI165) were used to model the rail-pad and ballast. The shape functions of all the elements can be found in [182].

To justify the influence of mesh size on simulation results, the FE model was run with different mesh sizes at the contact surface (from 2 mm to 1 mm). It was noticed that the finer the mesh was generated, the higher the pressure would be obtained. The value of pressure was converging with the mesh of 1.3 mm (1174 MPa) and 1 mm (1229 MPa).The difference between the pressure values of 1.3 mm and 1 mm was only 4%. Zhao et al. [48] discussed the effect of mesh size on the accuracy of the simulation results, and it was indicated that this mesh size was sufficiently fine for the wheel/rail contact problem. Therefore fine mesh (1 x 1 mm) was generated at the contact surface and coarse mesh was applied for those regions furthest from the contact surface. The FEM mesh of 363,427 elements and 393,387 nodes is illustrated in Figure 4.3.

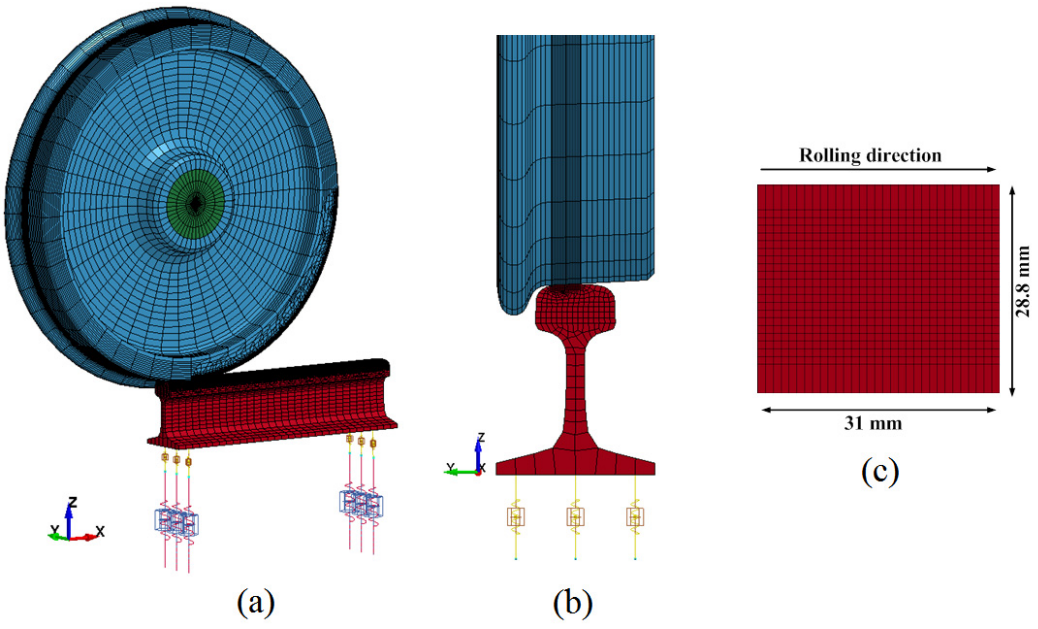

Figure 4.3 Non-uniform mesh of FEM model and fine mesh (1 x 1 mm) at the contact surface (a) Overall view (b) Side view (c) Mesh at the contact surface

To characterise wheel-rail contact, the automatic surface to surface contact (ASTS) algorithm and Coulomb friction were applied to describe frictional rolling. The Coulomb friction law [183] is described by the following equation:

$$\begin{cases} \tau_{\lim} = \mu P_o \\ \|\tau\| \leq \tau_{\lim} \end{cases} \quad (4-1)$$

where P_o is maximum contact pressure; μ is friction coefficient. and $\tau_{\lim}$ is limiting frictional stress. In ANSYS/LS-DYNA [183], the friction coefficient is calculated from dynamic friction coefficient μ_d and static friction coefficient μ_s, exponential decay coefficient DC and relative sliding velocity at contact point V_{sl} by the following equation:

$$\mu=\mu_d+(\mu_s-\mu_d)e^{-DCV_{sl}} \quad (4\text{-}2)$$

The equivalent shear stress τ for the 3D model is determined as follows:

$$\|\tau\| = \sqrt{\tau_x{}^2 + \tau_y{}^2} \quad (4-3)$$

A classical bi-linear elastic-plastic material model was utilised for the wheel and rail materials and an initial velocity state was applied to the wheelset at the first time step to obtain a quick and stable state for the dynamic model.

4.2.2. Input parameters

The wheelset, which was simulated as a rigid body, was set rolling at 80 km/h under an axle load of 130 kN. In wheel/rail contact, the vertical load exerted on the wheelset should be varied around a mean value due to the effects of vibration from both the vehicle and the track components. However the length of the track modelled in this study was 600 mm, which led to a very short travelling time of the wheel

(0.027sec). Hence the axle load was assumed to be constant during this short time, and the effect of the lateral force produced by the lateral movement of the wheelset respect to the track was neglected. A constant coefficient of friction of 0.45 was used for dry contact conditions [7-8]. The properties [48, 184] of wheel-rail materials and the track components are listed in Table 4.1.

Since these simulations were for straight track, the lateral and spin creepages were not considered. In order to predict the relationship between the coefficient of adhesion and creepage under the described conditions, both the software CONTACT [59] and the proposed FEM model were used to calculate the traction forces and coefficients of adhesion under different values of longitudinal creepage (from 0%~1.6%). The program CONTACT was developed from the well known rolling contact theory of Kalker [66], where the constitutive law was formulated from the relationship between traction and displacement using the general elastic theory. The contact regions on the wheel/rail were considered to be elastic half-space, which is usually employed in most railway vehicle equations.

Table 4.1 Values of input parameters

Components	Parameters	Values
Railpad	Stiffness	200E6 N/m
	Damping	50E3 N.s/m
	Height	0.075 m
Sleeper	Mass	314 kg
	Spacing	0.6 m
Ballast	Stiffness	$125x10^6$ N/m
	Damping	$310x10^3$ N.s/m
	Height	0.25 m
Wheel and Rail	Young's modulus	210 GPa
	Poisson's ratio	0.3
	Density	7800 kg/m^3
	Yield Stress	0.8 GPa
	Friction coefficient	0.45

Two situations corresponding to low and high adhesion levels were chosen for the following values of creepage. In this study, the constant friction coefficient was applied; hence the adhesion coefficient was kept constant after it reached the critical point (or also called saturation point). The values of creepage were selected before the saturation value to examine the influence of different adhesion levels on contact stresses. These values were also referenced from [4] and the adhesion curve (Figure 4.6):

- Case 1: longitudinal creepage ξ_x=0.28% (low adhesion)
- Case 2: longitudinal creepage ξ_x=0.47% (high adhesion)

Moreover, the stress states under a full slip condition (case 3) were also examined to compare with those from case 1 and case 2:

- Case 3: longitudinal creepage ξ_x=1.2% (full slip)

4.3. Results and discussions

4.3.1. Validation of FE model

The accuracy of FEM model was verified by classical methods such as CONTACT [59] and Polach's model [70-71]. Table 4.2 summarises the forces in the contact area for various locomotives. The amplitude of contact loads between FEM, CONTACT, and Polach's model were in good agreement. All three solutions produced equal normal forces for two cases, but the traction forces in case 1 ($\xi_x = 0.28\%$) were lower than in case 2 ($\xi_x = 0.47\%$). The levels of adhesion obtained from the finite element models were 25.36% for case 1 and 35.71% for case 2. This increase in adhesion led to a significant rise in the traction force from about 32.9 kN (low

adhesion) to 46.4 kN (high adhesion). This change would result in a variation of tangential stress distribution and will be discussed further in the next sections.

In the FEM method the boundary of the contact zone was determined by examining the interface nodal pressure. A node belongs to the contact area if the magnitude of the nodal pressure P_n (n: node number) is greater than zero:

$$|P_n| > 0 \qquad (4-4)$$

The shape of contact patch is illustrated in Figure 4.4. Since the new wheel/rail profiles were used in these simulations and the radius of wheel-rail curvature does not vary along this contact location, the contact zone was elliptical [40]. The three-dimensional illustration of the contact pressure can be observed in Figure 4.5. The contact pressure distributed within the contact patch in two cases of adhesion levels was found almost the same. The maximum pressure reached the values of 1232 MPa and 1229 MPa for the low and high adhesion, respectively. The pressure values were negative because the directions of coordinate system and normal load were in opposite direction.

Table 4.2 Contact forces between wheel/rail

Methods	Contact Force (kN)				Adhesion level = Traction force/Normal force (%)	
	Normal Force		Traction force			
	Low Adhesion	High Adhesion	Low Adhesion	High Adhesion	Low Adhesion	High Adhesion
FEM	129.71	129.88	32.90	46.39	25.36	35.71
CONTACT [59]	130	130	31.50	49.00	24.00	37.69
Polach [70]	130	130	30.33	43.04	23.33	33.11

Table 4.3 Results of normal contact problem

Methods	Contact patch						Maximum pressure (MPa)	
	Semi-axis a (mm)		Semi-axis b (mm)		Ratio a/b			
	Low Adhesion	High Adhesion	Low Adhesion	High Adhesion	Low Adhesion	High Adhesion	Low Adhesion	High Adhesion
FEM	9.9	9.9	6.02	6.02	1.65	1.65	1232	1229

Table 4.4 Contact results under full slip condition

Methods	Contact patch			Contact force (kN)		Maximum pressure (MPa)
	Semi-axis a (mm)	Semi-axis b (mm)	Ratio a/b	Normal force	Traction force	
FEM	9.9	6.02	1.65	129.86	57.46	1220

Table 4.5 Comparison of non-canted and canted rails (high adhesion)

Rail	Contact patch			Contact force		Adhesion level = traction force/normal force (%)	Maximum pressure (MPa)
	Semi-axis a (mm)	Semi-axis b (mm)	Ratio a/b	Normal Force (kN)	Traction force (kN)		
Non-canted	10	6.22	1.61	130.00	47.50	37.05	1222
Canted	9.9	6.02	1.65	129.88	46.39	35.71	1229

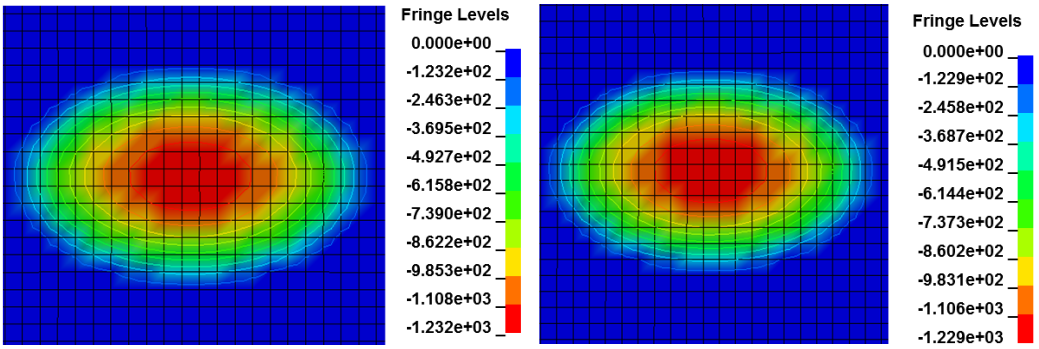

(a) Creepage ξ_x=0.28% (b) Creepage ξ_x=0.47%

Figure 4.4 Contours of nodal interface pressure (MPa) on rail surface (mesh size 1x1 mm)

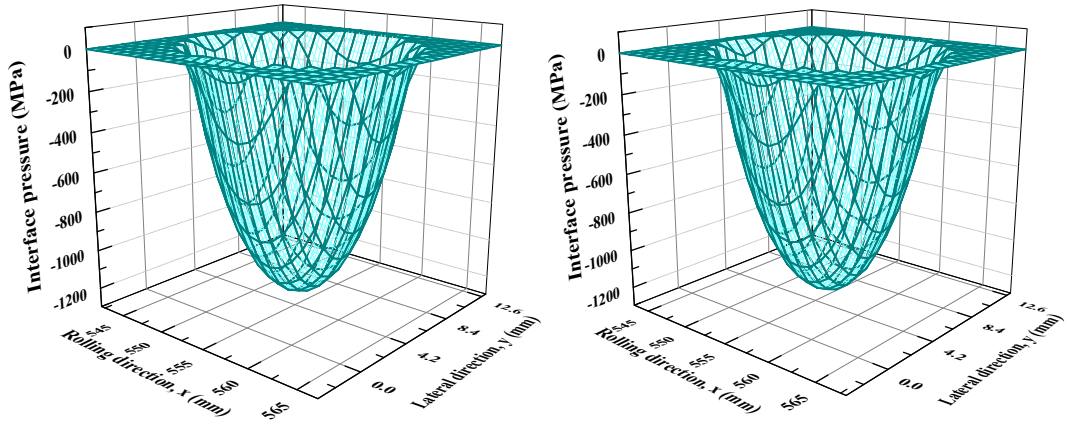

(a) Creepage ξ_x=0.28% (b) Creepage ξ_x=0.47%

Figure 4.5 3D distribution of nodal interface pressure on the rail surface

The dimension of the contact patch obtained from FEM is given in Table 4.3. The results showed that the contact patch and the contact pressure were similar for both low and high rail adhesion levels, which confirmed the findings from [95]. The contact results under a full slip condition in Table 4.4 also indicated a negligible influence of adhesion conditions on normal contact parameters (contact area, interface pressure), although the traction force increased significantly to 57.46 kN with a higher creepage.

From the above results it could be concluded that the FEM results agree well with the classical results, which meant the proposed model could be used to analyse the stress in more complex situations.

4.3.2. Traction force between wheel and rail

To understand the influence of creepage on traction forces and the coefficient of adhesion, the program CONTACT and FEM were run to determine the adhesion-creepage curves. For an axle load of 130 kN and a rolling speed of 80 km/h, the relationship between traction force (or creep force) and creepage under dry contact is illustrated in Figure 4.6. These traction curves were similar to those obtained from the experiments in [26, 29]. It was also noticed that the FEM result was slightly lower than the CONTACT result before the creepage reached the critical value.

When creepage was small, the traction force increased linearly with the creepage. Under dry contact conditions the critical traction force was 57 kN for a creepage of 1% (Figure 4.6). In other words, full slip was obtained at this value of creepage. The curve of the coefficient of adhesion versus creepage for the same load condition is also shown in Figure 4.6. A maximum coefficient of adhesion of 0.45 at 1% creepage was obtained from a dry coefficient of friction of 0.45 in the FEM models and CONTACT models.

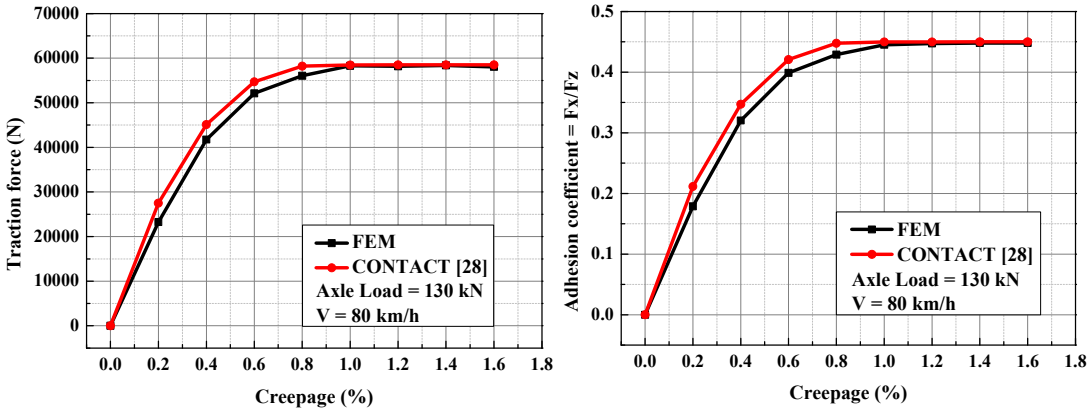

(a) Traction curve (b) Adhesion curve

Figure 4.6 Traction curve and adhesion curve (dry contact, friction coefficient = 0.45, F_z = 130 kN, V = 80 km/h)

4.3.3. Effects of a canted rail and worn wheel/rail profiles

Since the cant angle is usually applied on the rail nowadays to improve passenger comfort and also the rail life, there is a need to examine whether a canted rail has any remarkable influence on the contact zone before doing any further analysis. Moreover, the effect of the worn wheel/rail on the contact patch was also examined.

4.3.3.1. Influence of a canted rail

Simulations for a rail canted 2.86^{o} and a non-canted rail under high adhesion conditions were conducted to investigate the effects of a canted rail.

The locations of the contact zones on the surfaces of the canted/non-canted rail are shown in Figure 4.7. The contact zone on the non-canted rail was found near the rail gauge where damage might frequently occur, especially on the curved track [37].

The rail web could be bent faster if a normal load was regularly exerted at this contact location of non-canted rail. Whereas the contact zone on a canted rail was located at the centre of the contact patch, a normal load could be distributed more evenly on the rail web at this spot. The stress contours showed that the maximum normal stress on non-canted rail was slightly higher than a canted rail.

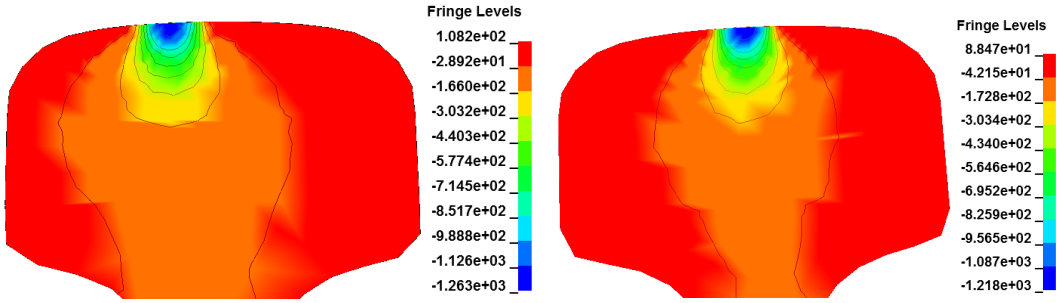

(a) Non-canted rail (b) Canted rail

Figure 4.7 Normal stress (MPa) contours on the cross section of non-canted and canted rails

A comparison of canted/non-canted rail under high adhesion is summarised in Table 4.5. The differences between the results were small, which could be explained by the minor change of radius of wheel-rail at the contact zones under a cant angle of 2.68^{o}. However, the results showed that the contact area decreased if the rail was canted. Thus the applied cant angle might help the rail to bear less stress, and rail life therefore could be improved.

4.3.3.2. Influence of worn wheel-rail profiles

In the wheel/rail contact area, both rolling and sliding may occur. The curvature of the wheel/rail at the contact area would be changed after quite a long time in service due to sliding of a wheel on a rail. In order to investigate the influence of the worn profiles on the shape of the contact zone and the pressure distribution, the worn

wheel/rail were also applied in the simulation. Plotted in Figure 4.8 are the worn profiles of ANZR1 wheel and 60kg/m rail provided by RailCorp Australia [185].

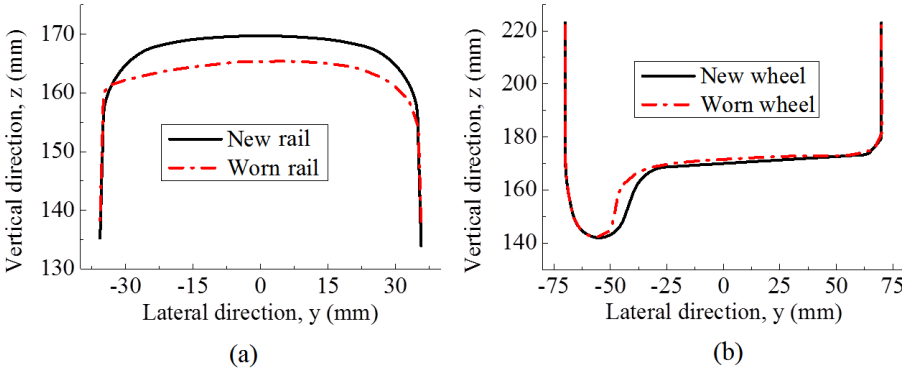

Figure 4.8 Wheel/rail profiles (a) rail profiles (b) wheel profiles

The comparison of the shape of the contact patch and the distribution of contact pressure between the new-profile and worn-profile simulations is shown in Figure 4.9. It was observed that the shape of the contact zone were no longer elliptical in the simulation using the worn profiles. When the contact patch from the worn profile was compared to the new profiles, the length of lateral axis 2b increased by 1.5 mm from 12.04 mm to 13.54 mm (Figure 4.9b), and the increase appeared on the upper side of the longitudinal axis.

The interface pressure within the contact area on the worn rail can be observed in Figure 4.10. For the worn-profile, the maximum pressure of 1259 MPa was higher than the value 1229 MPa from the new-profile simulations. The difference of pressure between two simulations could be explained by the change of the contact zone. The increase of contact pressure may increase the chance to cause damages within the contact zone.

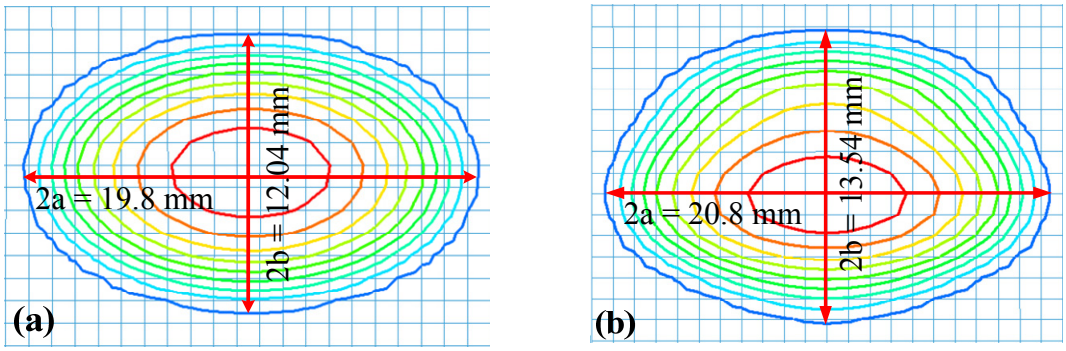

Figure 4.9 Shapes of contact zone (a) new profiles (b) worn profile (ξ_x=0.47%, mesh size 1 x1 mm)

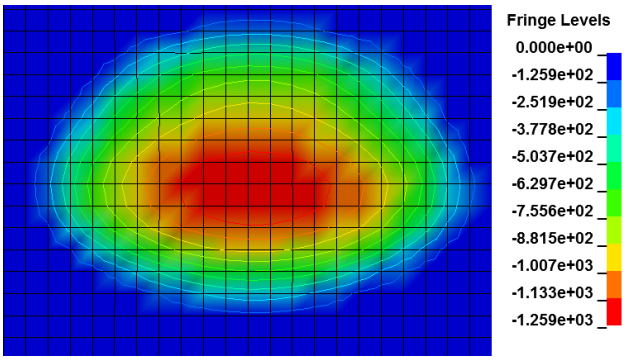

Figure 4.10 Contact pressure distribution of worn-profile simulation (ξ_x=0.47%, mesh size 1 x 1 mm)

4.3.4. Stress states in wheel-rail contact

This section presents the detailed stress distributions of two adhesion cases at the same simulation time of 0.0245s when a stable state was reached. As stated in section 4.3.1, the pressure in the contact patch was not affected by the adhesion condition in the contact patch; hence this section focused mainly on the tangential stress components.

4.3.4.1. Contact patch characteristics

The contact area under frictional rolling is generally divided into stick/slip regions. The sub-divisions of these two regions and distribution of shear stress within the elliptical contact zone are illustrated in Figure 4.11 and Figure 4.12, respectively.

Since Coulomb friction was used, the resulting shear stresses were distributed on the contact interface. When the magnitude of the shear stress is smaller than the critical shear stress, a sticking state (where there is no motion between the contact surfaces) occurs. Alternatively, if the shear stress is equal to the critical value then relative sliding takes place. The profiles of the adhesion/slip distribution illustrated in Figure 4.11 were similar for the two cases. A stick region appeared at the leading edge of the contact zone, while the slip zone covered the remaining area at the trailing edge of the contact patch. The unequal levels of adhesion resulted in different ratio of stick /slip zone for case 1 and case 2. Under low adhesion the number of nodes in the stick region occupied 67% of the total contact nodes which was much more than those in the slip region. In case 2, however, the number of sticking nodes was reduced to 46% of the total contact nodes, which meant that the increase of longitudinal creepage from 0.28% to 0.47% definitely led to a reduction in the area of adhesion and an increase in the slip area.

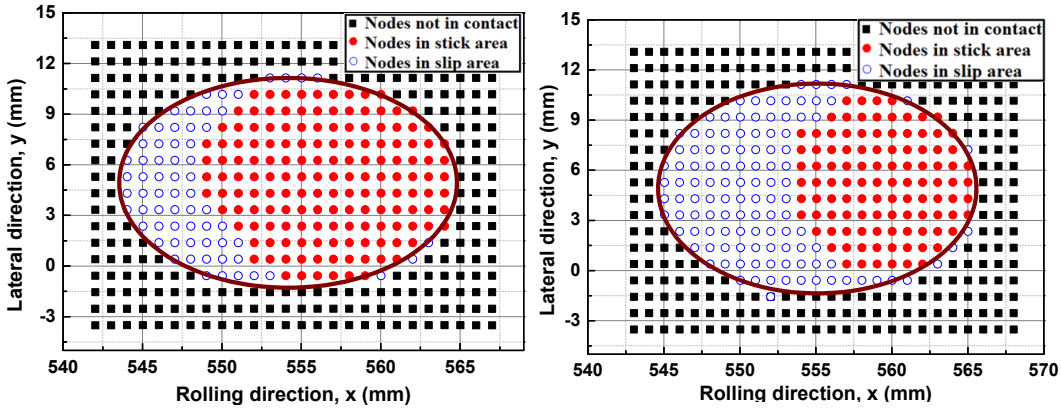

(a) Creepage ξ_x=0.28% (b) Creepage ξ_x=0.47%

Figure 4.11 Sub-division of stick/slip regions in the contact zone

The surface stress distribution and the shear stress limit along the centre line of the contact zone are plotted in Figure 4.12. The curve ABCA' represented the surface shear stress limit determined from Coulomb's friction law. Since the interface pressure and friction were the same for the high and low adhesion cases, the curves ABCA' were similar. The curve ADCA' represented the surface shear stress obtained from the FEM models. At the adhesion zone, the curve ADCA' lied below the curve ABCA' which meant the magnitude of surface shear stress never exceeded the limit. At the slip zone however, part of the shear stress curve CA' coincided with the limiting curve ABCA'. The maximum shear stress increased from 400 MPa in the low adhesion state to 515 MPa in the high adhesion state as a result of a higher creepage and traction force (Table 4.3).

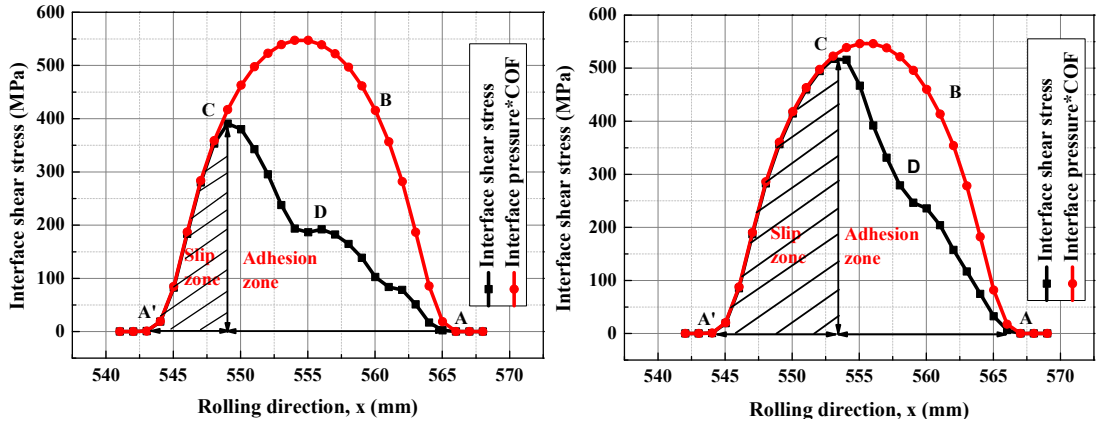

(a) Creepage ξ_x=0.28% (b) Creepage ξ_x=0.47%

Figure 4.12 Shear stress distributions in the contact patch

4.3.4.2. Tangential stress components

All three applied stress components and von Mises stress distributions across the contact zone are shown in Figure 4.13. It was noted that the surface longitudinal stress σ_x at the trailing edge was positive for both cases and the peak of σ_x in case 1 appeared to be lower than case 2. Besides, the σ_x curve was no longer symmetrical

like the σ_z curve and the peak value was shifted away from the centre of the contact patch. Furthermore the stress fields were not confined within the contact patch for frictional rolling; i.e, if a tangential force appeared, the stress σ_x extended beyond the contact area. This stress pattern had been qualitatively compared to the results obtained from the frictional rolling model of a cylinder on a plane in [186], and it was found that the stress distribution of these two frictional rolling cases was similar.

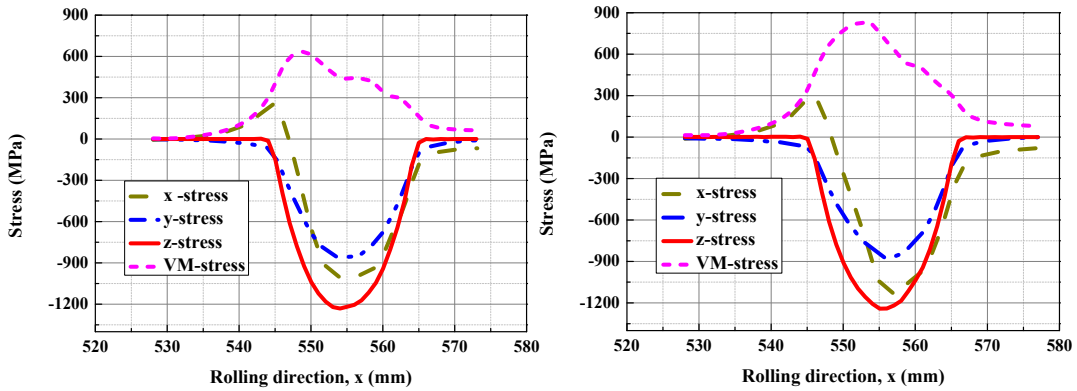

(a) Creepage ξ_x=0.28% (b) Creepage ξ_x=0.47%

Figure 4. 13 Three stress components and von Mises stress (MPa)

Figure 4.14 shows the time-history longitudinal stress state of one element (190163) at the centre of the contact patch (stick zone) on the surface of the rail. The elements in these two cases were 554 mm from the starting point of the rail. From the figure, the longitudinal stress state of the element before and after touching the wheel at this point on the surface of the rail could be observed. When the wheel was still far from this element, the longitudinal stress was approximately zero, but as the wheel approached closer two distinguishing regions of longitudinal stress (tensile and compressive) appeared in turn. The value of the longitudinal stress was negative (tensile stress) as the wheel moved in contact, and became positive (compressive stress) when the wheel began moving away from this element, while such phenomenon was not seen with the stress states in the other two directions (σ_y and σ_z). The large tensile stress of 1130 MPa might contribute to the crack initiation at the rail surface.

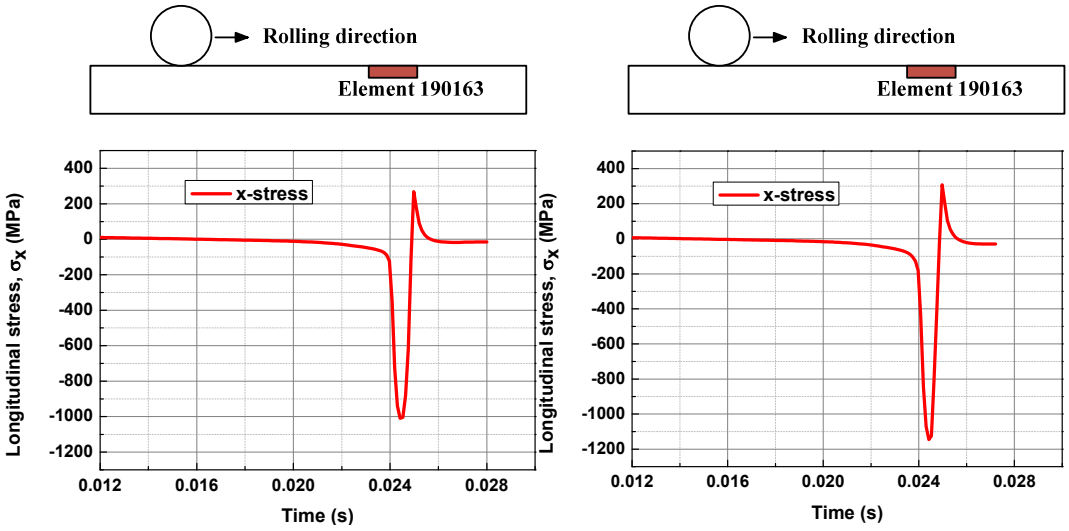

(a)Creepage ξ_x=0.28% (b) Creepage ξ_x=0.47%

Figure 4.14 Time history longitudinal stress $\boldsymbol{\sigma_x}$ of element 190163

The phenomenon of a longitudinal stress σ_x state in the rolling direction can be explained in Figure 4.15 where B is considered to be the target element. The wheel rolling process can be divided into five phases:

- Phase 1: before the wheel touches the contact point. Since the wheel is still far from the contact zone, the magnitude of longitudinal stress at the target element B remained at zero.
- Phase 2: the wheel begins to touch element A which is close to the target element B. Element A has stretched from the right to the left which is opposite to the rolling direction, and hence the stress of target element B is tensile.
- Phase 3: the wheel is just above the target element B. The stretch and tensile stress of element B reached their maximum values.
- Phase 4: the wheel begins to pass over the target element B, and touches element C on the right of B. The movement of element C from left to right tended to compress the target element B. Therefore, the stress of element B at this phase became compressive.

- Phase 5: the wheel is far away from the target element B, and the stress values returned to zero.

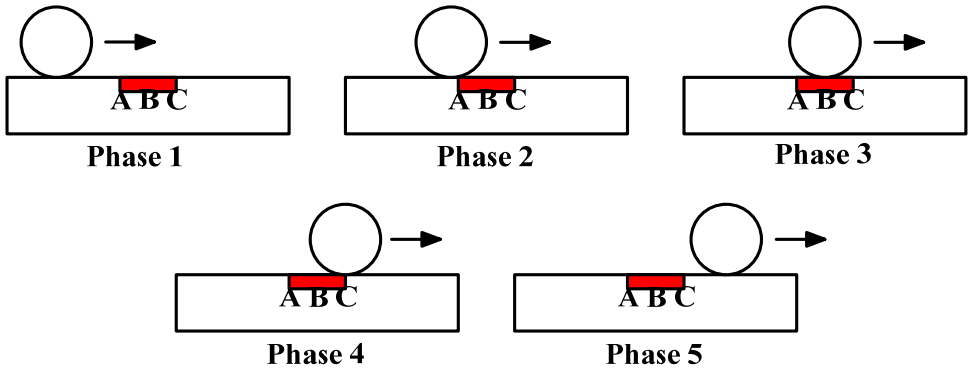

Figure 4.15 Five phases of rolling process

The same tendencies could be found in case 3 (full slip condition). As illustrated in Figure 4.16, the higher the creepage the further the peak value of σ_x had shifted from the centre, and there were also two regions (positive and negative) of σ_x on the surface of the rail. Moreover the maximum von Mises stress within the contact zone increased from 837 MPa (high adhesion, creepage ξ_x=0.47%) to 900 MPa (full slip, creepage ξ_x=1.2%).

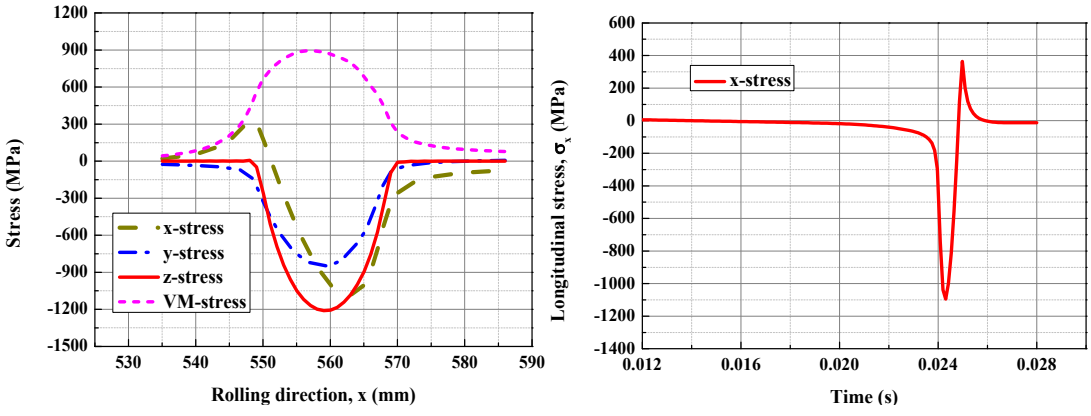

(a) Stress states on rail surface (b) Time history longitudinal stress σ_x

Figure 4.16 Stress distributions under full slip condition (creepage ξ_x=1.2%)

The appearance of tensile and compressive longitudinal stress σ_x in Figure 4.14 could also be seen from the "isosurface contours" plotted in Figure 4.17. No matter which side of the stress regions (tensile or compressive), the maximum longitudinal stress in a high adhesive state was larger than in a low adhesive state. Under low adhesion the absolute maximum values of stress in the positive and negative stress regions was 281 MPa and 1037 MPa respectively, while they increased to 320 MPa and 1156 MPa at a high level of adhesion.

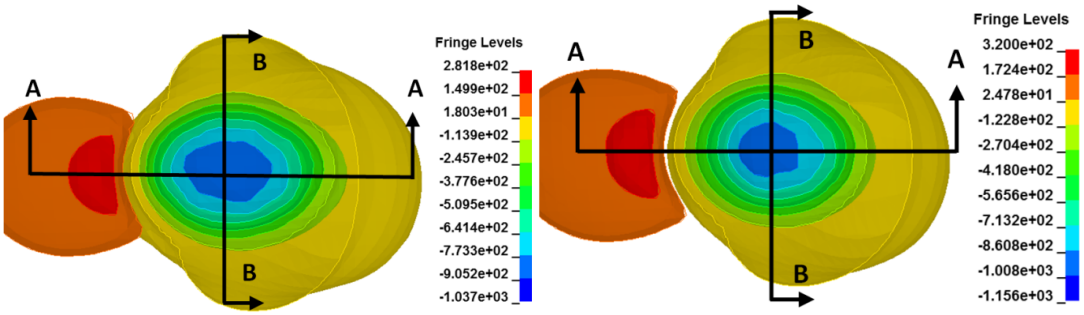

(a) Creepage ξ_x=0.28% (b) Creepage ξ_x=0.47%

Figure 4.17 Isosurface contour along the rolling direction (MPa)

The distributions of longitudinal stress σ_x and lateral stress σ_y on the cross sections of the wheel and rail are shown in Figures 4.18 and 4.19. The overall pattern of stress distributed on the wheel and rail were similar. The cross section AA of Figure 4.17 is illustrated in Figure 4.18. As shown in Figure 4.14 and Figure 4.17, they were compressive at the trailing edge and tensile at the leading edge of the contact zone. Moreover, the compressive and tensile regions not only appeared on the rail but also on the wheel.

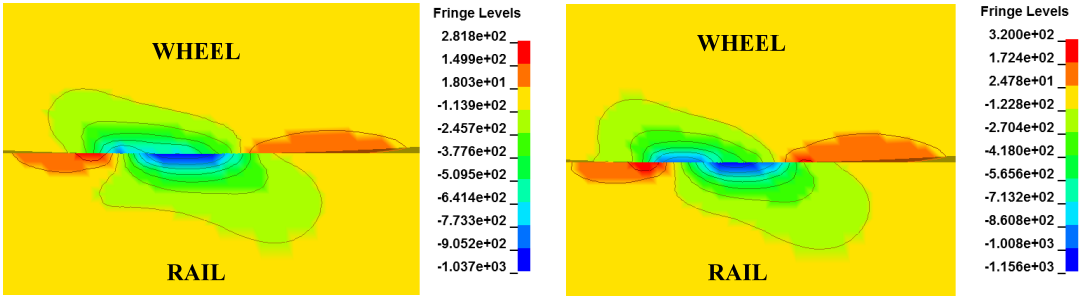

(a) Creepage ξ_x=0.28% (b) Creepage ξ_x=0.47%

Figure 4.18 Longitudinal stress distributions on the cross section AA (MPa)

Figure 4.19 illustrates the butterfly shapes of lateral stress distribution on the lateral cross sections BB of Figure 4.17 in two cases. Since the effect of lateral creepage was negligible in this study the magnitude of lateral stress in case 1 differs to case 2 by a small amount, and the enlargement of butterfly wings to the sub-surface material of wheel/rail were almost the same.

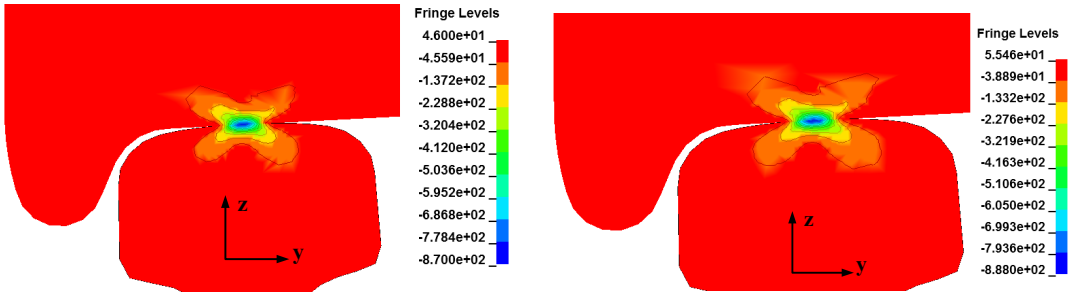

(a) Creepage ξ_x=0.28% (b) Creepage ξ_x=0.47%

Figure 4.19 Lateral stress distributions on lateral cross section BB (MPa)

From the above discussions, varying the adhesion condition obviously causes serious changes in the stick/slip region, traction force, and tangential stress components. The increasing of stress due to high adhesion level possibly results in damage initiation on the rail.

4.3.4.3. Von Mises stress distribution

The distributions of von Mises stress on the rails for two levels of adhesion are illustrated in Figure 4.20. Such contours have a similar pattern to those from [95]. As the tangential force in case 1 was lower than case 2, the maximum von Mises stress in case 1was 786 MPa which was lower than 837 MPa in case 2.

The three contours at two lateral cross sections (section 1 and 2 are in stick and slip region respectively), and one longitudinal section along the rolling direction (section 3) under high adhesion condition are also shown in Figure 4.20. There is a discrepancy in the maximum stress location between the two lateral cross sections. Close to the slip region, the maximum von Mises stress occurred at the top surface of the rail, whereas the peak stress in the stick region was located around 3 mm below the rail surface. These descriptions can be seen clearly in the plot of stress in the rolling direction (section 3). The higher stress in the slip region on the contact surface may cause surface damage (plastic flow, wear, or surface cracks) to occur in this region, although a high sub-surface stress in the sticking region can also initiate damage below the surface as well. Moreover, the slip region in the high adhesion situation was larger than in the low adhesion state, and hence can potentially cause damage to a larger area.

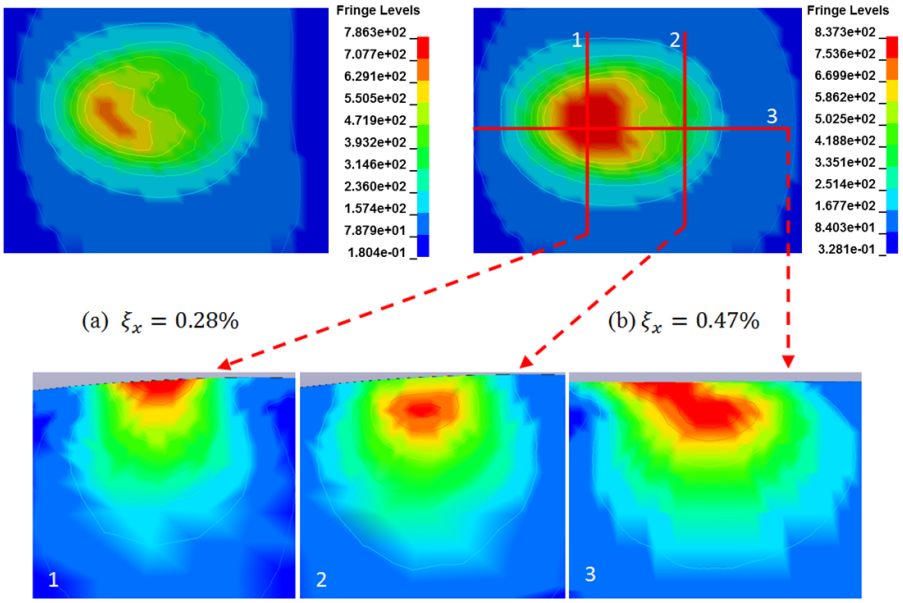

(c) Von-Mise stress distribution on cross section 1, 2 and 3 for creepage ξ_x=0.47%

Figure 4.20 Von Mises stress distribution (MPa)

Table 4.6 shows the comparison of the stresses on the wheel and the rail for high adhesion cases. It was found that the maximum shear stress on the rail and the wheel were almost the same, but the maximum von Mises stress on the wheel was slightly higher than that on the rail due to different mesh size (wheel elements: 1.1 mm, rail elements: 1 mm). However, the penetration of maximum stress on the wheel (4 mm) was deeper than that on the rail (2 mm). Therefore damage could be appeared on the wheel at the deeper position, leading to some wheel damages such as shelling or spalling [10].

Table 4.6 Comparison of stress on the wheel and the rail, ξ_x=0.47%

Contact bodies	Maximum shear stress (MPa)	Maximum von Mises stress (MPa)	Penetration of maximum stress (mm)
Rail	515	837	2
Wheel	517	850	4

In comparison to the low and high adhesion, the von Mises stress under full slip condition was much higher (Figure 4.21). The maximum von Mises stress may be up to 900 MPa at the contact surface and sub-surface as well. In addition, the region where maximum stress occupied the surface of the rail was clearly larger than in Figure 4.20. The maximum stress penetrated up to 4 mm below the sub-surface, which means not only the surface could be damaged but sub-surface was also likely suffered under this contact condition. Hence, if a full slip condition occurs, the combination of higher stress and enlargement of maximum stress region will lead to apotential damage over a wider area.

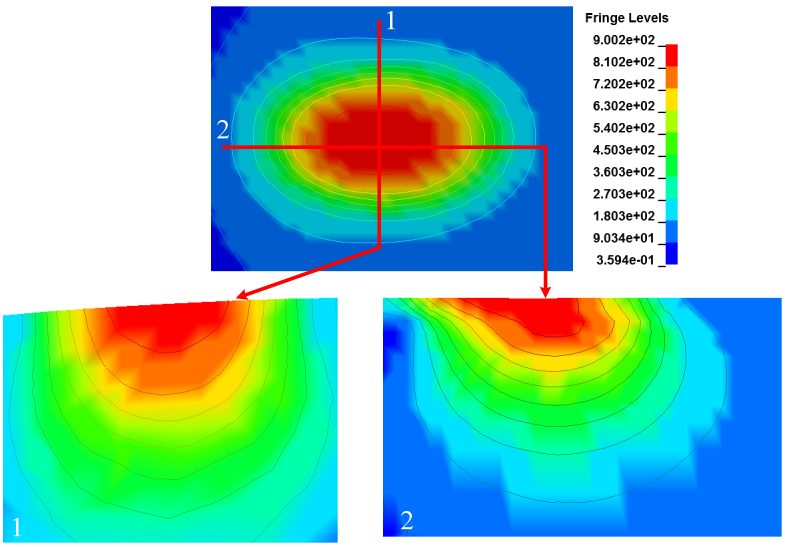

Figure 4.21 Von Mises stress distribution under full slip condition

4.3.5. Material response to contact stress

As discussed, the rails were normally exerted to a high wheel load through a relatively small contact zone. During their operational life, rails typically experience millions of load cycles from the passage of train wheels. The response of material subjected to repeated loading is governed by stress, strain, wear, and temperature change [135], and can be any types: elastic, elastic shakedown, plastic shakedown, and ratchetting. Plastic shakedown and rachetting normally occur in the contact zone of rail heads, and cause the fatigue initiation of surface cracks called “head checks”. For a specific contact load and geometry, diagrams called “shakedown maps” [187-

188] have been very useful in the FE modelling phase of rolling contacts, where they can be used to evaluate the response of the material and anticipate the position (surface/sub-surface) which can suffer the greatest damage.

The shakedown map identifying the response of material for the simulations is plotted in Figure 4.22. The load factor is given as P_0/k on the vertical axis, where P_0 is the maximum contact pressure, k is the material yield strength in shear (in this calculation, k = 234 MPa [139]). The contact friction is given as μ on the abscissa. The results obtained from the simulations are summarised in Table 4.7.

Table 4.7 Simulation cases

Parameters	Creepage ξ_x		
	0.28%	0.49%	1.2%
μ	0.45	0.45	0.45
P_0 (MPa)	1232	1229	1220
P_0/k	5.265	5.252	5.213

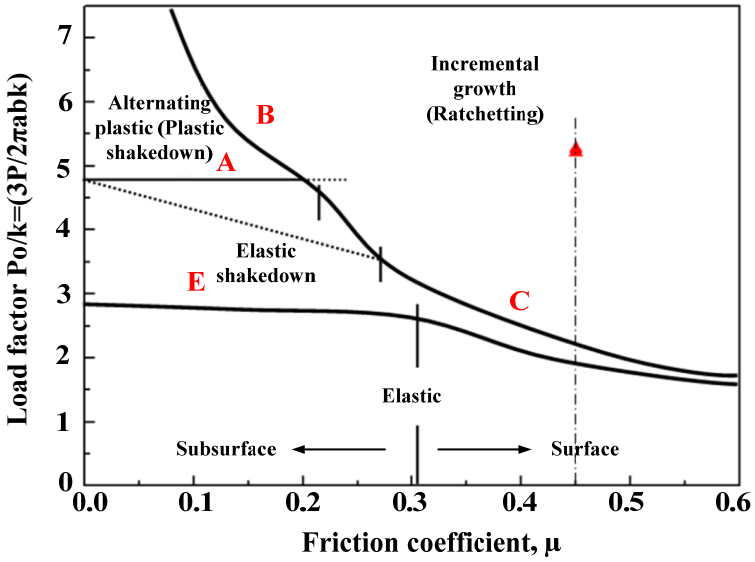

Figure 4.22 Shakedown map predicting the response of material in simulations [20]

A: Upper bound to elastic shakedown limit against alternating plasticity
B: Upper bound to plastic shakedown limit against incremental growth
C: Upper bound to elastic shakedown limit against incremental growth of surface strain
E: Elastic limit
(....) Lower bound to elastic limit

As shown in the diagram, the responses of rail material in all the simulations fell into the ratchetting region due to the high friction force and contact load exerted on the rails. It was then predicted that the material would accumulate additional plastic deformation for every cycle until it finally failed. Moreover, the damage was anticipated to occur on the surface rather than sub-surface.

4.4. Conclusions

The aim of this chapter was to provide a detailed comparison of frictional rolling stress state under low/high adhesion and full slip conditions. The results in the present investigation can be summarised as follows:

(1) Compared to the low adhesion state, the results from FEM models have indicated that the adhesion area of the high adhesion case will be reduced, but the coefficient of adhesion was higher.

(2) The contact location on the surface of the rail could be shifted from the centre of the rail head to near the rail gauge if a non-canted rail was used instead of a canted rail. Using a canted rail may help the rail web from bending and improve the life of the rail.

(3) The changes of the wheel/rail profiles (worn profiles) lead to the changes of the contact patch. The contact patch would no longer be elliptical and the contact pressure could be increased within the contact zone.

(4) The influence of adhesion on normal contact parameters (contact area, interface pressure) was almost negligible. However varying the adhesion condition from low to high can cause significant changes to the stick/slip region, traction force, and tangential stress components.

(5) The stress field in the rolling direction should be divided into tensile and compressive regions and the maximal stress in high adhesion conditions were higher than those in the low adhesion states.

(6) There was a significant increase of von Mises stress when the coefficient of adhesion increased. The higher stress in the slip region on the contact surface may cause surface damage (plastic flow, wear or surface crack) to occur in this region, although a high sub-surface stress can also initiate damage below the surface. Moreover, an increase of slip zone can cause the surface damage to a wider area, especially under the full slip condition.

(7) Based on the shakedown map, the response of materials under the contact conditions described in this chapter were predicted to be ratchetting, and the damage was anticipated to appear on the surface.

In this chapter, the detailed stress states and material responses on the straight track were presented. However, the contact phenomenon on the curved track could be more complicated due to the influences of many other factors such as angle of attack (AOA), or lateral force, possibly resulting in a more severe stress on the rail. Hence it is necessary to investigate the wheel-rail contact on the curved track, which will be presented in the next chapter of this thesis.

CHAPTER 5

PREDICTION OF DAMAGE FORMATION ON CURVED TRACK FOR VARIOUS WORN STATUS OF WHEEL/RAIL PROFILES

In wheel/rail contact, rolling phenomenon on the curved track can be much more complicated than that on the straight track, especially on a sharp curved track. Due to the influences of super-elevation (also called track cant), angle of attack (AOA) and rail cant, stress states on the high rail are significantly different from that on the low rail. Therefore, the appearances of damages on the low and high rails are different as well. These damages can result in rail failures, subsequently leading to the vehicle derailments. In this chapter, a realistic finite element model using Australian wheel/rail profiles (ANZR1 wheel and 60 kg rail) was developed to investigate the wheel/rail contact on the low and high rail of a curved track under high adhesion condition. Based on the contact stress states, surface damage mechanisms of curved rail track was determined. The new and worn profiles were utilized in the simulation to examine different contact situations: new wheel/new rail, new wheel/worn rail, and worn wheel/worn rail contacts. The obtained results showed that the two-point contact might appear on the high rail of the curved track and the stress distributions at each contact location were varied depending on the contact location and AOA. Moreover, the response of material on the rail head was predicted to be in the

ratchetting mode. Regarding the damage predictions, the rail corrugation tended to be formed on the low rail rather than the high rail; and it is easier for the fatigue defects to be developed on the standard carbon rail compared with hardened rail.

The content of this chapter has been published in [37-38]:

***K. D. Vo**, H. T. Zhu, A. K. Tieu, and P. B. Kosasih, "FE method to predict damage formation on curved track for various worn status of wheel/rail profiles," Wear, vol. 322-323, pp. 61-75, 2015.*

***K. D. Vo**, A. K. Tieu, H. T. Zhu, and P. B. Kosasih, "Rolling contact stress states of two contact points on curved track," presented at the 10th World Congress on Railway Research, Sydney, Australia, 2013.*

5.1. Introduction

As the train travels on a curved track, the vehicle and any passengers inside are influenced by the centrifugal force which is proportional to the square of the train velocity and inversely proportional to the radius of the track curvature. To neutralize the effects of centrifugal force on passengers, superelevation is usually applied to the curve by lowering the inside rail and raising the outside rail by an equal amount. Since a significant discrepancy of the height is created between the inner and outer rails (or the so-called low and high rail, respectively), the contact position and stresses on these two rails are also different.

The wheel/rail contact on curved track may be conformal or non-conformal [189]. The non-conformal contact on the low rail can be analysed with some classical theories introduced in chapter 2. Nevertheless contact on the rail gauge/wheel flange on the high rail cannot be analysed accurately due to the half-space and linear elastic assumptions in these models. Hence finite element method (FEM) has been considered as an efficient tool to analyse the wheel/rail contact phenomenon. With this method, the elastic-plastic material properties of contact bodies can easily be set up, and contact analysis on the rail gauge is not limited by the half space assumption.

The recently developed AC locomotive (high adhesion locomotive) has brought many advantages to the railway operation such as the improvements of braking efficiency, driving efficiency, reliability and maintainability. With AC traction, the braking effort can be much higher because the drive system in braking operates in traction mode to eliminate wheel slip. Besides the adhesion levels by AC locomotive are much higher so the locomotive can be significantly lighter for the same amount of braking. However the more frequent the AC locomotives are utilized, the higher traction force is exerted on the track structure, and possibly lead to the initiation of crack either on the rail head (squats) or along the gauge corner of the high rail (head checks) [190-192]. Rail stress analysis is a crucial element to provide understanding and prediction of the damage behaviour of the contact bodies [20]. The higher stress

exerted on the wheel/rail would produce a more serious damage at the contact zone [35]. Nonetheless very few numerical studies on damage analysis of curved track condition were found, especially under higher adhesion contact where the stress can be very high. Therefore this chapter presented a comprehensive 3D elastic-plastic explicit finite element model of rolling contact on a curved track to reveal the stress states and to predict the damage of the rails on a curved track under high adhesion conditions.

From the literature, it is noted that the comparison of the stress states on the low/high rails of a curved track has not yet fully introduced and the influence of the worn status of the contact bodies is still unknown. The parameters of AOA, curvature and rail cant have not been considered. However, these parameters are important since they have a significant influence on the contact stresses at the contact zone, leading to different damage scenarios. Hence the simulations in this research had been conducted to model the rolling contact of the wheel on both the low and high rails. Not only the new profiles but also the worn profiles were also utilized to construct the model, and to examine the behaviours of the contact zone and the stress status produced on the new/worn low/high rails. Moreover, a cant angle of 2.86^{o} [181] had been applied on the rail, the wheels were controlled to contact with the rails at different angle of attack (AOA) to investigate its effects. The dynamic effects had also been considered by including some sub-components of the track system such as sleepers, rail pad and ballast. The result of contact loads was presented. Additionally, predictions of the rail material response and the formation of contact fatigue defect and corrugations based on the shakedown map and experimental data respectively had been discussed.

5.2. Finite element model

The schematic of finite element models constructed from ANSYS/LS-DYNA code is shown in Figure 5.1. In order to simulate the effects of the curved track, the rail cant

angle and angle of attack denoted by α and β, respectively, were applied. All parameters were selected carefully from the literature review and realistic operating conditions in Australian railways.

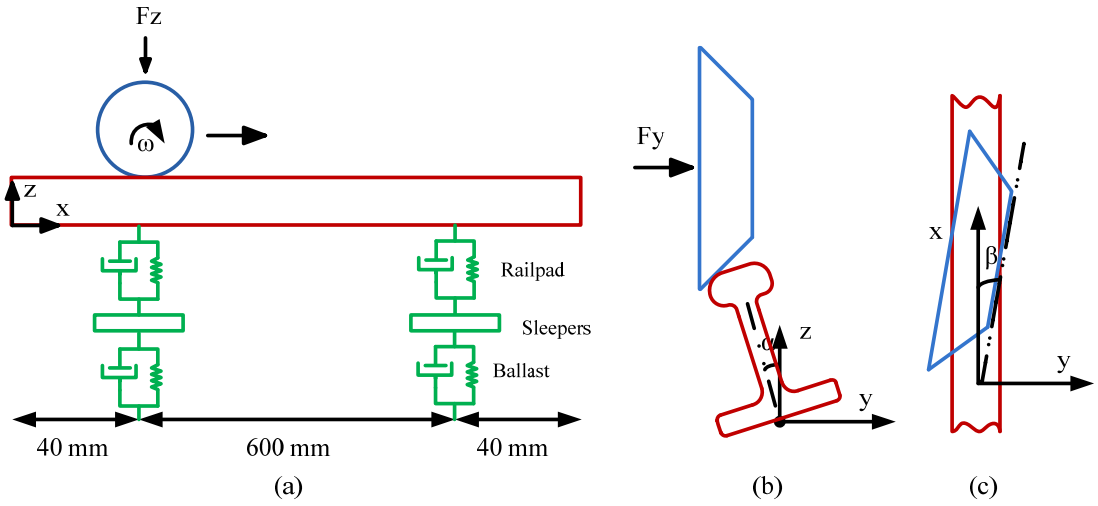

Figure 5.1 Schematic diagram of curved track dynamic model on (a) xOz plane, (b) yOz plane and (c) xOy plane (Fz: normal wheel load, Fy: lateral wheel load, ω: angular velocity)

In this chapter, the influence of the conditions of new/worn contact bodies on stress states was considered. The new profiles followed exactly the Australian profiles standard (ANZR1 wheel [172] and 60 kg/m rail [173]). The wheel radius was 470 mm. The three worn profiles (worn high rail, worn low rail, and worn wheel) were obtained from on-site measurements and provided by Railcorp Australia [185]. The measured profiles had shown that there was a significant change in the rail profile due to wear as well as plastic deformation, which might affect the contact locations and stress states on the rail head. The new/worn wheel/rail profiles are illustrated in Figure 5.2; and the detailed dimensions of the new profiles could be found in [172-173]. To simulate the high and low rail, the wheel positions and cant direction on the low rail and high rail were set differently. In particular, the low rail was canted to the right side and the high rail was canted in the opposite direction (Figure 5.3). Moreover the inner and outer sides of the low and high rails were also clearly distinguished (Figure 5.2).

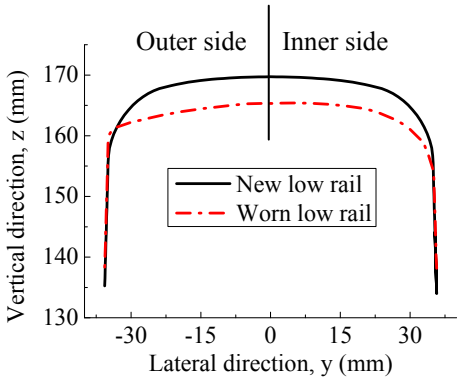

(a) Low rail

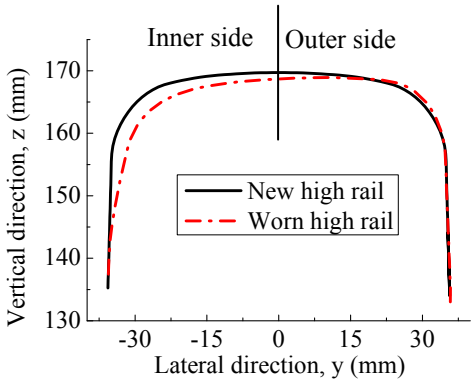

(b) High rail

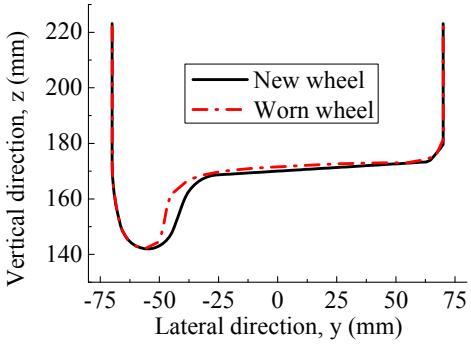

(c) ANZR1 wheel

Figure 5.2 New/worn wheel/rail profiles

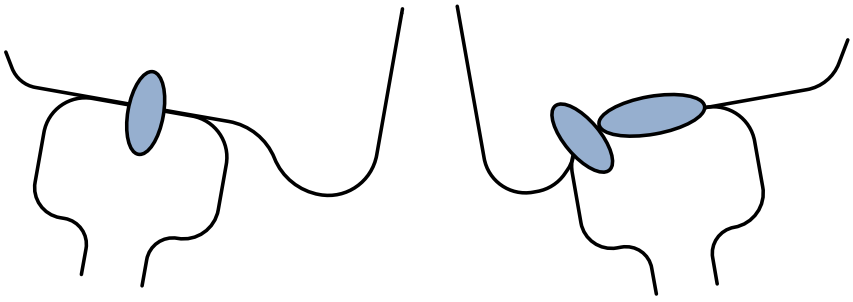

Figure 5.3 Possible wheel-rail contact on (a) low rail (b) high rail

The wheel and rail were simulated using the classical plastic kinematic hardening material model [193]. The following kinds of elements: solid elements (wheel/rail), mass elements (sleepers) and spring-damping elements (railpads and ballast) were

applied to build the FE model. The wheel-rail material properties and the parameters of railpad, sleeper and ballast can be found in Table 4.1 in the previous chapter. In addition, a non-uniform mesh was created in which fine mesh (1.3x1.3 mm) and coarse mesh could be found at the contact and the far-contact surfaces, respectively, resulting in a total of 497855 elements. It was verified in chapter 4 and [48] that this mesh size was adequately fine for the wheel/rail contact problem, as it was necessary to balance against long computational time (one week per run). Different mesh regions generated in FE model are shown in Figure 5.4. The movement of the bottom surface of the rail was restricted in the x and y directions, and the two ends of the rail was constrained in the rolling direction x.

Simulation had been carried out for the following cases of the wheel-rail contact on a curved track:

- Case 1: new wheel – new low/high rails.
- Case 2: new wheel – worn low/high rails.
- Case 3: worn wheel – worn low/high rails.

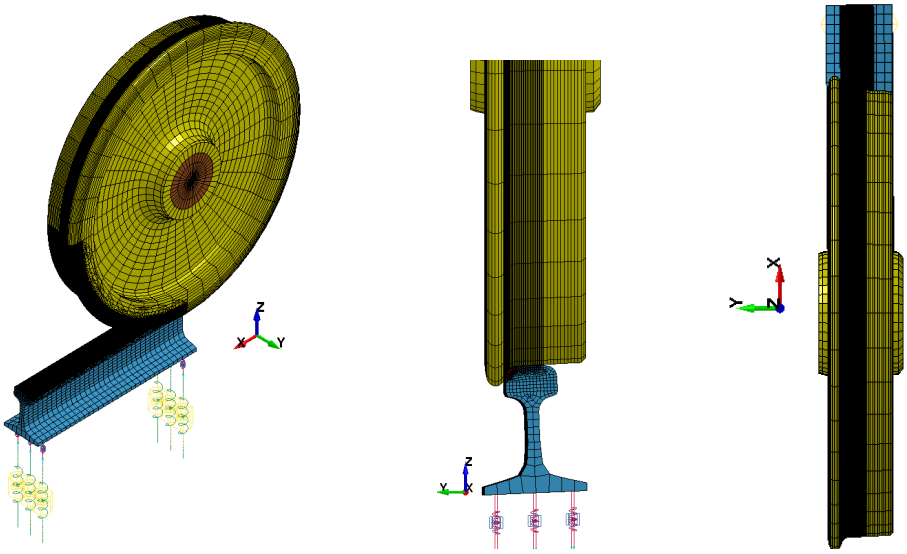

Figure 5.4 Three-dimensional (3D) mesh of FE model

The loading condition for high adhesion was referenced from [177]. The vibration of wheel and the track-vehicle interaction may enhance the stresses exerted on the rails. However the simulations in the present work were conducted for a very short track which resulted in very short travelling time of the wheel on the rail (0.103 s); these effects, therefore, would be neglected to simplify the input conditions. The wheel was placed very close above the rail at the beginning to avoid the high impact load. The contact between the wheel and the rail was defined by Coulomb's law of friction and the automatic surface to surface (ASTS) contact algorithm [182]. The slave and master surfaces were generated internally in LS-DYNA from the part ID given for each surface. Two values of friction coefficient for dry contact were applied on the rail surface at two different locations, with the friction on the rail gauge ($\mu = 0.22$) lower than that on the rail head ($\mu = 0.4$) [10, 36]. The wheel loads were applied at the wheelset which was modelled as a rigid body (non-deformed part) and glued with the wheel. The rolling speed was set at 21 km/h, and an initial velocity was also applied to ensure the stable state could be achieved quickly. Moreover the wheel was controlled to contact with the rail at two angle of attack (AOA = $1/3^o$ and $2/3^o$). Since the Australian rail is normally canted by an angle of 2.86^o (1 in 20) [181], an equivalent cant angle was applied on both the low and high rails. The wheel load and other input parameters were obtained from a Multibody Simulation (MBS) that was carried out by a collaborating research team in Central Queensland University (CQU) [177]. Details of loading conditions are outlined in Table 5.1. The creepage value of 8% was applied to ensure the high adhesion condition [36, 177].

Table 5.1 Input parameters for FE models

Parameters	Values	Unit
Normal wheel load, Fz	120	kN
Lateral wheel load, Fy	20.8	kN
Forward velocity, V	21	km/h
Rail cant angle, α	2.86^o	degree
Angle of Attack (AOA), β	$1/3^o$ and $2/3^o$	degree
Coefficient of friction (COF), μ	0.4 (rail head) and 0.22 (rail gauge)	

5.3. Results and discussions

5.3.1 Validation of FEM model

The FE models described above were run on a HPC Cluster with parallel processors to reduce the calculation time. In order to validate the FE model, the results of strain at the middle of rail web had been compared with the data achieved by strain gauge measurement from the technical report TR.169 of AC high adhesion locomotive [178]. The values of strain obtained from FE simulations varied from 119 to 229 microstrain, compared to the data of 85 to 245 microstrain from the report TR.169. . Although the comparison of strain was qualitative due to the coarse mesh at the rail web in FE models (shown in Figure 5.4), the results of FE models were still comparable and showed an agreement with those obtained from strain gauge measurement. Moreover the value of strain on the high rail web was found to be lower than that on the low rail, and this phenomenon could be observed from both FEM model and on-site measurements.

Other than this, the contact forces obtained from FE model had also been validated with the results from the Multi-body Simulation (MBS) in [177]. For instance, if using MBS model, the contact forces between the wheel attached to the 1st axle and the low rail were 39.8 kN, 6.8 kN and 119 kN for longitudinal, lateral and vertical loads, respectively. Those values compared well to the corresponding FEM results 38.2 kN (longitudinal), 6.6 kN (lateral) and 119 kN (vertical) for the same contact conditions. The maximum difference between FEM and MBS were respectively 7%, 6% and 2% for the longitudinal forces, lateral forces, and normal forces. It should be noted that the FE results were obtained when the wheel was at the middle of the rail.

5.3.2 Examination of contact locations and contact pressure

The contact location was identified from the observation of the nodal contact pressure distribution on the rail surface. The region in contact should have the magnitude of interface pressure larger than zero. Illustrated in Figure 5.5 are the contact locations on the low and high rail. On the high rails, there were two contact zones located on the rail head and rail gauge; whereas there was only one contact spot on the head of the low rails. More details would be introduced in the sub-sections 5.3.2.1 and 5.3.2.2 below.

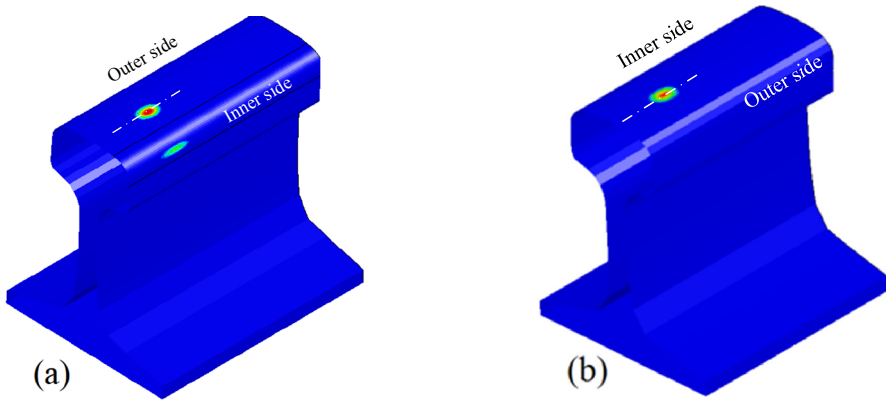

Figure 5.5 Contact locations on (a) high rail and (b) low rail (new wheel-new rail, AOA = 1/3^{o})

5.3.2.1 On the high rail

The contact location of the wheel on the high rail was examined for the following contact situation:

Case 1 (new wheel/new rail contacts)

As shown in Figure 5.6, for the new contact bodies, there were two contact points located at wheel flange/rail gauge and wheel tread/rail head of the rolling surfaces.

The two centres of contact patches were not aligned along the lateral direction due to the effect of AOA. The distance between two centres of contact zones on the rolling direction were denoted as d; and the higher AOA would result in an increase of the distance d. Since the radii of contact bodies' curvatures at two contact locations were different, the dimensions of contact zones were also different. In compassion to the dimensions of contact patch on the rail head, the longitudinal axis a on the rail gauge was nearly double that of the rail head, but the lateral axis b had been reduced by half. In this particular case, the maximum pressure on the rail head was larger than that on the rail gauge. For instance, if AOA = 2/3^o, the maximum pressure on the rail head and the rail gauge were 1059 MPa and 686 MPa, respectively.

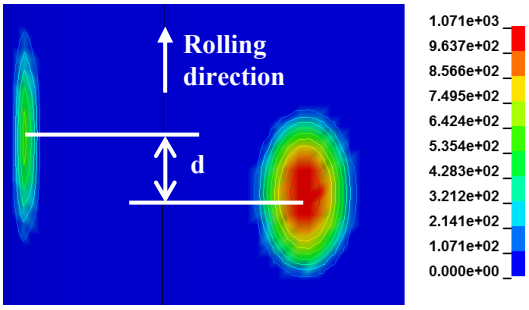

(a) AOA = 1/3^o

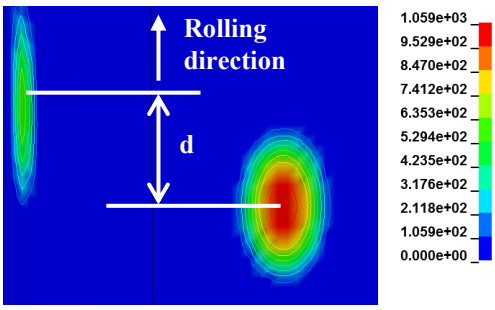

(b) AOA = 2/3^o

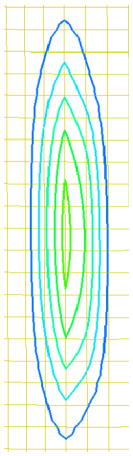

(c) Rail gauge contact (AOA = 1/3^o)

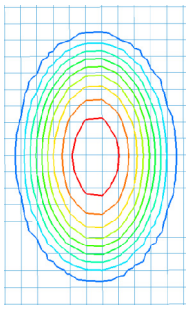

(d) Rail head contact (AOA = 1/3^o)

Figure 5.6 Contact pressure on the new high rail (new wheel-new rail contact, element size 1.3x1.3 mm)

Case 2 (new wheel/worn rail contact)

As the new wheel travelled on the worn rail, the shapes of the two contact patches located on the rail head and the rail gauge were found to be different from case 1 above, especially for the rail-head contact. It can be seen from Figure 5.7 that a decrease of the longitudinal axle (by 2.6 mm) and an increase of the lateral direction (by 1.3 mm) resulted in a more circular shape of the contact area on the rail head. In this case, the maximum pressure exerted on the rail head was found to be larger than that on the rail gauge. For instance, for AOA = 2.3^o the values of the maximum pressure on the rail head and the rail gauge were respectively 921 MPa and 733 MPa.

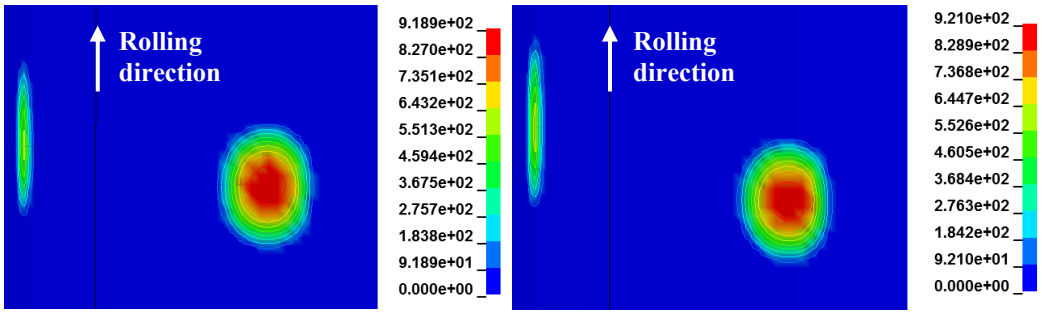

(a) AOA = 1/3^o (b) AOA = 2/3^o

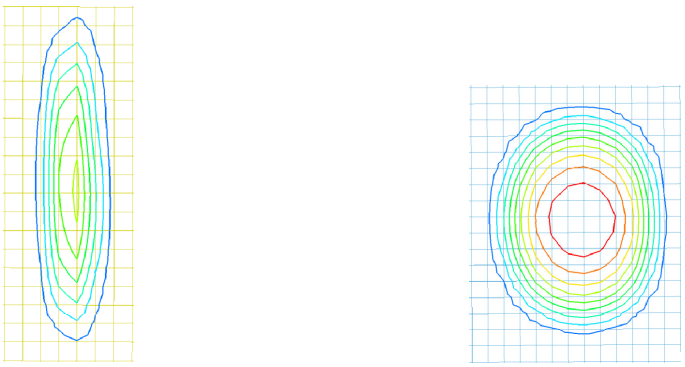

(c) Rail gauge contact (AOA = 1/3^o) (d) Rail head contact (AOA = 1/3^o)

Figure 5.7 Contact pressure on the high rail (new wheel-worn rail contact, element size 1.3x1.3 mm)

Case 3 (worn wheel/worn rail contact)

The contact pressure distribution obtained from the simulations with the worn profiles was different from that with the new profiles. It can be observed from Figure 5.8 that there were also two contact zones located on the rail head and rail gauge. However the shape and the magnitude of contact pressure at each zone had been changed. The geometries of the contact patches were non-elliptical, and this phenomenon were also found in [44] for the worn profile simulations. At the rail-head contact, if compared to the contact spot in case 1, there were a significant reduction of the length of longitudinal axis (by 6.5 mm) and an increase in the length of the lateral axis (by 3.9 mm). At the rail-gauge contact, the longitudinal axis was reduced by 3.9 mm, but the lateral axis was also increased by 5.2 mm. Moreover, the maximum pressure on the rail gauge was found higher than that on the rail head, which was quite different from the simulation with the new profiles. For example, the maximum value of contact pressure found on the rail gauge was 935 MPa and on the rail head was 552 MPa in the case AOA = 2/3°.

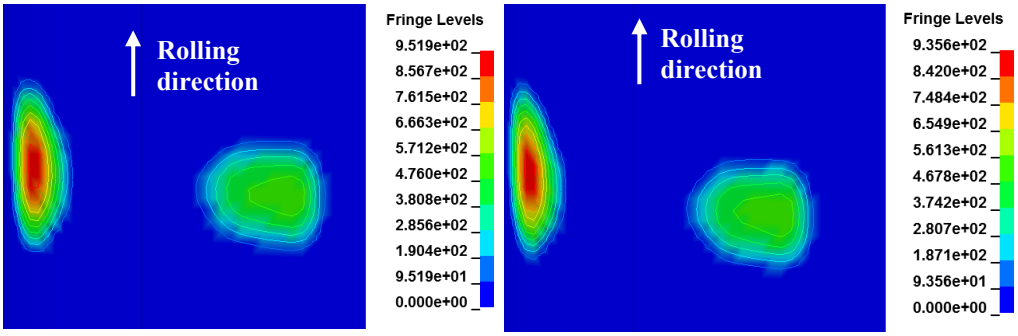

(a) AOA = 1/3° (b) AOA = 2/3°

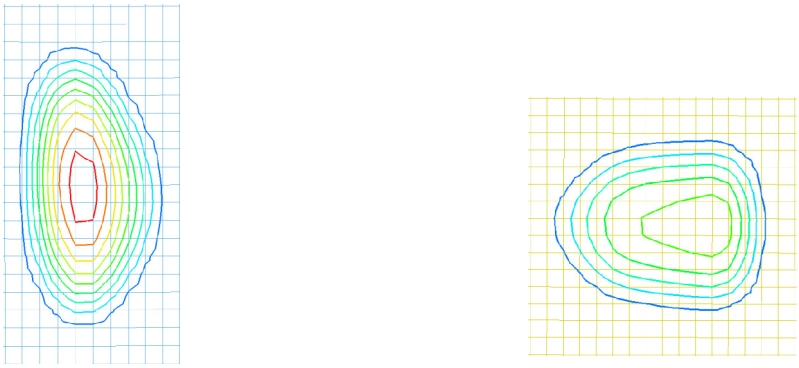

(c) Rail gauge contact (AOA = 1/3°) (d) Rail head contact (AOA = 1/3°)

Figure 5.8 Contact pressure on the worn high rail (worn wheel-worn rail contact, element size 1.3x1.3 mm)

The comparison of maximum contact pressure at the contact zones under different angle of attack is summarized in Table 5.2. As the angle of attack was increased from $1/3^o$ to $2/3^o$, the distance d between two centres of the contact zones were more than doubled. For instance, in case 1 (new wheel-new rail contact), such distance was 6.5 mm with AOA = $1/3^o$; and it was lengthened to 13 mm when AOA = $2/3^o$. The same finding had been presented in [49]. Among the simulations for the high rails, the maximum value of contact pressure (1070 MPa) was found at the rail-head contact of case 1 (AOA = $1/3^o$). In these particular cases, the increase of AOA caused the maximum pressure on the rail gauge to increase in case 1 (new wheel – new rail) and case 2 (new wheel – worn rail), but reduce in case 3 (worn wheel – worn rail). Conversely, the angle of attack had a minor influence on the maximum pressure on the rail head, and the maximum pressure was almost unchanged in all three cases. For instance, the values of maximum pressure for the AOA = $1/3^o$ and $2/3^o$ in case 3 were 554 MPa and 552 MPa, respectively.

Table 5.2 Interface pressure at different contact locations on the new/worn high rail

Parameters	Contact location	Case 1		Case 2		Case 3	
		$1/3^o$	$2/3^o$	$1/3^o$	$2/3^o$	$1/3^o$	$2/3^o$
P_0 (MPa)	Rail gauge	640	686	667	733	951	935
	Rail head	1070	1058	918	921	554	552
d (mm)		6.5	13	5.2	11.7	2	4

*Case 1: new wheel – new rail contact

Case 2: new wheel – worn rail contact

Case 3: worn wheel – worn rail contact

P_0: maximum pressure, d: distance between two centres of the contact zones

5.3.2.2 On the low rail

In order to compare with the contacts on the high rails, the simulations of wheel-low rail contact had been carried out under the same contact conditions:

Case 1 (new wheel/new rail contacts)

The contact zone placed on the rail head of the new low rails is illustrated in Figure 5.9, which was different from the two-point contact on the new high rail. Under different angle of attack, the maximum contact pressure were 1091 MPa for AOA = 1/3^{o} and 1016 MPa for AOA = 2/3^{o}; the distribution of pressure within the contact zone and the shape of contact spots were also different for two angles of attack. These shapes were not perfectly elliptical like those on the new high rail contact due to the angle of attack.

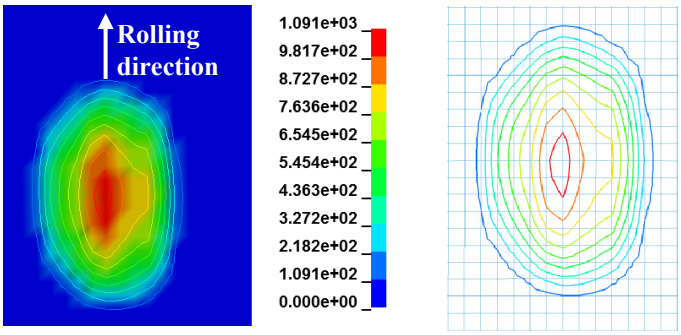

(a) AOA = 1/3^{o}

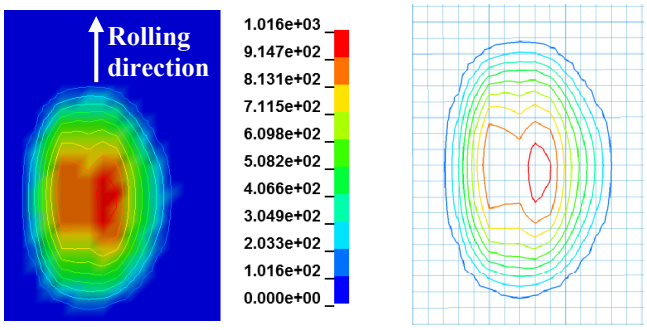

(b) AOA = 2/3^{o}

Figure 5.9 Contact pressure on the new low rail (new wheel-new rail contact, element size 1.3x1.3 mm)

Case 2 (new wheel/worn rail contacts)

The shape and the maximum pressure of the contact zone are shown in Figure 5.10. In this case, the angle of attack had minor influences on the contact zone located on the rail head. The maximum values of contact pressure were found almost equal (about 1150 MPa) and the shapes of the contact spots were also the same. The pear shape of the contact spot to the left side was due to the effect of AOA combined with worn curvature of the contact bodies.

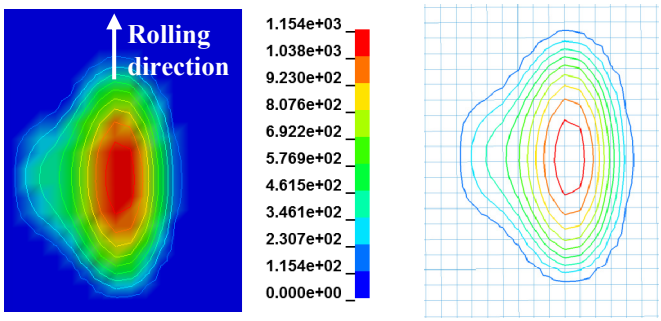

(a) AOA = 1/3°

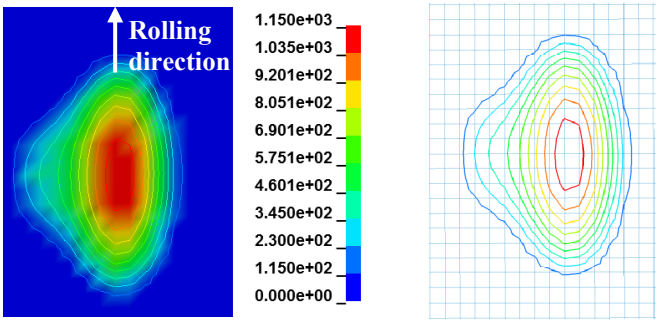

(b) AOA = 2/3°

Figure 5.10 Contact pressure on the worn low rail (new wheel-worn rail contact, element size 1.3x1.3 mm)

Case 3 (worn wheel/worn rail contacts)

Plotted in Figure 5.11 are the contact pressure distribution and the shape of contact area due to worn wheel-worn rail contact. In this case, the maximal values of contact pressure were 1052 MPa and 1007 MPa for AOA = 1/3° and 2/3°, respectively; and the shapes of two contact zone were not elliptic and also different from each other.

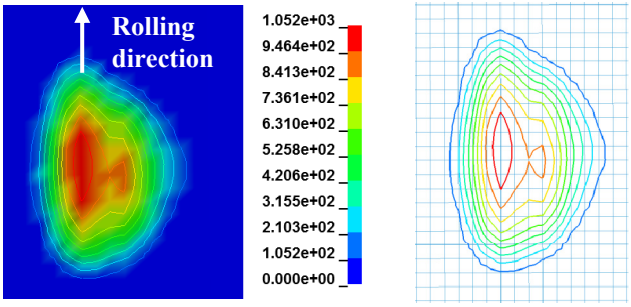

(a) AOA = 1/3°

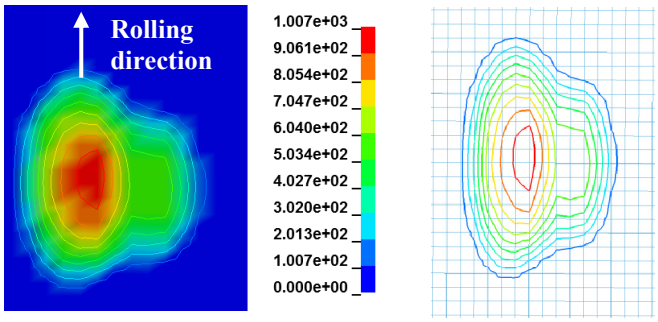

(b) AOA = 2/3°

Figure 5.11 Contact pressure on the worn low rail (worn wheel-worn rail contact, element size 1.3x1.3 mm)

The comparison of contact zones on the low and high rails for the same AOA = 1/3° is introduced in Table 5.3. It can be seen from the table that the pressure on the low rail was higher than that on the high rail in all three cases, and the same finding was found in [177]. Among these simulations, the maximum pressure exerted on the worn low rail of case 2 (new wheel-worn rail contact) was the highest (1154 MPa). The dimensions of the contact zones on different rails (low rail/high rail) or locations (rail gauge/rail head) were changed due to different angle of attack and worn status of the contact bodies. Unlike the contact on the rail head, the longitudinal axis of the contact patch on rail gauge was much longer than the lateral axis. For instance, on the rail gauge of the high rail (case 1), a = 12.3 mm whereas b = 2.6 mm. The dimensions of the contact zone on the head of low rail were larger than those on the high rail due to the load concentration at one location on the low rail. Hence the contact area on the low rails was larger than that on the high rails.

Table 5.3 Comparison of contact on high/low rails (AOA = 1/3^o)

Contact locations	Parameter	Case 1		Case 2		Case 3	
		Low rail	High rail	Low rail	High rail	Low rail	High rail
Rail head	a (mm)	10.4	9.7	10.4	9.1	11.0	6.5
	b (mm)	7.1	6.5	7.4	7.1	7.1	8.4
	P_0 (MPa)	1091	1070	1154	918	1052	554
Rail gauge	a (mm)	-	12.3	-	11.1	-	10.1
	b (mm)	-	2.6	-	2.6	-	5.2
	P_0 (MPa)	-	640	-	667	-	951

* a and b: length of semi axis on the longitudinal and lateral directions, respectively

5.3.3 Wheel/rail contact loads

Since there was only one contact zone on the low rail, the contact loads therefore would be concentrated at only one location. On the high rail, however, the applied loads would be divided and distributed on two contact spots. An example of the contact forces over the travelling time for one case is illustrated in Figure 5.12. Initially the wheel was placed at a small distance above the rail. Hence the contact forces were high at very first few time steps due to the impact between the wheel and the rail, and the stable states were achieved at the later time steps.

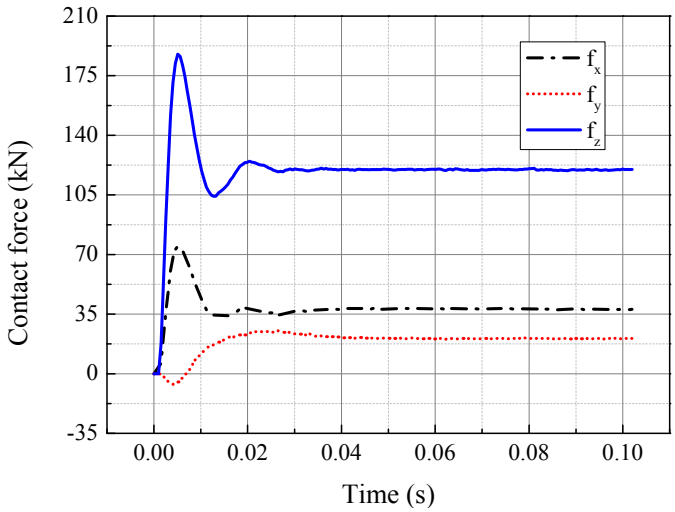

Figure 5.12 Contact forces on the low rail (case 1 – low rail)

The contact forces in three directions (longitudinal, lateral and vertical) on the low and high rails for AOA = 1/3^{o} are summarized in Table 5.4. On the head of the low rail, the contact forces were almost equal for the three cases. Nevertheless the contact forces on the high rail were changed depending on the contact locations and new/worn contact bodies, especially the difference of contact force between case 3 from that of cases 1 and 2. For instance, the longitudinal force on the rail head of case 3 was 6.18 kN which was much smaller than that in case 1 (44.89 kN) and case 2 (43.90 kN), but this force on the rail gauge of case 3 (37.85 kN) was found higher than that in case 1 (4.15 kN) and case 2 (4.26 kN). Although the contact forces at each contact locations might be different from case 1 to case 3, the total contact forces at two locations were found almost the same for all three cases. In comparison to low rail, the total longitudinal force on the high rail was higher, whereas the total lateral and vertical contact forces were almost equal.

Table 5.4 Contact forces (kN) at different contact zones on low/high rail (AOA = 1/3°)

Location	Parameter	Case 1		Case 2		Case 3	
		Low rail	High rail	Low rail	High rail	Low rail	High rail
Rail head	f_x	38.37	44.89	38.39	43.90	39.47	6.18
	f_y	20.54	3.56	20.84	3.54	20.98	15.77
	f_z	119.97	112.47	119.46	110.37	119.80	23.46
Rail gauge	f'_x	-	4.15	-	4.26	-	37.85
	f'_y	-	17.11	-	17.20	-	3.94
	f'_z	-	8.09	-	8.82	-	95.33
Total force	Σf_x	38.37	49.04	38.39	48.16	39.47	44.03
	Σf_y	20.54	20.67	20.84	20.74	20.98	19.71
	Σf_z	119.97	120.56	119.46	119.19	119.80	118.79

* f_x and f'_x: longitudinal contact force on the rail head and rail gauge, respectively.
f_y and f'_y: lateral contact force on the rail head and rail gauge, respectively.
f_z and f'_z: vertical contact force on the rail head and rail gauge, respectively.

5.3.4 Rolling contact stresses

As discussed in chapter 4, the contact area in wheel-rail frictional rolling contact is normally divided into stick/slip regions. The maximum shear stress within the contact area is calculated by the contact pressure multiplied by the friction coefficient. If the magnitude of shear stress is smaller than the maximum shear stress a sticking state occurs. Alternatively, if the shear stress is equal to the maximum value, the relative sliding appears [35]. In this section, the rolling contact stresses on the rail surfaces were presented. Furthermore a comparison of the stress states produced on the low/high rails and new/worn contact bodies was also discussed.

5.3.4.1 Surface shear stress

Shown in Table 5.5 are the maximum shear stresses on the rail surfaces of the low and high rails. In comparison between the low rails, the change of AOA from 1/3^o to 2/3^o led to a small reduction of stress magnitude on the rail head. For instance, in case 1, the values of shear stress on low rail were 430 MPa and 405 MPa for 1/3^o and 2/3^o, respectively. On the high rails, the maximum shear stress on the rail gauge was lower than that on the rail head. For example, in case 1 (AOA = 1/3^o) the maximum shear stress on the rail head was 427 MPa, whereas that on the rail gauge was 128 MPa. In general the maximum shear stress on the low rail was higher than that on the high rail, and the highest value was 461 MPa on the rail head of the low rail in case 2.

Table 5.5 Maximum shear stress (MPa) at contact zones

AOA	Location	Case 1		Case 2		Case 3	
		Low rail	High rail	Low rail	High rail	Low rail	High rail
1/3^o	Rail head	430	427	461	365	422	221
	Rail gauge	-	128	-	153	-	208
2/3^o	Rail head	405	423	459	372	414	219
	Rail gauge	-	144	-	139	-	205

5.3.4.2 Von Mises stress

The distributions of von Mises stress on the cross sections are shown in Figures 5.13-5.17. The contours of von Mises stress on the rail head and rail gauge had a similar pattern to those from [95, 150].

On the high rails

In case 1 and 2, the maximum stress on the rail head was found to be higher than that on the rail gauge. For instance, with AOA = 1/3^o, the maximum values on the rail

head and rail gauge in case 1 were 734 MPa and 527 MPa, respectively (Figure 5.12a). Conversely, the higher stress could be found on the rail gauge rather than on the rail head in case 3. As shown in Figure 5.14a (case 3, AOA = 1/3^o, the maximum stress on the rail gauge was 585 MPa, whereas 388 MPa was the highest stress value on the rail head. Moreover, the higher angle of attack in these cases had a minor effect on the magnitude of stress. As shown in Figure 5.15, the difference between the maximum stresses in two situations of AOA (1/3^o and 2/3^o) was only 5.7 MPa.

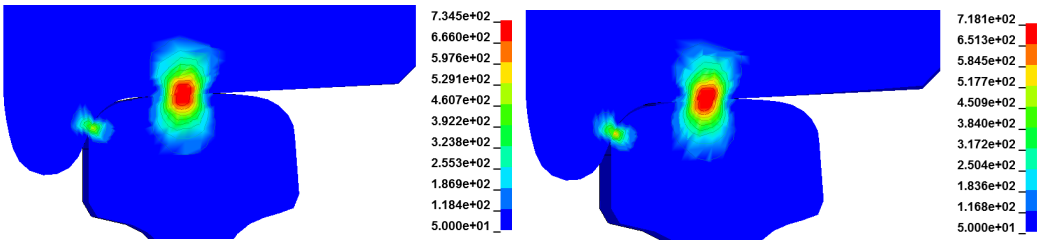

(a) AOA = 1/3^o (b) AOA = 2/3^o

Figure 5.13 Von Mises stress on the new high rail (case 1: new wheel-new rail contact)

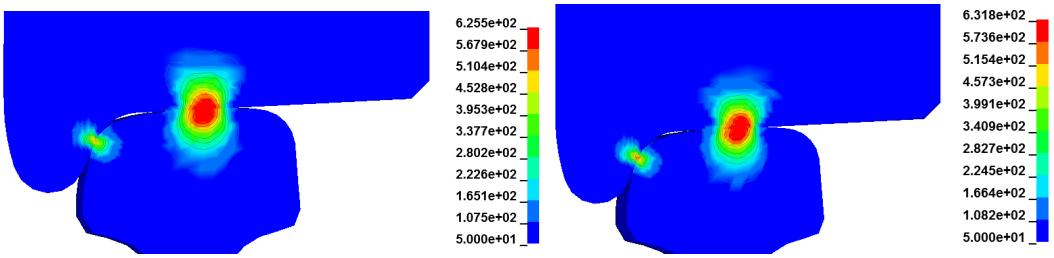

(a) AOA = 1/3^o (b) AOA = 2/3^o

Figure 5.14 Von Mises stress on the worn high rail (case 2: new wheel-worn rail contact)

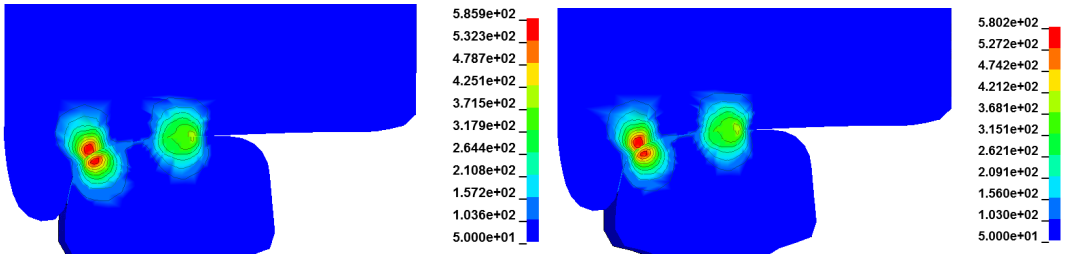

(a) AOA = 1/3^{o} (b) AOA = 2/3^{o}

Figure 5.15 Von Mises stress on the worn high rail (case 3: worn wheel-worn rail contact)

The stress distribution on the rail gauge in case 3 is enlarged and illustrated in Figure 5.16. It could be observed that the maximum stress was formed beneath the rail surface at a distance of about 2 mm. This was due to a low friction contact on the rail gauge (μ = 0.22) and could contribute to subsurface damage on the gauge. In contrast, the maximum stress on the rail head was located at the contact surface, and could potentially lead to surface damage initiations (Figures 5.13 and 5.14). The situation of high friction on the rail gauge (μ = 0.4) was tested to examine the change of stress state (Figures 5.16c and 5.16d). As the coefficient of friction on the rail gauge increased, the location of maximum stress was shifted to the contact surface and the maximum stress was also higher (660 MPa compared to 580 MPa in case AOA = 2/3^{o}).

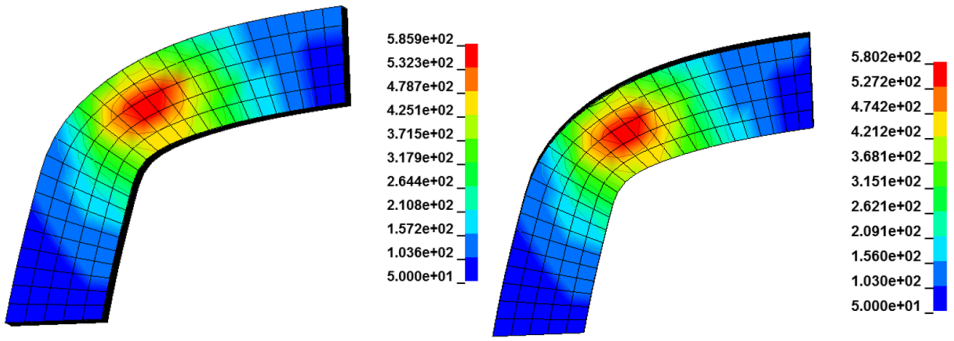

(a) AOA = 1/3^{o} (μ = 0.22) (b) AOA = 2/3^{o} (μ = 0.22)

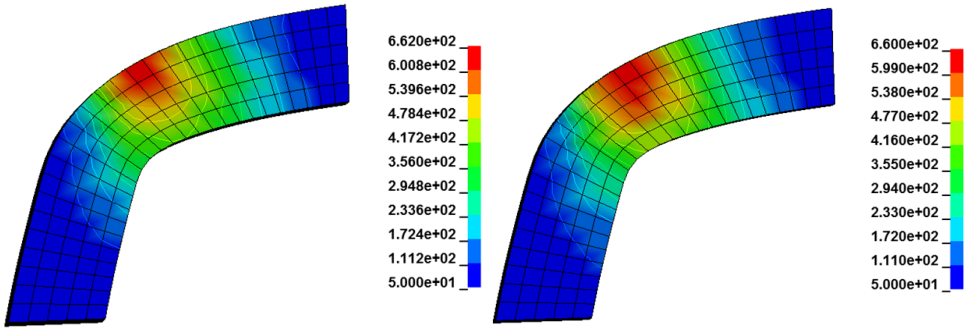

(c) AOA = 1/3° (μ = 0.4) (d) AOA = 2/3° (μ = 0.4)

Figure 5.16 Von Mises stress distribution on the rail gauge (case 3: worn wheel-worn rail contact)

On the low rails

As there was only one contact zone on the low rail, the stress distributions on the head of the low rails of a curved track should be similar to those on the straight track, which had been published in [35]. An example of stress distribution on the worn low rail in case 3 (worn wheel-worn rail contact, AOA = 2/3°) can be observed in Figure 5.17. The maximum von Mises stress of 749 MPa was located on the surfaces of both the rail head and the wheel tread

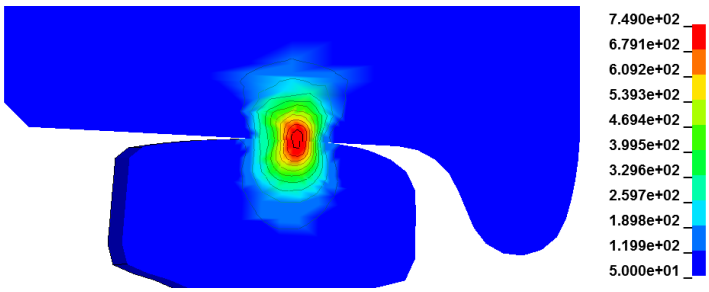

Figure 5.17 Von Mises stress distribution on the low rail (worn wheel – worn rail contact, AOA = 2/3°)

The maximal stress on the low rails in three cases is summarized in Table 5.6. Since the contact forces concentrated at only one location on the rail head, the maximum von Mises stress on the low rails was found higher than that on the high rails. In

these particular cases, the highest stress of 813 MPa could be found in case 3 (worn wheel – worn rail contact) where AOA = 1/3°.

Table 5.6 Maximum von Mises stress (MPa) on the low rails

Cases	AOA = 1/3°	AOA = 2/3°
1	795	774
2	774	790
3	813	749

Table 5.7 shows the comparison of the stresses on the wheel and the rail for case 1 (AOA = 2/3°). It was found that the maximum shear stress on the rail and the wheel were almost the same. Moreover the maximum von Mises stress on the wheel tread was slightly higher than that on the rail head, but this stress on the wheel flange was slightly lower than that on the rail gauge. The penetration of maximum stress on the wheel was deeper than that on the rail. Therefore damage could be appeared on the wheel at the deeper position, leading to some wheel damages such as shelling or spalling [10].

Table 5.7 Comparison of stress on the wheel and the rail (case 1, AOA = 2/3°)

Rails	Contact locations	Maximum shear stress (MPa)	Maximum von Mises stress (MPa)	Penetration of maximum stress (mm)
Low Rail	Rail head	405	744	1.4
	Wheel tread	407	780	3.5
High Rail	Rail head	423	718	2
	Wheel tread	427	745	4
	Rail gauge	144	584	0.7
	Wheel flange	149	560	1.3

5.4. Potential damage on the rails

Under high adhesion condition, the contact stresses on the rails were higher than that under low adhesion conditions [35]. The higher stress would increase the chance of damage initiation. These damages could result in the rail failures, subsequently leading to the vehicle derailments. In this section, the prediction of possible damages on the rails was presented in details.

5.4.1 Material response to the contact stress

In general, cracks on the rail are categorized into two groups which are subsurface-initiated cracks and surface-initiated cracks. These cracks often result from the metallurgical defects, the travelling intensity and the axle load [190]. Two typical types of cracks originated at the rail surface are named as:

- Squats: usually occur at the running surface of the rail on straight track or on the large-radius curved track [20, 152]. Such defects were caused by excessive contact load [194-195], or high train speed [196]. They are assumed to develop from White Etching layer (WEL) [197], which is created at high temperature from high loads and severe deformation on the surface of the rail [156].
- Head checks: generally show up on the curved track, in particular on the gauge corner of the outer rail (high rail) [187]. Wheel passing causes the gross plastic deformation which leads to cracks.

In this chapter, the shakedown diagram [139, 188] was applied to estimate the material response and to anticipate the position (surface/subsurface) of the greatest damage on the rail. Figure 5.18 shows the shakedown map identifying the response of material. The load factor was given as P_o/k on the vertical axis, where P_o was the maximum contact pressure, k was the material yield strength in shear (in this

calculation, k = 234 MPa [198]). The contact friction was given as μ on the abscissa. Results obtained from the simulations are summarized in Table 5.8.

Table 5.8 Simulation cases (AOA = 1/3°)

Case	Rail	Location	μ	P_0 (MPa)	P_0/k
1	Low	Rail head	0.40	1091	4.662
	High	Rail head	0.40	1070	4.573
		Rail gauge	0.22	640	2.735
2	Low	Rail head	0.40	1154	4.932
	High	Rail head	0.40	918	3.923
		Rail gauge	0.22	667	2.850
3	Low	Rail head	0.40	1052	4.496
	High	Rail head	0.40	554	2.368
		Rail gauge	0.22	951	4.064

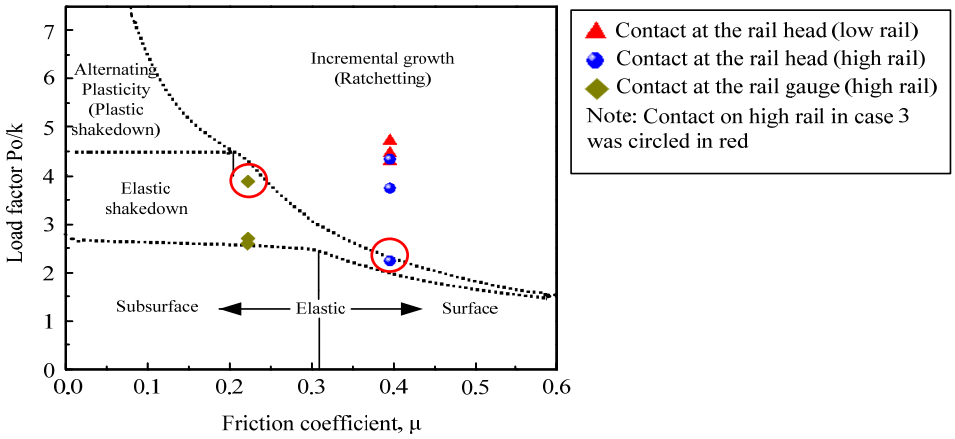

Figure 5.18 Shakedown map to predict the response of rail material

As shown in the map, for those contact zones on the rail head, the response of material mainly fell in the rachetting region which was due to high traction force and high contact load exerted on the rails. Damage at this location was predicted to occur

on the surface rather than the sub-surface, whereas the response of material in the elastic shakedown region applied to the contacts on the rail gauge. However on the high rail of case 3 (points circled in red), the pressure on the rail gauge was quite high compared to that on the rail head. In this case, the response of material on the rail gauge was close to the rachetting region, whereas that on the rail head was in the elastic shakedown region. Hence if the pressure on the rail gauge was high enough, the response of material on the rail gauge would be more severe than that on the rail head and damage could be initiated on the rail gauge of the high rail (which is also called head checked).

5.4.2 Contact fatigue defect

It could be seen from section 3.3 that under high adhesion contact condition, the shear stress was relative high, especially on the low rail (Table 5.5). The association of wheel/rail defect development and high shear stress had been well addressed in the literature [10, 198]. The growth of this defect had never been desirable due to a considerable effort required to maintain the track. They would potentially develop and result in rail failures and serious accidents if not detected and maintained in time. The predicted stress range for the crack formation was obtained from experimental work [198-199], whereby a range of laboratory tests was carried out to characterize and predict the service performance of rail and wheel materials. Moreover this work was carried out for the same rail profiles used in this thesis. Hence the stress range obtained in this thesis is realistic and applicable for the current study. The plot of maximum shear stress which could be applied to predict the fatigue defects, as suggested in [198-199], is illustrated in Figure 5.19.

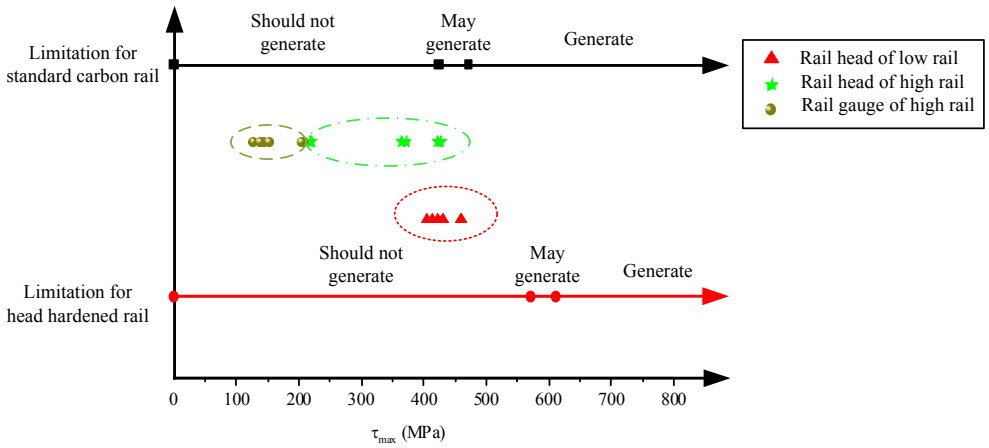

Figure 5.19 Prediction of fatigue defect formation

As shown in the map, the maximum shear stress on the rail gauge of the high rails were well below the limitation to cause the fatigue defects, whereas the maximum shear stress on the head of both low and high rails were much closer to the threshold of fatigue initiation. The maximum shear stress exerted on the low rail was 461 MPa, which fell in the region indicating that defects might develop on the standard carbon rail but well below that region of the head hardened rail. The illustration of the hardened layer on the rail was drawn in Figure 5.20. The values of the depths from the rail head and two sides of the rail gauge were denoted as l and l', respectively. It was introduced in [173] that for 50 kg rail, l = 20 – 35 mm and l' = 15 – 23 mm; for 60 kg and 68 kg rails, l = 25 – 40 mm and l' = 15 – 23 mm.

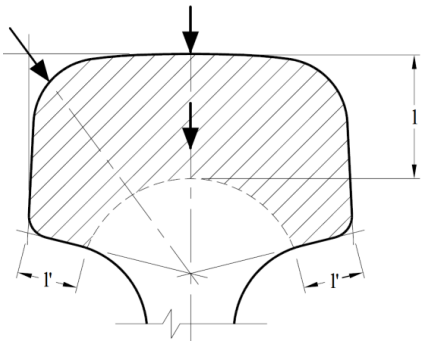

Figure 5.20 Depth of the hardened layer on rail [173]

In this study, head hardened rail was used and the stress penetration was well within the hardened layer; it was, therefore, predicted that the fatigue defects would not be initiated under this contact conditions. However the simulation had been conducted for only one pass of the wheel, if the rail subjected to many rolling passes of a wheel, the rail material should be softened at a higher temperature and crack might be formed after a certain number of rolling.

5.4.3 Rail corrugation

Rail corrugation has been one of the most serious and expensive problem experienced by the transit systems. The formation of corrugation is due to large creepage [200] and/or high axle load combined with dynamic behaviour from the track system and vehicle [201-202]. In order to predict the formation of rail corrugation, a method based on the cyclic deformation behaviour of rail steels under compression loading has been applied in [203-204]. The work had suggested that above a certain value of contact pressure the rail material would continue to plastically deform if subjected to cyclic loading, and therefore corrugation should be formed. Shown in Figure 5.21 is the average value of contact pressure that might generate the corrugation for the tangent track.

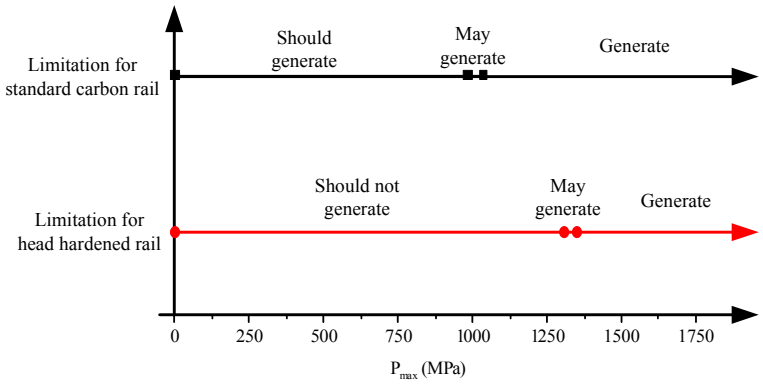

Figure 5.21 Limitation to form rail corrugation on tangential track

On the curve track, the adhesion condition could be increased and the limitation to cause the shakedown rail corrugation should be diminished. For a curved track with a radius of 400 m or less, the allowable contact pressure to develop the rail corrugation was lower as shown in Figure 5.22 [203]. From the diagram, it was predicted that the rail corrugation had a tendency to be formed on the low rail rather than the high rail. Compared to the strength of the head hardened rail (993 MPa and above), all the low rail cases (1007 – 1154 MPa) were found falling in the "may-generate" or "generate" regions. However for some cases of high rail (case 1: 1070 MPa for AOA = 1/3^o and 1058 MPa for AOA = 2/3^o) where the contact pressure exceeded the allowable value, the corrugation could be generated. On the gauge of the high rails, the values of contact pressure (640 – 951 MPa) were not high enough to develop the corrugation. The pressure value of 951 MPa was very close to 1000 MPa in may-generate region, thus the corrugation could also occur.

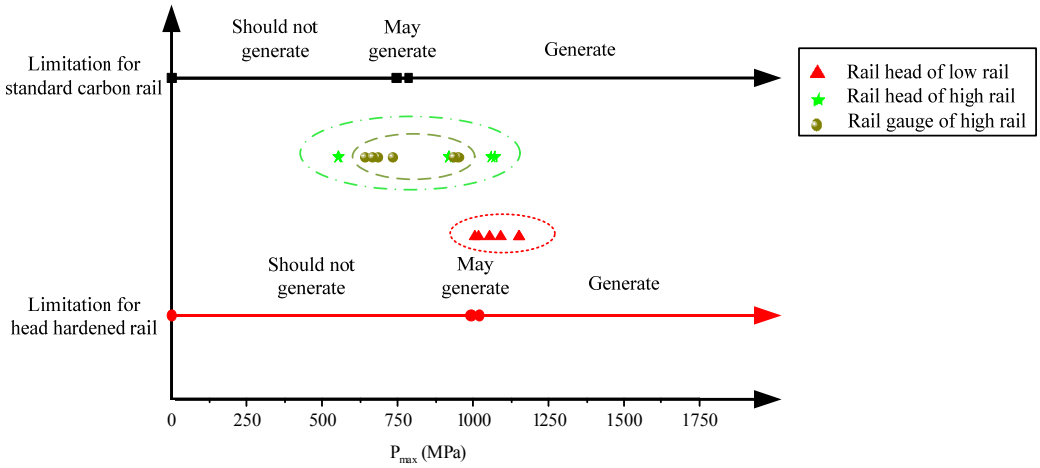

Figure 5.22 Prediction of rail corrugation formation

5.5. Conclusions

The wheel/rail contact on the curved track was analysed in this chapter. A comparison of the stress states between the new/worn low/high rails and some

predictions related to damage had been provided. From the obtained results, the following conclusions can be made:

(1) On a curved track, the wheel can contact with the rail at either one or two locations. The two-point contact is normally found on the high rail (rail gauge-wheel flange and rail head-wheel tread). Moreover the shape of the contact zones on the curved track is not always elliptical due to the effects of angle of attack and the worn profiles.

(2) The magnitude and distribution of contact pressure and stresses are significantly influenced by the contact locations, worn status of the contact bodies (new/worn profiles) and angle of attack. As the worn wheel contacts with the worn rail, the maximum pressure on the rail gauge are higher than that on the rail head.

(3) The contact force on the gauge of a high rail will be increased if using the worn profiles. Moreover the total longitudinal force on the high rail is found to be higher than that on the low rail which facilitates damage initiation.

(4) The maximum von Mises stress on the rail gauge is very high in the case of worn wheel-worn rail contact, which results in a possible damage at this contact location.

(5) Under high adhesion contact, the responses of the rail material on the rail head are predicted falling in the ratchetting region and the damage would appear on the surface if initiated. For the contacts on the rail gauge, the responses are predicted to be elastic shakedown, but can approach the ratchetting region if the contact pressure is high enough.

(6) In these particular cases, the fatigue defects on the rails are not anticipated to form for the head hardened rail but can be developed for the standard carbon rail.

(7) On the curved track, the rail corrugation tends to be created on the low rail rather than the high rail. In these particular cases, it is predicted that the corrugation would be formed on the rail head of all low rails and case 1 of high rail, but not on the rail gauge of any cases

In practice, loading conditions on the low and high rails are different from each other. However it was assumed that these contact conditions were to be the same on both the low and high rails in this chapter. Therefore further investigation of wheel-rail contact by AC and DC locomotives under diverse operational conditions in practice will be carried out in the next chapter of this thesis. Moreover, temperature and wear on rail would also be calculated analytically to justify the influences of adhesion conditions on wheel/rail contact.

CHAPTER 6

COMPARISONS OF STRESS STATES, WEAR AND HEAT GENERATED BY AC VERSUS DC LOCOMOTIVES

The following chapter provides an estimation of the wheel/rail contact stresses, wear and heat generated by AC and DC drives on both the worn low/high rails. The investigation was carried out on the leading and trailing axles of the third locomotive, where the axle load is more severe than that on the first and second locomotives. Two types of locomotives (AC and DC) currently run in Australia were evaluated under diverse operational situations (wheel loads, angle of attack and adhesion level). Commercial software LS-DYNA was utilized to build up a comprehensive wheel/rail contact model. The numerical model was constructed based on Australian wheel/rail profiles and sub-components of the track such as railpads, sleepers, and ballast. Moreover the analytical method and the shakedown diagram were also applied to evaluate the temperature rise on the rail and the response of the material, respectively. Calculation of wear volume on rail was then performed using the Archard's wear model.

The content of this chapter has been published in [36, 55, 205]:

***K. D. Vo**, A. K. Tieu, H. T. Zhu, and P. B. Kosasih, "A comparison of stress and heat generated by AC versus DC locomotives under diverse operational conditions," Wear, vol. 328-329, pp. 186-196, 2015*

***K. D. Vo**, A. K. Tieu, H. T. Zhu, and P. B. Kosasih, "A tool to estimate the wheel/rail contact and temperature rising under dry, wet and oily conditions," Computers in Railways XIV: Railway Engineering Design and Optimization, vol. 135, p. 191, 2014.*

***K. D. Vo**, A. K. Tieu, and H. T. Zhu, "Wheel-rail contact by FEM modelling in Final report Project R3.119: Locomotive Adhesion," CRC for Rail Innovation, Australia 2013.*

6.1. Introduction

In Australia, both AC and DC locomotives are widely used such as models Cv40-9i (DC) [206], C44ACi (AC) [207], and GT46C ACe (AC) [208]. The AC locomotives have brought to railway operators many advantages such as the improvement of slip control, maintainability and braking efficiency. Further achievements are the higher adhesion values and the reduction of the number of locomotive to haul a larger load [3, 5].

Regardless the merit benefits gained from using the high adhesion locomotive, it is predicted that the AC locomotive can also produce damages on the rail. For instance, the wear process at the wheel/rail interface is linked to energy dissipated in the contact which is created by the combination of traction and creepage. The higher is the adhesion, the higher contact forces and creepage increase, and therefore the wear development will be problematic. Besides, the severe shear stress from high adhesion condition can facilitate the crack initiation [209]. In addition to wear, the material strength is known to be considerably influenced by temperature. An increase of temperature due to friction force may soften the strength of the wheel/rail material. “White Etching Layer” can be formed [131-132] at the surface of contact bodies if the temperature exceeds 700^{o}C [130].

Studies on railway systems have been conducted for more than a century, and many modelling approaches for the wheel/rail contact have been proposed. The advantages and disadvantages of these models were discussed in chapter 2 of the literature review. Among the completed research so far, it can be seen that little discussion on rail damages by AC and DC locomotive could be found. Moreover the reports of potential long-term effects on high adhesion condition on the track components have been limited to date. In this chapter, the comparison of stress state, wear and heat generated on the rails were presented. Practical contact conditions were simulated to reflect the contact conditions by AC and DC locomotives which are normally utilized in Australia, such as C44ACi (AC) and GT46C ACe (AC). Since the normal

wheel loads on the leading axle (1st axle) and trailing axle (3rd axle) are the lightest and heaviest, respectively, the FEM simulations were conducted for these two axles. To simulate the practical conditions of in-service wheel-rail contact, input parameters of FE model were referenced from output of Multibody Simulation (MBS) carried out by the collaborative research team at Central Queensland University. In addition to the numerical model, an analytical model was also applied to compute the temperature rise on the rail surface. Moreover the shakedown map was utilized to predict the response of material. Field evidences were also provided to support the numerical study and wear volume on the rail was calculated using the Archard wear model.

6.2. Numerical model

The finite element model was coded in the commercial software ANSYS/LS-DYNA [183] and the post processing was carried out in LS-PREPOST. The details of models are introduced in the following sub-sections.

6.2.1. FE model description

The mesh of FE model including a whole wheel, 600 mm rail, and some sub-components of the track such as sleepers, railpads and ballast are illustrated in Figure 6.1. These sub-components are designed to absorb the high impact load and reduce the high frequency vibration from the railway vehicle. The angle of attack and the rail cant angle were also applied to take into account the effect of a curved track.

The following elements: solid element (wheel/rail), mass element (sleepers) and spring-damping elements (railpad and ballast) were selected to build up the model. A

non-uniform but very fine mesh (1.3 x 1.3 mm) was generated at the contact surfaces. It was verified in chapter 4 and [48] that this mesh size was adequately fine for the wheel/rail contact problem, as it was necessary to balance against long computational time (one week per run). The contact between the wheel and the rail was defined by the automatic contact surface to surface (ASTS) contact algorithm and Coulomb's friction model. Wheel loads and velocity was applied to the wheelset. Input data for the FEM model can be found in the next section.

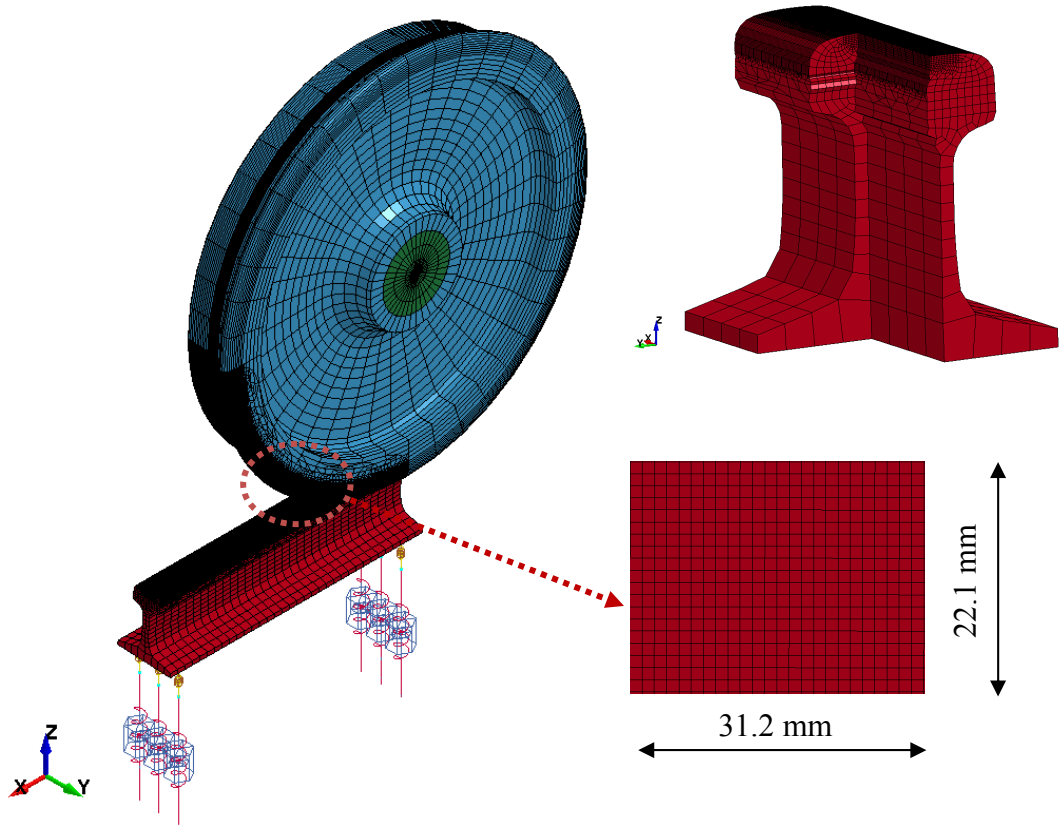

Figure 6.1 Finite element mesh

6.2.2. Input parameters

The number of finite element cases conducted in this chapter included 8 cases, which cover for a variety of locomotive types (AC: C44ACi and DC: GT46C ACe), axles

(leading axle and trailing axle), rails (low and high rail), and contact load conditions (velocity, forces, angle of attack, creepages, and adhesion coefficient). The adhesion coefficient was obtained from the following equations:

$$\text{Adhesion coefficient} = \sqrt{\left(\frac{F_{nx}}{F_n}\right)^2 + \left(\frac{F_{ny}}{F_n}\right)^2} \tag{6.1}$$

where F_{nx}, F_{ny}, and F_n are the contact forces respected to the contact area.

The input data acquired from the Locomotive Multibody Simulation (MBS) using GENSYS is summarised in Table 6.1. Nine rigid masses were included in the MBS model: one car-body, two bogie frames and six wheelsets [177]. The individual wheelset traction control strategy implemented in Gensys model, and slip for each axle was based on the average rotational velocity [210]. A variable friction based on Polach's theory was employed. In order to compare the results achieved from MBS and FEM models, the same values of friction coefficient from MBS were applied in the FEM models.

All simulation cases were run for the normal 4800 tonne trains with three locomotives head end on a 240 m radius curve [177]. The worn profiles of the Australian standard wheel/rail, i.e ANZR1 wheel and 60 kg rail were used to construct MBS and FEM models. It took about 0.1 second for the wheel travelled on 600 mm rail with the velocity of 5.83 m/s and 6.38 m/s. Therefore, the adhesion coefficient was assumed to be constant after it reached the saturation point, and negative slope of the creep curve was negligible. Additionally, since there was no high frequency obtained from MBS models during this short time duration, the mean values of all parameters from MBS models were applied to the FEM models.

Table 6.1 Input parameter for FEM models [36, 177]

Case	Loco type	Axle	Rail	Contact conditions											
				V (m/s)	ω (rad/s)	AOA (mrad)	Creepage (%)		Wheel load (kN)			Friction coefficient		Adhesion coefficient	
							nux	nuy	F_x	F_y	F_z	Cp1	Cp2	Cp1	Cp2
1	C44ACi (AC)	Leading (1^{st} axle)	Low	5.83	11.89	17.5	8.5	1.8	34.4	10.5	103.3	0.39	0.22	0.35	
2			High	5.83			8.1	1.8	33.9	14.2	97.0	0.39	0.22	0.34	0.22
3		Trailing (3^{rd} axle)	Low	5.83	11.34	2.2	4.4	0.1	47.3	20.8	131.6	0.43	0.22	0.36	
4			High	5.83			3.1	0.1	28.7	1.3	94.4	0.44	0.22	0.31	
5	GT46C ACe (DC)	Leading (1^{st} axle)	Low	6.38	13.51	16.4	7.4	1.6	32.2	11.7	110.7	0.34	0.22	0.3	
6			High	6.38			7.0	1.6	27.5	12.8	92.0	0.34	0.22	0.29	0.22
7		Trailing (3^{rd} axle)	Low	6.38	12.89	1.1	3.2	0.2	40.3	25.8	135.5	0.37	0.22	0.29	
8			High	6.38			2.0	0.2	19.5	1.1	84.3	0.38	0.22	0.23	

Note:

- V: train velocity; ω: angular velocity; AOA: angle of attack; F_x, F_y, F_z: wheel loads on the longitudinal, lateral and normal directions, respectively.
- Cp1: contact point 1 (wheel tread-rail head contact); cp2: contact point 2 (wheel flange-rail gauge contact).
- Traction simulation results were provided by the Centre for Railway Engineering, Central Queensland University using Gensys Multi-body simulation software [177, 211-213]

6.3. Analytical model to calculate temperature rise

The frictional contact between the wheel and the rail always results in a rise of temperature on the contact surfaces. The temperature rise on and/or below the rail surface can be theoretically calculated from the heat flow rate at the rail surface $\dot{q}_r$, and the thermal penetration coefficient of rail $\beta_r = \sqrt{\lambda \rho c}$, using the following equation [119-120, 214]:

$$\Theta_r(\xi, \zeta) = \frac{\dot{q}_r}{\beta_r}\sqrt{\frac{2a}{\upsilon_r}} f(\xi, \zeta) \tag{6.2}$$

where a and υ_r are the semi-axis in the rolling direction and the velocity of the rail, respectively. $\xi = x/a$ and $\zeta = z/\delta$ are dimensionless coordinates and δ is the thermal penetration depth.

At the rail surface ($\zeta = 0$):

- For $-1 \leq \xi \leq 1$ (within the contact area)

$$f(\xi,\zeta)=\sqrt{\xi+1} \tag{6.3}$$

- For $\xi > 1$ (outside of contact area)

$$f(\xi, \zeta) = \sqrt{\xi + 1} - \sqrt{\xi - 1} \tag{6.4}$$

Below the rail surface ($\zeta \neq 0$):

- For $-1 \leq \xi \leq 1$ (within the contact area)

$$f(\xi, \zeta) = \sqrt{\frac{2(\xi + 1)}{\pi}} \exp\left[-\frac{\zeta^2}{2(\xi + 1)}\right] - \zeta \mathrm{erfc}\left[\frac{\zeta}{\sqrt{2(\xi + 1)}}\right] \tag{6.5}$$

- For $\xi > 1$ (outside of contact area)

$$f(\xi,\zeta)=\left\{\sqrt{\frac{2(\xi+1)}{\pi}}\exp\left[-\frac{\zeta^2}{2(\xi+1)}\right]-\zeta\mathrm{erfc}\left[\frac{\zeta}{\sqrt{2(\xi+1)}}\right]\right\}-\left\{\sqrt{\frac{2(\xi-1)}{\pi}}\exp\left[-\frac{\zeta^2}{2(\xi-1)}\right]-\zeta\mathrm{erfc}\left[\frac{\zeta}{\sqrt{2(\xi-1)}}\right]\right\} \quad (6.6)$$

The expression erfc is called the complementary error function. The thermal properties for rail are as follow: thermal conductivity λ = 50 W/K m, density of the rail ρ = 7800 kg/m^3, and specific heat capacity c = 450 J/kg K [55].

6.4. Results and discussions

Simulation was run on the high performance computer (HPC) and it took five days for one simulation. In this section, the results of stress from the numerical model and temperature rise from the analytical model under different contact conditions are discussed in details.

6.4.1. Validation of FE model

To validate the FEM model, the wheel/rail contact forces obtained from FEM and MBS models were compared. It was found that the results gained from the two models matched up very well (shown in Table 6.2). The maximum differences between these two models were respectively 7%, 6% and 2% for the longitudinal, lateral and normal forces. Additional validation with the data of strain gauge measurement from the technical report TR. 169 [178] also helped to confirm the validity of the FEM model. The values of strain obtained from FE simulations varied

from 119 to 229 microstrain, compared to the data of 85 to 245 microstrain from the report TR.169. Although the comparison of strain was qualitative due to the coarse mesh at the rail web in FE models, the results of FE models were still comparable and showed an agreement with those obtained from strain gauge measurement.

Table 6.2 Total wheel-rail contact forces from MBS and FEM

Case	Loco type	Axle	Rail	Total contact force from MBS models (kN)			Total contact force from FE models (kN)		
				Fx	Fy	Fz	Fx	Fy	Fz
1	C44ACi (AC)	1st axle	Low	34.4	10.5	103.3	36.4	10.9	103
2			High	33.9	14.2	97.0	33.3	16.7	97.5
3		3rd axle	Low	47.3	20.8	131.6	49.3	20.2	131
4			High	28.7	1.3	94.4	28.4	1.2	94.2
5	GT46CACe (DC)	1st axle	Low	32.2	11.7	110.7	33.7	11.4	111
6			High	27.5	12.8	92.0	27.1	13.1	91.5
7		3rd axle	Low	40.3	25.8	135.5	39.1	25.4	136
8			High	19.5	1.1	84.3	18.9	1.2	84.2

6.4.2. Wheel-rail contact stress

6.4.2.1. On the leading axle (1st axle)

The comparisons in this section are for the contact between the wheels attached to the leading axle and the low/high rails.

a. On the low rails (case 1 versus case 5)

Results of the finite element models on the low rails were considered with regards to:

Contact zone and contact pressure

Figure 6.2 illustrates the shapes of the contact patches and contact pressure distributions on the rail surface. It can be seen that the shapes of the contact zones are not totally elliptical due to the unsmoothed irregular worn profiles applied in these simulations. Since the normal wheel load applied on the 1st axle in case 5 was higher than that in case 1, the contact pressure exerted in the rail surface was higher as well. The maximum pressure in case 1 (AC) was 1349 MPa compared to 1395 MPa in case 5 (DC).

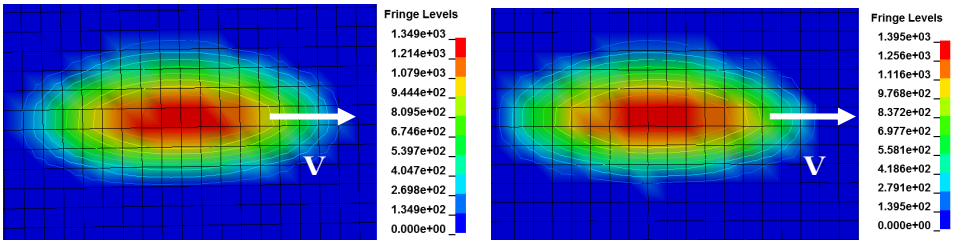

(a) AC– case 1 (b) DC – case 5

Figure 6.2 Interface pressure distributions on low rails (MPa) (1st axle, element size 1.3 x 1.3 mm)

Contact shear stress

The contour distributions of contact shear stress in the contact zone are shown in Figure 6.3. As the result of a higher adhesion coefficient (0.35 in case 1 and 0.3 in case 5), the contact shear stress produced by the AC loco (case 1) was higher than that by DC loco (case 5). The maximum shear stress on case 1 was 525 MPa, while it reduced to 480 MPa in case 5.

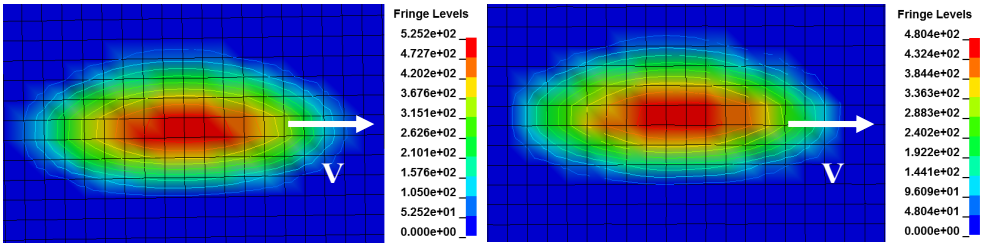

(a) AC– case 1 (b) DC – case 5

Figure 6.3 Contact shear stress distribution on low rails (MPa) (1st axle, element size 1.3 x 1.3 mm)

Von Mises stress

Plotted in Figure 6.4 are the von Mises stress distributions on the rail surfaces and lateral cross sections of the low rails. The maximum stress (832 MPa) resulted from travelling of AC loco (case 1) on the low rail was higher than 819 MPa produced by DC loco (case 5).

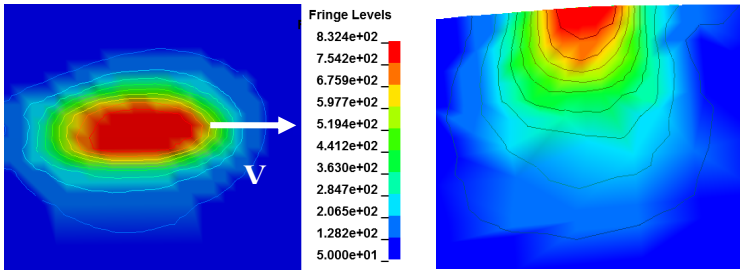

(a) AC – case 1

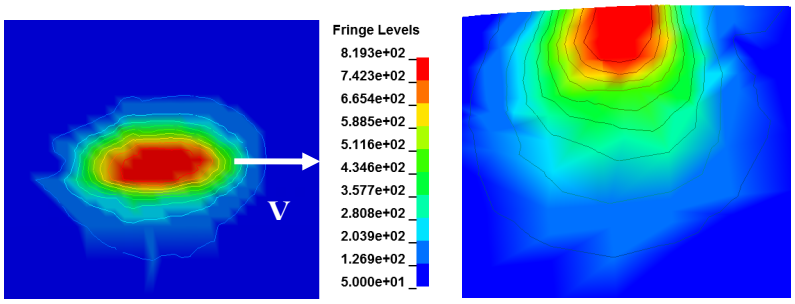

(a) DC – case 5

Figure 6.4 Von Mises stress distribution on low rails (MPa) (1st axle)

b. On the high rails (case 2 versus case 6)

On a curved track, the wheel comes into contact with the high rail at two points (on the rail gauge and the rail head) [38]. The appearance of two-point contact depends on the worn status of the profiles, radius of the curved track and the angle of attack (AOA).

Contact zone and contact pressure

Contact pressure was distributed to two points on the high rail as shown in Figure 6.5. In case 2 (AC – high rail), the maximum pressures of 723 MPa and 628 MPa were located on the gauge and head of the high rail, respectively. The peaks of pressure of 681 MPa and 675 MPa were observed on the rail head and the rail gauge in case 6. These values on the high rails were found to be lower compared to those on the low rails (case 1 and 5) on the same leading axles. The two-point contact had pressure distributed to two places and thus reduced the load at each contact point.

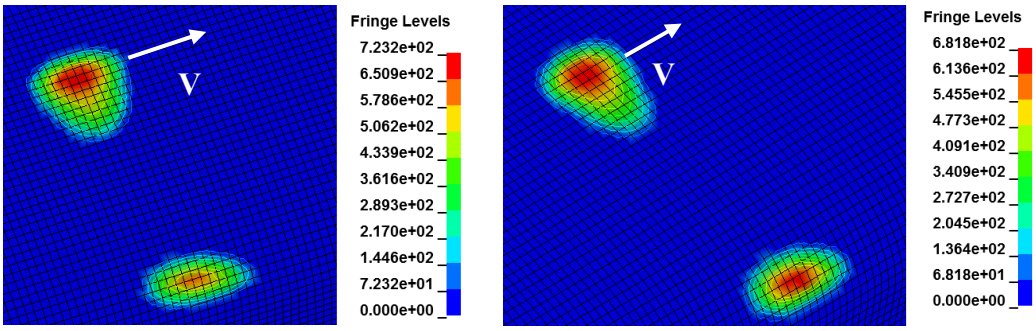

(a) AC– case 2 (b) DC – case 6

Figure 6.5 Interface pressure distribution on high rails (MPa) (1st axle, element size 1.3 x 1.3 mm)

Contact shear stress

The results of shear stress shown in Figure 6.6 are for the high rails of case 2 (AC) and case 6 (DC). The higher shear stresses could be found on the rail head instead of

the rail gauge, which shows the same tendency as the contact pressure distribution discussed above (Figure 6.5). On the rail head, the maximum shear stresses were 283 MPa (case 2) and 234 MPa (case 6), but they reduced to 137 MPa and 146 MPa on the rail gauge for case 2 and case 6, respectively.

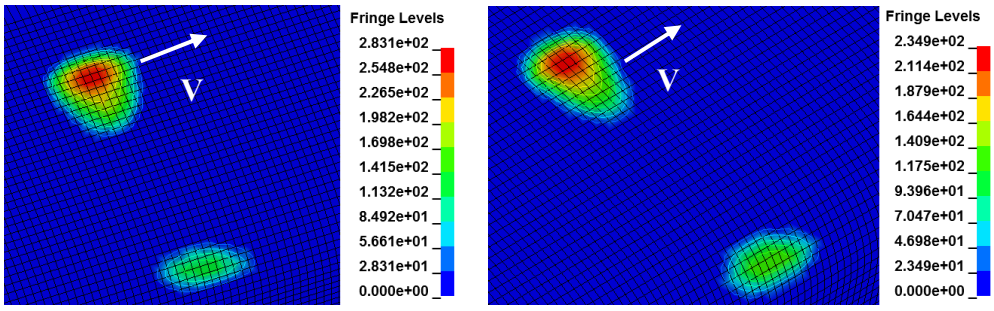

(a) AC– case 2 (b) DC– case 6

Figure 6.6 Shear stress distribution on high rails (MPa) (1st axle, element size 1.3 x 1.3 mm)

Von Mises stress

Since the contact pressure and shear stress were reduced on the high rails compared to low rails, the von Mises stress at the two contact spots of high rails were also lower. As shown in Figure 6.7, the highest values on the rail head were 532 MPa (Case 2) and 472 MPa (case 6) compared to 832 MPa (case 1) and 819 MPa (case 5). Furthermore the maximum stress on the rail gauge was not as high as on the rail head (416 MPa in case 2 and 430 MPa in case 6), and the location of the critical value was below the rail surface.

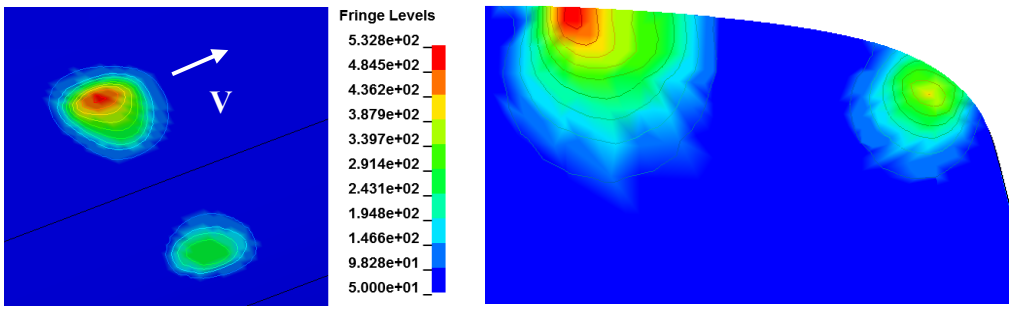

(a) DC – case 2

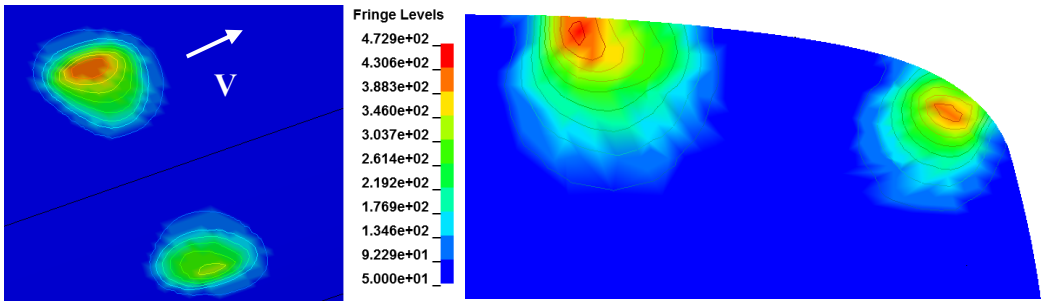

(b) DC – case 6

Figure 6.7 Von Mises stress distribution on high rails (MPa) (1st axle)

A summary of the stress exerted on the low and high rails by the wheel connected to the leading axle (1st axle) of AC loco and DC loco is presented in Table 6.3. The results showed that the contact pressure and stresses on the low rail were much more severe compared to those on the high rails. For instance the maximum contact pressure was 1349 MPa in case 1 (AC – low rail), but it was considerably reduced to 723 MPa in case 2 (AC – high rail). Moreover a major reduction of maximum shear stress as well as the von Mises stress was also observed in case 2 (AC – high rail) when compared to case 1 (AC – low rail). In comparison to DC locomotive, the shear stress and von Mises stress by AC locomotive were higher because of the greater adhesion generated by AC locomotive.

Table 6.3 Summarization of stress calculation (leading axle)

Rail	Case	Loco types	Axle	Maximum contact pressure (MPa)	Maximum shear stress (MPa)	Maximum von Mises stress (MPa)
Low	1	AC	Leading	1349	525	832
	5	DC	Leading	1395	480	819
High	2	AC	Leading	723	283	532
	6	DC	Leading	681	234	473

6.4.2.2. On the trailing axle (3rd axle)

The stress values generated on the rails by the trailing axle (3rd axle) were expected to be higher than that by the leading axle (1st axle) due to higher wheel loads. It was found that the patterns of stress distribution were the same for all low rails, but these stresses were altered by the angle of attack (AOA) for the cases of high rail. Thus only the contact stresses on the high rail were demonstrated in this section, and the results of all cases by the trailing axle are listed in Table 6.4.

a. On the high rails (case 4 versus case 8)

As shown in Table 6.1, the values of AOA by the trailing axle were considerably small compared to that by the leading axle. For instance, the AOA values of the AC loco were 17.5 mrad for the leading axle, but only 2.2 mrad for the trailing axle. This resulted in a single contact spot on the surface of the high rail in case 4 and 8, which was different from two-point contact in case 2 and 6.

Contact zone and contact pressure

Shown in Figure 6.8 are the geometries of the contact zones and the contact pressure distributions on the high rails in case 4 (AC) and 8 (DC). Since the contact load was concentrated at one zone, the contact pressure was found to be higher than the two-point contact case. For example, the maximum of pressure found in case 4 was 965 MPa, whereas it was only 723 MPa in case 2 (Figure 6.5a).

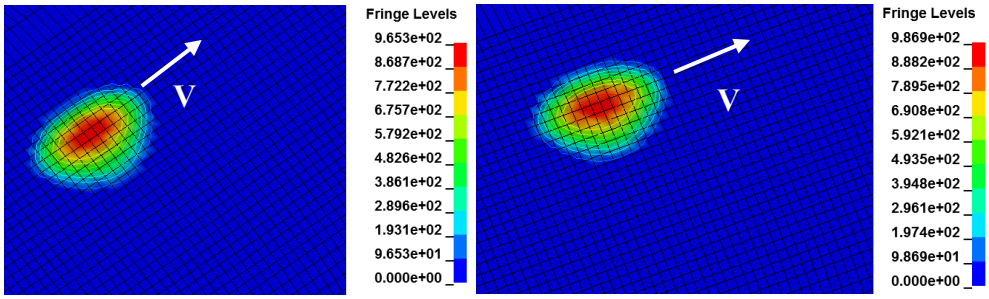

(a) AC– case 4 (b) DC– case 8

Figure 6.8 Interface pressure distribution on high rails (MPa) (3rd axle, element size 1.3 x 1.3 mm)

Contact shear stress

The maximum shear stresses in case 4 and 8 were 340 MPa and 299 MPa, respectively as shown in Figure 6.9. Since the adhesion level by DC loco (case 8, adhesion coefficient 0.23) was not as high as that by the AC loco (case 4, adhesion coefficient 0.31), the corresponding shear stress was also lower as predicted. However a higher shear stress would lead to an earlier damage initiation.

Von Mises stress

The von Mises stress distributions on the high rail surfaces are plotted in Figure 6.10. Under the load condition of the 3rd axle, the highest values were 649 MPa for case 4 (AC) and 631 MPa (DC). It was noted that the peak of the von Mises stress was found on and below the rail surface in case 4 (high adhesion coefficient 0.31), but it was located below the rail surface in case 8 (low adhesion coefficient 0.23). For high adhesion condition, the peak of stress was closer to the rail surface. Damage was expected to be initiated at the sub-surface of material in the low adhesion state and could be at and/or beneath the surface of rail under high adhesion circumstance.

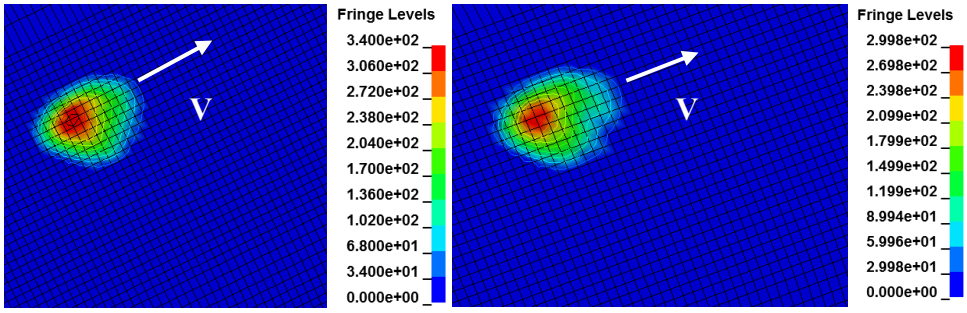

(b) AC – case 4 (b) DC – case 8

Figure 6.9 Shear stress distribution on high rails (MPa) (3rd axle, element size 1.3 x 1.3 mm)

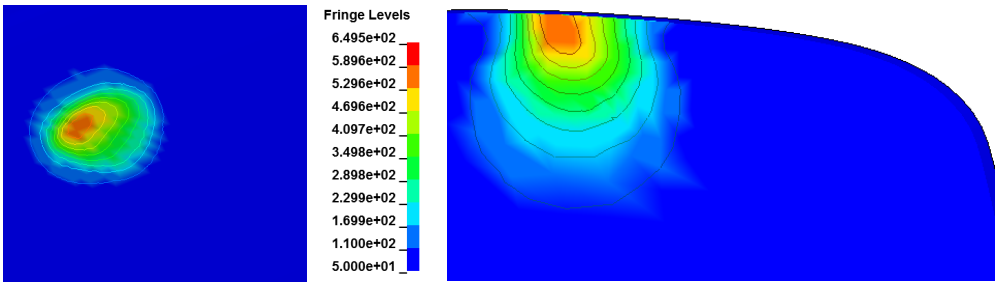

(a) AC– case 4

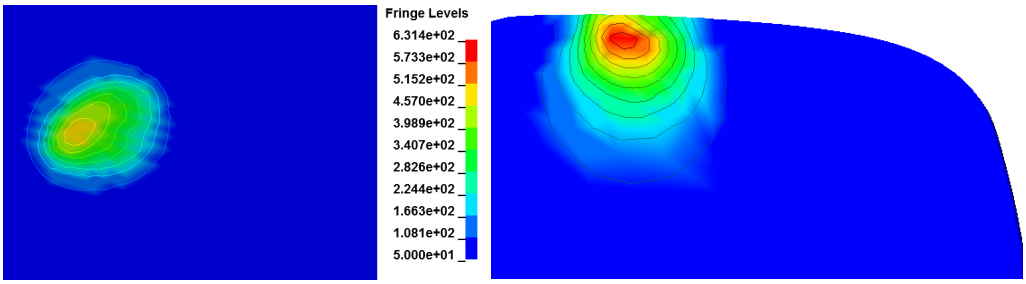

(b) DC – case 8

Figure 6.10 Von Mises stress distribution on high rails (MPa) (3rd axle)

The stresses on both the low and high rails produced by the 3rd axle are given in Table 6.4, which show a similar trend with Table 6.3. The stresses on the rails were increased if the drive was changed from DC to AC type, and the results obtained on the low rails were higher compared to the high rails.

Table 6.4 Summary of stress calculation (trailing axle)

Rail	Case	Loco types	Axle	Maximum contact pressure (MPa)	Maximum shear stress (MPa)	Maximum von Mises stress (MPa)
Low	3	AC	Trailing	1446	614	862
	7	DC	Trailing	1460	544	846
High	4	AC	Trailing	965	340	649
	8	DC	Trailing	986	300	631

6.4.3. Temperature rise

The analytical model utilized to calculate the temperature rising was validated by comparing to the results from the literature [119]. Based on this model, two worst cases for AC drive (case 3) and DC drive (case 7) were then chosen to evaluate the temperature rise on the rail. The obtained results from MBS model showed that the creepage on the longitudinal direction was dominant if compared to that on the lateral direction. Therefore the longitudinal creepage was used to calculate the temperature rise. It should also be noted that the thermal effects of the 1st and 2nd axle were neglected in this calculations, and the results of temperature was for one pass of the 3rd axle.

Plotted in Figure 6.11 are the theoretical results of temperature on and below the rail surfaces for two cases of FEM simulations. It was found that the maximum temperature exerted by AC (case 3) was noticeably higher than that by DC (case 7) due to the higher adhesion level produced by AC. The maximum value by AC locomotive was 400^{o}C, whereas it dropped off to 213^{o}C for the DC case. The peak temperature was positioned on the rail surface and at the trailing edge of the contact area. Furthermore the temperature gradually decreased below the rail surface. The heat penetrated to a depth of 0.237 mm in case 3, and 0.227 mm in case 7. At high

temperature, the rail material will be softened and crack will be initiated quicker [215].

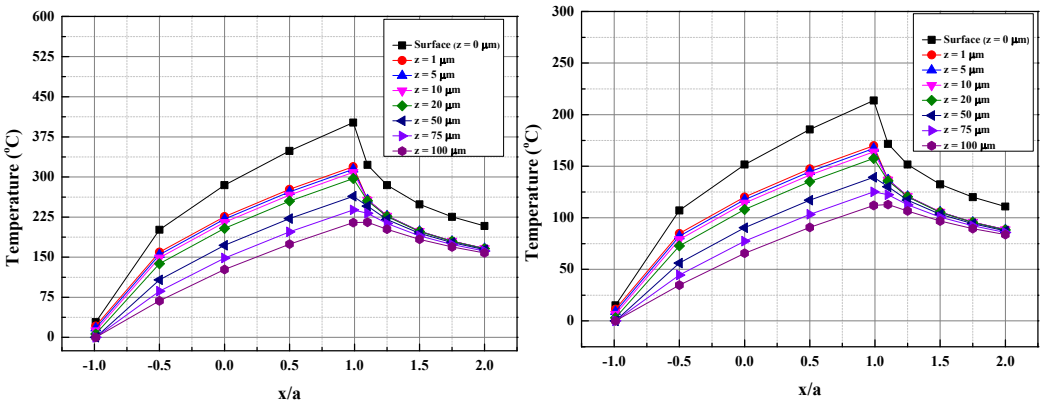

(a) Case 3 – low rail(AC) (b) Case 7 – low rail (DC)

Figure 6.11 Temperature rise on and below the rail surface by analytical method

As a train travels on a railway track, one point on the rail can be subjected to the repeated loading from many wheels attached to the locomotive. V. Gupta et al [216-217] found that the temperature on the contact surface can be increased higher if subjected to the repeated loading. Especially in the AC case where the adhesion level is significantly high, the maximum temperature in case 3 can be expected to reach 500°C [217]. The temperature for a formation of White Etching Layer (WEL) is 700°C. Moreover the hydrostatic pressure is known to promote WEL formation by reducing the temperature of the austenite transformation [218]. Since the contact pressure was relatively high in these particular cases, WEL would be expected to be formed at a temperature below 700°C. Further calculation of temperature for multi-pass of the wheels is required to completely estimate the wheel/rail thermal contact problems. A 3D thermal model for multi-pass contacts is described in chapter 7.

Field evidences showed a strong support for the prediction of the formation of white etching layer [219] and thermal damage [53] on the rail. Figure 6.12a showed a thin white layer of about 40 μm on the rail surface and also crack appeared on this layer. It was found that the depth of the white etching layer was related to the temperature

values. The higher is the temperature, the deeper the white etching layer penetrates on the rail [220]. In other words, the higher creepage results in a thicker white etching layer on the rail surface. Therefore, the white etching layer produced by the leading axle (1st axle) was anticipated to be thicker than that by the trailing axle (3rd axle) due to the higher creepage (shown in Table 6.1). Moreover rail scraping and melting were found on site observation due to high temperature wheel/rail contact, shown in Figures 6.12b and 6.12c.

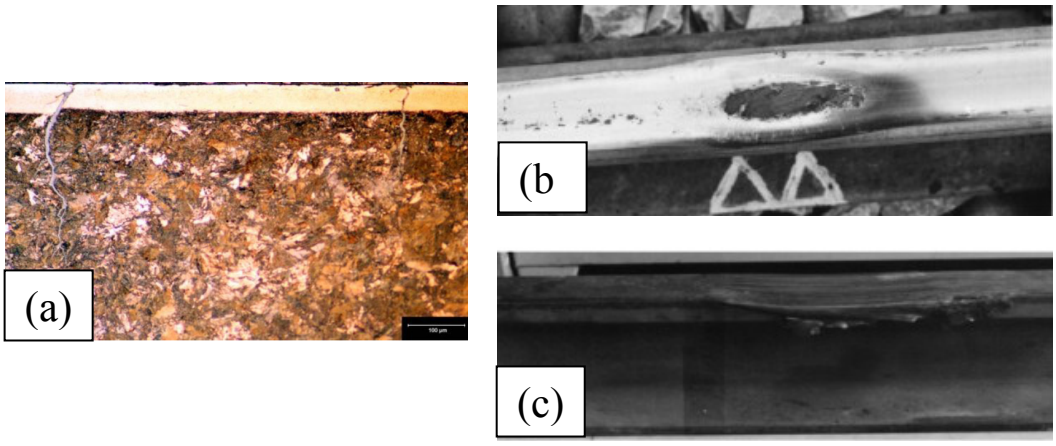

Figure 6.12 Thermal defect on rails (a) Formation of WEL [219], (b) Rail scraping [53], (c) Rail melting [53].

6.4.4. Material response to contact stress

The response of material subjected to the repeated loading is governed by stress, strain, wear and temperature change [135], and can be any kinds of the followings: (i) perfectly elastic, (ii) elastic shakedown, (iii) plastic shakedown, and (iv) rachetting [138]. An efficient tool normally applied to anticipate the response of material and position (surface/sub-surface) of the greatest damage initiation is shakedown map [20].

Drawn in Figure 6.13 was the shakedown diagram utilized to evaluate the response of the low/high rail material under the operation of (AC) and (DC) drives. Given on the vertical axis is the load factor, P_0/k, where P_0 is the maximum pressure and k is the material yield strength in shear (k = 234 MPa [139]). As shown in the map, the material response of the low rail was more serious than that of the high rail due to the load concentration at one point. For those rail-head contacts, the combination of high traction force and high pressure had most of the material responses fallen into the rachetting domain. Damage on the rail head was predicted to be initiated at the rail surface, whereas that on the rail gauge would be below the rail surface. As shown in Figure 6.14, field tests were conducted in Brisbane, Australia [219] to prove the possible development of squat on the rail head. This map presented the rolling contact fatigue damage only and the wear calculation could be found in the next section.

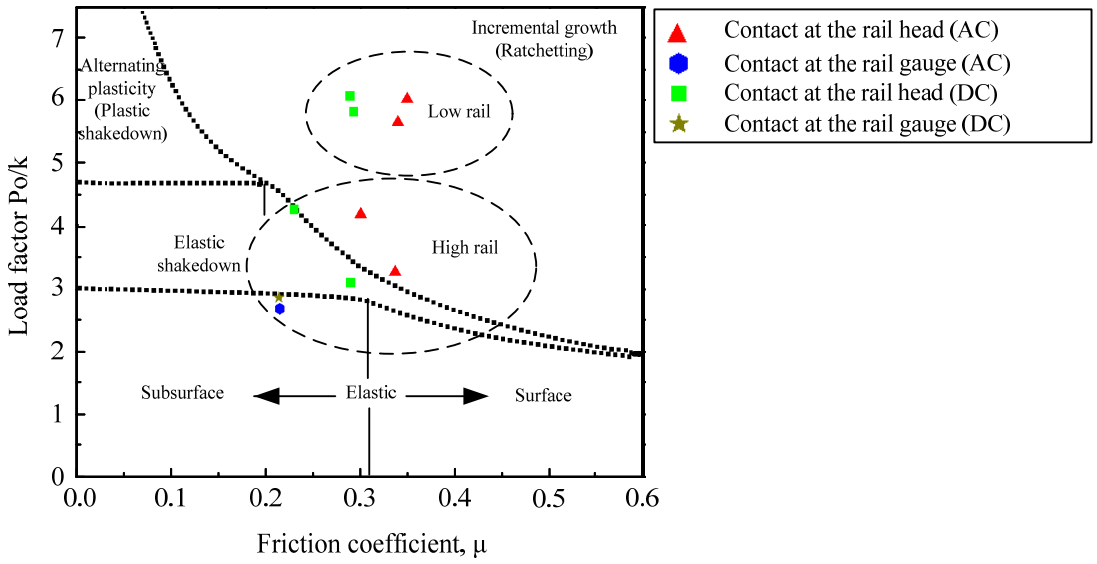

Figure 6.13 Shakedown diagram to predict the response of material

Figure 6.14 Squat on the rail head in Brisbane, Australia [219]

6.4.5. Wear on the rails

Wear phenomenon on the wheel/rail has been recognized to be connected to energy dissipation (the product of creep forces and creepages in the contact surface) [221]. In this study, wear calculation was also carried out. According to Archard wear model [222], the volume of material removed from the contact surface is proportional to the sliding distance and the normal force, and is inversely proportional to the hardness of the material:

$$V_w = k\frac{sF_z}{3H} \tag{6.7}$$

where k is the wear coefficient, V_w (m^3) is the volume of material unattached from bulk material, F_Z (N) is the normal force, and H (Hv) is the hardness of the rail material. For hardened steel, k = 10^{-4} [150, 223] and H = 359 Hv [173]. The sliding distance s is calculated as follows:

$$s = \delta L \tag{6.8}$$

δ is the mean value of longitudinal and lateral creepages and L (m) is the rolling distance (L = 0.6 m).

The wear map for these particular wheel-rail contact cases is illustrated in Figure 6.15. In comparison between different axles, the amount of worn material produced by the leading axle (1st axle) was more than that by the trailing axle (3rd axle) due to the higher creepage. For the same axles, wear on the low rail was more severe than that on the high rail due to the higher normal force.

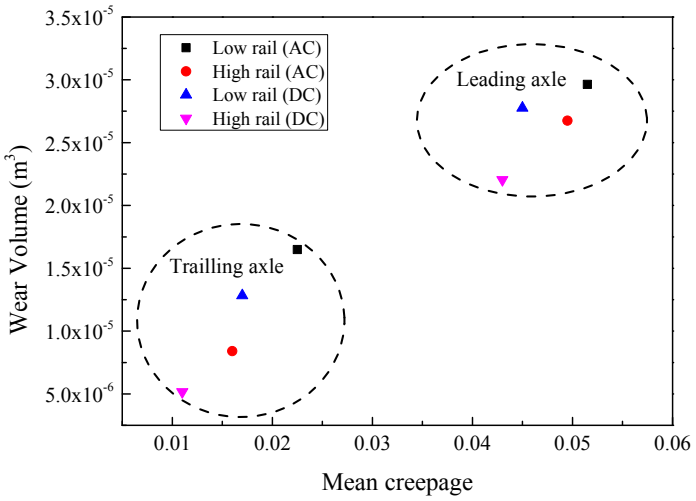

Figure 6.15 Wear volume on rail

6.5. Conclusions

A number of wheel/rail contact simulation cases for AC loco and DC loco have been carried out on both the low and high rails under a mixture of operational circumstances (contact loads, angle of attack, adhesion levels and worn wheel/rail profiles). The stress analysis of 8 cases has been presented. Furthermore the results of temperature rise for some selected cases and the responses of rail material have also been discussed. The key conclusions achieved from the present work were summarised as follows:

(1) Among the 8 cases, it should be noted that very high pressure and contact stresses are found in case 3 (Trailing axle – Low rail) and case 7 (Trailing axle – Low rail).

(2) On a high rail of a curved track, the wheel load can be distributed at two zones on the rail surface if the angle of attack between the wheel and the rail is high enough. Moreover the magnitudes of stress and pressure exerted on the high rails are lower than that on the low rails.

(3) In comparison between the axles of AC and DC drives, the stress values from AC drive are more severe than that from DC drive due to the higher adhesion level. This does not mean that AC traction is inherently worse as the operating points of the AC and DC locomotives are not the same. If the load balancing speed and torque condition of the DC locomotive was made closer to the AC, traction forces would be higher and so stress values closer to the same. In identical conditions, differences are expected to be insignificant – depending on differences in bogie design.

(4) In comparison between the axles of the same drives (either AC or DC drives), the magnitudes of stress and pressure produced by the trailing axle are higher than those by the leading axle.

(5) High temperature is generated on the rail surface, especially in the cases of AC drive with high adhesion level. The peak of temperature is at the trailing edge of the contact area and a very thin layer of rail material is penetrated by heat. Moreover the temperature on the rails is expected to be increased because of the effect of repeated loading from many wheels on the railway vehicle.

(6) The stress analysis carried out considers only one case of curving and traction at slow speed, hence higher stresses on the low rail. The results should only be used in this context. The overall differences in due to the operation of AC

and DC locomotives in regards to rail stresses and forces on track structures is a much larger discussion and cannot be inferred from these limited results.

(7) Wear on the low rail was more severe than that on the high rail. Furthermore the material volume worn away from the rail by the leading axle (1st axle) was more than that by the trailing axle (3rd axle) due to the higher creepage.

In this chapter, it was noticed that the temperature under high adhesion condition can be very high. However the analytical method only showed the two-dimensional (2D) temperature distribution on the rail and the thermal stress and strain have not been discussed. Therefore a three-dimensional (3D) FE model will be presented in the next chapter to investigate the influences of high adhesion condition on thermal stress/strain and the rail damage.

CHAPTER 7

THE INFLUENCE OF TEMPERATURE DUE TO HIGH ADHESION CONDITION ON RAIL DAMAGE

The aim of this chapter is to determine the temperature rise due to high adhesion contact and the thermal influence on the wear of rail and its life. A three-dimensional (3D) elasto-plastic finite element model was applied to evaluate the growth of temperature, thermal residual stress and strain. The numerical model employed the moving heat source code developed by Goldak within ANSYS/LS-DYNA. The mechanical and thermal properties of the rail material were governed by the temperature. The influence of multi-passes from multiple wheels attached to the locomotives on one point of the rail was also taken into account. The results indicated that after six wheel passes, the temperature due to the high adhesion condition was sufficiently high (723^{o}C) to form the White Etching Layer (WEL) known to be associated with the rolling contact fatigue (RCF) on the rail surface. Moreover the rail material would be softened by high temperature, which resulted in the acceleration of wear process. Finally the results of thermal stress and strain from FE model were used as input to the Kapoor's rachetting model to determine the number of wheel rolling cycles leading to rail damage.

The content of this chapter has been published [224]:

***K. D. Vo**, A. K. Tieu, H. T. Zhu, and P. B. Kosasih, "The influence of high temperature due to high adhesion on rail damage," Wear, vol. 330-331, pp. 571-580, 2015.*

7.1. Introduction

Studies of railroad have shown that the wheel operating temperature can normally reach between 100^{o}C to 300^{o}C [115] for rolling contact, and during braking up to 600^{o}C [126, 128]. The rail temperature also depends on the sliding velocity and can reach 630^{o}C – 1000^{o}C [53, 129]. Furthermore one point on the rail is normally subjected to a repeated loading from many wheels. The temperature field on the rail, therefore, increases with every cycle of rolling and potentially results in the formation of White Etching Layer (WEL) [164] from which cracks can be initiated [131-132, 164]. It was found that the temperature has a significant influence on the wheel-rail contact stress [126], and the combination of thermal stress and thermal softening enhances the rail wear rate [121]. Hence, the temperature effects on the rail life need to be investigated thoroughly.

Contact temperature under actual railway operating conditions can hardly be measured, so the analytical or numerical methods have been utilized. Reviews of these methods were presented in chapter 2. Nevertheless most of the numerical model for thermal problems up to now have been carried out in two-dimension, and very few 3D numerical models with limitations (coarse mesh or for the wheel only) were proposed. The wheel-rail profiles are non-symmetrical due to worn rail and unsymmetrical wheel. Therefore, a 3D model is necessary to analyse the results of thermal stress/strain in all directions (longitudinal, lateral and vertical) correctly. This chapter introduced a 3D thermo-elasto-plastic finite element wheel-rail contact model to calculate the temperature field and thermal stress induced by frictional rolling under high adhesion condition. The moving heat source code developed by Goldak et al. [225] was implemented in the current FE model and the temperature-dependent material properties were also applied. The results were compared to the analytical model presented in chapter 6. Moreover, repeated rolling of many wheels was considered to evaluate its influences on the temperature, thermal residual stress and the formation of White Etching Layer on the rail. A 2D-FE model of WEL was also set up to examine the contact forces and stress distribution on the WEL. From

the obtained results, the discussion of thermal influence on wear of the rail material and an estimation of the rail life based on the Kapoor's ratchetting model [137, 139, 191] were also presented.

7.2. Numerical model

The coupled thermal-mechanical model was developed by the finite element software ANSYS/LS-DYNA and LS-PREPOST. The details of models are introduced in the following sub-sections.

7.2.1. Model of wheel-rail contact

When a wheel rolls on a rail, the contact area and the pressure distribution can be obtained by the Hertz theory [40-41]. The normal pressure distribution is determined as follows:

$$P(x',y') = P_0\sqrt{1-\frac{x'^2}{a^2}-\frac{y'^2}{b^2}} \tag{7.1}$$

$$\begin{cases} x' = x - x_0 \\ y' = y - y_0 \end{cases} \tag{7.2}$$

where x' and y' are the local longitudinal and lateral coordinates, respectively; x_0 and y_0 denote the coordinates of the centre of the contact area; a and b are the semi-axis of the contact area in the x and y directions, respectively. The maximum pressure P_0 is calculated from the normal contact force Fz by the following equation:

$$\mathrm{P_0} = \frac{3\mathrm{F_Z}}{2\pi\mathrm{ab}} \tag{7.3}$$

Based on the Coulomb's friction law [57], the distribution of the tangential stress is given as follows:

$$\tau(x, y) = \mu P(x, y) \tag{7.4}$$

where μ is the friction coefficient. The heat flux distribution within the contact patch due to friction is given as:

$$q(x, y) = \mu v_s P(x, y) \tag{7.5}$$

where v_s is the sliding velocity. The heat partition δ = 0.5 is assumed [129]. This assumes that the heat generated is equally transferred to the wheel and the rail. The heat flux absorbed by the rail surface is calculated by:

$$q_r(x, y) = \delta q(x, y) \tag{7.6}$$

The heat applied by the wheel rolling on the rail is similar to the moving of a heat source along a steel bar. Hence the moving heat source technique was applied in this study to model the thermal problem of wheel-rail contact. Goldak's heat source model [225] based on a Gaussian distribution of power density was chosen. In this model the size and shape of the heat source is assumed to be an ellipsoidal energy deposition profile centered at the middle of the heat source, and decay exponentially with distance. As the shape of the wheel-rail contact area is also elliptical [35, 55], the Goldak's model therefore is appropriate this study. The mathematical expression of Goldak's model is described as [226]:

$$\dot{q}'''_{(x,y,z)} = \frac{6\sqrt{3}\dot{q}}{r_x r_y r_z \pi\sqrt{\pi}} e^{-\left(\frac{3x^2}{r_x{}^2}\right)} e^{-\left(\frac{3y^2}{r_y{}^2}\right)} e^{-\left(\frac{3z^2}{r_z{}^2}\right)} \tag{7.7}$$

where r_x, r_y, r_z are the semi-axis of the heat source. The heat rate $\dot{q}$ is substituted by the frictional heat flux calculated from Equation (7.6).

7.2.2. Finite element model

The schematic of the finite element model is illustrated in Figure 7.1. Simulation was carried out for 100-mm length, 50-mm width and 5-mm height of the rail (AS60, Australian standard rail [173]). The temperature generated due to frictional wheel-rail rolling contact was replaced by a moving heat source on the rail surface. The heat source was initiated at the beginning of the rail (Oxyz) and was moved along the central line of the rail.

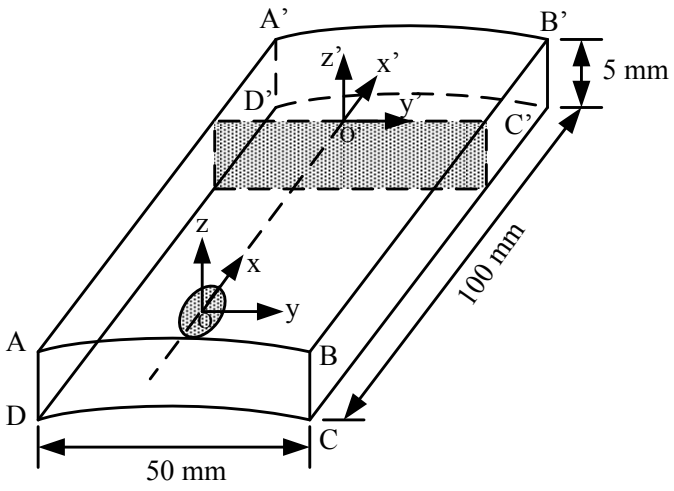

Figure 7.1 Schematic of finite element model

Figure 7.2 shows the finite element mesh of the numerical model. On the running surface, the model was finely meshed with the 1x1 mm elements as recommended in [35, 48]. Since heat penetrates a very thin layer of the contact surface, for instance, 0.113 mm in [55], a much finer mesh of 0.05 mm was generated to capture the change of temperature in the vertical direction, resulting a total of 56060 eight-node solid elements and 62398 nodes. The elastic-plastic-thermal and thermal-isotropic material models [193] were applied to simulate the mechanical and thermal properties of the rail, respectively. The displacements and rotations of the nodes at the bottom of the rail (DCC'D' – Figure 7.1) were constrained in all directions. The elements on the planes ABCD and A′B′C′D′ were restricted from moving in the x direction. The wheel-rail contact patch was subjected to a heat flux boundary. The remaining open surface area of the rail was governed by a heat convection boundary, which means heat can flow from the rail into the surrounding air by convection on

the free surface [182]. The corresponding heat transfer coefficient h_c was chosen to be 10 W/Km^2 [120], and the ambient temperature was 30^{o}C.

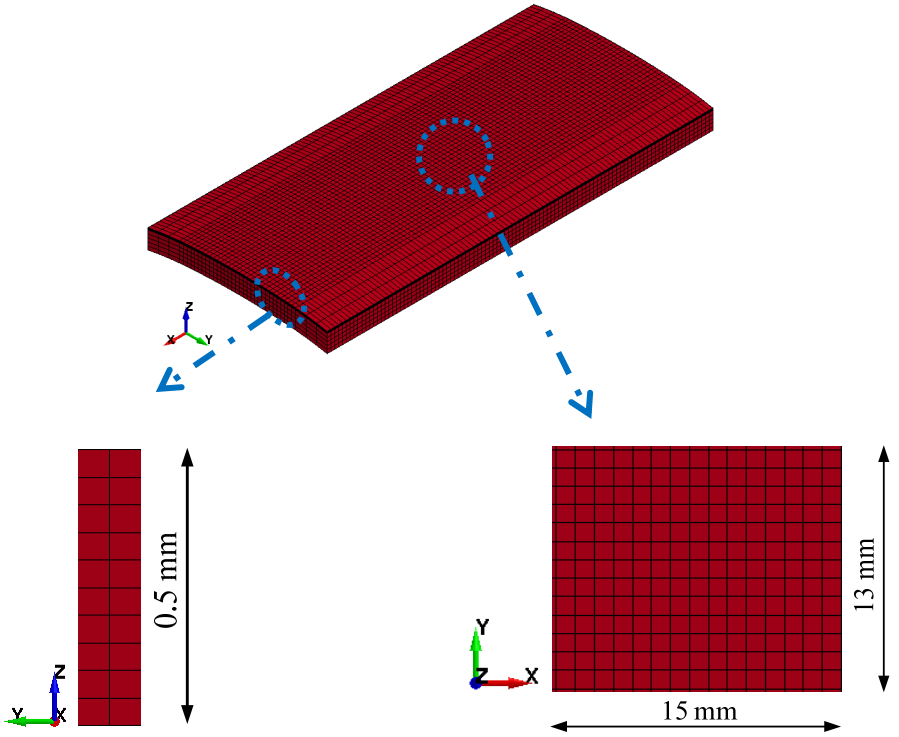

Figure 7.2 Finite element mesh (Δx = 1 mm, Δy = 1 mm, Δz = 0.05 mm)

The temperature-dependent material was adopted to capture the changes of rail material properties change with the temperature. The mechanical properties and thermal properties of the steel rail are summarized in Tables 7.1 and 7.2, respectively.

Table 7.1 Mechanical properties of rail [53, 227]

Temperature, T (^oC)	Young's modulus, E (GPa)	Poisson's ratio, ν	Yield strength, σ_y (MPa)	Coefficient of thermal expansion, α ($x10^{-6}\ ^oC^{-1}$)	Hardening modulus, E_P (GPa)
24	213	0.295	800.0	9.89	22.7
230	201	0.307	802.1	10.82	26.9
358	193	0.314	735.8	11.15	21.3
452	172	0.32	649.4	11.27	15.6
567	102	0.326	468.1	11.31	6.2
704	50	0.334	362.0	11.28	1.0
900	43	0.345	330.4	11.25	0.1

Table 7.2 Thermal properties of rail [53, 227]

Temperature, T (^oC)	Specific heat, C (J/kg^oC)	Thermal conductivity, K (W/m^oC)
0	419.5	59.71
350	629.5	40.88
703	744.5	30.21
704	652.9	30.18
710	653.2	30.00
800	657.7	25.00
950	665.2	27.05
1200	677.3	30.46

7.2.3. Simulation cases

A number of wheel-rail contact conditions were applied to compare the AC locomotives (high adhesion) and DC locomotive (low adhesion). Three locomotive types, which are normally used in Australia were evaluated, namely C44ACi (AC),

GT46C ACe (AC) and Cv40-9i (DC) [206]. Moreover, contacts at different axles were also considered. Input data for FE models were obtained from the combination of the traction simulations using GENSYS [228] and the finite element simulations using LS-DYNA [36], which covered different locomotive types, axle locations and contact load conditions. The positions of axles are illustrated in Figure 7.3. A summary of simulation cases is presented in Table 7.3. The values of contact pressure from the previous chapters were applied in this model. The slip rate by AC locomotive was higher than that by DC locomotive. The higher slip rate results in a higher adhesion level [35]. Different values of velocity has been was chosen throughout the thesis ranging from 21 km/h to 80 km/h to test the effect of velocity on the rail stress. However since the longitudinal length of the simulated domain was short (100 mm), such slow speed of 21 km/h was chosen to obtain the converged result within short time.

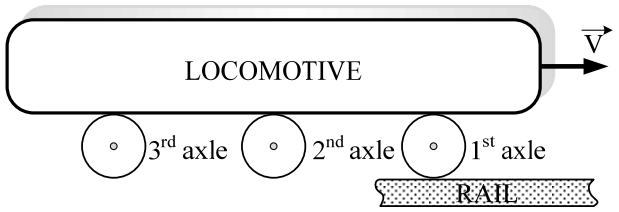

Figure 7.3 Position of axle on locomotive

Table 7.3 Simulation cases

Case	Locomotive	Axle	P_{max} (MPa)	μ	T_0 (^oC)	S_r (%)
1	C44ACi (AC)	1st	1349	0.39	30	8.5
2		3rd	1446	0.43	30	4.4
3	GT46C ACe (AC)	1st	1343	0.39	30	8.3
4		3rd	1471	0.44	30	3.3
5	Cv40-9i (DC)	1st	1395	0.34	30	7.4
6		3rd	1460	0.38	30	3.2

Note:

- Input data were provided by the Centre for Railway Engineering, CQUniversity using Gensys Multi-body simulation software and by University of Wollongong using LS-DYNA finite element simulation software [177].
- P_{max}: maximum contact pressure; μ: friction coefficient; T_0: ambient temperature; S_r: slip rate.

In the case of the dynamic braking, the wheel would be locked and slide along the rail surface, and the temperature could be significantly high. Therefore a simulation of wheel-rail sliding contact was also conducted to compare the temperature resulted from the rolling contact and sliding contact.

7.3. Results and discussions

7.3.1. Model validation

Validation of the 3D FE model was carried out by comparing the results to the existing data from the theoretical investigations [36, 55]. It was found that the 3D-FE temperature was lower than that obtained by the 2D-analytical temperature. For the same contact condition of case 2, the maximum temperature values calculated from the 2D analytical model and 3D FE model were 400^{o}C and 342^{o}C, respectively.

To further validate the 3D model, a 2D FE model was set up to evaluate the results between the models. The maximum temperature due to one wheel pass for all 6 cases obtained from 2D and 3D models are given in Table 7.4. The width of the 3D model domain was 50 mm (shown in Figure 7.1) which was wider than the width of contact area (10 mm). As expected, the 3D-FE values were also lower than the 2D-FE values. For example, the highest temperature for case 2 was 342^{o}C from 3D FE model, and 394^{o}C from 2D FE model. However, the values from 2D FE model (394^{o}C) and 2D analytical model (400^{o}C) were comparable. The temperature from the 3D model was found to be lower than the values from both the two 2D analytical and FE models due to the difference of the width DC (drawn in Figure 7.1). More simulations with various widths of the domain were performed to examine its effect on the temperature, and the results are plotted in Figure 7.4. The graph shows the temperature with the narrower width of DC had a higher temperature, approaching

the 2D values. The wider the width of DC is, the larger the contact area is. Therefore, more heat from the surface can be transferred from the rail to the ambient air, leading to a lower temperature in 3D FE model.

Table 7.4 Maximum temperature on the rail surface (one wheel pass)

Case	Loco	Axle	T_{max} (°C)	
			3D FEM	2D FEM
1	C44ACi (AC)	1st	522	610
2		3rd	342	394
3	GT46C ACe (AC)	1st	501	602
4		3rd	274	327
5	Cv40-9i (DC)	1st	430	503
6		3rd	235	269

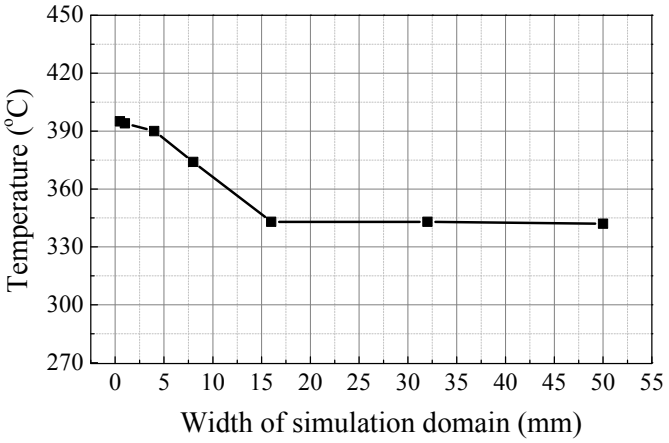

Figure 7.4 Temperature versus width of simulation domain

7.3.2. Temperature on the rail

The distributions of temperature on the rail surface and the cross section of the rail for case 1 (1st axle, AC drive: C44ACi) are shown in Figure 7.5. The maximum

temperature of one wheel pass in this case was 522°C which did not reach the critical temperature (about 720°C [219]) for phase transformation. Moreover, the temperature was not only confined at the contact zone, but also distributed along the rolling direction on the rail. The temperature at one point rises as the wheel touched the rail and did not recover immediately to the ambient temperature. On the cross section, the distribution of temperature appeared to be symmetrical along the dash line (Figure 7.5a) and penetrated a thin layer below the rail surface (0.35 mm).

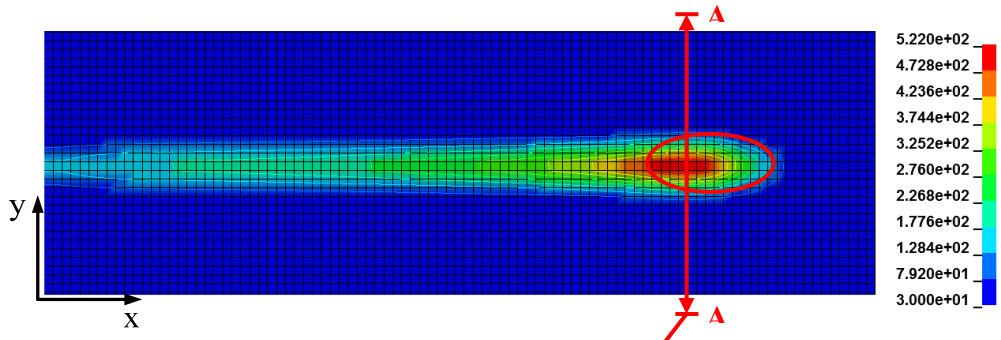

(a) Rail surface

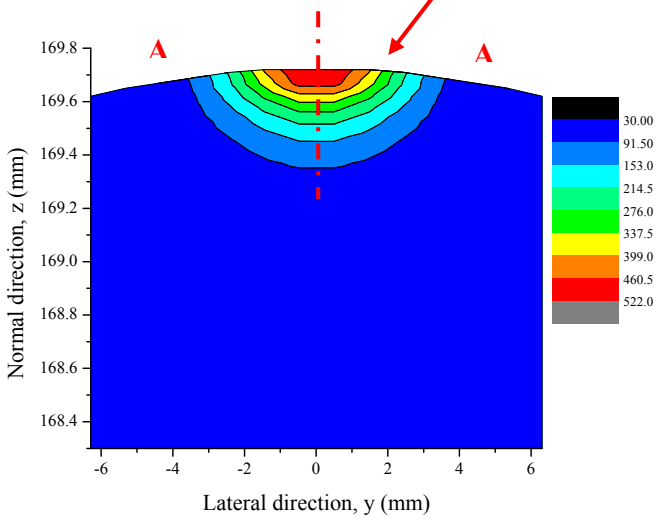

(b) Cross section A-A

Figure 7.5 Temperature contours (°C) on the surface and cross section of the rail (case 1)

Plotted in Figure 7.6 are the temperature of 3D model of the points along the dash line in Figure 7.5b and the temperature histories of the selected points with different

depths. The highest temperature was located at the rail surface and decreased below the rail surface. The deeper below the surface the point was, the lower the temperature reduced. As the wheel passes the contact point, the rail cooled down quickly to the value which was slightly higher than the ambient temperature.

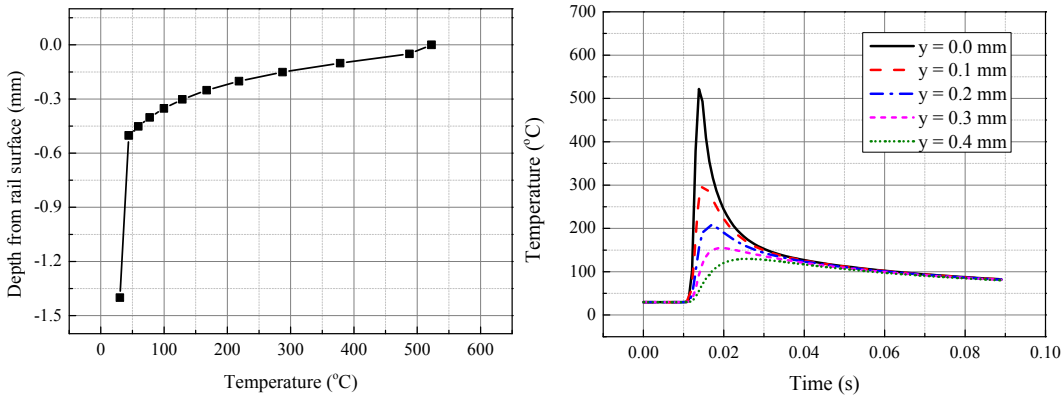

(a) (b)

Figure 7.6 (a) Temperature distribution and (b) temperature history of the rail material along the normal direction (Case 1)

The temperature rise over the running time at one point on the rail surface is shown in Figure 7.7. Since the slip rate on the 1st axle was higher for both AC and DC locomotives compared to the slip rate on the 3rd axle (Table 7.3), the temperature by the 1st axle, therefore, was also higher than that by the 3rd axle. For instance, the temperature in case 1 (1st axle) and case 2 (3rd axle) were 522°C and 342°C respectively. This tendency was consistent with the results calculated by the analytical method in [219]. In comparison:

- Between AC locomotives, the temperature produced by the loco C44ACi was higher than that by the loco GT46C ACe due to the higher slip rate of C44ACi compared to that of GT46 Ace. For example, the temperature in case 2 (3rd axle – AC: C44ACi) was 342°C, and it decreased to 274°C in case 4 (3rd axle – AC: GT46C ACe).
- Between AC and DC locomotives, the temperature produced by the AC locomotive was higher than that by the DC locomotives due to the higher slip

rate by AC. For instance, the temperature in case 3 (1st axle – AC: GT46C ACe) was 501°C, whereas it reduced to 430°C in case 5 (1st axle – DC: Cv40-9i).

- Among the 6 cases, the highest temperature (522°C) was produced in case 1 (1st axle – AC: C44ACi) and the lowest temperature (235°C) was generated in case 6 (3rd axle – DC: Cv40-9i).

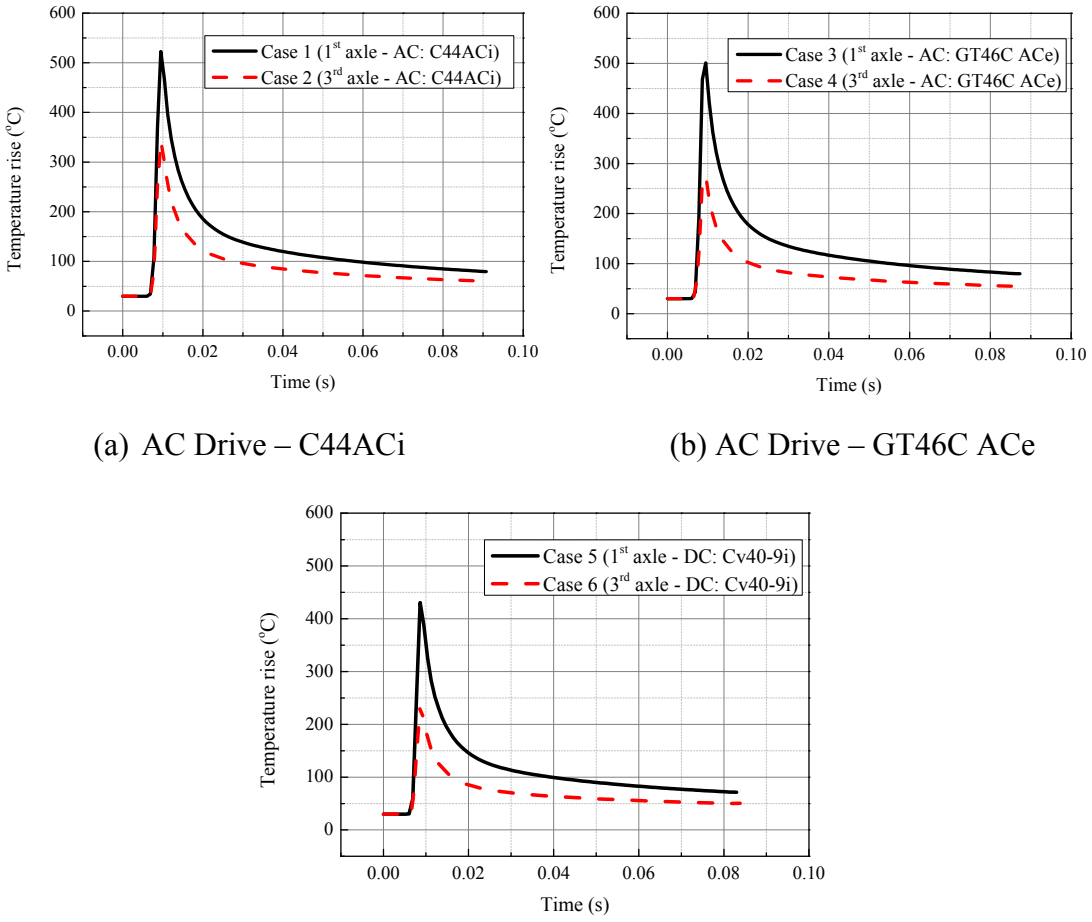

(a) AC Drive – C44ACi

(b) AC Drive – GT46C ACe

(c) DC Drive – Cv40-9i

Figure 7.7 Temperature rise at element 19280 on the rail surface (°C)

Since the highest and lowest temperatures were produced by locomotives C44ACi (AC) and Cv40-9i (DC), the results of the next sections were mainly demonstrated for these two locomotives.

The temperature rises due to the multi-pass of the wheels attached to the railway vehicles (AC: C44ACi and DC: Cv40-9i) are illustrated in Figure 7.8. As discussed, the temperature of one point on the rail did not reduce to the ambient temperature right after the first wheel pass (Figure 7.5). The residual heat at that point combined with the heat produced by the next wheel pass, resulting in an increase in temperature. The higher the numbers of wheel passes, the higher the value of temperature would be increased until it reaches an equilibrium between heat gain and heat losses. Furthermore the rate of the temperature rise for the 1st axle was quicker than that for the 3rd axle. After seven wheel passes, the temperature in case 1(1st axle-AC) was elevated by 201°C from 522°C (1st wheel pass) to 753°C (7th wheel pass). Nevertheless, a lower temperature rise of 113°C from 342°C (1st wheel pass) to 455°C (7th wheel pass) was noticed in case 2 (3rd axle-AC). If the rail is in contact with more than seven wheels, the temperature rise is anticipated to be higher. Extrapolation for cases 2 and 6 was use to examine how the temperature possibly increased after the 100th wheel pass. From the nine values of temperature for nine wheel passes, extrapolation for the 100th wheel pass was done by using spline method [229] available in Origin 8.6 [230]. It was found that the temperature could be as high as 1479°C and 947°C for case 2 and case 6, respectively as the 100th wheel passed the rail. This was a rough extrapolation as it was based on a small number of wheel passes. However it can provide a conservative guide on the limit temperature rise in practice. In [129], a temperature rise of 1000°C was predicted.

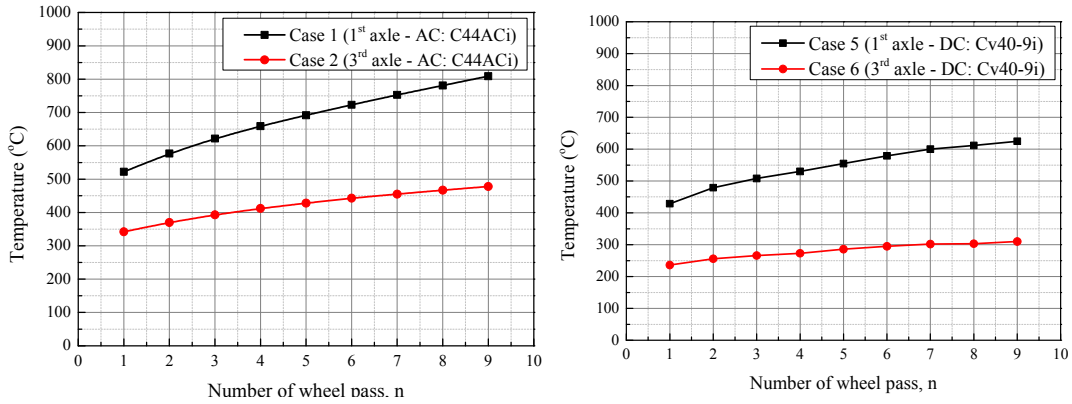

(a) AC Drive – C44ACi (b) DC Drive – Cv40-9i

Figure 7.8 Temperature rise due to multi-pass of the wheels (°C)

In practice, the train has more than just one loco, and each loco includes several axles (Figure 7.9). For each locomotive type, simulations for the wheels connected to two locos running on the rail were also carried out. In these models, it was assumed that there were three axles attached to one loco. The 1st, 2nd and 3rd wheel passes (n = 1, 2, 3) belonged to the 1st, 2nd and 3rd axles of loco 1; and loco 2 included the 4th, 5th and 6th wheel passes (n = 4, 5, 6). The distance between two wheels was 1700 mm.

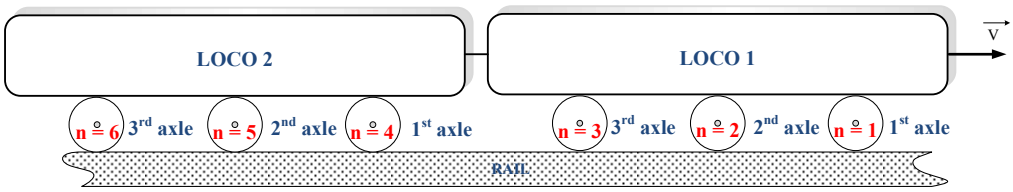

Figure 7.9 Practical scenarios of running train (n: number of wheel pass)

Figure 7.10 shows the practical temperature rise due to multi passes. The pattern of temperature rise on the rail in practice was found to be dissimilar from Figure 7.8. In particular, the temperature kept increasing after the 1st wheel pass (n = 1) in Figure 7.8 due to the applied constant slip rate of all wheels, whereas the temperature decreased in practice (Figure 7.10) after the 1st wheel pass of loco 1 (n = 1) due to the lower slip rate of the 2nd and the 3rd axles compared to the 1st axle. Once the wheel attached to the 1st axle of loco 2 passed the rail (n = 4), the temperature increased again due to the increasing of the slip rate. In comparison:

- Between the axles in the same loco of the same locomotive type, the temperature produced by the 1st axle was higher than that by the 2nd and 3rd axles due to the higher slip rate.
- Between the two locos of the same locomotive types: the temperature produced by loco 2 was higher than that by the loco 1 for all axles. As the loco 1 passed by, the residual heat which was higher than the ambient temperature was produced on the rail. Hence when the loco 2 passed by the rail, the residual hear added to the temperature produced by loco 2 resulted in the higher temperature than that by loco 1.

- Between different locomotive types, the temperature produced by AC Drive was still higher than that DC Drives. For instance, after the 4th wheel pass (n = 4), the temperature values by C44ACi (AC) and GT46C ACe (AC) were 626°C and 599°C, respectively; whereas it was 491°C by Cv40-9i.

Although the temperature produced in practice were lower than the cases considered in this study after the same number of wheel passes, but it still showed the tendency of temperature increasing after a certain number of wheel passes. In practice, there should be more than two locos for one train running on the rail, possibly forming a higher value of temperature.

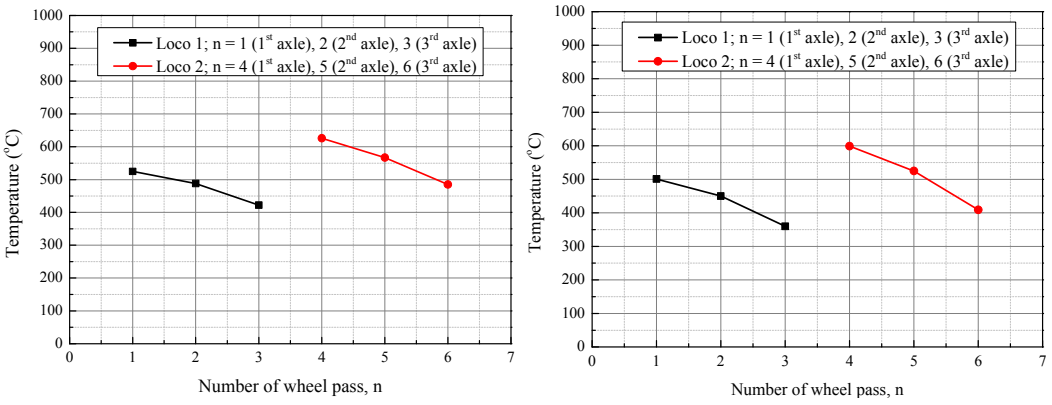

(a) AC Drive – C44ACi

(b) AC Drive – GT46C ACe

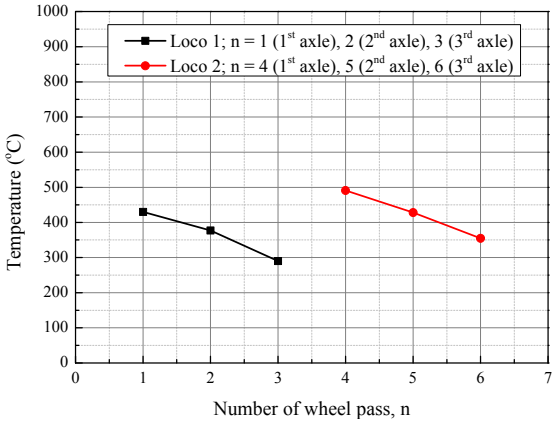

(c) DC Drive – Cv40-9i

Figure 7.10 Temperature rise due to two locos (°C) (n: number of wheel pass)

To compare the values of temperature formed by sliding contact with rolling contact, more simulations of the wheel sliding on the rail were conducted. Shown in Figure 7.11 are the temperature rises due to sliding of the wheel on the rail under different conditions. The maximum temperature could be reached up to 1050^{o}C in the sliding contact, whereas it was 522^{o}C in rolling contact (Figure 7.7). The temperature due to braking was significantly higher than that by the normal rolling in Figure 7.7 as expected. Moreover the temperature maintained at the value of above 800^{o}C in about 2.4 ms in braking. It should be noted that simulation for braking phenomenon was carried for one wheel pass due to limitation of time. If there are multi wheel passes, the temperature could be higher and the time duration to maintain the temperature at more than 800^{o}C should be longer. Numerical simulation conducted by Chen et al. [129] also confirmed the temperature during braking could be noticeably high after one wheel pass (more than 1000^{o}C for smooth rail and up to 1300^{o}C for corrugated rail). Such high temperature potentially can cause changes of material properties which would be discussed in later sections of this chapter.

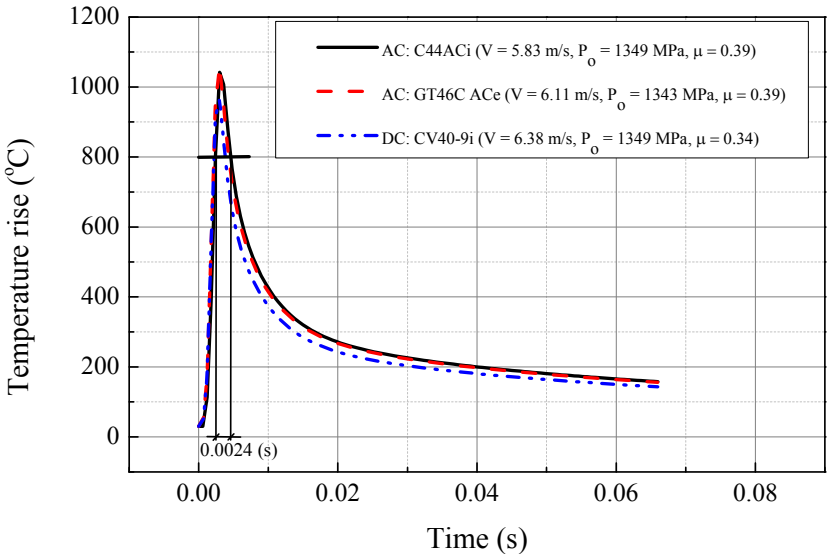

Figure 7.11 Temperature rise due to braking

7.3.3. Thermal stress-strain

This section presents the results of the stress and strain obtained from the 3D-coupled thermal mechanical mentioned above. The results primarily focused on locomotives C44ACi (AC, cases 1 and 2) and Cv40-9i (DC, cases 5 and 6).

7.3.3.1. Effective thermal plastic strain

Figure 7.12 shows the contours of the effective plastic strain on the rail surface for the 1st and 3rd axles of the AC locomotive (cases 1 and 2). Since the slip rate and the temperature of the 1st axle were more severe than those of the 3rd axle, it was anticipated that the effective plastic strain produced by the 1st axle would be higher as well. Indeed, the maximum value from case 1 (1st axle) was 0.38%, whereas it was only 0.063% in case 2 (3rd axle). Additionally the effective thermal plastic strain appeared along the travelling direction of the wheel on the rail surface.

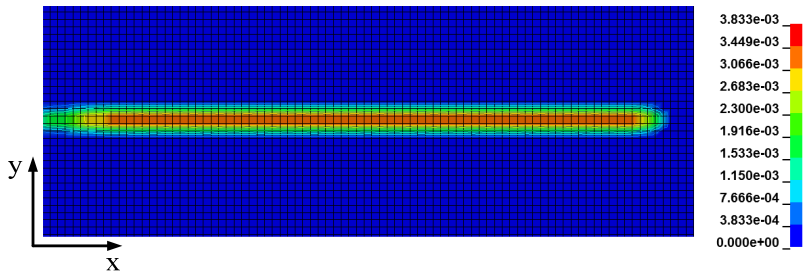

(a) Case 1 (1st axle – AC: C44ACi)

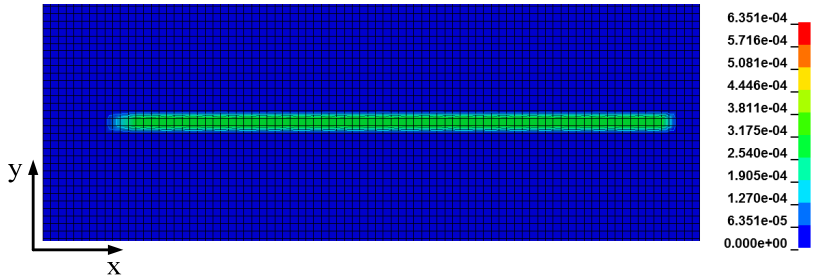

(b) Case 2 (3rd axle – AC: C44ACi)

Figure 7.12 Effective plastic strain distribution of the rail surface (1st wheel pass)

Figure 7.13 illustrates the effective plastic strain change with the number of wheel passes and along the depth of the rail. As a result of the low temperature and slip rate, the plastic strain in case 6 was very small even after several wheel passes. On the other hand, plastic strain on the rails in cases 1, 2 and 5 were higher as a result of the high temperature. It was found that the lower the temperature was, the longer the time for the thermal plastic strain to reach the stabilized condition was required. For example, after two to three wheel passes, the stable state of plastic strain was achieved for cases 1 and 5. However the value kept on rising even after the sixth wheel pass for case 2. The maximum effective plastic strain of cases 1 (AC – 1st axle), 2 (AC – 3rd axle), 5 (DC – 1st axle) were 0.41%, 0.21%, and 0.31%, respectively. As expected, for the same axle location, the plastic strain due to AC Drive was higher than that by the DC Drive (case 1 compared case 5). Along the vertical direction (Fig. 10b), the maximum effective plastic strain was located at the rail surface, and such value would be progressively reduced at points further way from the interface. For case 6, the effective plastic strain along the vertical direction at the 4th wheel pass was very small even at the surface due to the low temperature generated at this pass (260^{o}C).

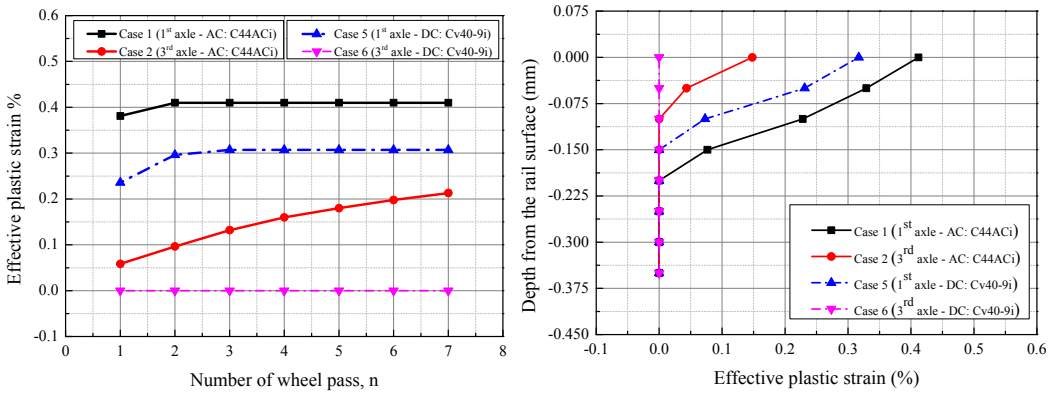

(a) (b)

Figure 7.13 Variation of effective plastic strain (a) on surface with wheel passes (b) along the vertical direction at the 4th wheel pass

7.3.3.2. Residual von Mises stress

The distribution of von Mises stress on the rail surface for case 2 is shown in Figure 7.14. The maximum von Mises stress in this case was 760 MPa which was located at the contact zone. As the wheel passed one point on the rail surface, there was still stress remaining on that point and along the rolling path (the so-called residual stress). It should be noted that von Mises stress was not constant along the rolling direction, whereas effective plastic strain was constant in Figure 7.12. This can be explained by assuming that von Mises stress was a function of temperature and plastic strain as follows:

$$\sigma_{VM} = a_1 T^{a_2} \varepsilon^{a_3} \tag{7.8}$$

where a_1, a_2, a_3 are constants, σ_{VM} is von Mises stress, T is temperature and ε is plastic strain. At any two points on the rail surface:

$$\frac{\sigma_{VM1}}{\sigma_{VM2}} \approx \frac{a_1 {T_1}^{a_2} {\varepsilon_1}^{a_3}}{a_1 {T_2}^{a_2} {\varepsilon_2}^{a_3}} \tag{7.9}$$

At point A in Figure 7.14, $\sigma_{VM1} = 282$ MPa, $T_1 = 150^oC$. At point B, $\sigma_{VM2} = 760$ MPa, $T_2 = 342^oC$, and $\varepsilon_1 = \varepsilon_2$. Equation 7.9 became $1.9 \approx 2.2$.

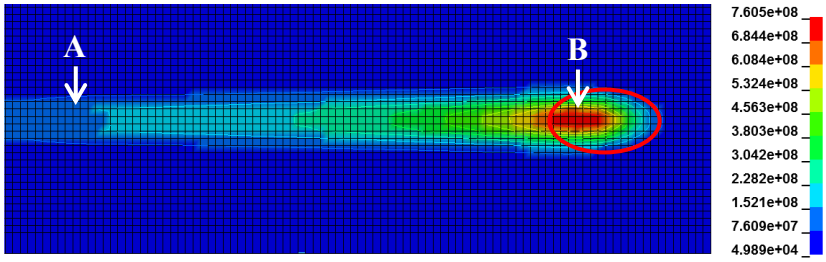

Figure 7.14 Von Mises stress distribution on the rail surface (case 2)

Figure 7.15 exhibits the alterations of the residual von Mises stress on the rail surface material over the number of wheel passes for both the AC and DC locomotives. As plotted, the residual von Mises stress kept increasing after the first

wheel pass, and the stable state was achieved after about four wheel passes. The maximum residual von Mises stress for case 1 (1st axle – AC), 2 (3rd axle – AC), 5 (1st axle – DC) and 6 (3rd axle – DC) were 230, 85, 169 and 68 MPa. The residual stress by the 1st axle was higher than that by the 3rd axle in the same locomotive. Moreover, residual stress produced by the AC locomotive was larger than that by the DC locomotive. Among these cases, the largest and lowest magnitudes of residual stress were found in case 1 and case 6 respectively.

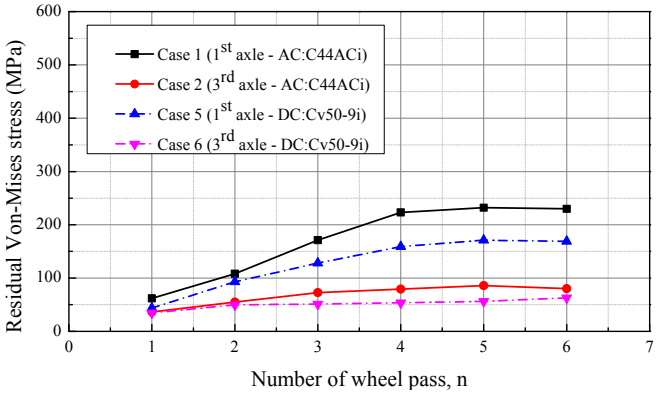

Figure 7.15 Residual von Mises stress at the rail surface

Residual von Mises stress in practice is performed in Figure 7.16. As mentioned in section 7.3.2, the wheels in practice have different values of slip rate, leading to the different temperature. It should be noted that the practical residual stress in Figure 7.16 was lower than that in Figure 7.15 due to the lower temperature. At the sixth wheel pass, the residual stress by DC loco (138 MPa) was found to be lower than that by two AC locos (215 MPa and 191 MPa). In comparison between two AC locos, the C44ACi loco produced a higher residual stress than that by the GT46C ACe loco due to the higher slip rate.

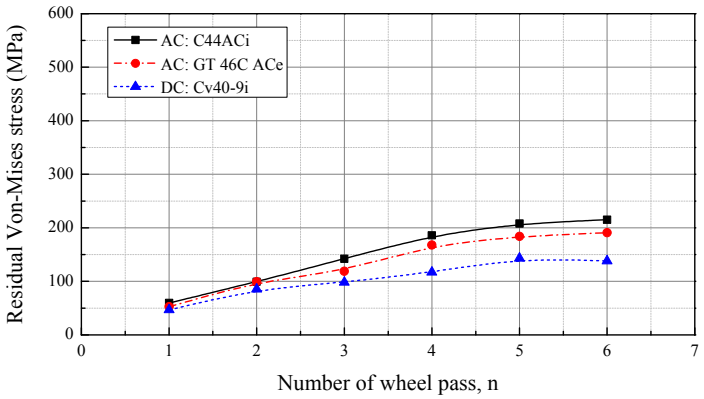

Figure 7.16 Residual von Mises stress in practice

7.3.4. Influences of temperature on the formation of WEL, wear and rail life

As the temperature increased significantly in the contact zone, especially for the 1st axle, the temperature may affect the microstructure, wear and rail life. In this section, a discussion of the thermal effects is presented.

7.3.4.1. Formation of white etching layer (WEL)

a. Origin and mechanism of formation of WEL

The rail in modern railway systems is subjected to intense use with fast train velocities and large axle loads, which cause structural defects and changes of the rail surfaces resulting from serious wear and rail corrugation. For instance, at high temperature, the microstructure of the rail material can be altered, such as the appearance of WEL on the rail surface. Takahashi et al. [218] found that WEL was generated by martensite transformation after a rapid austenitazation caused by

frictional heating, and the thermal equilibrium austenization temperature (727^{o}C in Fe-C alloys).

It is known that austenite transformation normally occurs through nucleation and growth, which suggests that this transformation needs a limited time, including an initial time of incubation. We have to consider the time taken for austenite transformation in order to judge whether or not austenization is possible during the time of contact. Experiment on rapid heating using laser radiation conducted by Speich et al. [231] has showed that the growth rate of austenite into pearlite was nearly 479 nm ms^{-1} at 829^{o}C in 0.96 wt.% carbon pearlitic steel and that rate increased with temperature. Ganeev [232] reported that it took 6 ns for irradiation by pulse laser to harden a surface region of 3-8 μm in depth of 0.6 wt.% carbon pearlitic steel. These reports indicate that the nucleation and growth of austenite in pearlitic steel were sufficiently fast to complete austenite transformation while the high temperature was maintained by frictional contact.

In this study, the temperature increased significantly after several passes of the wheels, especially for the wheel-rail contacts by the 1st axle where the slip rate was significantly high. For instance, the temperature reached 723^{o}C after six wheel passes on the rail surface in case 1 (Figure 7.8), which was sufficiently high to create the WEL. For some cases (2 and 6), the temperature values were too low to generate WEL even after several wheel passes.

In practical cases (Figure 7.10), the temperature was also far below the austenization temperature (727^{o}C) to form the White Etching Layer. However, it was known that the hydrostatic pressure would promote the WEL formation by lowering the temperature to 500^{o}C of the austenite transformation [133]. The WEL, therefore, can still potentially be generated in these cases. The temperature in the case of braking (Figure 7.11) was significantly high (more than 1000^{o}C) and this high temperature was maintained within 2.4 ms, which was long enough to form the WEL on the rail surface.

The prediction of WEL formation for these particular cases was confirmed by the experimental investigation conducted by Sarvesh et al. [220] on the same Australian standard rail (AS60) utilized in this study. Figure 7.17 shows WEL on the surface of the rail cut from the on-site track. The evidence showed that the depths of WEL on the two rail samples were different, respectively 310 µm and 250 µm. This can be explained by the dissimilar temperature. The higher the heat is generated, the deeper the white etching layer would be. In the current study, the highest temperature 723^{o}C and lowest temperature 295^{o}C temperatures after six wheel passes were calculated in case 1 and case 6, respectively. If formed, the depth of the WEL hence should be the thickest in case 1 and the thinnest in case 6.

Moreover, the microstructure observation also demonstrated the appearance of the transverse brittle cracks in WEL (Figure 7.17b), which are consistent with the examination of Carrol et al. [132] who examined cracking of a WEL in twin disc experiment. Further metallurgical analysis in [220] indicated that a WEL was the metallurgical feature associated with the surface damage and rail failure caused by severe wheel braking.

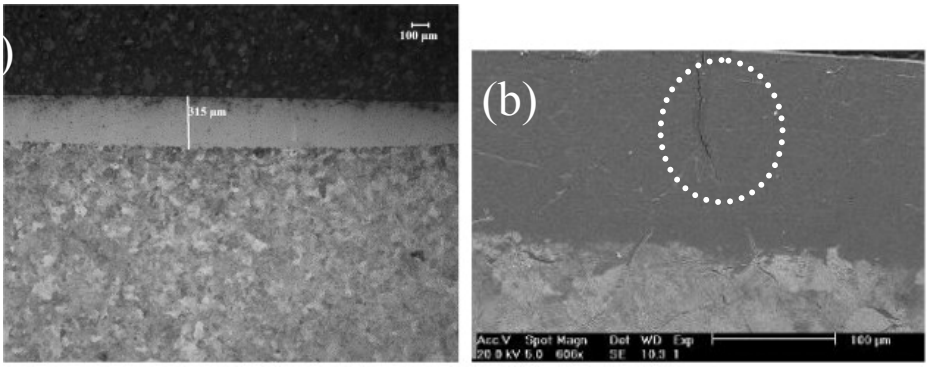

Figure 7.17 (a) An overview at near the edge of the WEL (depth ~ 300 µm), bulk microstructure, (b) surface crack in WEL [220]

b. Stress analysis of WEL

From the above discussion, it could be seen the potential of formation of white etching layer on the rail surface. Therefore a sub-2D-elastic-plastic FE model was used to investigate the stress state in WEL. The schematic and FE mesh of the WEL model were performed in Figure 7.18, including a wheel, 110-mm rail and a white etching layer of 10-mm length and 300-μm depth. In this sub-model, the wheel was modelled as a rigid body. Since the hardness of the rail material (359 Hv [173]) was found to be much lower than the WEL's hardness (600 Hv) [219], the elastic-plastic material had been applied for the rail and WEL was assumed to be elastic. The material properties of the rail and WEL are listed in Table 7.5.

The wheel was set to roll on the rail with the velocity of 5.83 m/s under the normal load of 130 kN. Since the longitudinal length of the domain was short, such slow speed was chosen in order to obtain the converged result within short time. The 2D-solid element and 2D-surface-to-surface contact with the friction coefficient of 0.4 [183] were utilized. Moreover very fine mesh at the WEL and the region near the WEL were generated, in which the element size was as small as 50 μm. The boundary condition was applied so that the bottom line of the rail was constrained in all directions whereas two sides were permitted to move along the vertical direction (y axis).

Table 7.5 Material properties

Material	Young's Modulus (GPa)	Yield Strength (GPa)	Density (kg/m^3)	Poisson ratio
Rail	210	0.8	7800	0.3
WEL	210	Elastic	7800	0.3

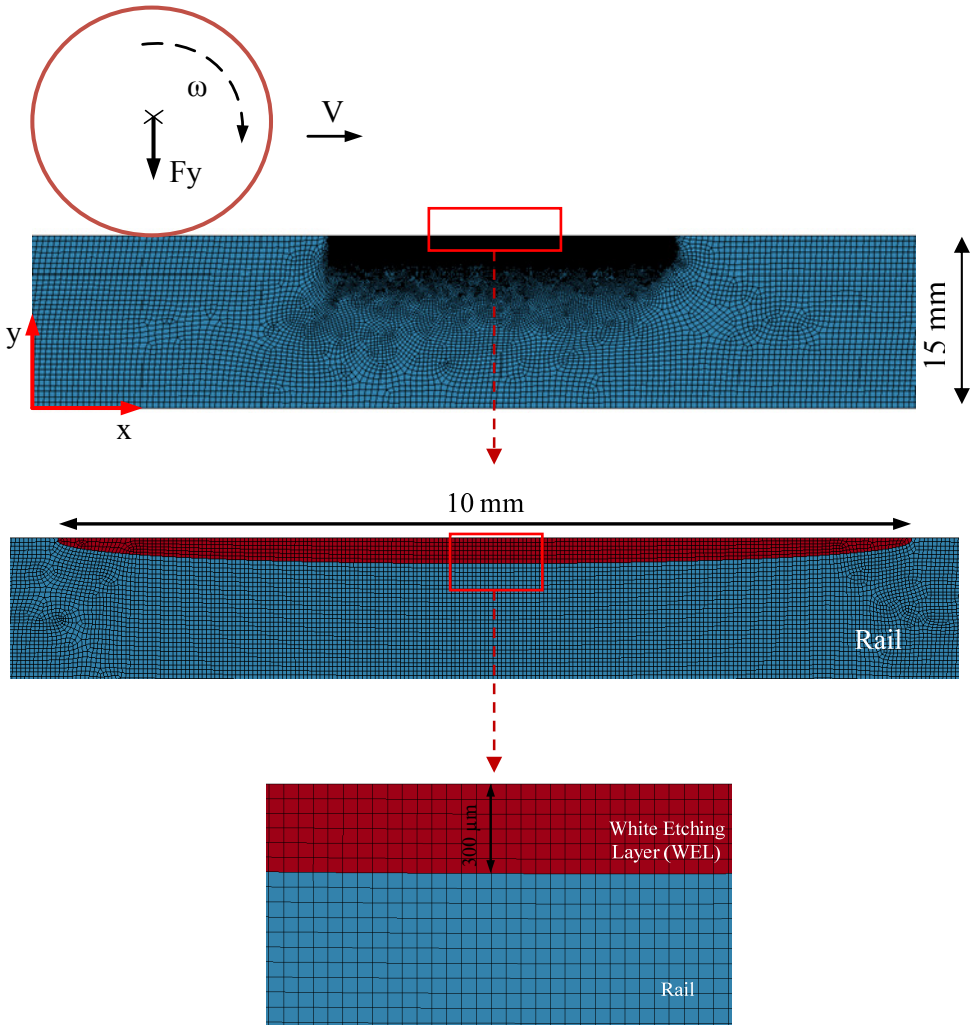

Figure 7.18 FE mesh of WEL model

Figure 7.19 illustrates the normal contact force and traction force produced during contact. The contact process could be sub-divided into two phases as follows:

- W-R contact (the wheel contacting the rail): At this stage, the wheel was still far away from the WEL or had already passed by the WEL. The maximum normal contact force at this phase was found to be the same with the applied normal wheel load (130 kN) and the highest achieved traction force was 50 kN.
- W-WEL contact (the wheel contacting the White Etching Layer): As the wheel contacted the WEL, the contact forces between the wheel and the rail became zero. However the contact forces on the WEL started increasing, and

reached the values which were the same with those produced by the W-R contact (130 kN and 50 kN for the normal force and traction force, respectively).

During the stable state, the contact forces fluctuated around the mean values (130 kN and 50 kN for normal contact force and traction force, respectively). The maximum and minimum normal contact forces were 135 kN and 126 kN, respectively. As for traction forces, the maximum and minimum values were 52 kN and 43 kN.

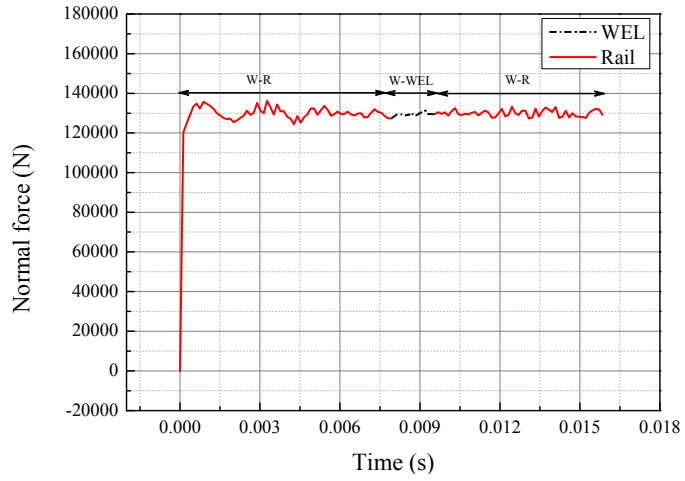

(a) Normal force

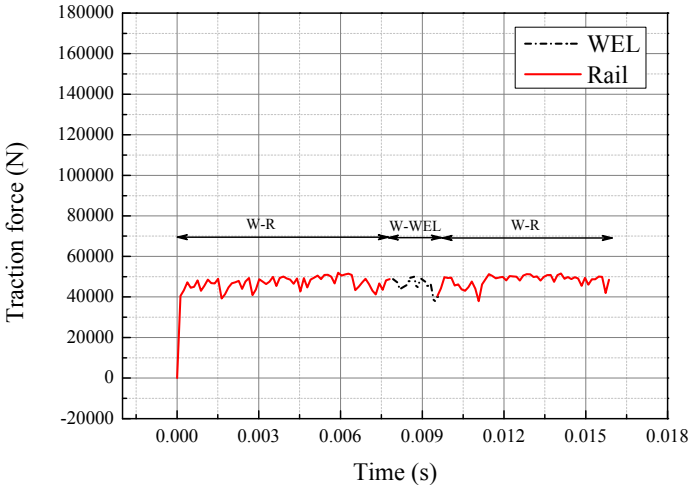

(b) Traction force

Figure 7.19 Contact forces (W: wheel, R: rail, WEL: white etching layer)

Shown in Figure 7.20 are the von Mises stress distributions on the rail surface at three stages: passing (1) starting points A, (2) middle point B, and (3) ending point C of WEL. The middle point of the WEL experienced the highest stress value (520 MPa) if compared to the two end points of the WEL (425 MPa and 381 MPa for the left and the right sides of WEL, respectively). Therefore the crack within the WEL, if initiated, would potentially be developed at the middle point first. The difference of stress values at two side of WEL could be due to the fluctuation of the contact forces (shown in Figure 7.19). The stress regions on the two sides were found to be larger than that in the middle due to the support of the boundary condition applied on the two sides of the rail. In practice, the length of white etching layer could be longer, giving more chance to form the crack on anywhere within its length. Once the crack has been initiated at the middle of WEL, it develops rapidly until it reaches the interface between the WEL and base material due to the brittle nature of martensite [132]. At this point, the different microstructure between WEL and base material would alter the crack's direction and slow its propagation [131].

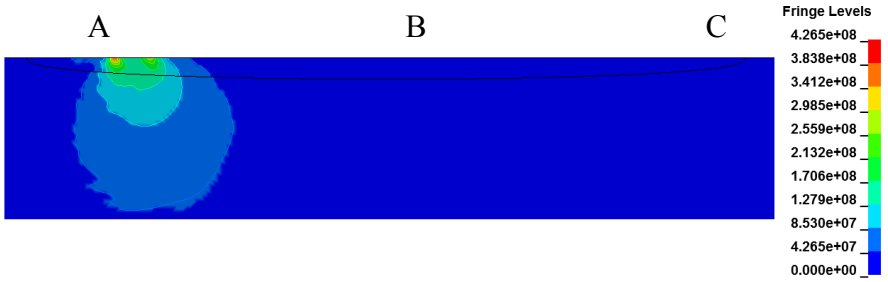

(a) Stage 1: passing the starting point of WEL

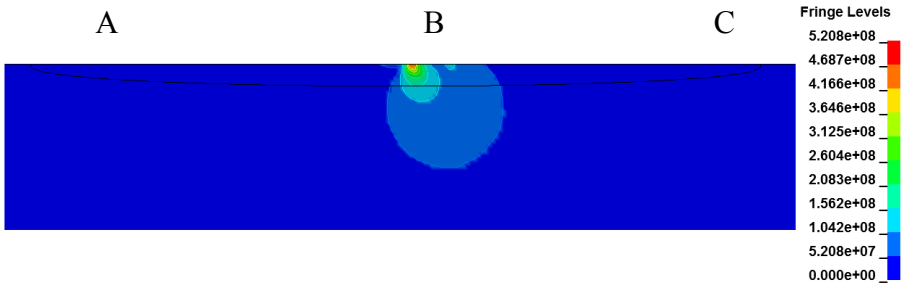

(b) Stage 2: passing the middle point of WEL

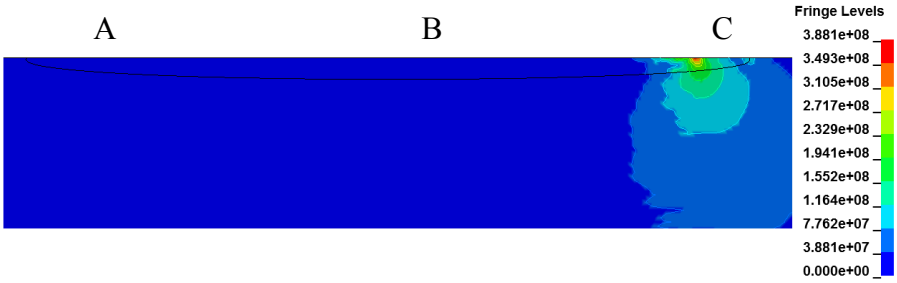

(c) Stage 3: passing the ending point of WEL

Figure 7.20 Von Mises stress distribution on the white etching layer (WEL)

7.3.4.2. Wear

In wheel-rail contact, the severity of rail and wheel wear has been studied and classified into several types of wear based on its mechanisms. Williams [50] categorized wear into mild wear and severe wear. In comparison to the original surface, a smoother surface is generated if mild wear occurs, but a rougher surface resulted from the severe wear. Moreover, the plastic deformation and oxide wear debris in severe wear are more extensive than in mild wear. It has also been

hypothesized that temperature contributes to the wear transition [233]. Therefore the numerical data of temperature obtained from the current research is essential for wheel-rail wear study.

Experimental results from twin-disc test [51] found that high temperature of around 200 – 300^{o}C induced wear transition. Numerical data [215] confirmed that the transition from mild to severe wear appeared at the temperature above 350^{o}C. In this study, the temperature produced under high adhesion condition was significantly high, predominantly after several wheel passes. Hence the wear on the rail surface for these particular cases can be attributed to severe wear.

As discussed previously, high slip rate resulted in high temperature. The high temperature due to high slip rate would enhance the wear rate [119]. In comparison to the slip rate by the 3rd axle, the slip rate by the 1st axle is higher (Table 7.3), which meant the wear rate by the 1st axle was also more severe than that by the 3rd axle. If comparison between locomotives was made, the slip rate by the AC locomotives was higher than that by the DC locomotive. Hence the wear rate by the AC locomotives was more dominant.

Since the temperature increases, the hardness of material should be influenced. The dependency of rail hardness on temperature was calculated by the following equation [234]:

$$\text{Vicker Hardness (HV)} \sim c \times \text{yield strength} \qquad (7.10)$$

where c is constant determined by geometrical factor. The hardness and the yield strength of the hardened rail used in this study are 359 Hv and 800 MPa, respectively [173], therefore the value of c is 0.44. The values of hardness are listed in Table 7.6. It could be seen that the rail hardness decreased as the temperature increased, which affected the wear phenomenon on the rail. Hence the wear volume (plotted in Figure 6.15, section 6.4.5 of chapter 6) should be re-calculated with the new values of hardness.

Table 7.6 Dependency of rail hardness on temperature

Temperature (^{o}C)	24	230	358	452	567	704	900
Yield strength (MPa)	800[173]	802.1	735.8	649.4	468.1	362.0	330.4
Hardness (Hv)	359[173]	359.9	330.2	291.4	210.1	162.4	148.2

The calculation of wear volume could be found in section 6.4.5 of chapter 6. Figure 7.21 shows the wear volume on the rail surface with and without consideration of temperature effects (Figure 7.21a and Figure 7.21b, respectively). It should be noted that the wear volume by the first axle was higher than that by the 3rd axle due to the higher slip rate in both Figures 7.21a and 7.21b. As the wear volume is inversely proportional to the hardness of material, the reduction of hardness due to high temperature resulted in the increasing of wear volume. For instance, the wear volume by the 1st axle of AC loco in Figure 7.21a (without consideration of temperature) was 2.96E-5 m^3, whereas it was increased to 6.69E-5 m^3 in Figure 7.21b (with consideration of temperature) due to the reduction of hardness at high temperature. Since the temperature by the 3rd axle of DC locomotive was low (280^{o}C), hardness of rail material was mostly unchanged at this temperature (Table 7.6). Hence wear volume by the 3rd axle of DC locomotive was minor although temperature effect was considered.

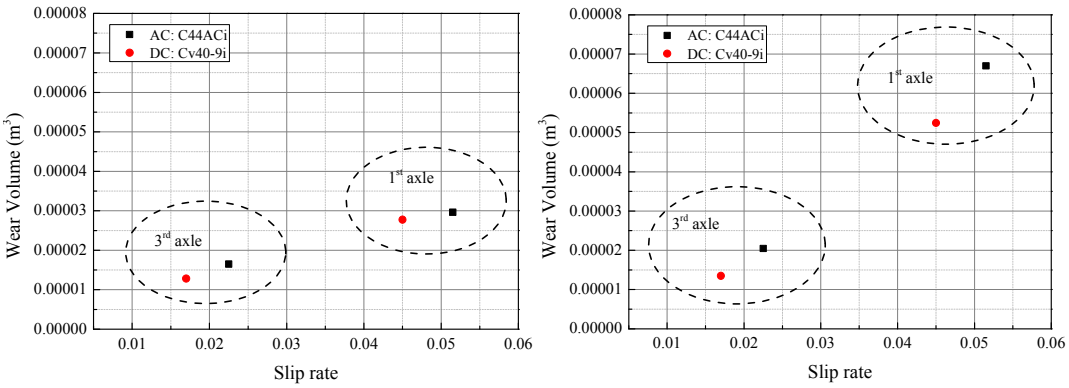

Figure 7.21. Wear volume on the rail (a) without consideration of temperature (b) with consideration of temperature

7.3.4.3. Rail life

Under different contact loads, the rail material may respond in one of the four ways: elastic, elastic shakedown, plastic shakedown and ratchetting [138]. Ratchetting (which means the plastic formation is accumulated in every cycle) is the response of the material if subjected to the cyclic contact conditions given in Table 7.3 [35-36]. During this process, the rail material can be hardened due to the plastic strain, but may also be softened if the temperature increases. Shown in Figure 7.22 is the influence of temperature on the yield strength of the rail material. If the temperature at the contact zone surpasses 250^{o}C, the yield strength reduces. The temperature produced by the 1st axle (cases 1 and 5) in this study was found high (more than 250^{o}C), which could accelerate the thermal softening on the rail.

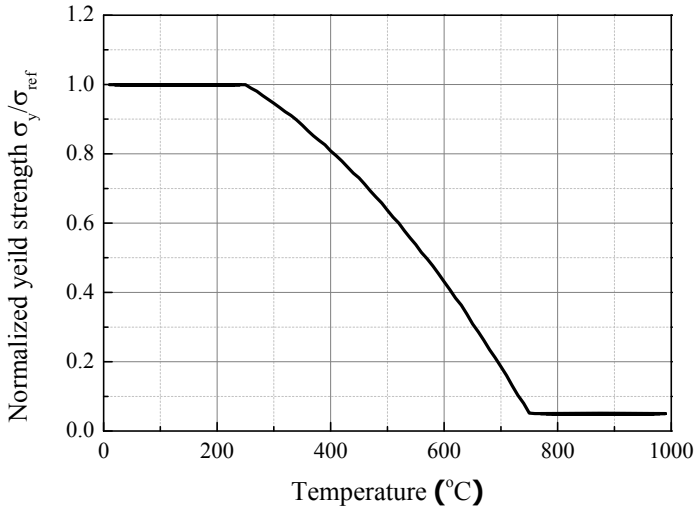

Figure 7.22 Influence of temperature on yield strength [121, 215]

With the ratchetting mode, the accumulation of plastic deformation continues until the ductility of the material is exceeded and the rail ruptures. The Kapoor model [139] was chosen to estimate the rail life. The number of cycles to failure is determined by the following equations:

$$N_f = \frac{\varepsilon_c}{\Delta\varepsilon_r} \tag{7.11}$$

ε_c is the critical strain for failure by ratchetting, and ε_c = 11.5 used in this chapter is obtained from the experiment [138-139]. $\Delta\varepsilon_r$ is the equivalent ratchetting plastic strain per cycle and is calculated as:

$$\Delta\varepsilon_r = \sqrt{(\Delta\tilde{\varepsilon})^2 + \left(\Delta\tilde{\gamma}/\sqrt{3}\right)^2} \tag{7.12}$$

$\Delta\tilde{\varepsilon}$ and $\Delta\tilde{\gamma}$ are the average ratchetting axial and shear strain per cycle.

Table 7.7 presents the qualitative comparison of the number of cycles to crack initiation due to the ratchetting by AC and DC locomotives with consideration of the thermal effect. In comparison:

- Between the axles in the same locomotive, the rail life by the 3rd axle is longer than that by the 1st axle due to the lower temperature and slip rate produced by the 3rd axle.

- Between the axles in different locomotives, the rail life by the AC locomotive is lower than that by the DC locomotive due to the higher temperature generated by AC locomotive.

Table 7.7 Prediction of number of cycles to crack initiation

Cases	Locomotives	Axle	$\Delta\varepsilon_r$ (10^{-3})	N_f (cycles)
1	C44ACi (AC)	1st	12.35	931
2		3rd	6.41	1794
5	Cv40-9i (DC)	1st	9.49	1212
6		3rd	3.79	3034

It should be noted that the number of cycle to crack initiation in this study is relatively low. Ringsberg [138] confirmed that among the models for analysing crack initiation, such as equivalent strain approach, critical plane model, energy and energy density model and empirical models, using the Kapoor's empirical equation resulted in the shortest time to fatigue initiation. Wickramasinghe et al. [235-236] found that for the friction coefficient of 0.35, the number of cycle to form damage was 3000 cycles [235] by applying Kapoor's model, which was comparable to the values in Table 7.7 for high friction conditions (0.34-0.44). Additionally, for P_o=1386 MPa and μ = 0.3, Ringsberg [237] calculated that the crack would be formed after about 3680 cycles by using the Kapoor's model. However, Ringsberg [138] also predicted that the crack could be initiated on the rail after approximately 80000 cycles, which was longer than the value obtained in the current study. This could be explained as the contact conditions in [138] were less severe (F_z = 120 kN, and μ = 0.25) than those in the current study (F_z = 134 kN, and μ = 0.34-0.44). Another contribution to the large variation on predicted number of cycles to crack initiation is that Ringsberg's model considered the critical plane of the damage and combined the influence of plastic shakedown and ratcheting phenomena on crack initiation.

Once the crack was initiated, it would be propagated if subjected to repeated loading until. Canadinc et al. [238] found that for the crack length of 3 mm and contact

pressure of 1500 MPa, the crack growth rate would be 5.5 μm/cycle. The number of cycle to cause the crack in Figure 7.17 propagate to a certain length of 300 μm would be 55 cycles of wheel/rail contact. However this was a qualitative estimation and further study need to be carried out to investigate the crack propagation on the rail.

7.4. Conclusions

A 3D finite element model to calculate the temperature rise on the rail under high adhesion contact has been introduced, which is a new contribution. The influences of temperature on damage, wear and rail life (cycles to fracture initiation) are elucidated. The findings can be summarized as follows:

(1) High temperature is generated due to the high adhesion contact condition. The highest temperature is located on the rail surface and decreased below the surface. In comparison:
   - Between AC locomotives, the temperature produced by the loco C44ACi is higher than that by the loco GT46C ACe.
   - Between AC and DC locomotives, the temperature generated by the AC locomotive was higher than that by the DC locomotives.

(2) The residual heat of the previous wheel pass combined with the heat produced by the next wheel pass, produce an increase of temperature. Although the temperature in practice does not increase as high as the cases considered in this study, but high temperature is possibly formed if many locos are applied on one train.

(3) The lower is the temperature, the longer the time is required for the plastic strain to reach the stabilized condition. The residual von Mises stress produced by the 1st axle is higher than that by the 3rd axle.

(4) After several wheel passes or in barking case, the temperature created by the AC locomotive sufficiently reaches the critical value of 720^{o}C, a threshold when the white etching layer can be formed.

(5) Crack initiated in the white etching layer may lead to the rail failure. The stress value at the middle of WEL was higher than that at the two end points of WEL. Therefore the crack, if initiated, would be initially formed at the middle of WEL.

(6) The reduction of rail hardness due to the frictional heat results in the increasing of wear on the rail. The temperature in these particular cases is high enough to support the transition from mild to severe wear. Moreover the wear rate by the AC locomotives is more dominant if compared to DC locomotives.

(7) In these particular cases, the rail material responds in the ratchetting mode. The higher temperature by the 1st axle compared to the 3rd axle in both the AC and DC locomotives results in a shorter number of cycles to initiate rail fracture.

CHAPTER 8

CONCLUSIONS AND SUGGESTIONS FOR FURTHER DEVELOPMENTS

The core innovation embedded in this thesis is the numerical modelling of the wheel-rail contact problems and the rail damage associated to high adhesion conditions. The innovative findings are distributed in four key chapters:

- ***Chapter 4*** models the wheel-rail contact problems and material response on a straight track under low/high adhesion condition.
- ***Chapter 5*** provides some predictions of damage formation due to wheel-rail contact on a curved track.
- ***Chapter 6*** focuses on wheel-rail contact stress states generated by AC and DC Drives on both the worn low/high rails under diverse practical contact conditions.
- ***Chapter 7*** presents a comprehensive 3D coupled thermal-mechanical model to estimate temperatures rise due to high adhesion contact, the formation of White Etching Layer (WEL), and the thermal influence on the rail life. Multi-wheel pass on the rail is considered and residual stress is also calculated.

In this chapter, the findings are synthesized and the suggestions for further development are proposed.

8.1. Conclusions

This dissertation has sought to investigate the influence of high adhesion condition on damage formation in wheel/rail contact, particularly on the rails. Answers have been searched for the following queries:

(1) On a straight track, what are the impacts of high adhesion conditions on the wheel-rail contact characteristics and material behaviours?
(2) On a curved track, how are the stress states and the formation of rail damages affected by high adhesion condition?
(3) Under diverse operational conditions, how are the stress states and heat generated by AC versus DC locomotives?
(4) How is the rail temperature induced by high adhesion conditions and its influence on rail life?

The detailed analysis and conclusions for each question can be found in chapters 4 to 7. In this chapter, the findings are summarised as follows:

8.1.1. Wheel-rail contact on a straight track

The contact location on the surface of the rail can be shifted from the centre of the rail head to near the rail gauge if a non-canted rail is used instead of a canted rail. Using a canted rail may help the rail web avoid bending and improve the life of the rail.

The influence of adhesion on normal contact parameters (contact area, interface pressure) is negligible. However varying the adhesion condition from low to high can cause significant changes to the stick/slip region, traction force, and tangential stress components. Compared to the low adhesion state, the adhesion area of the high adhesion case is reduced, but the coefficient of adhesion is higher.

The stress field in the rolling direction is divided into tensile and compressive regions and the maximum stress in high adhesion conditions are higher than those in the low adhesion states.

The von Mises stress increases significantly with the coefficient of adhesion. The high stress in the slip region on the contact surface can produce surface damage (plastic flow, wear or surface crack), although a high sub-surface stress may also initiate damage below the surface. Moreover, an increase of the slip zone can cause the surface damage to a wider area, especially under the full slip condition.

Based on the shakedown map, the response of rail materials on a straight track were predicted to be ratchetting, and damage was anticipated to appear on the rail surface.

8.1.2. Wheel-rail contact on a curved track

On a curved track, the wheel can contact with the rail at either one or two locations. The two-point contact is normally found on the high rail (rail gauge-wheel flange and rail head-wheel tread). Moreover the shape of the contact zones on the curved track is not always elliptical due to the effects of angle of attack and the worn profiles.

The magnitude and distribution of contact pressure and stresses are significantly influenced by the contact locations, worn status of the contact bodies (new/worn profiles) and angle of attack. When the worn wheel is in contact with the worn rail, the maximum pressure on the rail gauge is higher than that on the rail head.

Under high adhesion contact, the responses of the rail material on the rail head are in the ratchetting region and damage appears on the surface if initiated. For the contacts

on the rail gauge, the responses are predicted to be in elastic shakedown mode, but can potentially approach the ratchetting region if the contact pressure is high enough.

The fatigue defects on the rails are not anticipated to form on the head hardened rail but can develop for the standard carbon rail. On the curved track, the rail corrugation tends to be created on the low rail rather than the high rail.

8.1.3. Comparison between AC and DC locomotives

In comparison:

- Between the axles of the same drives (either AC or DC drives), the magnitude of stress and pressure produced by the trailing axle are higher than that by the leading axle.
- Between the axles of AC and DC drives, the stress values from AC drive is more severe than that by DC drive due to the higher adhesion level. This does not mean that AC traction is inherently worse as the operating points of the AC and DC locomotives are not the same. If the load balancing speed and torque condition of the DC locomotive is made closer to the same, traction forces would be higher and so stress values closer to the same.

Wear on the low rail is more severe than that on the high rail. Furthermore the material volume worn away from the rail by the leading axle (1st axle) is more than that by the trailing axle (3rd axle) due to the higher creepage.

8.1.4. Influences of temperature rise on rail damage

A 3D thermo-elasto-plastic model of the contact has been successfully set up to calculate the temperature rise and stresses in the rail under multiple wheel passes.

High temperature is generated due to high adhesion contact condition. The highest temperature is located on the rail surface and gradually decreased below the surface. In comparison between:

- AC locomotives, the temperature produced by the loco C44ACi is higher than that by the loco GT46C ACe.
- AC and DC locomotives, the temperature generated by the AC locomotive is higher than that by the DC locomotives.

The residual heat of the previous wheel pass combined with the heat produced by the next wheel pass, resulting in an increase of temperature. After several wheel passes, the temperature produced by the AC locomotive can reach the critical value of 720^{o}C, a threshold when the White Etching Layer is formed.

The lower is the temperature, the longer the time is required for the plastic strain to reach the stabilized condition. The residual von Mises stress produced by the 1st axle is higher than that by the 3rd axle.

The reduction of rail hardness due to the frictional heat results in the higher wear on the rail. Moreover the temperature under high adhesion is high enough to support the transition from mild to severe wear, and the wear rate by the AC locomotives is more dominant compared to DC locomotives. The higher temperature by the 1st axle compared to the 3rd axle in both the AC and DC locomotives can result in a shorter rail life.

8.2. Suggestions for further developments

The wheel-rail contact associated to high adhesion contact conditions was presented in this thesis. A full understanding of the wheel-rail contact associated to high adhesion will improve the model accuracy and benefit railway industry. The following recommendations are offered for further development of the current research:

- Due to the computational time limitation of finite element method, the dynamic effect of the axle load caused by the vibration of the vehicle and the track components was neglected. The lateral force on the straight track was also assumed to be zero. If all these effects are included, the stress level is expected to be higher and so the damage can be initiated. These effects can be analyzed by carrying out a 2D model or 3D model with part of the wheel/rail to reduce the computational cost.
- Roughness on the contact surfaces was not considered in all the simulation cases. The combination of roughness and high adhesion condition can raise the stress levels and also damage initiations. Therefore future study of locomotive adhesion should examine the influence of surface roughness. A physical roughness may be created by randomly moving the nodes of the contact surface in space optionally to their plane, or implementing of a roughness subroutine into LS-DYNA.
- In wheel/rail contact, the wheel damage/failure requires critical attentions, as wheel failure can result in catastrophic consequences. Additional study of wheel damage is recommended to provide a thorough understanding of high adhesion effects on both wheel and rail damage formation. A 3D themo-elastic-plastic model for the wheel should be considered.
- This study provides prediction of damage formation under diverse contact conditions. However the fracture mechanics aspect has not been investigated. In other words, a further study of cack propagation on the wheel/rail under high adhesion contact will be beneficial. Both Element Free Galerkin (EFG) and/or eXtended Finite Element Method (XFEM) cohesive fracture methods

which are available in the LS-DYNA software can be applied to investigate crack propagation.

- It should be noted that the current model of WEL is limited in two dimensions, and the material properties of WEL was predicted based on the theoretical equations. In order to thoroughly investigate the behaviour and crack development on WEL, a three-dimensional model can be built in the future. Moreover, experiments are required to examine the material properties of WEL changing with temperature to provide the appropriate input data for the 3D model.

APPENDIX A

WHEEL-RAIL GEOMETRIES

A.1. ANZR1 WHEEL PROFILE [172]

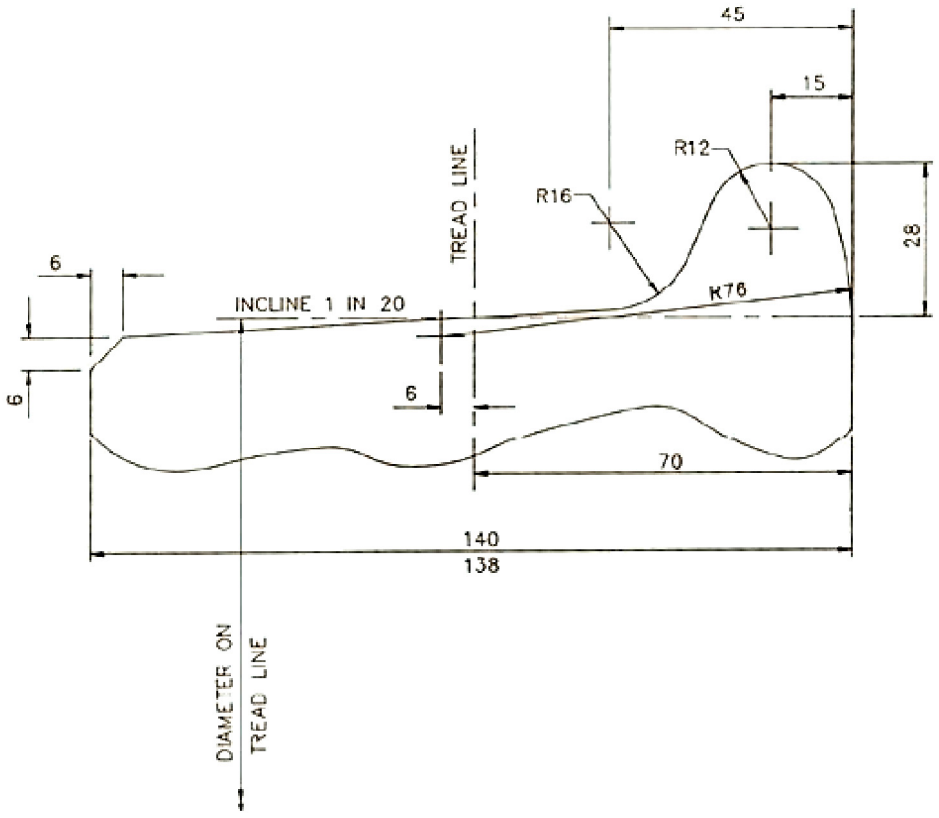

A.2. 60 KG RAIL PROFILE [173]

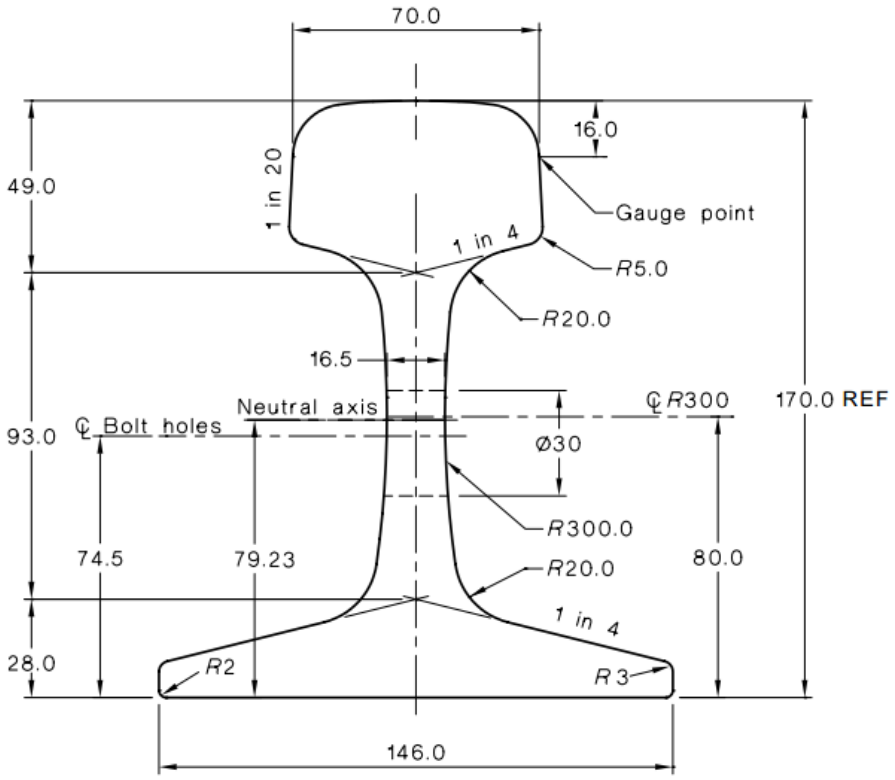

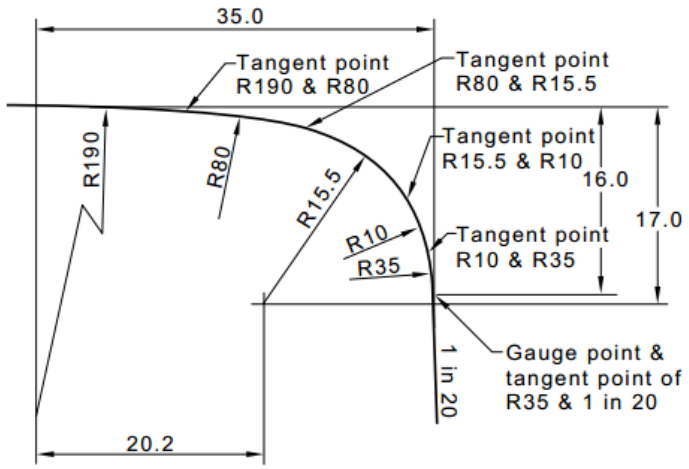

REFERENCES

[1] A. T. S. Bureau, "Derailment of Train 5PS6 near Bates, South Australia, 19 April 2008," Australian Transport Safety Bureau 2010.

[2] "Australian Rail Safety Occurrence Data from 1 July 2012 to 30 June 2012," Australian Transport Safety Bureau, 2012.

[3] N. Ramsey, F. Szanto, and P. Hewison, "Introducing The Next Generation Locomotive To The Ausralian Rail Network," in *Proccedings of Conference on Railway Engineering*, Perth, 2008, pp. 471-479.

[4] M. Latour and M. Nuendel, "Advantages and Benefits of Modern AC Traction Technology - Example Refurbishment and New Locomotives," in *Proccedings of Conference on Railway Engineering*, Perth, 2008, pp. 495-504.

[5] I. P. Milroy, R. A. Johnson, and P. S. Gaertner, "Performance of AC diesel-electric locomotives in typical Australian tasks," in *Railroad Conference, 1996., Proceedings of the 1996 ASME/IEEE Joint*, 1996, pp. 35-40.

[6] http://www.railway-technical.com/tract-02.shtml.

[7] U. Olofsson and T. Telliskivi, "Wear, plastic deformation and friction of two rail steels—a full-scale test and a laboratory study," *Wear,* vol. 254, pp. 80-93, 2003.

[8] H. Harrison, T. McCanney, and J. Cotter, "Recent developments in coefficient of friction measurements at the rail/wheel interface," *Wear,* vol. 253, pp. 114-123, 2002.

[9] http://www.republiclocomotive.com/ac_traction_vs_dc_traction.html.

[10] S. Iwnicki, *Handbook of railway vehicle dynamics*. Boca Raton: Taylor & Francis, 2006.

[11] C. Esveld, *Modern railway track*. The Netherlands: MRT Productions, 2001.

[12] A. Fenander, "Frequency dependent stiffness and damping of railpads," *Proceedings of the Institution of Mechanical Engineers. Part F, Journal of rail and rapid transit,* vol. 211, pp. 51-62, 1997.

[13] J. Maes, H. Sol, and P. Guillaume, "Measurements of the dynamic railpad properties," *Journal of Sound and Vibration,* vol. 293, pp. 557-565, 2006.

[14] S. Yella, M. Dougherty, and N. K. Gupta, "Condition monitoring of wooden railway sleepers," *Transportation Research Part C: Emerging Technologies,* vol. 17, pp. 38-55, 2009.

[15] G. Zi, D. Y. Moon, S.-J. Lee, S. Y. Jang, S. C. Yang, and S.-S. Kim, "Investigation of a concrete railway sleeper failed by ice expansion," *Engineering Failure Analysis,* vol. 26, pp. 151-163, 2012.

[16] W. M. Zhai, K. Y. Wang, and J. H. Lin, "Modelling and experiment of railway ballast vibrations," *Journal of Sound and Vibration,* vol. 270, pp. 673-683, 2004.

[17] C. Rigueiro, C. Rebelo, and L. Simões da Silva, "Influence of ballast models in the dynamic response of railway viaducts," *Journal of Sound and Vibration,* vol. 329, pp. 3030-3040, 2010.

[18] C. F. Bonnett, *Practical railway engineering*. Hackensack, NJ: Distributed by World Scientific Pub, 2005.

[19] S. Iwnicki, "Simulation of wheel–rail contact forces," *Fatigue & Fracture of Engineering Materials & Structures,* vol. 26, pp. 887-900, 2003.

[20] U. Zerbst, R. Lundén, K. O. Edel, and R. A. Smith, "Introduction to the damage tolerance behaviour of railway rails – a review," *Engineering Fracture Mechanics,* vol. 76, pp. 2563-2601, 2009.

[21] A. Johansson, J. C. O. Nielsen, R. Bolmsvik, A. Karlström, and R. Lundén, "Under sleeper pads—Influence on dynamic train–track interaction," *Wear,* vol. 265, pp. 1479-1487, 2008.

[22] W. Li, G. Xiao, Z. Wen, X. Xiao, and X. Jin, "Plastic deformation of curved rail at rail weld caused by train–track dynamic interaction," *Wear,* vol. 271, pp. 311-318, 2011.

[23] C. Madshus and A. M. Kaynia, "High-speed railway lines on soft ground: dynamic behaviour at critical train speed," *Journal of Sound and Vibration,* vol. 231, pp. 689-701, 2000.

[24] Z. Wen, G. Xiao, X. Xiao, X. Jin, and M. Zhu, "Dynamic vehicle–track interaction and plastic deformation of rail at rail welds," *Engineering Failure Analysis,* vol. 16, pp. 1221-1237, 2009.

[25] M. Lindahl, "Track geometry for high-speed railways: A literature survey and simulation of dynamic vehicle response " Royal Institute of Technology, 2001.

[26] W. Zhang, J. Chen, X. Wu, and X. Jin, "Wheel/rail adhesion and analysis by using full scale roller rig," *Wear,* vol. 253, pp. 82-88, 2002.

[27] Y. Berthier, S. Descartes, M. Busquet, E. Niccolini, C. Desrayaud, L. Baillet, and M. C. Baietto-Dubourg, "The role and effects of the third body in the wheel–rail interaction," *Fatigue & Fracture of Engineering Materials & Structures,* vol. 27, pp. 423-436, 2004.

[28] X. S. Jin, W. H. Zhang, J. Zeng, Z. R. Zhou, Q. Y. Liu, and Z. F. Wen, "Adhesion experiment on a wheel/rail system and its numerical analysis," *Proceedings of the Institution of Mechanical Engineers, Part J: Journal of Engineering Tribology,* vol. 218, pp. 293-304, 2004.

[29] H. Doi, T. Miyamoto, Y. Nishiyama, S. Ohe, and H. Kamachi, "A new experimental device to investigate creep forces between wheel and rail," *Wear,* vol. 271, pp. 40-46, 2011.

[30] H. Chen, T. Ban, M. Ishida, and T. Nakahara, "Adhesion between rail/wheel under water lubricated contact," *Wear,* vol. 253, pp. 75-81, 2002.

[31] E. A. Gallardo-Hernandez and R. Lewis, "Twin disc assessment of wheel/rail adhesion," *Wear,* vol. 265, pp. 1309-1316, 2008.

[32] K. Nagase, "A Study of Adhesion Between the Rails and Running Wheels on Main Lines: Results of Investigations by Slipping Adhesion Test Bogie," *Proceedings of the Institution of Mechanical Engineers, Part F: Journal of Rail and Rapid Transit,* vol. 203, pp. 33-43, January 1, 1989 1989.

[33] E. Niccolini and Y. Berthier, "Wheel–rail adhesion: laboratory study of "natural" third body role on locomotives wheels and rails," *Wear,* vol. 258, pp. 1172-1178, 2005.

[34] S. Descartes, C. Desrayaud, E. Niccolini, and Y. Berthier, "Presence and role of the third body in a wheel–rail contact," *Wear,* vol. 258, pp. 1081-1090, 2005.

[35] K. D. Vo, A. K. Tieu, H. T. Zhu, and P. B. Kosasih, "A 3D dynamic model to investigate wheel–rail contact under high and low adhesion," *International Journal of Mechanical Sciences,* vol. 85, pp. 63-75, 2014.

[36] K. D. Vo, A. K. Tieu, and H. T. Zhu, "Final report Project R3. 119: Locomotive Adhesion, Appendix 1: Wheel-rail contact by FEM modelling," CRC for Rail Innovation, Australia 2013.

[37] K. D. Vo, A. K. Tieu, H. T. Zhu, and P. B. Kosasih, "Rolling contact stress states of two contact points on curved track " presented at the 10th World Congress on Railway Research, Sydney, Australia, 2013.

[38] K. D. Vo, H. T. Zhu, A. K. Tieu, and P. B. Kosasih, "FE method to predict damage formation on curved track for various worn status of wheel/rail profiles," *Wear,* vol. 322–323, pp. 61-75, 2015.

[39] H. Sugiyama and Y. Suda, "Wheel/Rail Two-Point Contact Geometry With Back-of-Flange Contact," *Journal of Computational and Nonlinear Dynamics,* vol. 4, pp. 011010-6, 2009.

[40] W. Yan and F. Fischer, "Applicability of the Hertz contact theory to rail-wheel contact problems," *Archive of Applied Mechanics,* vol. 70, pp. 255-268, 2000.

[41] K. L. Johnson, *Contact mechanics*. New York: Cambridge University Press, 1985.

[42] A. A. Shabana, K. E. Zaazaa, and H. Sugiyama, *Railroad vehicle dynamics: a computational approach*. Boca Raton: CRC Press, 2008.

[43] A. Ekberg, H. Bjarnehed, and R. Lundbéan, "A fatigue life model for general rolling contact with application to wheel/rail damage," *Fatigue & Fracture of Engineering Materials & Structures,* vol. 18, pp. 1189-1199, 1995.

[44] T. Telliskivi and U. Olofsson, "Contact mechanics analysis of measured wheel-rail profiles using the finite element method," *Proceedings of the Institution of Mechanical Engineers, Part F: Journal of Rail and Rapid Transit,* vol. 215, pp. 65-72, 2001.

[45] T. Telliskivi and U. Olofsson, "Wheel–rail wear simulation," *Wear,* vol. 257, pp. 1145-1153, 2004.

[46] T. Telliskivi, U. Olofsson, U. Sellgren, and P. Kruse, "A tool and a method for FE analysis of wheel and rail interaction," *Proceedings of the ANSYS Conference in Pittsburgh (on CD), Pennsylvania,* 2000.

[47] M. Wiest, E. Kassa, W. Daves, J. C. O. Nielsen, and H. Ossberger, "Assessment of methods for calculating contact pressure in wheel-rail/switch contact," *Wear,* vol. 265, pp. 1439-1445, 2008.

[48] X. Zhao and Z. Li, "The solution of frictional wheel–rail rolling contact with a 3D transient finite element model: Validation and error analysis," *Wear,* vol. 271, pp. 444-452, 2011.

[49] A. Sladkowski and M. Sitarz, "Analysis of wheel–rail interaction using FE software," *Wear,* vol. 258, pp. 1217-1223, 2005.

[50] W. J.A, "Wear modelling: analytical, computational and mapping: a continuum mechanics approach," *Wear,* vol. 225-229, Part 1, pp. 1-17, 1999.

[51] R. Lewis and U. Olofsson, "Mapping rail wear regimes and transitions," *Wear,* vol. 257, pp. 721-729, 2004.

[52] Z. Wen, X. Jin, and W. Zhang, "Contact-impact stress analysis of rail joint region using the dynamic finite element method," *Wear,* vol. 258, pp. 1301-1309, 2005.

[53] L. Wu, Z. Wen, W. Li, and X. Jin, "Thermo-elastic–plastic finite element analysis of wheel/rail sliding contact," *Wear,* vol. 271, pp. 437-443, 2011.

[54] S. Cao, J. Zhang, C. Sun, and J. Zhang, "Wheel-Rail Slide Thermal-Elastic Coupled Analysis," in *Information Engineering and Computer Science, 2009. ICIECS 2009. International Conference on*, 2009, pp. 1-4.

[55] K. D. Vo, A. K. Tieu, H. T. Zhu, and P. B. Kosasih, "A tool to estimate the wheel/rail contact and temperature rising under dry, wet and oily conditions," *Computers in Railways XIV: Railway Engineering Design and Optimization,* vol. 135, p. 191, 2014.

[56] F. W. Carter, "On the Action of a Locomotive Driving Wheel," *Proceedings of the Royal Society of London. Series A,* vol. 112, pp. 151-157, August 3, 1926.

[57] V. Popov, "Coulomb's Law of Friction," in *Contact Mechanics and Friction*, ed: Springer Berlin Heidelberg, 2010, pp. 133-154.

[58] J. J. Kalker, "A strip theory for rolling with slip and spin, Proc. Koninkl. Ned. Akad. Wetenschap. Ser. B," pp. 10–62, 1967.

[59] http://www.kalkersoftware.org/.

[60] K. J.J, "Wheel-rail rolling contact theory," *Wear,* vol. 144, pp. 243-261, 1991.

[61] J. J. Kalker, "Rolling with slip and spin in the presence of dry friction," *Wear,* vol. 9, pp. 20-38, 1966.

[62] J. J. Kalker, "Simplified theory of rolling contact " Department of Mathematics, Delft University of Technology 1973.

[63] J. J. Kalker, "A Fast Algorithm for the Simplified Theory of Rolling Contact," *Vehicle System Dynamics,* vol. 11, pp. 1-13, 1982/02/01 1982.

[64] J. J. Kalker, *Three-Dimensional Elastic Bodies in Rolling Contact*: Springer, 2010.

[65] E. A. H. Vollebregt, "User guide for CONTACT, J.J. Kalker's variational contact model," Delft University, 2012.

[66] K. E. Zaazaa and A. L. Schwab, "Review of Joost Kalker's Wheel-Rail Contact Theories and Their Implementation in Multibody Codes," *ASME Conference Proceedings,* vol. 2009, pp. 1889-1900, 2009.

[67] Lubrication, W. Group, D. J. Haines, and E. Ollerton, "Contact Stress Distributions on Elliptical Contact Surfaces Subjected to Radial and Tangential Forces," *Proceedings of the Institution of Mechanical Engineers,* vol. 177, pp. 95-114, June 1, 1963 1963.

[68] J. J. Kalker, "On the rolling contact of two elastic bodies in the presence of dry friction," Doctoral Thesis, Delft, 1967.

[69] J. J. Kalker, "The tangential force transmitted by two elastic bodies rolling over each other with pure creepage," *Wear,* vol. 11, pp. 421-430, 1968.

[70] O. Polach, "A fast wheel–rail forces calculation computer code " *Vehicle Syst. Dyn. Suppl,* vol. 33, pp. 728–739, 1999.

[71] O. Polach, "Creep forces in simulations of traction vehicles running on adhesion limit," *Wear,* vol. 258, pp. 992-1000, 2005.

[72] M. Blundell, D. Harty, and E. Society of Automotive, *Multibody systems approach to vehicle dynamics*. Warrendale, Pa: Published on behalf of Society of Automotive Engineers Inc, 2004.

[73] O. C. Zienkiewicz, R. L. Taylor, and J. Z. Zhu, *The finite element method: its basis and fundamentals*. Oxford: Butterworth Heinemann, 2013.

[74] E. Meli, S. Magheri, and M. Malvezzi, "Development and implementation of a differential elastic wheel-rail contact model for multibody applications," *Vehicle System Dynamics,* vol. 49, pp. 969-1001, 2011.

[75] S. Falomi, M. Malvezzi, E. Meli, and A. Rindi, "Determination of wheel–rail contact points: comparison between classical and neural network based procedures," *Meccanica,* vol. 44, pp. 661-686, 2009.

[76] S. Magheri, M. Malvezzi, E. Meli, and A. Rindi, "An innovative wheel–rail contact model for multibody applications," *Wear,* vol. 271, pp. 462-471, 2011.

[77] E. Meli and A. Ridolfi, "An innovative wheel–rail contact model for railway vehicles under degraded adhesion conditions," *Multibody System Dynamics,* pp. 1-29, 2013.

[78] G. Schupp, C. Weidemann, and L. Mauer, "Modelling the contact between wheel and rail within multibody system simulation," *Vehicle System Dynamics,* vol. 41, pp. 349-364, 2004.

[79] H. Sugiyama, K. Araki, and Y. Suda, "On-line and off-line wheel/rail contact algorithm in the analysis of multibody railroad vehicle systems," *Journal of Mechanical Science and Technology,* vol. 23, pp. 991-996, 2009.

[80] H. Sugiyama, K. Araki, and Y. Suda, "Development of wheel/rail contact procedure in multibody railroad vehicle dynamics," *Nihon Kikai Gakkai Ronbunshu, C Hen/Transactions of the Japan Society of Mechanical Engineers, Part C,* vol. 75, pp. 607-615, 2009.

[81] K. E. Zaazaa, "Elastic force model for wheel/rail contact in multibody railroad vehicle systems," Dissertation/Thesis, University of Illinois, Chicago, 2003.

[82] J. Xiaoyu and J. Xuesong, "Numerical simulation of wheel rolling over rail at high-speeds," *Wear,* vol. 262, pp. 666-671, 2007.

[83] W. Daves and F. D. Fischer, "Modelling of the plastification near the rough surface of a rail by the wheel–rail contact," *Wear,* vol. 253, pp. 241-246, 2002.

[84] L. Ramanan, R. Krishna Kumar, and R. Sriraman, "Thermo-mechanical finite element analysis of a rail wheel," *International Journal of Mechanical Sciences,* vol. 41, pp. 487-505, 1999.

[85] J. Ahlström and B. Karlsson, "Modelling of heat conduction and phase transformations during sliding of railway wheels," *Wear,* vol. 253, pp. 291-300, 2002.

[86] T. C. Kennedy, C. Plengsaard, and R. F. Harder, "Transient heat partition factor for a sliding railcar wheel," *Wear,* vol. 261, pp. 932-936, 2006.

[87] R. Lundén, "Contact region fatigue of railway wheels under combined mechanical rolling pressure and thermal brake loading," *Wear,* vol. 144, pp. 57-70, 1991.

[88] A. Chudzikiewicz and A. Myśliński, "Thermoelastic wheel–rail contact problem with elastic graded materials," *Wear,* vol. 271, pp. 417-425, 2011.

[89] W. Qi, J. Zhang, C. Sun, and S. Wang, "Finite Element Analysis of Wheel-Rail Thermal-Contact Coupling When the Wheel's Sliding," in *Information Engineering and Computer Science, 2009. ICIECS 2009. International Conference on*, 2009, pp. 1-4.

[90] J. Zhang, S. Sun, and X. Jin, "Numerical Simulation of Two-Point Contact Between Wheel and Rail," *Acta Mechanica Solida Sinica,* vol. 22, pp. 352-359, 2009.

[91] M. A. Arslan and O. Kayabaşı, "3-D Rail–Wheel contact analysis using FEA," *Advances in Engineering Software,* vol. 45, pp. 325-331, 2012.

[92] Hibbitt, *ABAQUS Theory Manual (version 6.8)*: Hibbitt, Karlsson and Sorenson Inc., 2003.

[93] Z. Wen, L. Wu, W. Li, X. Jin, and M. Zhu, "Three-dimensional elastic–plastic stress analysis of wheel–rail rolling contact," *Wear,* vol. 271, pp. 426-436, 2011.

[94] Y. Jiang, B. Xu, and H. Sehitoglu, *Three-dimensional elastic-plastic stress analysis of rolling contact* vol. 124. New York, NY: American Society of Mechanical Engineers, 2002.

[95] X. Zhao, Z. L. C. Esveld, and R. Dollevoet, "The Dynamic Stress State of the Wheel-Rail Contact," *Proceedings of the 2nd IASME/WSEAS Int. Conf. on Continuum Mechanics,* pp. 127-133, 2007.

[96] S. Kumar and S. P. Singh, "Threshold Stress Criterion in New Wheel/Rail Interaction for Limiting Rail Damage Under Heavy Axle Loads," *Journal of Manufacturing Science and Engineering,* vol. 114, pp. 284-288, 1992.

[97] P. J. Mutton and E. F. Alvarez, "Failure modes in aluminothermic rail welds under high axle load conditions," *Engineering Failure Analysis,* vol. 11, pp. 151-166, 2004.

[98] J. Deng, Q. Liu, F. Wang, and X. Wu, "Influence of train velocity on rail contact fatigue damage and how to select rail for high-speed," *Gang Tie Fan Tai (Iron Steel Vanadium Titanium),* vol. 27, pp. 48-54, 2006.

[99] N. Correa, O. Oyarzabal, E. G. Vadillo, J. Santamaria, and J. Gomez, "Rail corrugation development in high speed lines," *Wear,* vol. 271, pp. 2438-2447, 2011.

[100] V. M. Bogdanov, A. P. Goryachev, I. G. Goryacheva, M. N. Dobychin, S. M. Zakharov, V. G. Krivonogov, I. A. Soldatenkov, and O. G. Chekina, "Study of wheel-rail friction, wear and cumulative damage," *Journal of Friction and Wear,* vol. 17, pp. 7-20, 1996.

[101] W. J. Wang, T. F. Liu, H. Y. Wang, Q. Y. Liu, M. H. Zhu, and X. S. Jin, "Influence of friction modifiers on improving adhesion and surface damage of wheel/rail under low adhesion conditions," *Tribology International,* vol. 75, pp. 16-23, 2014.

[102] R. Lewis and U. Olofsson, *Wheel-rail interface handbook*. Oxford: CRC Press, 2009.

[103] B. Croft, E. Vollebregt, and D. Thompson, "An Investigation of Velocity-Dependent Friction in Wheel-Rail Rolling Contact," in *Noise and Vibration Mitigation for Rail Transportation Systems*. vol. 118, T. Maeda*, et al.*, Eds., ed: Springer Berlin / Heidelberg, 2012, pp. 33-41.

[104] E. A. H. Vollebregt and H. M. Schuttelaars, "Quasi-static analysis of two-dimensional rolling contact with slip-velocity dependent friction," *Journal of Sound and Vibration,* vol. 331, pp. 2141-2155, 2012.

[105] M. A. Heckl and I. D. Abrahams, "Curve squeal of train wheels, part 1: mathematical model for its generation," *Journal of Sound and Vibration,* vol. 229, pp. 669-693, 2000.

[106] J. G. Giménez, A. Alonso, and E. Gómez *, "Introduction of a friction coefficient dependent on the slip in the FastSim algorithm," *Vehicle System Dynamics,* vol. 43, pp. 233-244, 2005/04/01 2005.

[107] J. Piotrowski, "Kalker's algorithm Fastsim solves tangential contact problems with slip-dependent friction and friction anisotropy," *VEHICLE SYSTEM DYNAMICS,* vol. 48, pp. 869-889, 2010/07/01 2010.

[108] A. Rovira, A. Roda, R. Lewis, and M. B. Marshall, "Application of Fastsim with variable coefficient of friction using twin disc experimental measurements," *Wear,* vol. 274–275, pp. 109-126, 2012.
[109] V. Reddy, G. Chattopadhyay, P.-O. Larsson-Kråik, and D. J. Hargreaves, "Modelling and analysis of rail maintenance cost," *International Journal of Production Economics,* vol. 105, pp. 475-482, 2007.
[110] Windarta, M. B. Sud, and M. B. Baharom, "Prediction of contact temperature on interaction between rail and wheel materials using pin-on-disc method," *Journal of Applied Sciences,* 2012.
[111] J. Sundh and U. Olofsson, "Relating contact temperature and wear transitions in a wheel–rail contact," *Wear,* vol. 271, pp. 78-85, 2011.
[112] E. A. Gallardo-Hernandez, R. Lewis, and R. S. Dwyer-Joyce, "Temperature in a twin-disc wheel/rail contact simulation," *Tribology International,* vol. 39, pp. 1653-1663, 2006.
[113] T. Vernersson, "Thermally induced roughness of tread braked railway wheels: Part 2: modelling and field measurements," *Wear,* vol. 236, pp. 106-116, 1999.
[114] T. Vernersson, "Thermally induced roughness of tread-braked railway wheels: Part 1: brake rig experiments," *Wear,* vol. 236, pp. 96-105, 1999.
[115] K. D. Cole, C. M. Tarawneh, A. A. Fuentes, B. M. Wilson, and L. Navarro, "Thermal models of railroad wheels and bearings," *Internation Journal of Heat and Mass Transfer,* vol. 53, pp. 1636-1645, 2010.
[116] M. A. Tanvir, "Temperature rise due to slip between wheel and rail—an analytical solution for hertzian contact," *Wear,* vol. 61, pp. 295-308, 1980.
[117] F. D. Fischer, E. Werner, and W. Y. Yan, "Thermal stresses for frictional contact in wheel-rail systems," *Wear,* vol. 211, pp. 156-163, 1997.
[118] F. D. Fischer, W. Daves, and E. A. Werner, "On the temperature in the wheel–rail rolling contact," *Fatigue & Fracture of Engineering Materials & Structures,* vol. 26, pp. 999-1006, 2003.
[119] I. M. Widiyarta, F. J. Franklin, and A. Kapoor, "Modelling thermal effects in ratcheting-led wear and rolling contact fatigue," *Wear,* vol. 265, pp. 1325-1331, 2008.
[120] M. Ertz and K. Knothe, "A comparison of analytical and numerical methods for the calculation of temperatures in wheel/rail contact," *Wear,* vol. 253, pp. 498-508, 2002.
[121] A. M. S. Asih, K. Ding, and A. Kapoor, "Modelling the Effect of Steady State Wheel Temperature on Rail Wear," *Tribology Letters,* vol. 49, pp. 239-249, 2013/01/01 2013.
[122] M. Ertz and K. Knothe, "Thermal stresses and shakedown in wheel/rail contact," *Archive of Applied Mechanics,* vol. 72, pp. 715-729, 2003.
[123] O. O. Evtushenko, S. Konieczny, and V. M. Semerak, "Investigation of the Temperature Field Induced in the Process of Friction of a Wheel against a Rail," *Materials Science,* vol. 38, pp. 709-716, 2002/09/01 2002.
[124] V. Gupta, G. T. Hahn, P. C. Bastias, and C. A. Rubin, "Thermal-Mechanical Modelling of the Rolling-Plus-Sliding With Frictional Heating of a Locomotive Wheel," *Journal of Manufacturing Science and Engineering,* vol. 117, pp. 418-422, 1995.
[125] M. Spiryagin, K. S. Lee, H. H. Yoo, O. Kashura, and S. Popov, "Numerical calculation of temperature in the wheel–rail flange contact and implications for lubricant choice," *Wear,* vol. 268, pp. 287-293, 2010.

[126] K. Knothe and S. Liebelt, "Determination of temperatures for sliding contact with applications for wheel-rail systems," *Wear,* vol. 189, pp. 91-99, 1995.
[127] F. J. Franklin, T. Chung, and A. Kapoor, "Ratcheting and fatigue-led wear in rail–wheel contact," *Fatigue & Fracture of Engineering Materials & Structures,* vol. 26, pp. 949-955, 2003.
[128] J. Ahlström and B. Karlsson, "Microstructural evaluation and interpretation of the mechanically and thermally affected zone under railway wheel flats," *Wear,* vol. 232, pp. 1-14, 1999.
[129] Y.-C. Chen and S.-Y. Lee, "Elastic-Plastic Wheel-Rail Thermal Contact on Corrugated Rails During Wheel Braking," *Journal of Tribology,* vol. 131, pp. 011401-011401, 2008.
[130] W. Lojkowski, M. Djahanbakhsh, G. Bürkle, S. Gierlotka, W. Zielinski, and H. J. Fecht, "Nanostructure formation on the surface of railway tracks," *Materials Science and Engineering: A,* vol. 303, pp. 197-208, 2001.
[131] R. I. Carroll and J. H. Beynon, "Rolling contact fatigue of white etching layer: Part 2. Numerical results," *Wear,* vol. 262, pp. 1267-1273, 2007.
[132] R. I. Carroll and J. H. Beynon, "Rolling contact fatigue of white etching layer: Part 1: Crack morphology," *Wear,* vol. 262, pp. 1253-1266, 2007.
[133] M. Shaban Ghazani and B. Eghbali, "Pressure induced martensite transformation in plain carbon steel," *Materials Science and Technology,* vol. 27, pp. 1599-1601, 2011.
[134] A. F. Bower and K. L. Johnson, "Plastic flow and shakedown of the rail surface in repeated wheel-rail contact," *Wear,* vol. 144, pp. 1-18, 1991.
[135] G. E. Dieter, *Mechanical metallurgy*. New York: McGraw-Hill, 1986.
[136] A. Kapoor and J. A. Williams, "Shakedown limits in rolling-sliding point contacts on an anisotropic halfspace," *Wear,* vol. 191, pp. 256-260, 1996.
[137] A. Kapoor and K. L. Johnson, "Plastic Ratchetting as a Mechanism of Metallic Wear," *Proceedings of the Royal Society of London. Series A: Mathematical and Physical Sciences,* vol. 445, pp. 367-384, 1994.
[138] J. W. Ringsberg, "Life prediction of rolling contact fatigue crack initiation," *International Journal of Fatigue,* vol. 23, pp. 575-586, 2001.
[139] J. W. Ringsberg, M. Loo-Morrey, B. L. Josefson, A. Kapoor, and J. H. Beynon, "Prediction of fatigue crack initiation for rolling contact fatigue," *International Journal of Fatigue,* vol. 22, pp. 205-215, 2000.
[140] J. Xiao, F. Zhang, and L. Qian, "Numerical simulation of stress and deformation in a railway crossing," *Engineering Failure Analysis,* vol. 18, pp. 2296-2304, 2011.
[141] M. Busquet, L. Baillet, C. Bordreuil, and Y. Berthier, "3D finite element investigation on the plastic flows of rolling contacts—correlation with railhead microstructural observations," *Wear,* vol. 258, pp. 1071-1080, 2005.
[142] C. P, "Predicting the wear of rails on curves from laboratory data," *Wear,* vol. 181-183, Part 1, pp. 11-19, 1995.
[143] J. Tomas, "Prediction of wheel profile wear—comparisons with field measurements," *Wear,* vol. 253, pp. 89-99, 2002.
[144] S. C. Lim, "Recent developments in wear-mechanism maps," *Tribology International,* vol. 31, pp. 87-97, 1998.
[145] Y. Jin, M. Ishida, and A. Namura, "Experimental simulation and prediction of wear of wheel flange and rail gauge corner," *Wear,* vol. 271, pp. 259-267, 2011.

[146] G. Vasić, F. J. Franklin, and D. I. Fletcher, "Influence of partial slip and direction of traction on wear rate in wheel-rail contact," *Wear,* vol. 270, pp. 163-171, 2011.
[147] http://en.wikipedia.org/wiki/Archard_equation.
[148] W. J. Wang, J. Guo, Q. Y. Liu, M. H. Zhu, and Z. R. Zhou, "Study on relationship between oblique fatigue crack and rail wear in curve track and prevention," *Wear,* vol. 267, pp. 540-544, 2009.
[149] R. Lewis and R. S. Dwyer-Joyce, "Wear mechanisms and transitions in railway wheel steels," *Proceedings of the Institution of Mechanical Engineers, Part J: Journal of Engineering Tribology,* vol. 218, pp. 467-478, 2004.
[150] C. Chongyi, W. Chengguo, and J. Ying, "Study on numerical method to predict wheel/rail profile evolution due to wear," *Wear,* vol. 269, pp. 167-173, 2010.
[151] J. Seo, S. Kwon, H. Jun, and D. Lee, "Fatigue crack growth behavior of surface crack in rails," *Procedia Engineering,* vol. 2, pp. 865-872, 2010.
[152] G. Baumann, H. J. Fecht, and S. Liebelt, "Formation of white-etching layers on rail treads," *Wear,* vol. 191, pp. 133-140, 1996.
[153] M. Takikawa and Y. Iriya, "Laboratory simulations with twin-disc machine on head check," *Wear,* vol. 265, pp. 1300-1308, 2008.
[154] Y. Zhou, S. Wang, T. Wang, Y. Xu, and Z. Li, "Field and laboratory investigation of the relationship between rail head check and wear in a heavy-haul railway," *Wear,* vol. 315, pp. 68-77, 2014.
[155] R. Heyder and M. Brehmer, "Empirical studies of head check propagation on the DB network," *Wear,* vol. 314, pp. 36-43, 2014.
[156] A. Kapoor, D. I. Fletcher, F. J. Franklin, A. E. Beagles, M. Burstow, R. Allen, G. Evans, and J. Jaiswal, "Management and Understanding of Rolling Contact Fatigue " Rail Safety and Standards Board 2006.
[157] M. Pletz, W. Daves, W. Yao, W. Kubin, and S. Scheriau, "Multi-scale finite element modeling to describe rolling contact fatigue in a wheel–rail test rig," *Tribology International,* vol. 80, pp. 147-155, 2014.
[158] J. W. Ringsberg and T. Lindbäck, "Rolling contact fatigue analysis of rails inculding numerical simulations of the rail manufacturing process and repeated wheel-rail contact loads," *International Journal of Fatigue,* vol. 25, pp. 547-558, 2003.
[159] B. Dirks and R. Enblom, "Prediction model for wheel profile wear and rolling contact fatigue," *Wear,* vol. 271, pp. 210-217, 2011.
[160] W. Jianxi, X. Yude, L. Songliang, and W. Liying, "Probabilistic prediction model for initiation of RCF cracks in heavy-haul railway," *International Journal of Fatigue,* vol. 33, pp. 212-216, 2011.
[161] J. W. Ringsberg and A. Bergkvist, "On propagation of short rolling contact fatigue cracks," *Fatigue & Fracture of Engineering Materials & Structures,* vol. 26, pp. 969-983, 2003.
[162] S. Bogdański and M. W. Brown, "Modelling the three-dimensional behaviour of shallow rolling contact fatigue cracks in rails," *Wear,* vol. 253, pp. 17-25, 2002.
[163] Y. Liu, L. Liu, and S. Mahadevan, "Analysis of subsurface crack propagation under rolling contact loading in railroad wheels using FEM," *Engineering Fracture Mechanics,* vol. 74, pp. 2659-2674, 2007.

[164] J. Seo, S. Kwon, H. Jun, and D. Lee, "Numerical stress analysis and rolling contact fatigue of White Etching Layer on rail steel," *International Journal of Fatigue,* vol. 33, pp. 203-211, 2011.
[165] B. Stanisław, "Liquid–solid interaction at opening in rolling contact fatigue cracks," *Wear,* vol. 258, pp. 1273-1279, 2005.
[166] S. Bogdański and P. Lewicki, "3D model of liquid entrapment mechanism for rolling contact fatigue cracks in rails," *Wear,* vol. 265, pp. 1356-1362, 2008.
[167] M. Kaneta and Y. Murakami, "Effects of oil hydraulic pressure on surface crack growth in rolling/sliding contact," *Tribology International,* vol. 20, pp. 210-217, 1987.
[168] U. Olofsson and R. Nilsson, "Surface cracks and wear of rail: A full-scale test on a commuter train track," *Proceedings of the Institution of Mechanical Engineers, Part F: Journal of Rail and Rapid Transit,* vol. 216, pp. 249-264, July 1, 2002 2002.
[169] K. D. Van and M. H. Maitournam, "Rolling contact in railways: modelling, simulation and damage prediction," *Fatigue & Fracture of Engineering Materials & Structures,* vol. 26, pp. 939-948, 2003.
[170] J. Seo, S. Kwon, and D. Lee, "Effects of surface defects on rolling contact fatigue of rail," *Procedia Engineering,* vol. 10, pp. 1274-1278, 2011.
[171] http://www.ptc.com.
[172] "ESR 0001-G RSU APPENDIX G DRAWINGS," ed: Engineering Standard Rolling Stock, Jun 2010.
[173] "AS 1085.1-2002/Amdt 1-2005 : Railway track materials - Steel rails," ed: Standards Australia, 2005.
[174] http://www.lstc.com/.
[175] http://www.ansys.com.
[176] http://www.csimsoft.com.
[177] C. Cole, M. Spiryagin, Y. Q. Sun, K. D. Vo, K. A. Tieu, H. Zhu, and P. Meehan, "R3. 119: Locomotive Adhesion, final report 2013 " CRC for Rail Innovation, Australia, 2013.
[178] M. B. Kerr, "Technical Report TR.169 - AC High Adhesion Locomotives," 2011.
[179] B. Allotta, E. Meli, A. Ridolfi, and A. Rindi, "Development of an innovative wheel–rail contact model for the analysis of degraded adhesion in railway systems," *Tribology International,* vol. 69, pp. 128-140, 2014.
[180] P. Blau, "Embedding Wear Models into Friction Models," *Tribology Letters,* vol. 34, pp. 75-79, 2009/04/01 2009.
[181] "ESC 230 Sleeper and track support," ed: RailCorp Engineering Standard, 2012.
[182] J. O. Hallquist, *LS-DYNA Theoretical Manual.*: Livermore Software Technology, 2006.
[183] *Ansys Theory Reference for the Mechanical APDL and Mechanical Applications*: ANSYS, Inc., 2009.
[184] D. M. Steffens, "Identification and Development of a Model of Railway Track Dynamic Behaviour," Masters by Research, 2005.
[185] http://www.transport.nsw.gov.au/railcorp.
[186] J. Smith and C. K. Liu, "Stresses due to tangential and normal loads on an elastic solid with application to some contact stress problems," *Journal of Applied Mechanics,* vol. 20, pp. 157-166, 1953.

[187] A. R. S. Ponter, A. D. Hearle, and K. L. Johnson, "Application of the kinematical shakedown theorem to rolling and sliding point contacts," *Journal of the Mechanics and Physics of Solids,* vol. 33, pp. 339-362, 1985.

[188] J. Farley, L. C. Wrobel, and K. Mao, "Low cycle fatigue simulation and fatigue life prediction of multilayer coated surfaces," *Wear,* vol. 269, pp. 639-646, 2010.

[189] W. Huimin and J. M. Wang, "Non-Hertzian conformal contact at wheel/rail interface," in *Railroad Conference, 1995., Proceedings of the 1995 IEEE/ASME Joint*, 1995, pp. 137-144.

[190] D. F. Cannon and H. Pradier, "Rail rolling contact fatigue Research by the European Rail Research Institute," *Wear,* vol. 191, pp. 1-13, 1996.

[191] F. J. Franklin and A. Kapoor, "Modelling wear and crack initiation in rails," *Proceedings of the Institution of Mechanical Engineers, Part F: Journal of Rail and Rapid Transit,* vol. 221, pp. 23-33, 2007.

[192] M. Akama, "Development of Finite Element Model for Analysis of Rolling Contact Fatigue Cracks in Wheel/Rail Systems," *Quarterly Report of RTRI,* vol. 48, pp. 8-14, 2007.

[193] *LS-DYNA Keyword User's Manual* vol. 2: Material models: Livermore Software Technology Corporation (LSTC), March 04, 2013.

[194] Z. Li, X. Zhao, C. Esveld, R. Dollevoet, and M. Molodova, "An investigation into the causes of squats—Correlation analysis and numerical modeling," *Wear,* vol. 265, pp. 1349-1355, 2008.

[195] Z. Li, R. Dollevoet, M. Molodova, and X. Zhao, "Squat growth—Some observations and the validation of numerical predictions," *Wear,* vol. 271, pp. 148-157, 2011.

[196] P. Clayton and M. B. P. Allery, "Metallurgical Aspects of Surface Damage Problems in Rails," *Canadian Metallurgical Quarterly,* vol. 21, pp. 31-46, 1982/01/01 1982.

[197] L. Wang, A. Pyzalla, W. Stadlbauer, and E. A. Werner, "Microstructure features on rolling surfaces of railway rails subjected to heavy loading," *Materials Science and Engineering: A,* vol. 359, pp. 31-43, 2003.

[198] G. P. Tew, S. Marich, and P. J. Mutton, "A review of track design procedures - Rails," Railways of Australia Publication, 1991.

[199] K. Twidle, S. Soeleiman, G. P. Tew, B. H. P. Company, and R. o. Australia, *The Enhanced Rail Selection Module for the Railways of Australia*: Broken Hill Company Proprietary Limited, 1991.

[200] A. Matsumoto, Y. Sato, H. Ono, M. Tanimoto, Y. Oka, and E. Miyauchi, "Formation mechanism and countermeasures of rail corrugation on curved track," *Wear,* vol. 253, pp. 178-184, 2002.

[201] Y. Sato, A. Matsumoto, and K. Knothe, "Review on rail corrugation studies," *Wear,* vol. 253, pp. 130-139, 2002.

[202] S. L. Grassie, "Rail corrugation: advances in measurement, understanding and treatment," *Wear,* vol. 258, pp. 1224-1234, 2005.

[203] S. Marich, "Comments on some possible consequences associated with high tractive effort locomotives," Rail Services Australia 2013.

[204] P. J. Mutton and S. Marich, "Requirements for Wheel and Rail Materials," presented at the 6th International Rail Track Conference, Melbourne, Australia, March 1986.

[205] K. D. Vo, A. K. Tieu, H. T. Zhu, and P. B. Kosasih, "A comparison of stress and heat generated by AC versus DC locomotives under diverse operational conditions," *Wear,* 2014, revision has been submitted.
[206] P. Clark, *The Australian Locomotive Guide*: Rosenberg Publishing, 2012.
[207] http://en.wikipedia.org/wiki/UGL_Rail_C44aci.
[208] http://en.wikipedia.org/wiki/Downer_EDI_Rail_GT46C_ACe.
[209] B. Bhushan, *Modern tribology handbook*. London: CRC Press, 2001.
[210] M. Spiryagin, C. Cole, Y. Q. Sun, M. McClanachan, V. Spiryagin, and T. McSweeney, *Design and Simulation of Rail Vehicles*: Taylor & Francis, 2014.
[211] M. Spiryagin, C. f. R. Engineering, Y. Q. Sun, C. R. Cole, A. George, S. Simson, and I. Persson, "Influence of Lateral Components of Coupler Forces on the Wheel-Rail Contact Forces for Hauling Locomotives under Traction," presented at the the 13th Mini Conference on Vehicle System Dynamics, Identification and Anomalies, Budapest, Hungary, 2012.
[212] M. Spiryagin, A. George, Y. Q. Sun, C. Cole, T. McSweeney, and S. Simson, "Investigation of locomotive multibody modelling issues and results assessment based on the locomotive model acceptance procedure," *Proceedings of the Institution of Mechanical Engineers, Part F: Journal of Rail and Rapid Transit,* vol. 227, pp. 453-468, September 1, 2013 2013.
[213] M. Spiryagin, A. George, Y. Q. Sun, and C. R. Cole, "Locomotive model acceptance procedure based on international standards," presented at the The 2nd Joint International Conference on Multibody System Dynamics, Stuttgart, Germany, 2012.
[214] S. Simson and S. Mohan, "Temperature calculations for rails under frictional contact - Progress report on R3-105," CRC for Rail Innovation , December, 2009.
[215] A. M. S. Asih, K. Ding, and A. Kapoor, "Modelling rail wear transition and mechanism due to frictional heating," *Wear,* vol. 284–285, pp. 82-90, 2012.
[216] V. Gupta, G. T. Hahn, P. C. Bastias, and C. A. Rubin, "Thermal-Mechanical Modelling of the Rolling-Plus-Sliding With Frictional Heating of a Locomotive Wheel," *Journal of Engineering for Industry,* vol. 117, pp. 418-422, 1995.
[217] V. Gupta, G. T. Hahn, P. C. Bastias, and C. A. Rubin, "Calculations of the frictional heating of a locomotive wheel attending rolling plus sliding," *Wear,* vol. 191, pp. 237-241, 1996.
[218] J. Takahashi, K. Kawakami, and M. Ueda, "Atom probe tomography analysis of the white etching layer in a rail track surface," *Acta Materialia,* vol. 58, pp. 3602-3612, 2010.
[219] W. Daniel, "Final Report on the Rail Squat Project R3.105," CRC for Rail Innovation, 2013.
[220] S. Pal, W. J. T. Daniel, C. H. G. Valente, A. Wilson, and A. Atrens, "Surface damage on new AS60 rail caused by wheel slip," *Engineering Failure Analysis,* vol. 22, pp. 152-165, 2012.
[221] F. Braghin, R. Lewis, R. S. Dwyer-Joyce, and S. Bruni, "A mathematical model to predict railway wheel profile evolution due to wear," *Wear,* vol. 261, pp. 1253-1264, 2006.
[222] J. F. Archard, "Contact and Rubbing of Flat Surfaces," *Journal of Applied Physics,* vol. 24, pp. 981-988, 1953.

[223] S. Kalpakjian and S. R. Schmid, *Manufacturing processes for engineering materials*. Upper Saddle River, N.J: Prentice Hall, 2008.
[224] K. D. Vo, A. K. Tieu, H. T. Zhu, and P. B. Kosasih, "The influence of high temperature due to high adhesion on rail damage," *Wear,* 2014, accepted.
[225] J. Goldak, A. Chakravarti, and M. Bibby, "A new finite element model for welding heat sources," *Metallurgical Transactions B,* vol. 15, pp. 299-305, 1984/06/01 1984.
[226] *LS-DYNA keyword user's manual* vol. 1: Livermore Software Technology Corporation (LSTC), March 04, 2013.
[227] B. Talamini, J. Gordon, and A. B. Perlman, "Investigation of the Effects of Sliding on Wheel Tread Damage," in *ASME International Mechanical Engineering Congress and Exposition, November*, 2005, pp. 5-11.
[228] M. Spiryagin, A. George, Y. Sun, and C. Cole, "Final report Project R3. 119: Locomotive Adhesion, Appendix 2: MBS simulation results for locomotive models," CRC for Rail Innovation 2013.
[229] O. Corporation, *Origin 8 User Guide*. Northampton, USA, 2007.
[230] http://www.originlab.com/.
[231] G. R. Speich, V. A. Demarest, and R. L. Miller, "Formation of austenite during intercritical annealing of dual-phase steels," *Metallurgical transactions. A, Physical metallurgy and materials science,* vol. 12 A, pp. 1419-1428, 1981.
[232] R. A. Ganeev, "Low-power laser hardening of steels," *Journal of Materials Processing Technology,* vol. 121, pp. 414-419, 2002.
[233] H. Krause and G. Poll, "Wear of wheel-rail surfaces," *Wear,* vol. 113, pp. 103-122, 1986.
[234] http://en.wikipedia.org/wiki/Vickers_hardness_test.
[235] I. U. Wickramasinghe, D. Hargreaves, and D. De Pellegrin, "Predicting crack initiation due to ratchetting in rail heads using critical element analysis," *International Journal of Materials Science and Engineering,* vol. 77, pp. 850-856, 2013.
[236] I. U. Wickramasinghe, "Investigation of surface ratchetting due to rail/wheel contact," Doctor of philosophy, Faculty of Science and Engineering, Queensland University of Technology, Queensland, Australia, 2013.
[237] J. W. Ringsberg, "Cyclic ratchetting and failure of a pearlitic rail steel," *Fatigue & Fracture of Engineering Materials & Structures,* vol. 23, pp. 747-758, 2000.
[238] D. Canadinc, H. Sehitoglu, and K. Verzal, "Analysis of surface crack growth under rolling contact fatigue," *International Journal of Fatigue,* vol. 30, pp. 1678-1689, 2008.